POLYTECHNIQUE MONTRÉAL

affiliée à l'Université de Montréal

Effect of shot peening on the axial fatigue life of 300M steel

AMRITA BAG

Département de génie mécanique

Thèse présentée en vue de l'obtention du diplôme de *Philosophiæ Doctor*

Génie mécanique

Septembre 2019

POLYTECHNIQUE MONTRÉAL

affiliée à l'Université de Montréal

Cette thèse intitulée :

Effect of shot peening on the axial fatigue life of 300M steel

présentée par **Amrita BAG**

en vue de l'obtention du diplôme de *Philosophiæ Doctor*

a été dûment acceptée par le jury d'examen constitué de :

Aurelian VADEAN, président
Myriam BROCHU, membre et directrice de recherche
Martin LÉVESQUE, membre et codirecteur de recherche
Nihad BEN SALAH, membre
Mario GUAGLIANO, membre externe

DEDICATION

To my grandparents, brother and parents

"The mind, once stretched by a new idea, never returns to its original dimensions."

—Ralph Waldo Emerson

ACKNOWLEDGEMENTS

First of all, I would like to acknowledge my deepest gratitude to Prof. Myriam Brochu and Prof. Martin Lévesque for providing me this wonderful opportunity of pursuing a Ph.D. at Polytechnique Montréal. If not for your valuable feedback, guidance and expertise, the completion of this thesis would not have been possible. You were always available to address my queries and give me a nudge in the right direction with your constructive criticism, unwavering support and encouragement. You have been the perfect mentors to me.

I would like to thank the wonderful group of people with whom I had the privilege to work with throughout the course of my Ph.D., particularly Hongyan for the finite element modelling, Dorian for the residual stress measurement, Fubin, Thierry, Charles, Julio, Rubo, Jihane, Paul and not to forget my interns Rohan and Diego. Special thanks to Ilyass for helping me with the French course during my first year at Polytechnique and Yahya for helping me with 3D printing. Each of you have helped me gather a fundamental piece to complete this life size puzzle.

I would not miss this opportunity to acknowledge the excellent technical support provided by Josée Laviolette, Isabelle Nowlan, Martin Cardonne, and Jean-François Daigle. I also offer my sincere gratitude to Prof. Philippe Bocher for his expert comments during my article redactions. He was extremely patient and pointed out the nitty gritty to be considered to make sure my writing truly highlighted my efforts.

I would like to thank the financial partners of the project, namely Consortium of Research and Innovation in Aerospace Québec (CRIAQ), the Natural Sciences and Engineering Research Council of Canada (NSERC), Pratt & Whitney Canada, Bell Helicopter Textron Canada, L3-Communications MAS, Héroux Devtek and the Mathematics of Information Technology and Complex Systems (MITACS). The collaborators were extremely co-operative and resourceful, and actively participated to bring this project to fruition. I would also like to acknowledge the assistance received from Mr. Arnaud Divialle and Ms. Cristina Del Vasto during my internship at Héroux Devtek.

I would also like to express my sincere gratitude to the members of my jury for giving their valuable feedback and suggestions that helped improve the thesis appreciably.

Over the years, I have truly come to admire this city, its people and their culture. But the people who made me really feel at home were Bikram and Sayani. You have been a blessing in disguise and have gifted me moments I will cherish forever. I would also like to thank all my friends in India and Canada for including me in your lives and for being in mine.

Finally, I owe my all to my beloved parents, Asit and Mina, my brother Tuhin, and my grandparents whose never ending love, faith and support have kept me going for all these years.

RÉSUMÉ

Le grenaillage est un procédé de déformation à froid couramment utilisé en fabrication aérospatiale. Ce procédé consiste à assujettir la surface d'une pièce métallique à un bombardement par billes projetées à grande vitesse. Il en résulte une déformation plastique de la surface accompagnée de contraintes résiduelles de compression et de matière écrouie dans la couche superficielle. Les contraintes résiduelles de compression et l'écrouissage s'opposent à amorçage et à la propagation des fissures. Ces effets sont donc favorables à la durée de vie en fatigue des pièces. Les effets désirables du grenaillage sont toutefois en compétition avec l'augmentation de la rugosité qui accompagne ce procédé, ce qui peut augmenter la concentration des contraintes et réduire la durée de vie en fatigue. Par conséquent, il est critique de régler les conditions opératoires du grenaillage afin de générer des contraintes résiduelles de compression suffisantes tout en conservant une rugosité de surface minimale. Les industries aérospatiales effectuent actuellement les opérations de grenaillage avec des réglages prédéfinis et sans faire appel aux mécanismes physiques sous-jacents.

Cette étude approfondit la connaissance des effets des réglages du grenaillage sur la durée de vie en fatigue de l'acier 300M sur un axe science des matériaux. Cet alliage sert habituellement dans les trains d'atterrissage des aéronefs. Cette étude cerne les caractéristiques qui influencent la durée de vie en fatigue du matériau pour les conditions d'essai fournies. L'étude sert aussi à déterminer si ces opérations de grenaillage sont bénéfiques et à quantifier ce bénéfice. Les résultats pourront servir aux industries aérospatiales pour optimiser leurs opérations de grenaillage sans devoir programmer des séries d'essais coûteuses.

Une série rigoureuse d'essais a été complétée afin de caractériser les propriétés globales micro structurelles (la taille des grains) et macro structurelles (propriétés mécaniques monotones et cycliques) du matériau. Les essais ont aussi évalué le comportement des fissures longues. Des essais de fatigue d'éprouvettes grenaillées et non-grenaillées ont été effectués par la suite. Deux amplitudes de contrainte ont servi aux essais de fatigue, soit 55% et 65% de la limite d'élasticité. La rugosité de surface, les contraintes résiduelles, et la relaxation des contraintes durant le chargement cyclique ont été quantifiés. La propagation des fissures courtes a aussi été étudiée. Les caractéristiques menant à l'amorçage des fissures ont été identifiées et décrites selon leurs tailles,

leurs types, leurs compositions, et leurs fréquences d'occurrence. Les résultats représentent une contribution importante à la documentation disponible sur l'acier 300M grenaillé.

Il a été observé que les conditions de grenaillage étudiées n'ont aucune influence significative sur la durée de vie en fatigue du matériau pour de basses amplitudes de contrainte. Toutefois, les contraintes résiduelles de compression ont pu empêcher l'amorçage des fissures en surface. La durée de vie en fatigue a été gérée principalement par la taille des inclusions non-métalliques du matériau, peu importe l'état de la surface. Une relation empirique en loi de puissance entre la durée de vie en fatigue et la taille des inclusions a été proposée. De plus, la taille de l'inclusion la plus grande présente dans un volume donné d'acier a été prévue par analyse statistique. Cette dernière prévision a été accomplie à l'aide du modèle d'extremum de Gumbel.

Pour l'amplitude de contrainte la plus grande, la durée de vie en fatigue est gérée par deux types de discontinuités. Les discontinuités sont des discontinuités matérielles (des inclusions) et des discontinuités associées aux procédés (des traces de la rectification et du grenaillage). Pour comparer les durées de vie en fatigue des éprouvettes, il est nécessaire de prendre en compte la dispersion des durées de vie. La dispersion a été prise en compte à l'aide de l'estimateur statistique B-basis. Le B-basis est souvent utilisé dans le secteur aérospatial. Le B-basis a servi à estimer une limite inférieure pour la durée de vie en fatigue de chaque état de surface.

Un modèle analytique a été produit pour prévoir la durée de vie en fatigue en fonction de concepts de la mécanique de la rupture : la propagation des fissures longues et le facteur d'intensité de contrainte. Pour chaque condition de grenaillage, le modèle prend en compte la taille réelle des discontinuités causant amorçage des fissures pour prévoir le pire cas statistique de durée de vie en fatigue. Le modèle permet aussi de prévoir la caractéristique précise causant amorçage des fissures. Il a été trouvé que les effets désirables des contraintes résiduelles de compression, en combinaison avec les effets néfastes de la rugosité, déterminent la discontinuité dominante causant la défaillance. La compétition entre les caractéristiques capables de causer amorçage de fissures a été clairement démontrée en comparant les facteurs d'intensité de contrainte associés aux discontinuités.

Le modèle analytique et les limites statistiques obtenues par B-basis ont généré des prévisions similaires de durée de vie en fatigue limitée par amorçage de fissures causées par inclusions en surface ou sous la surface. Le B-basis a permis de choisir la condition S230-8A comme étant la

condition optimale. Cependant, la valeur élevée du B-basis dans ce cas est associée à la faible dispersion des durées de vie. La faible dispersion s'explique par des rugosités de surface similaires et systématiques produites par la condition de grenaillage S230-8A. La valeur B-basis de la condition S230-8A est plus élevée selon le modèle analytique, ce qui démontre que les effets des contraintes résiduelles de compression sont importants au modèle dû aux effets souhaitables de ces contraintes. La condition S230-4A, quant à elle, a mené à des fissures amorcées par des inclusions subsurfaciques dans 75% des cas et a produit des durées de vie en fatigue comparables à celles de la condition S230-8A. Le 25% complémentaire correspond à des fissures s'étant amorcées près des discontinuités associées aux procédés en absence de discontinuités de grande taille. Les fissures de ce 25% ont mené à une durée de vie en fatigue minimale deux fois plus longue que celle de la condition S230-8A. Ceci mène à la conclusion que la condition S230-4A représente le meilleur compromis entre les effets souhaitables des contraintes résiduelles de compression (pour empêcher amorçage des fissures et retarder leur propagation) et la rugosité indésirable induite par le grenaillage. La conclusion est donc que les billes S230, plus grandes, projetées à une intensité faible de 4A, permettent un grenaillage optimal la durée de vie en fatigue de l'acier 300M pour de hautes amplitudes de contrainte.

Le modèle analytique a été modifié pour inclure les effets des contraintes résiduelles de compression et de la microstructure, qui affectent la propagation des fissures courtes dans les éprouvettes grenaillées. Le modèle amélioré a permis la prévision des durées de vie en fatigue d'éprouvettes en sablier rectangulaires avec une justesse d'environ 15%. Ces éprouvettes sont celles avec lesquelles ont été effectuées les essais de propagation de fissures courtes.

Le modèle analytique produit représente un outil fiable pour la sélection des meilleures conditions de grenaillage pour la performance en fatigue axiale pour une contrainte donnée. De plus, la large gamme de résultats expérimentaux générés dans la cadre de cette étude pourront servir de référence pour la validation de modèles futurs.

ABSTRACT

Shot peening is a cold working process widely used in the aerospace industry, which consists in bombarding a metallic component's surface with high velocity shots. This plastically deforms the surface and induces compressive residual stresses and strain hardening in the material's surface layer. These compressive residual stresses and cold work inhibit crack initiation and delay short crack propagation, which is beneficial to fatigue life. Nevertheless, a possible detrimental effect of shot peening is the associated roughness which produces stress concentrations that can reduce fatigue life. Therefore, the proper choice of peening conditions yielding sufficiently high compressive residual stresses while maintaining minimum surface roughness is crucial.

Currently, the aerospace industries use pre-set conditions for peening without proper knowledge of the underlying physical mechanisms. The present study aims to provide a better understanding of the effects of the different peening conditions on the fatigue life of 300M steel (typically used in aircraft landing gears) from a material science perspective. The study identifies the features that influence the fatigue life of the material under the given testing conditions and whether peening is indeed beneficial, and if so, to what extent. This would aid the aerospace industries to optimize the peening process in order to harness its benefits to the fullest, thereby eliminating the need for costly trial and errors.

A rigorous experimental campaign was launched to firstly characterize the bulk material microstructural (grain size) and macrostructural properties (monotonic and cyclic mechanical properties) as well as long crack propagation behavior. This was followed by fatigue testing of unpeened and peened specimens at two stress amplitudes (55% and 65% of the yield strength). Surface roughness, residual stresses and their relaxation during cyclic loading were quantified. Short crack propagation behavior was also studied for these specimens. Features responsible for fatigue crack initiation were identified and characterized in terms of size, type, composition and occurrence frequency. The generated results add significantly to the scarce literature available for shot peened 300M steel.

It was observed that the studied peening conditions had no significant influence on the fatigue life of the material at the lower stress amplitude. Nevertheless, the compressive residual stresses were able to prevent surface crack initiation. The fatigue life was mainly governed by the size of the material non-metallic inclusions irrespective of the surface condition. An empirical power law

relationship was therefore proposed between the fatigue life and inclusion size. In addition, the largest inclusion present in a given volume of steel was statistically predicted using the Gumbel extreme value model.

At the higher stress amplitude, the fatigue life was governed by two types of discontinuities, material discontinuities (inclusions) and process-related discontinuities (grinding marks and peening induced discontinuities). To compare the fatigue lives of the specimens, it is necessary to consider the fatigue life dispersion. This consideration is taken into account by B-basis, which is a statistical estimate commonly used in the aerospace sector. Hence, B-basis was used to calculate a statistical lower bound for the fatigue lives for each surface condition.

An analytical fatigue life prediction model was developed based on fracture mechanics concepts of stress intensity factor and long crack propagation. The model took into account the actual crack initiating discontinuity sizes and successfully predicted the worst-case fatigue life scenarios, as well as the responsible crack initiation feature for each peening condition. The coupled beneficial effect of CRS and the detrimental effect of roughness was found to determine the dominant discontinuity causing failure. The competition between the crack initiating features was well demonstrated by comparing the stress intensity factors characterizing the discontinuities.

The analytical model and the statistically obtained B-basis values yielded similar fatigue lives for crack initiation caused by surface and subsurface inclusions. Using B-basis, the best shot peening condition was found to be the one using S230 shot at an intensity of 8A. However, the high B-basis in this case was related to the low dispersion in fatigue lives resulting from similar and systematic roughness features produced by this peening condition. The B-basis value for the specimens peened using S230 shot at 8A intensity was higher than the analytical model prediction, showing that the effect of CRS needs to be considered in the model. This reflects the beneficial effect of peening induced CRS in delaying crack propagation. For the specimens peened with S230 shot at an intensity of 4A, 75% of the cracks initiated at subsurface inclusions and produced similar fatigue lives as those peened using S230 shot at 8A intensity. The remaining 25% cracks which initiated at the process induced surface discontinuities in absence of large inclusions, nevertheless, exhibited a minimum fatigue life about 2 times higher than that for the specimens peened using S230 shot at 8A intensity. This shows that the condition using S230 shot at an intensity of 4A represents the optimal trade-off between the beneficial effect of CRS in preventing crack initiation from surface

inclusions and delaying crack propagation, and the detrimental effect of the peening induced surface roughness. Therefore, it was concluded that peening with larger S230 shot at a low peening intensity of 4A would yield the best fatigue life for the studied 300M steel subjected to higher stress amplitude conditions.

The analytical model was further modified to incorporate the effect of the compressive residual stresses and microstructure that affect short crack propagation behavior in peened specimens. The improved model was able to predict with an accuracy of ~15%, the average fatigue life of rectangular hourglass specimens on which the short crack propagation tests were performed.

The analytical model could thus offer a reliable tool to guide the choice of optimum peening conditions at the desired stress level based on their axial fatigue performance. In addition, the vast experimental data generated in this study would serve as valuable input for validating life prediction models developed in future.

TABLE OF CONTENTS

LIST OF TABLES

LIST OF FIGURES

LIST OF SYMBOLS AND ABBREVIATIONS

Symbols

a	Surface crack length or depth
a_c	Critical crack size corresponding to fracture toughness
c	Half the surface crack length or depth
A	Coefficient of the empirical relationship between inclusion size and fatigue life
A'	Material constant depending on the stress amplitude
$\sqrt{area}$	Area of the inclusion projected onto the plane normal to the loading direction
$\sqrt{area_R}$	Equivalent discontinuity size of a surface roughness feature
b	Exponent of the empirical relationship between inclusion size and fatigue life
b'	Constant depending on material softening and applied strain range
C	Paris law coefficient
C'	Short crack propagation coefficient
CI_{95}	95% confidence interval at 99.9 % probability
δ	Crack tip opening displacement
D	Shot diameter
D_s	Smallest microstructural feature present in the material (grain size, average inclusion size, etc.)
da/dN	Crack growth rate
$\Delta\varepsilon$	Applied strain range
$\%El$	% Elongation
E	Elastic modulus
φ	Parametric angle
f	Factor accounting for inclusion location in Murakami's equation for K_{Imax}

F	Dimensionless quantity accounting for the specimen and crack geometry
$f^{GEV}(x)$	pdf of GEV distribution
$f^{Ln}(x)$	pdf of a log-normal distribution
$f^{W}(x)$	pdf of a Weibull distribution
$F(y)$	Cumulative distribution function of the Gumbel extreme value analysis
G	Potential energy required for crack extension in elastic conditions
h	Average largest inclusion size
(h, p)	Anderson-Darling goodness of fit test coefficients
h_{pd}	Depth of a peening dimple
Hv or H	Vickers microhardness
i	Rank of an observation
J	J- integral
J_{el}	J- integral's value for elastic behavior
K	Stress intensity factor
K_c	Fracture toughness
$K.E.$	Kinetic energy of the shots
K_{Ic}	Plain-strain fracture toughness in mode I uniaxial loading
K_I	Stress intensity factor in mode I loading
K_{Imax}	Maximum value of stress intensity factor in mode I loading
$K_{Imax,i}$	Maximum stress intensity factor for surface or interior inclusions
K_{Imax,R_t}	Maximum stress intensity factor for surface roughness
K_{max}	Maximum stress intensity factor (corresponding to σ_{max})
K_{min}	Minimum stress intensity factor (corresponding to σ_{min})
K_{op}	Crack opening stress intensity factor (for closure affected cracks)

K_t	Stress concentration factor (ratio of the maximum local stress to the nominal stress)
$K_{t,rough}$	Stress concentration factor derived from the surface roughness parameters of surfaces with multiple dents
ΔK	Stress intensity factor range
ΔK_{eff}	Effective stress intensity factor range (for closure affected cracks)
ΔK_{th}	Threshold stress intensity factor range
l	Factor accounting for inclusion location in Murakami's equation for σ_w
l_1	Point of deviation from the constant stress range behaviour in Kitagawa-Takahashi diagram
l_2	Point of deviation from the constant stress intensity behaviour in Kitagawa-Takahashi diagram
m	Paris law exponent
m'	Short crack propagation exponent
m''	Material constant depending on the stress amplitude
m_s	Mass of shot
N	Number of fatigue cycles
N_f	Number of cycles to failure
$N_{f,LCP}$	Predicted fatigue life using long crack propagation (analytical model)
$N_{f,SCP}$	Predicted fatigue life using short crack propagation (analytical model)
N_i	Crack initiation life
N_{LC}	Long crack propagation life
N_{SC}	Short crack propagation life
N_t	Total fatigue life
P	Cumulative probability of observations

ΔP_{eff}	Effective load range free of crack closure
ΔP	Closure affected load range
P_{max}	Maximum load
P_{min}	Minimum load
P_O	Opening load
ρ	Shot density
R	Stress ratio (ratio of minimum to maximum alternating stress)
R^2	Coefficient of determination
R_a	Arithmetic mean roughness
r_p	Plastic zone size
R_{sm}	Spacing between adjacent peaks in a surface roughness profile
R_t	Highest peak to valley height in a surface roughness profile
½ S_2	X-ray elastic constant
S	Alternating stress amplitude
S_{op}	Crack opening stress (for closure affected cracks)
S_{eff}	Effective stress for crack propagation (for closure affected cracks)
ΔS_{eff}	Effective stress range (for closure affected cracks)
SEV	Statistics of Extreme Values
σ	Nominal stress
σ_a	Alternating stress amplitude
σ_0	Remote tensile stress
σ_{cy}	Cyclic yield strength
σ_{m1}	Mean stress at the first cycle
σ_{max}	Maximum alternating stress

σ_{mc}	Maximum CRS
σ_{min}	Minimum alternating stress
σ_{mN}	Mean stress at the Nth cycle
σ_N^{re}	Surface residual stress after N cycles
σ_s	Surface residual stress
σ_{UTS}	Ultimate Tensile Strength
$\sigma_{y,0.1}$	0.1% offset yield strength
$\sigma_{y,0.2}$	0.2% offset yield strength
σ_{ys}	Yield strength
σ_w	Fatigue strength
$\Delta\sigma_{th}$	Threshold stress range
U	Deviation from fully open crack compliance during loading part of fatigue cycle
ν	Poisson's ratio
V	Shot velocity
V_o	Reference volume for Gumbel extreme value analysis
V_{ref}	Original volume for Gumbel extreme value analysis
w	Width of a peening dimple
x_0	Depth at which the residual stresses become tensile
x_{exp}	Experimentally observed largest inclusion size
x_{max}	Largest predicted inclusion size using Gumbel extreme value analysis
x_{mc}	Depth at which maximum CRS occurs
y	Reduced variate
n	Total number of observations
Y	Factor accounting for both component and crack geometry

Abbreviations

AMS	Aerospace Material Specification
ASTM	American Society for Testing and Materials
cdf	Cumulative Distribution Function
CI	Confidence Interval
CRS	Compressive Residual Stress
COD	Crack Opening Displacement
CTOD	Crack Tip Opening Displacement
ECCI	Electron Channeling Contrast Imaging
EDS	Energy Dispersive Spectroscopy
EPFM	Elastic-Plastic Fracture Mechanics
FGA	Fine Granular Area
FL	Fatigue Life
GEV	Generalized Extreme Value
HCF	High Cycle Fatigue
HRc	Rockwell Hardness (C-scale)
HSS	High Strength Steels
LCF	Low Cycle Fatigue
LCP	Long Crack Propagation
LEFM	Linear Elastic Fracture Mechanics
LS	Long Transverse
LT	Longitudinal
MSC	Microstructurally Short Crack
pdf	Probability density function

PSB	Persistent Slip Band
PSC	Physically Short Crack
SCP	Short Crack Propagation
SE	Standard Error
SEM	Scanning Electron Microscopy
TEM	Transmission Electron Microscopy
TS	Short Transverse
VAR	Vacuum Arc Remelting
VHCF	Very High Cycle Fatigue
XRD	X-Ray Diffraction
wt.%	Weight %

LIST OF APPENDICES

CHAPTER 1 INTRODUCTION

Fatigue failure is said to occur when a component subjected to repeated loads fails at a stress much lower than its yield stress. This can be attributed to stress concentrations, microstructural or crystal discontinuities giving rise to cracks. These cracks grow to a critical size under cyclic load before the component fails catastrophically. These damage mechanisms are common and responsible for the failure of engineering structures such as bridges, aircraft, trains, etc.

Shot peening is a cold working process in which a ductile metallic surface is bombarded with small high velocity spherical media called 'shots'. The impact of these shots gives rise to a surface dimple as the metal surface yields. The induced tensile surface strains lead to surface compressive residual stresses (CRS) since the bulk material remains undeformed. The impact of the shots may also lead to a strain hardened layer as a result of an increased near surface dislocation density. These CRS and strain hardening are responsible for arresting short fatigue crack propagation or delaying surface crack initiation [1, 2]. Shot peening is governed by a large number of factors ranging from peening intensity, peening coverage, shot material, shot size, shot velocity, shot hardness, type of peening machine and peening time.

With the pressing new regulations on greenhouse gas emission reduction, manufacturers are striving for ways to decrease their aircraft masses. The development of a tool for predicting the fatigue life of a shot peened component can significantly contribute towards that objective since the ability to predict fatigue life and determine service limits always contributes to better design of mass optimized critical components.

Keeping in mind the objective towards mass reduction and better component design, a collaborative research project was undertaken to develop reliable tools to predict the effect of specific shot peening parameters on the fatigue life of 3 materials widely used in the aerospace industry: aluminum alloy 7050, nickel superalloy IN718 and 300M steel. The project involved the participation of 4 aerospace companies (Bell Helicopter Textron Canada, Pratt and Whitney Canada, L3-Communications MAS, Héroux Devtek), 3 universities (École Polytechnique de Montréal, École de Technologie Supérieure and McGill University) and 1 Collegial Center for Technology Transfer (Centre Technologique en Aérospatiale). The project was also financially supported by the Consortium for Research and Innovation in Aerospace of Québec (CRIAQ), the Natural Sciences and Engineering Research Council of Canada (NSERC) and Mathematics of

Information Technology and Complex Systems (MITACS). 1 M.Sc. and 5 Ph.D. students along with 4 Post-Doctoral fellows contributed to the project.

This Ph.D. is a part of the above research project which aims at studying the effectiveness of 3 shot peening conditions in improving the axial fatigue life of aerospace grade 300M steel at two stress amplitudes. 300M steel is a high strength low alloy steel and is extensively used in manufacturing aircraft landing gears. Landing gears experience cyclic loads during taxi, take-off and landing, which make them susceptible to fatigue cracking.

The results obtained from the study will ultimately guide the choice of optimum peening conditions for the material at the given testing conditions. Moreover, by understanding the physics behind how shot peening affects the material damage mechanism for specific loading conditions, aerospace industries will be able to make well-informed choices on the peening conditions instead of the usual trial and error, thereby saving time and money.

The report is organized as follows. Chapter 2 constitutes the literature survey which serves as the foundation to understand the basics regarding the material investigated, the mechanism of fatigue failure in general as well as in high strength steels similar to 300M, and the effect of shot peening on the characteristics influencing the fatigue life of the high strength steels. The global and principal objectives are presented in Chapter 3. Chapter 4 constitutes the methodology for the experimental campaign as well as the statistical and modelling techniques used. Chapter 5 describes the scientific approach and the relationship between the research objectives. Chapters 6 and 7 elaborate on the effect of various shot peening conditions on the fatigue life of the studied material submitted to low and high stress amplitudes, respectively. Chapter 8 discusses the effect of peening on short crack propagation in the given steel. Chapter 9 discusses the main findings of this work. Chapter 10 presents the conclusions and recommendations for future work.

CHAPTER 2 LITERATURE REVIEW

2.1 300M steel

300 M steel is a medium-carbon (0.4% C) high strength steel manufactured by vacuum arc remelting (VAR). It is essentially a modified version of AISI4340 steel containing Si, V and slightly higher quantities of C and Mo. 300M steel boasts an excellent combination of strength, toughness, ductility and hardenability. The 300M steel is heat treated according to the following heat treatment schedule defined by AMS 6257E standard:

- Normalization at 1700 ^{o}F (1200 K) for 1 h followed by air cooling.
- Austenitization at 1600 ^{o}F (1144 K) for 1 h followed by oil quenching.
- Double tempering at 575 ^{o}F (575 K) for 2 h followed by air cooling.

The 300M steel has a brittle microstructure in the as-quenched condition, consisting of a mixture of martensite plates and lathes and very few (less than 5%) partially twinned plates, as reported in the literature [3, 4]. The subsequent tempering treatment significantly increases its toughness, with a resulting microstructure consisting of tempered martensite lath and plates, as shown in Fig. 2.1. Youngblood and Raghavan [3] also reported the presence of very small amount of retained austenite (5 volume %) revealed by transmission electron microscopy (TEM). The AMS 6257E standard specifies a minimum prior austenite grain size of ASTM 6 (45 μm).

Tables 2.1 and 2.2 present the minimum and maximum composition requirements and minimum monotonic mechanical properties as specified by AMS 6257E standard, respectively.

Due to its excellent mechanical properties, 300 M steel is extensively used in aircraft landing gear and rotor shaft applications. These components are subjected to complex cyclic loads during their operation, which make them susceptible to failure by fatigue.

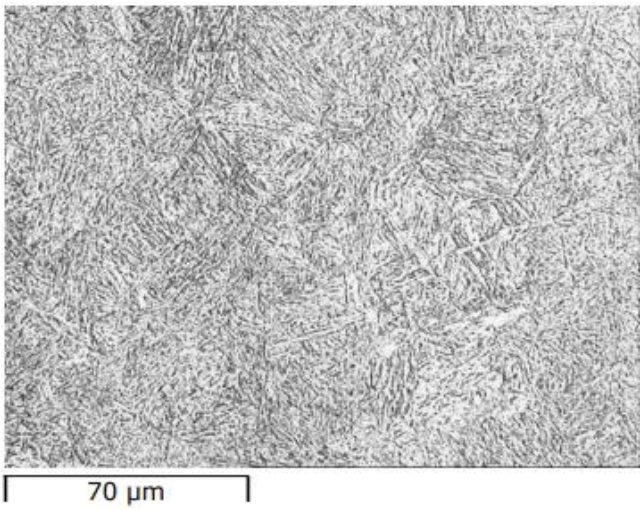

Figure 2.1 Optical micrograph of quenched and tempered 300M steel, etched using 2% Nital [4]

Table 2.1 The minimum and maximum wt. % of elements required in 300M steel (AMS 6257E)

	C	Mn	Si	P	S	Cr	Ni	Mo	V	Cu
Min.	0.40	0.65	1.45	--	--	0.70	1.65	0.35	0.05	--
Max.	0.44	0.90	1.80	0.010	0.008	0.95	2.00	0.45	0.10	0.35

Table 2.2 The minimum monotonic mechanical properties for 300M steel (AMS 6257E)

	$\sigma_{y,0.2}$ (MPa)	σ_{UTS} (MPa)	$\%El$	% Reduction in area
Min.	1586	1931	8	30

2.2 Fatigue

Fatigue is a failure mechanism that involves progressive cracking of the material due to cyclic stresses. It is usually influenced by the material microstructure, component or crack geometry,

loading conditions, temperature and environmental conditions. It manifests in broadly 4 stages: crack initiation, short crack propagation, long crack propagation, and final failure.

Therefore, the total fatigue life of a component (N_t) can be represented as a summation of life spent by the material in the first 3 stages as:

$$N_t = N_i + N_{SC} + N_{LC} \tag{2.1}$$

where N_i is the crack initiation life, N_{SC} is the short crack propagation life, N_{LC} is the long crack propagation life. Life is defined as the number of load cycles necessary to cause material failure.

Fatigue can be classified as low cycle or high cycle based on the applied stress level. Low cycle fatigue (LCF) occurs when the applied stresses are relatively high (close to the material's yield), which causes failure in less than 10^5 cycles. Plastic strains are produced in LCF which accumulate in each cycle and significantly reduce the component's service life. The crack initiation stage in LCF is usually shorter than the crack propagation stage.

In high cycle fatigue (HCF), strains are predominantly elastic as the applied stresses remain within 2/3 of the material's yield, leading to failure in 10^5 cycles or more. Consequently, the crack initiation stage is longer in HCF than the crack propagation stages. A material's fatigue life (especially in HCF) is commonly characterized by means of a $S-N$ curve or a Wöhler curve, where S denotes the magnitude of alternating stress and N, the number of cycles (in logarithmic scale). The $S-N$ curve for an unnotched 300M steel forging (at a stress ratio, $R = \sigma_{min} / \sigma_{max} =$ -1) having a σ_{UTS} of 1931 MPa (extracted from [5]) is presented in Fig. 2.2. This curve depicts that the material can withstand a fatigue life of more than 10^5 cycles below a stress amplitude of 896 MPa.

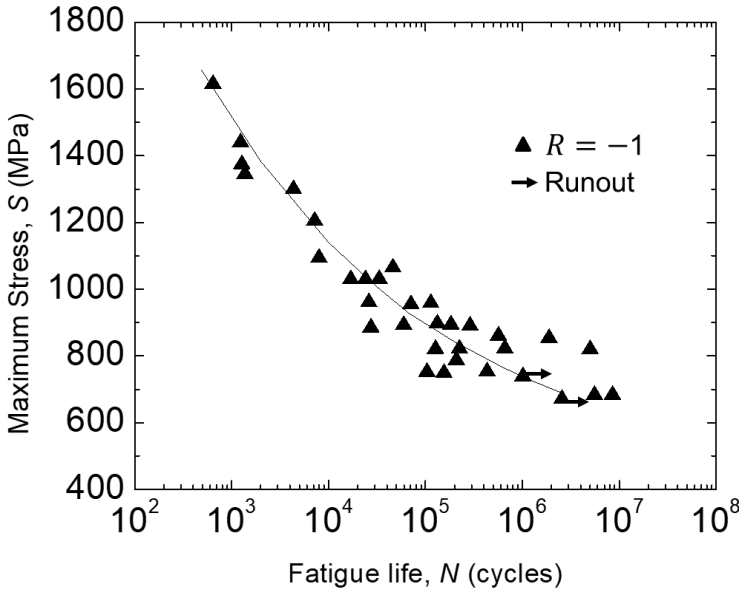

Figure 2.2 $S - N$ curve for an un-notched 300M steel forging (extracted from [5])

2.2.1 Crack initiation

Fatigue crack initiation is a weakest link phenomenon, i.e., fatigue crack initiates from the largest defect present. Crack initiation depends on the defect's stress concentration factor. The stress concentration factor, K_t is defined as the ratio of the maximum local stress to the nominal stress based on the component's net section.

In fatigue, the mechanism of crack initiation is governed by the movement of dislocations (inherent defects in crystal structure) across favourable crystallographic planes causing formation of persistent slip bands (PSBs). Irreversible slip results in the formation of features such as valleys (intrusions) or ridges (extrusions) at the surface [6] as illustrated in Fig. 2.3. These features are stress raisers that facilitate crack initiation.

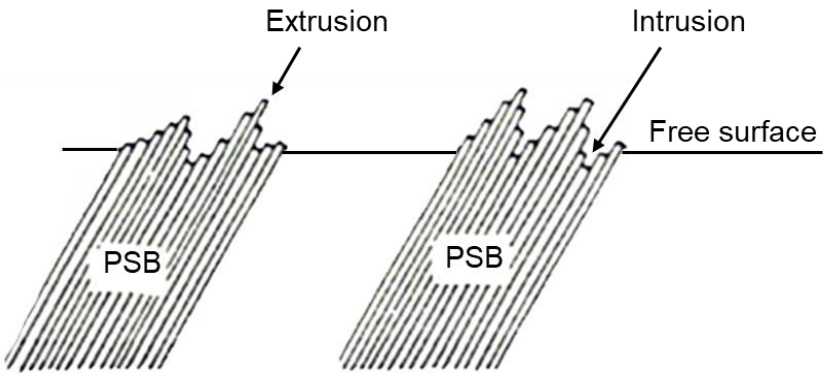

Figure 2.3 Irreversible dislocation slip along persistent slip bands (PSB) producing stress concentrating features (intrusions and extrusions) on the material surface during cyclic deformation (based on [6])

In engineering components, crack initiation is more likely to occur at stress concentrators resulting from component or material manufacturing. Kendall et al. [7] reviewed and listed the various sources of short crack initiation in steels, which include casting and welding defects, hydrogen cracks, inclusions, quench cracks and surface damage. Their study revealed that inclusions were responsible, in most cases, for crack initiation. This was corroborated by several research works, where most of the fatigue failures in unnotched high strength steels (HSS) occurring in very high cycle fatigue (VHCF) regime (10^8- 10^{10} cycles) [8-12] and some in the high cycle fatigue (HCF) regime (10^5- 10^7 cycles) originated at non-metallic inclusions [13-16]. It has been reported that the presence of inclusions above a certain quantity and size, have a deleterious effect on the tensile and fatigue properties in HSS [15-18]. Thus, it is essential to have proper knowledge of the origin of these inclusions and their influence on the material's fatigue properties, to better design parts made of HSS.

2.2.1.1 Inclusions in HSS

Inclusions are unwanted non-metallic chemical compounds resulting from steel manufacturing. Based on their sources, the inclusions in steel can be classified as indigenous and exogenous [19]. Indigenous inclusions are products of deoxidation, or precipitation, during cooling and solidification; for example, Al_2O_3 and SiO_2 inclusions from the addition of Al and Si deoxidisers. Exogenous inclusions arise from chemical and mechanical interactions of molten steel with its surroundings such as reoxidation, slag entrainment, and erosion of refractory lining; for example, CaO and MgO inclusions from contamination of molten steel with slag. The size, distribution and

composition of inclusions in steels vary depending on the type of steel and process by which it is manufactured.

The inclusions are stress concentrators, thereby serving as crack initiation sites during cyclic loading. Typical inclusion compositions found at the fatigue crack initiation sites in HSS include Ti(C, N), $CaO\text{-}Al_2O_3$, $CaO\text{-}Al_2O_3\text{-}MgO$, $CaO\text{-}Al_2O_3\text{-}SiO_2$ and $CaO\text{-}Al_2O_3\text{-}MgO\text{-}SiO_2$ [20, 21]. Figs. 2.4 a, b show a TiN and a $CaO\text{-}Al_2O_3$ inclusion observed at the fatigue crack initiation site of 100Cr6 bearing steel [21] and Fig. 2.4 c shows cracks initiating from a $CaO\text{-}Al_2O_3\text{-}MgO$ inclusion in 60Si2Cr spring steel [22].

The stress concentration is either due to a [9, 23] to the difference in the constituents' coefficient of thermal expansion or their stiffness.

Murakami and Endo [14] conducted an extensive review of several works demonstrating crack initiation mechanisms in HSS. They reported that the adhesion of inclusions to the matrix was not perfect in some cases and gaps often existed between them, which could be assimilated to small inherent cracks. Cracks could also arise from voids due to inclusions debonding during the first few load cycles. This hypothesis was also supported by Tanaka and Mura [24].

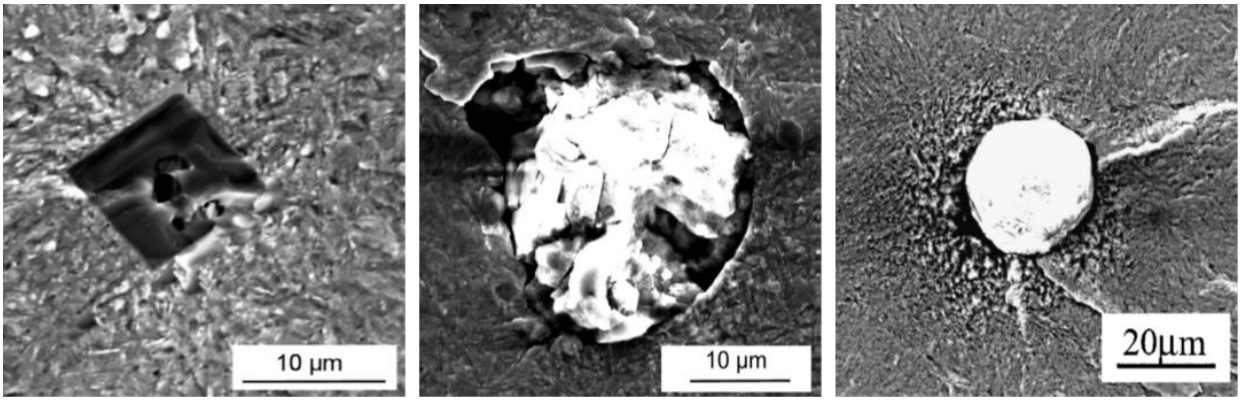

a. b. c.

Figure 2.4 SEM images showing fatigue cracks initiating from a. a TiN inclusion, and b. a $CaO\text{-}Al_2O_3$ inclusion in 100Cr6 bearing steel [21] and c. a $CaO\text{-}Al_2O_3\text{-}MgO$ inclusion in 60Si2Cr spring steel [22]

Therefore, Murakami and Endo [14] concluded that the use of stress intensity factor rather than a stress concentration factor (K_t) was more suitable to account for the stress localization at the inherent crack in the inclusion vicinity. In linear elastic fracture mechanics, stress intensity factor (K) instead of K_t is used to define the stresses in the vicinity of a crack tip by means of the following equation:

$$K = Y\,\sigma\sqrt{\pi c} \tag{2.2}$$

where σ is the nominal stress, c is half the crack length and Y is a factor accounting for both component and crack geometry. For mode I loading (or opening mode), where the crack grows in a plane normal to the loading direction, K is denoted as K_I.

Murakami [25] proposed a series of equations to define the stress intensity factor for inclusions considered as 3-D cracks. Figs. 2.5 a and b show an internal inclusion and a surface inclusion on the *x*-*y* plane of an infinite solid subjected to a uniform remote tensile stress σ_0, in the z-direction. The maximum value of the stress intensity factor along the crack front, K_{Imax}, is approximately given by:

$$K_{Imax} = f\,\sigma_0\sqrt{\pi\sqrt{area}} \tag{2.3}$$

where the crack size is denoted by the $\sqrt{area}$ parameter, which is the area of the inclusion projected onto the plane normal to the loading direction. The $area$ parameter is calculated by taking a smooth contour enclosing the inclusion for interior and surface cracks, as shown in Fig. 2.6. In case of surface cracks, however, the area enclosed between the free surface and the dotted lines in addition to the contour is considered. This is done to account for the increased critically stressed region when the inclusion is close to the surface. f accounts for the inclusion location and takes on the values of 0.5 for interior cracks and 0.65 for surface cracks or subsurface cracks in touch with the free surface, respectively [25]. This indicates that, for a given material, an inclusion located at the specimen's surface would cause a higher stress intensification, causing it to fail earlier than a specimen with an interior inclusion of the same size.

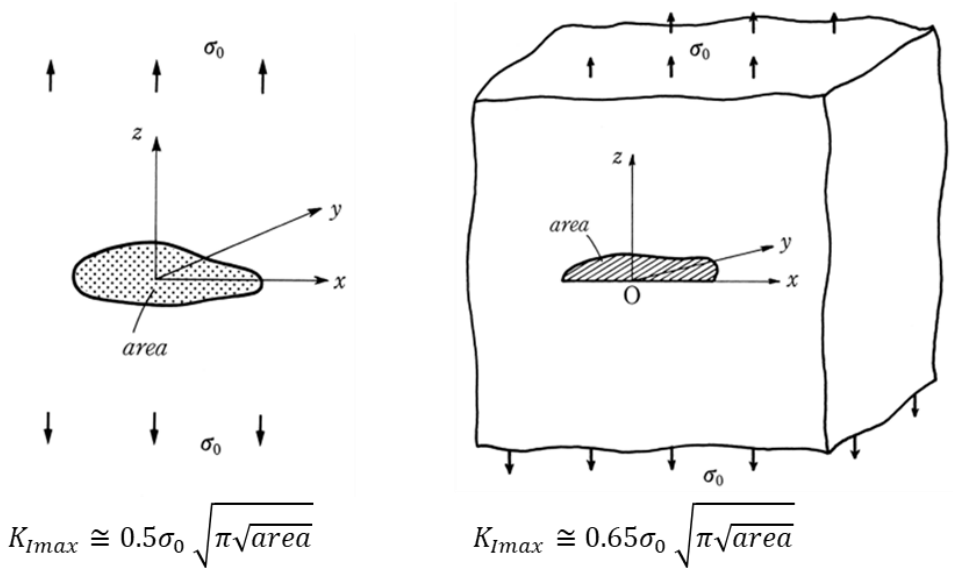

$K_{Imax} \cong 0.5\sigma_0 \sqrt{\pi\sqrt{area}}$ $K_{Imax} \cong 0.65\sigma_0 \sqrt{\pi\sqrt{area}}$

a. b.

Figure 2.5 Stress intensity factor for an arbitrarily shaped 3D a. internal crack and b. surface crack [25]

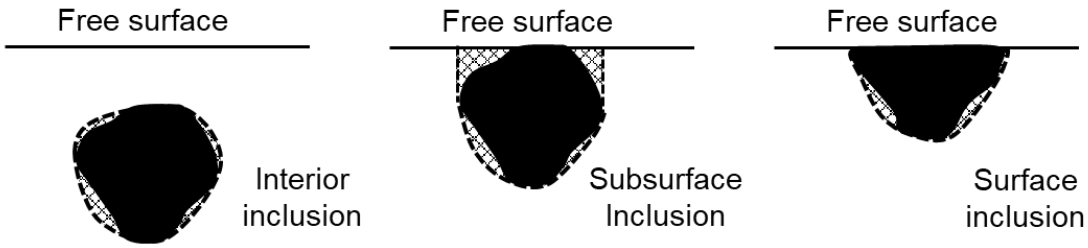

Figure 2.6 Murakami's [15] calculation of the '$area$' parameter (represented by shaded region) for interior inclusions, subsurface inclusions in touch with the free surface and surface inclusions

Fig. 2.7 shows the relationship between the K_{Imax} for various inclusions (TiN, CaO and AlCaO) found at the fatigue crack initiation sites of bearing steel (100Cr6) specimens and their corresponding axial fatigue lives (R = -1) in the VHCF regime [21]. The fatigue lives were found to decrease with an increase in K_{Imax} for all inclusion types.

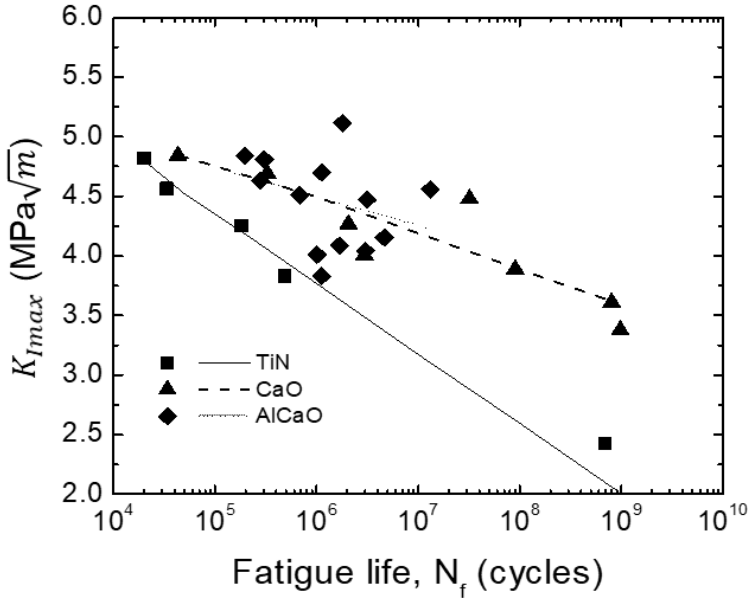

Figure 2.7 Stress intensity factor K_{Imax} vs. fatigue life, N_f for various inclusion types found at fatigue crack initiation sites for axially loaded 100Cr6 steel at R = -1 (adapted from [21]). The lines represent the decreasing trend of fatigue life with increasing stress intensity factor for each inclusion type

Steel industries manufacture "clean steels" using vacuum arc remelting (VAR) to control the inclusion size and content and keep them to a minimum. Murakami and Endo [14] predicted the lower bound for the experimental scatter of fatigue strength σ_w for various "clean" high strength steels as:

$$\sigma_w \cong l\,(Hv + 120)/(\sqrt{area})^{1/6} \tag{2.4}$$

The parameter $\sqrt{area}$ incorporates the inclusion size effect on the fatigue limit. The inclusion location influence on the fatigue limit is given by constant l that takes on the values of 1.56 for interior inclusions, 1.43 for surface inclusions, and 1.40 for subsurface inclusions in touch with the free surface. Eqn. (2.4) was validated for several HSS subjected to rotation bending and axial fatigue tests at R = -1 [25].

In practice, large inclusions can hardly be found because of their low incidence and the limited volumes that can be examined. Murakami et al. [26] applied the statistics of extreme values (SEV) to obtain the largest inclusion in a given steel volume to predict a lower bound for the HSS fatigue

strength. The authors [26] firstly measured the sizes of the largest inclusions observed using optical microscopy on metallographic samples in a small volume (~1.53 x 10^{-4} mm^3). The authors then described the inclusion size distribution using used the Gumbel extreme value model and successfully predicted the largest inclusion sizes in a much larger volume (~90 mm^3). The fatigue strength calculated using the obtained inclusion size was in good agreement with that experimentally observed for a tool steel tested in axial fatigue at R = -1 [26].

2.2.2 Short crack propagation

2.2.2.1 Short cracks

Most short cracks are less than a millimeter in size (generally 0.006-0.5 mm) and contrary to long cracks, their behavior cannot be described by the conventional linear elastic fracture mechanics (LEFM) concept.

Linear elastic fracture mechanics

The LEFM behaviour is governed by the state of small scale yielding due to the presence of an elastic field at the crack tip. In such cases, the plastic zone size satisfies:

$$2r_p \leq a/25 \tag{2.5}$$

where a is the crack length [27]. The stresses in the crack tip vicinity for LEFM Mode I loading (when the crack growth direction x is perpendicular to the applied stress direction y) can be represented as [28]:

$$\sigma_x = \frac{K_I}{\sqrt{2\pi r}} \cos\frac{\theta}{2}\left[1 - \sin\frac{\theta}{2}\sin\frac{3\theta}{2}\right] \tag{2.6 a}$$

$$\sigma_y = \frac{K_I}{\sqrt{2\pi r}} \cos\frac{\theta}{2}\left[1 + \sin\frac{\theta}{2}\sin\frac{3\theta}{2}\right] \tag{b}$$

$$\tau_{xy} = \frac{K_I}{\sqrt{2\pi r}} \cos\frac{\theta}{2}\sin\frac{\theta}{2}\cos\frac{3\theta}{2} \tag{c}$$

$$\sigma_z = 0 \text{ (plane stress)} \quad \text{or, } \sigma_z = \nu(\sigma_x + \sigma_y) \text{ (plane strain; } \varepsilon_z = 0) \tag{d}$$

$$\tau_{yz} = \tau_{zx} = 0 \tag{e}$$

where the stresses (σ) are defined with respect to the 3-D cartesian coordinate system. The polar co-ordinates, r and θ lie on the $x - y$ plane, which is normal to the crack plane. The z direction is

parallel to the crack's leading edge. Fig. 2.8 illustrates the co-ordinate system for the defined stresses. Note that for plane stress conditions, that is when the component is relatively thin in the z direction, $\sigma_z = 0$. However, for plane strain conditions occurring in thick components, the strain in the z direction $\varepsilon_z = 0$, in which case, σ_z depends on the stresses in the other two directions and the Poisson's ratio ν according to Hooke's law.

Eqns. 2.6 a-d suggest that the stresses approach infinity close to the crack tip ($r \to 0$). The stress field magnitude near the crack tip can be characterized through the value of the stress intensity factor for mode I loading K_I as [28]:

$$K_I = \lim_{r,\theta \to 0} \left(\sigma_y \sqrt{2\pi r}\right) = F\sigma\sqrt{\pi c} \tag{2.7}$$

where F is a dimensionless quantity that accounts for the specimen and crack geometry.

In cyclic loading, the stress intensity factor range, given by $\Delta K = K_{max} - K_{min}$, is used to represent the driving force for long crack propagation. It has been observed that for a given ΔK, the short cracks can show a much higher propagation rate, when compared to long cracks [29-33], but can also stop propagating.

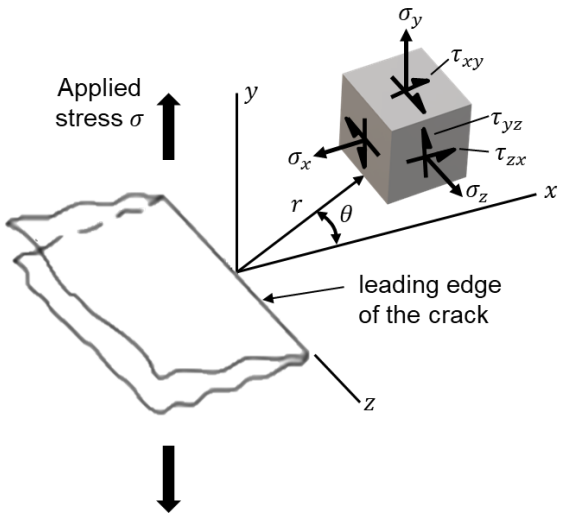

Figure 2.8 3D-coordinate system representing stresses near the crack tip (adapted from [28]). Crack grows in the x direction under the applied stress σ in y direction

According to LEFM, no crack can grow below a threshold stress intensity factor range, ΔK_{th}. Kitagawa and Takahashi [34] were the pioneers in discovering the abnormal behavior of the short

cracks, and the loss of LEFM similitude while characterizing their behavior. They [34] studied the growth of small surface cracks initiated at surface notches in HT-80 steel under uniaxial cyclic loading and found that the ΔK_{th} was constant for all cracks greater than 0.5 mm and deviated from this trend below 0.5 mm. Short crack initiation and growth were monitored by combining the surface replica method and the crack surface coloring method (or heat tint oxidation). They [34] developed the well-known Kitagawa-Takahashi diagram which is presented in Fig. 2.9. The figure shows that for an infinitesimal crack length, which represents a perfectly smooth unflawed specimen, one has to apply a stress range greater than the fatigue limit to initiate failure by fatigue. Therefore, when the threshold stress range $\Delta\sigma_{th}$ remains constant, the threshold stress intensity range ΔK_{th} has to change with changing crack length according to the relation, $\Delta\sigma_{th} = \Delta K_{th} / \sqrt{\pi c}$. Similarly, for long LEFM cracks, ΔK_{th} remains constant so that $\Delta\sigma_{th}$ evolves with varying crack length as shown by the dash-dotted line in the figure.

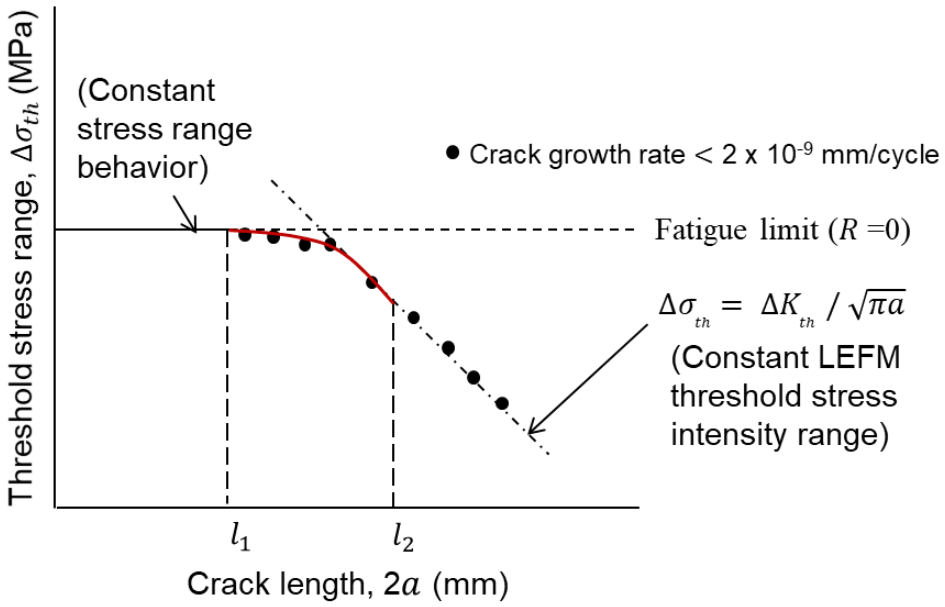

Figure 2.9 General form of Kitagawa-Takahashi diagram [34] where the red line represents the deviation of short cracks (having lengths between l_1 and l_2) from the constant fatigue limit behavior and the constant LEFM threshold stress intensity behavior of long cracks

Taylor and Knott [33] defined the two values of l_1 and l_2 (Fig. 2.9) depicting the points of deviation from the constant stress range and constant stress intensity behaviour. As can be seen, above l_2,

long crack growth dominates, and below l_1, the crack size has no effect on the fatigue strength. Therefore, having an estimate of both these parameters is important to identify the regime of short crack behaviour. It has been observed that the deviation from LEFM behaviour occurs at stresses above ($\sigma_{cy}/3$), σ_{cy} being the cyclic yield. Thus, considering fully reversed loading, the threshold stress range ($\Delta\sigma_{th}$) for LEFM is ($2\sigma_{cy}/3$).

Beyond the LEFM threshold stress range, when the plastic zone size exceeds $a/25$, the crack behaviour is mainly governed by elastic plastic fracture mechanics (EPFM).

Elastic plastic fracture mechanics

EPFM uses the concepts of J- integral or crack tip opening displacement (CTOD), instead of the stress intensity factor to characterize the conditions at the crack tip. The J- integral is obtained by evaluating the contour integral around an arbitrary closed path around the crack tip and is path independent. In the case of non-linear elastic behavior, its value is analogous to the potential energy required for crack extension in elastic conditions (G), which is related to the stress intensity factor K as [28]:

$$J_{el} = G = \frac{K^2}{E} \text{ (for plane strain)} \qquad (2.8)$$

$$= \frac{K^2}{E}(1 - \upsilon^2) \text{ (for plane stress)}$$

where J_{el} is J- integral's value for elastic behavior and E is the material's elastic modulus.

For elasto-plastic conditions, however, J represents the intensity of stress-strain fields around the crack tip and is no longer relevant to represent the potential energy for crack extension. It can be evaluated experimentally [35], analytically for simple geometries and loading conditions [36], or by finite element analyses for complex situations.

The calculation of CTOD or δ assumes that the crack tip undergoes plastic blunting due to the intense plastic deformation causing it to extend by a length of $\delta/2$. CTOD is measured as the crack face displacement normal to the original (unloaded) crack plane (Fig. 2.10). It can also be defined as the displacement at the intersection of a 90° vertex with the blunted crack flanks. CTOD is related to J by the following equation under elastic conditions [28] through:

$$\delta \approx \frac{K^2}{E\sigma_{ys}} \approx \frac{J}{\sigma_{ys}} \qquad (2.9)$$

where σ_{ys} is the material's yield strength.

Short crack regimes

Summarizing the works of various researchers [7, 27, 31, 33, 34, 37, 38], the short cracks can be categorized as follows:

a) Microstructurally short crack (MSC), where the crack length is of the order of microstructural features, such as grain diameter, inclusion size, or size of largest precipitate.
b) Mechanically short cracks, where crack length is comparable to the scale of local plasticity, for example crack embedded in the plastic zone of a notch, or with length equal to or less than its own crack tip plastic zone.
c) Physically short crack (PSC), which are cracks that are just physically small (usually 0.05 to 0.5 mm). Their crack tip plastic zone size is almost equivalent to their crack length [39].
d) Chemically small cracks, whose growth is influenced by the environment.

Short crack growth can be broadly classified into 2 stages: Stage I and Stage II EPFM. The microstructurally short cracks fall under the Stage I category while the mechanically and physically short cracks fall under Stage II. Fig. 2.11 (based on the Kitagawa-Takahashi plot in Miller's [27] review) schematizes the stress range vs. the crack length (log scale) for the short crack regimes discussed below.

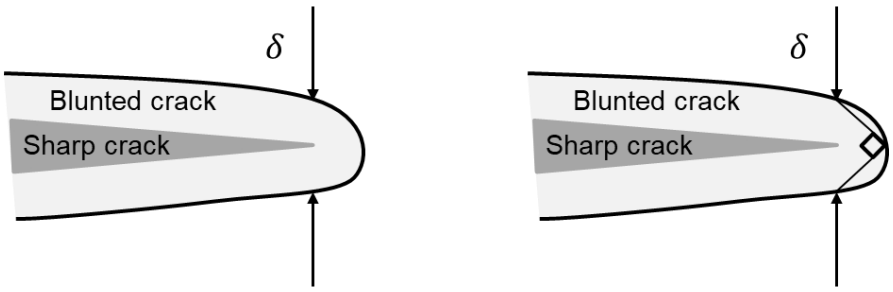

a. b.

Figure 2.10 CTOD (δ) estimated as crack face displacement a. normal to the original crack plane, b. at the intersection of a 90° vertex with the blunted crack flanks

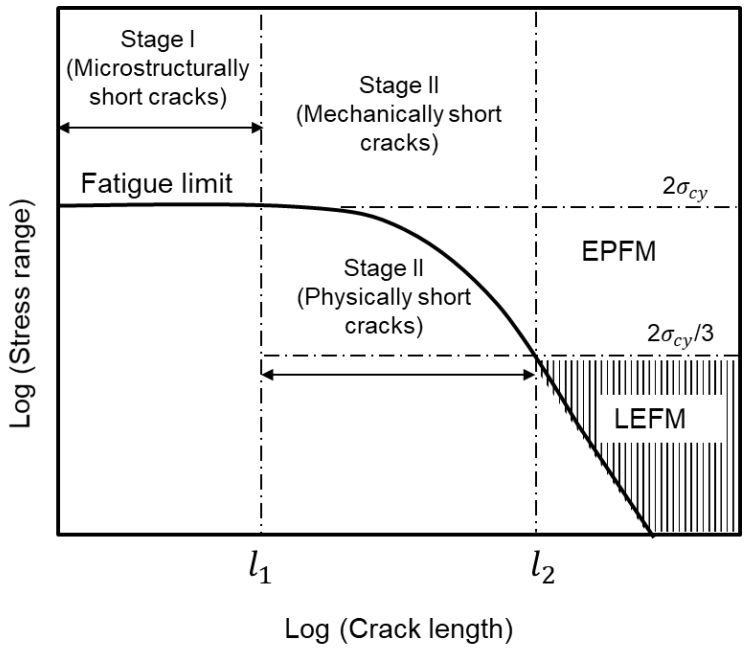

Figure 2.11 A Kitagawa- Takahashi type plot of stress range vs. crack length, showing the short crack regimes (based on [27]). The horizontal dotted lines at two-third and twice of the cyclic yield σ_{cy} represent the stress range limits for LEFM and Stage II physically short cracks, respectively. The vertical lines at l_1 and l_2 represent the crack length limits for Stage I microstructurally short cracks and Stage II EPFM cracks, respectively

2.2.2.1.1 Stage I cracks

According to the Kitagawa-Takahashi plot for 0.4% medium C steel produced by Brown [40], there exists a microstructural crack growth (MCG) regime where the crack length is of the order of microstructural features (< l_1 in Fig. 2.8) while the stress range is above the fatigue limit. The growth of these cracks is found to be severely affected by their interaction with the microstructure. The crack usually grows in a shear mode and is strongly influenced by the crystallographic planes. Brown [40] explained the behaviour of MCG cracks by employing the empirical equations of Hobson [41] who derived the short crack growth characteristics based on surface replication studies on uniaxial low cycle fatigue specimens of medium carbon steel. Brown [40] plotted crack growth rate da/dN as a function of crack length for short cracks in 0.4% carbon steel and showed that the MCG cracks exhibited an initial decelerating growth rate until the growth rate reached a minimum at a grain boundary barrier (l_1). Afterwards, the crack may exhibit an accelerating–decelerating growth pattern as it advances and encounters more barriers. Many such barriers other than grain

boundaries that can arrest cracks have been reported in literature, such as high strength phases, triple point corners, large inclusions, precipitates, pearlite zones, ferrite region in prior austenite grain boundaries, etc [33].

Lankford [37] reviewed the work of many other researchers and came to the conclusion that the short cracks mostly initiated from inclusions present in some preferentially oriented grains and grew at higher rates due to localized micro plasticity. He expressed views similar to Brown suggesting that the crack in early stages remains immersed in a local plastic zone and grows rapidly until it reaches a grain boundary barrier. At this point, the crack can either be arrested if the stress level is below the fatigue limit. If the stress level is above the fatigue limit, the crack can grow into the next grain, provided that micro plasticity can be initiated in the next grain. Lankford [37] believed that it was the total plastic displacement at the crack tip that was the driving force for the short crack growth.

2.2.2.1.2 Stage II EPFM cracks

As the crack grows, the plastic zone increases, and the effect of microstructural barriers diminishes. The Stage I crack then transitions to Stage II. The Stage II crack growth is described by EPFM at higher stress ranges, typically above $2\sigma_{cy}$ (mechanically short). Sometimes, LEFM is used to describe the short cracks growing at lower stress ranges [42], typically between $2\sigma_{cy}/3$ and $2\sigma_{cy}$ (physically short), when they are close to the LEFM threshold, by accounting for crack closure (see Section 2.2.2.1.3.2). Although a critical crack size for Stage I to Stage II transition has yet to be clarified, transitions were found to occur at crack sizes corresponding to 1 to 8 times the size of the microstructural barrier [37, 40, 43, 44]. The EPFM crack growth is Mode I controlled, meaning that the fracture surface is normal to the applied stress. Since the stresses are higher, the plastic zone size increases, and the crack traverses more grains with decreasing resistance. After going through approximately 10 grains (l_2) [33], the crack size exceeds the crack tip plastic zone, causing the growth rate to increase monotonically according to the LEFM criterion.

Based on the above discussion, the crack propagation rate vs. crack length for the Stage I, Stage II EPFM and LEFM long cracks has been diagrammatically represented in Fig. 2.12.

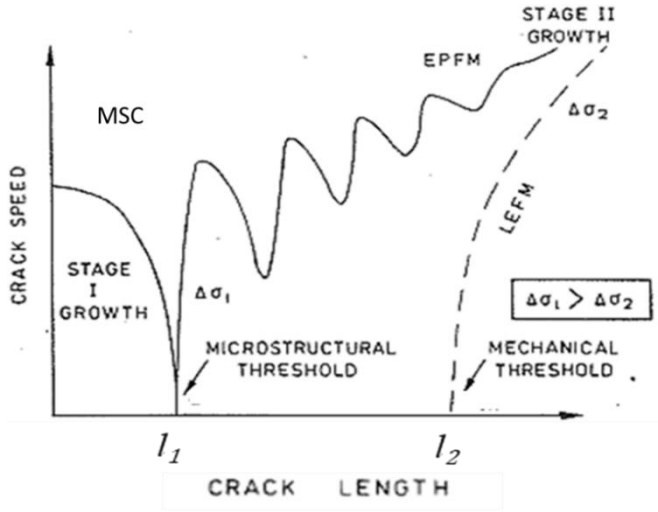

Figure 2.12 Crack growth pattern for Stage I, Stage II EPFM and LEFM long cracks (Adapted from [45])

2.2.2.1.3 Factors affecting short crack propagation

2.2.2.1.3.1 Effect of microstructure

The microstructural effects on short crack growth can be traced back to the work of Taylor and Knott [33]. They plotted l_2 values obtained from literature for different materials against 'structure size', D_s that is the smallest microstructural feature present in the material (grain size, average inclusion size, etc.) and established the correlation, $l_2 = 10D_s$. The authors [33] concluded that the growth rates for cracks of lengths smaller than l_2 are highly dependent on the surrounding microstructure. Microstructural barriers like a grain boundary may slow down the crack while a eutectoid colony may assist in rapid growth. Owing to their fine microstructures, HSS would have a smaller l_2 value, when compared to other materials. Taylor and Knott [33] mentioned that for HSS, l_2 may be smaller than 100 µm, which is less than the size of other structural defects such as inclusions. Moreover, they proposed that $l_1 \approx D_s$. This was based on the assumption that the crack growth at this stage is so rapid that it will be not be possible to record the crack length until it reaches a size corresponding to at least one microstructural unit. This was later experimentally verified by Brown [40] for a mild steel, where the Stage I crack transformed to Stage II EPFM after reaching a minimum crack growth rate at the first grain boundary (D_s = 100 µm).

Lankford [37] suggested that grain size was a major factor in influencing the size of the plastic zone for the short cracks. He hypothesized that, for smaller grains, the micro plastic zone size

would also be small and hence the crack growth rate would be very low. For large grains, however, the large plastic zone sizes will confer the crack with a high da/dN, which will allow it to grow rapidly and merge with the LEFM regime. He reported that, for 4340 steel, the length at which the cracks were arrested were 4 μm and 20 μm, corresponding to the minimum and maximum prior austenite grain size, respectively [46]. He also observed that if the orientation of the previous grain was identical to the next, no crack deceleration occurred. The dependence of short crack growth on the grain orientation was supported by Tanaka et al. [47, 48].

Miller [45] suggested that inclusion orientation (w.r.t. the loading direction) and shape played important roles in short crack retardation. De los Rios et al. [49] observed that the ferrite-pearlite interfaces were key features responsible for deceleration, and even arrest, of short fatigue cracks in a 0.4% C steel subjected to torsional fatigue loading at 350-400 MPa stress range. Similar results have been reported by various researchers where hard phases like pearlite and cementite have shown to reduce the crack growth rates in steels [48].

2.2.2.1.3.2 Effect of crack closure

Crack closure is a phenomenon that causes the premature contact of crack faces during the unloading portion of a fatigue cycle, compelling the crack to remain closed even when the applied forces are tensile. Plasticity induced closure occurs during fatigue loading at low stress ratios in which the crack faces are forced shut by compressive residual stresses acting at the crack tip. The greater the plastic zone wake of the crack tip, the higher is the buildup of compressive stresses. Roughness induced closure occurs due to contact of asperities on the fracture surfaces when Mode II (shear) displacements occur at near threshold intensities. Other mechanisms for inducing crack closure include transformation induced closure (closure due to austenite to martensite phase transformation near the crack tip at high deformations) and oxide induced closure (closure due to formation of oxide debris on the fracture surface), the details of which are not presented in this survey.

Therefore, when a tensile stress is applied on a closure affected crack, a part of the stress is spent in opening the crack (S_{op}) while the rest is spent in propagating the crack (S_{eff}). Therefore, the actual or effective stress range and the corresponding stress intensity factor range observed by the crack is ΔS_{eff} and ΔK_{eff}, respectively. Taylor and Knott [33] indicated that crack closure was another key factor responsible for the anomalous rapid growth rate of short cracks. Owing to their

small sizes, short cracks experience minimum or no closure at all. This would suggest that the short cracks experienced a higher ΔK_{eff} value when compared to the long cracks for the same applied ΔK [33]. The authors [33] raised a question on the credibility of comparing the short and long crack growth rates, as most of the short crack tests were done at low R ratios of 0 or 0.1, where the long crack was significantly affected by closure. On the other hand, using high R ratios to eliminate closure effects in the long crack regime would pose the risk of exceeding the yield strength during fatigue cycling, especially when a crack is short.

Tanaka et al. [50] attributed the abnormal behaviour of short cracks to a decrease in the ratio of the opening stress intensity factor to the maximum stress intensity factor ($K_{op}/\ K_{max}$) with a diminishing crack size. This was similar to what Taylor and Knott [33] indicated. Nevertheless, instances of roughness induced closure have been reported by Dowson et al. [51] where the short cracks showed increasing amounts of closure on crossing the grain boundary probably due to crack deflection. A combination of roughness and plasticity induced closure has been found to dominate the early short crack growth stages. Closure stress of the order of the maximum applied stress was observed by Morris [52] during the Stage I crack interaction in Al 7075 with a grain boundary. The closure stresses were found to drop as the crack advanced into the next grain by transitioning to Stage II. Therefore, it seems that the instant the crack tip crosses an interface is marked by significant closure levels that can affect short crack growth and hence, fatigue life predictions. Thus, incorporating the effect of closure is essential to compare short and long crack growth rates. From the above discussion, it appears that the need to include the effects of microstructure and crack closure in modeling short crack growth is essential.

2.2.3 Long crack propagation

The crack is said to transform into a Stage II LEFM crack, or a long crack, when its plastic zone size becomes much less than the crack length ($2r_p \leq a/25$) [27]. The crack develops two mutually perpendicular shear planes through which it propagates by equal shear decohesion on each plane. This gives it the appearance of propagating due to tensile forces perpendicular to its crack faces [45]. Under low stress conditions, the long crack growth can govern a significant portion of the component's fatigue life.

A typical log-log plot of da/dN vs. ΔK is depicted in Fig. 2.13, representing the 3 regimes of long crack growth. The regime A is associated with the existence of threshold stress intensity factor range (ΔK_{th}), and the crack growth is very slow, the average increment per cycle being smaller than the lattice spacing. The regime B or the linear portion of the curve, characterised by stable crack growth can be represented by the Paris' law [53] as:

$$\frac{da}{dN} = C(\Delta K)^m \tag{2.10}$$

where C and m are empirical constants depending on the material properties, microstructure, fatigue frequency, mean stress or load ratio, environment, loading mode, stress state and test temperature [6]. Fig. 2.14 represents the Paris regime in the da/dN vs. ΔK plot obtained by performing room temperature long crack propagation tests using 23-25 mm thick 300M compact tension specimens in low-humidity air at R = 0.08, 0.3 and 0.5 (adapted from [54]). The C and m extracted for R = 0.08 are 4.78 x 10^{-11} m/ (cycle. MPa$\sqrt{m}$) and 2.55, respectively. For steels, the average ΔK_{th} is reported to be about 5 MPa$\sqrt{m}$ [55].

Finally, the regime C represents rapid crack growth up to a stress intensity of K_c followed by brutal failure. K_c is also known as the material toughness or the material's ability to resist fracture. For mode I uniaxial loading, the plain-strain fracture toughness is denoted by K_{Ic}.

When the value of K is known for the component for the given loading conditions, the fatigue crack propagation life can be obtained by integrating Eqn. (2.10) from the initiation crack size to the final crack size corresponding to the material's fracture toughness.

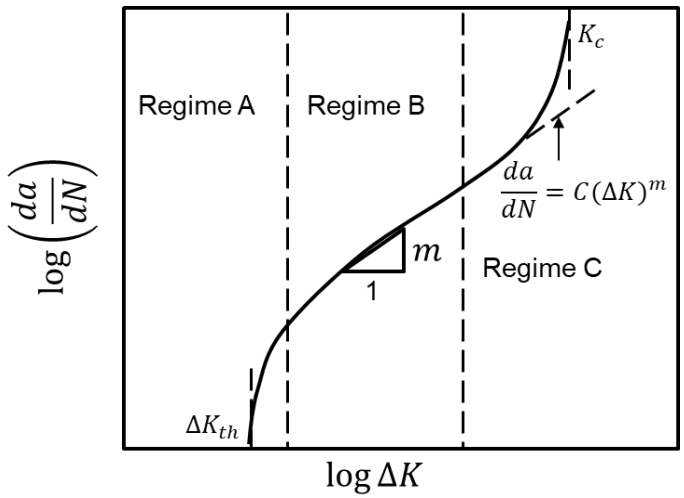

Figure 2.13 Crack growth rate da/dN vs. stress intensity factor range ΔK plot (log scale) showing different regimes of long fatigue crack propagation

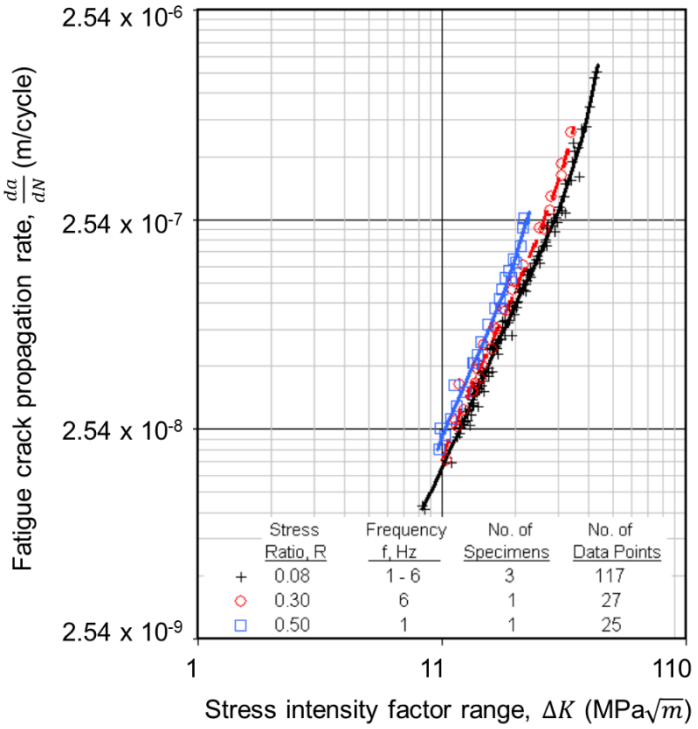

Figure 2.14 Paris regime (Regime B) in the da/dN vs. ΔK plot (log scale) for 300M steel at different R of 0.08, 0.3 and 0.5 (adapted from [54])

2.3 Shot peening parameters

2.3.1 Intensity

Shot peening intensity, also referred to as the Almen intensity, is a measure of the shot stream energy transferred to the part. Almen intensity is measured by peening a standardized thin steel plate, called 'Almen strip', for at least 4 different peening times, while keeping all other peening parameters constant. The resulting arc heights are measured using an 'Almen gage' and plotted against the corresponding peening times to produce a 'saturation curve'. The first point on the curve where the arc height increases by 10% by doubling the peening time T is the saturation point or the Almen intensity. Almen strips come under different thicknesses- N type (0.7874 ± 0.0254 mm), A type (1.2954 ± 0.0254 mm), and C type (2.3825 ± 0.0254 mm) for measuring low, medium and high intensities respectively. Figs. 2.15a and b depict the schematic for the Almen intensity measurement procedure and the typical intensity saturation curve, respectively.

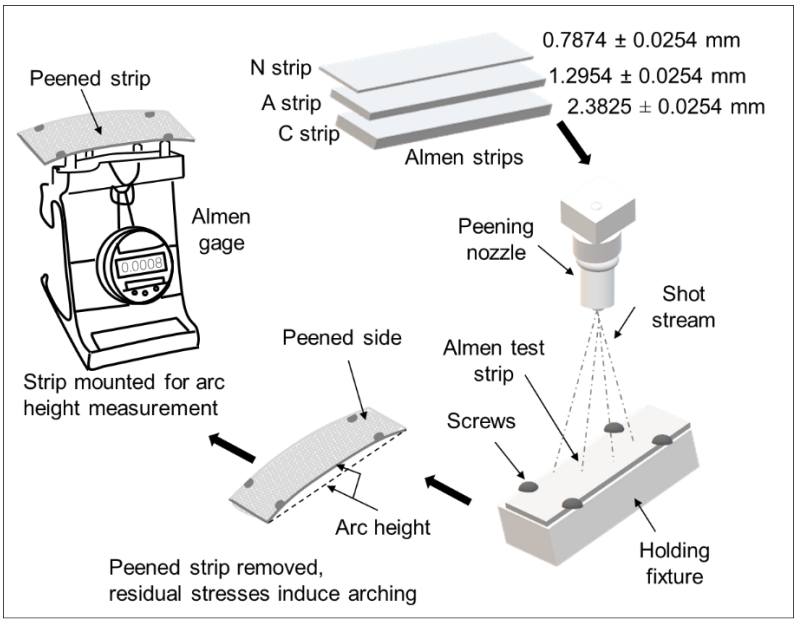

a.

Figure 2.15 a. Schematic for shot peening Almen intensity measurement, b. Intensity saturation curve (adapted from [56]). The Almen strip is peened by fixing it onto a holder with screws. The peened strip undergoes arching, the extent of which is measured by an Almen gage in terms of arc height. The Almen intensity is determined by repeating the measurements to produce a saturation curve

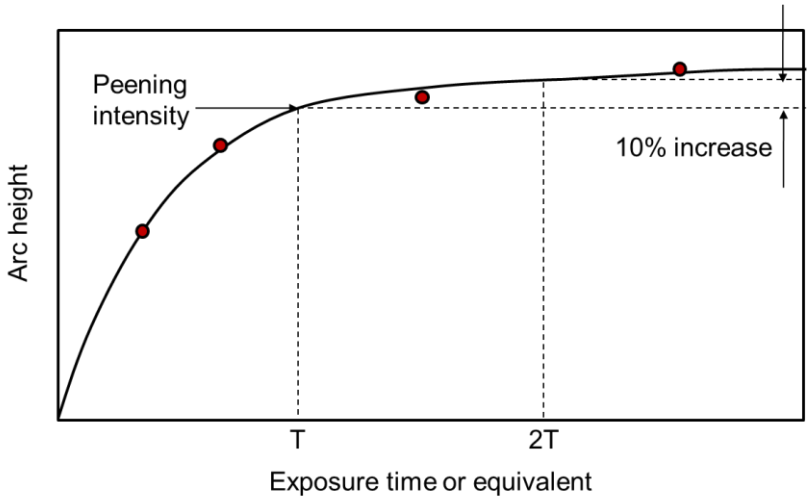

b.

Figure 2.15 a. Schematic for shot peening Almen intensity measurement, b. Intensity saturation curve (adapted from [56]). The Almen strip is peened by fixing it onto a holder with screws. The peened strip undergoes arching, the extent of which is measured by an Almen gage in terms of arc height. The Almen intensity is determined by repeating the measurements to produce a saturation curve (cont'd)

2.3.2 Coverage

Coverage is the percentage of the material's surface area impacted by the shots. 100% coverage (referred to as complete coverage) relates to the condition when the entire surface of a reference area is indented. Coverage of 'x' x 100% (x > 1) is defined as the coverage obtained for a peening time equal to 'x' times of that required for obtaining 100% coverage.

2.4 Effect of peening on surface characteristics

2.4.1 Effect of peening induced CRS on fatigue life

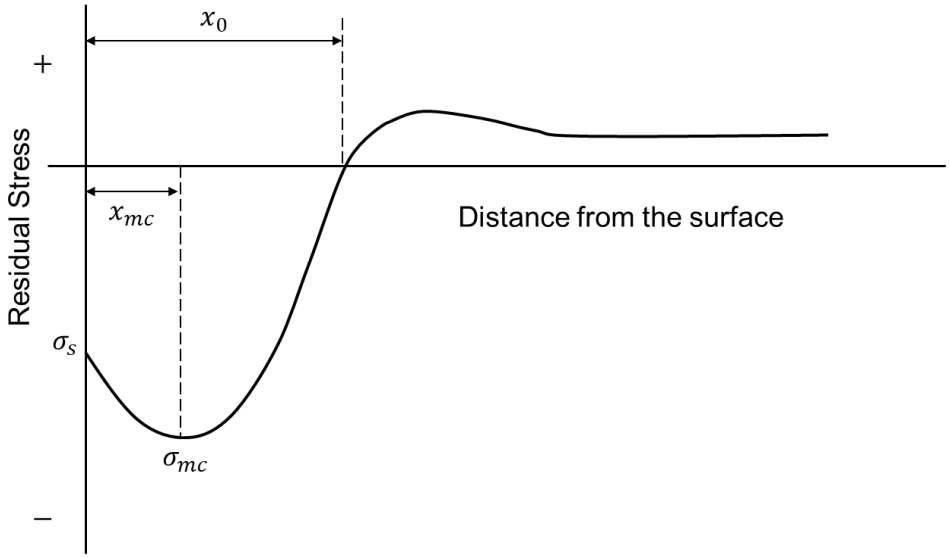

Figure 2.16 Typical CRS profile of a shot peened specimen

Fig. 2.16 shows the typical CRS profile of a shot peened specimen. It is characterized by the following parameters: the surface residual stress σ_s, maximum CRS σ_{mc}, depth at which maximum CRS occurs, x_{mc}, and the depth at which the residual stresses become tensile, x_0.

Many researchers have observed a strong correlation between the increase of CRS depth and fatigue life improvement [2-5]. Such trends have been observed for 4340 steels [2, 57]. Fatigue life, and hence CRS depth, is also related to the shot peening intensity and the coverage. Therefore, an appropriate choice of intensity and coverage parameters to ensure sufficiently deep CRS and thus, optimum fatigue life for the given material, is necessary.

Through thickness measurement of CRS on 4340 steel samples, shot peened at varying intensities (4 - 12A), can be obtained by X-ray diffraction (XRD) and subsequent layer removal by electro polishing. A higher peening intensity resulted in greater depth of CRS [1, 57, 58]. Similar trends were observed by Jayaram and Prevey [59] for 300M steel peened at 8A and 10A intensities. Therefore, with higher peening intensity, one would expect greater CRS depth hence a longer fatigue life. However, this is not always the case. The reasons for this exception include peening

induced surface roughness and CRS relaxation, which will be discussed in detail in Sections 2.4.3 and 2.4.4.

Intensities higher or lower than 6.3-8.3A using S230 type (0.58 mm diameter) cast steel shots at 200 % coverage, were found to decrease the rotating bending fatigue life of 4340 steel by 2-7 times at a stress amplitude of 931 MPa (62% of the 0.2% offset yield strength, $\sigma_{y,0.2}$) [2]. Similarly, 100% coverage produced longer LCF lives than those shot peened with a higher or lower coverage [60-62].

Therefore, based on literature, 100% coverage and a medium peening intensity (6-8A) appears to maximize the fatigue life of HSS like 300M steel. Nevertheless, the CRS distribution and hence the fatigue life is not entirely dependent on the Almen intensity and coverage, but several other parameters such as target material and shot hardness, shot size, shot velocity, peening angle, mass flow and pressure [63] [64], the details of which are not discussed in this work.

Although it is evident that peening induced CRS improve the total fatigue life of the component, it is necessary to understand how CRS affects the individual crack initiation and short crack propagation mechanisms.

2.4.2 Effect of peening on crack growth characteristics

The role of shot peening on fatigue life improvement can be physically explained in terms of crack initiation and crack propagation rate in the peened specimens. Berns and Weber [65] investigated the initiation and propagation of small fatigue cracks on prestrained peened and unpeened samples of a low strength high alloy CrMnV-steel subjected to cyclic 4 point bending. Pre-straining is plastic pre-deformation by bending done to create deep CRS within the material. They used ultrasonic surface waves to detect small cracks and to follow their extension. Five ultrasonic probes were used over the sample width to record individual crack activity. Three types of specimens were studied - a) prestrained at 1.2 times the yield strength; b) shot peened at 0.24A and prestrained as before, and c) shot peened at 0.32A Almen intensity under a prestrain of 0.75 times the yield strength and prestrained again at 1.2 times the yield strength. The authors [65] observed that all cracks started at the surface and not in the area of highest tensile residual stress. Significant delay in crack initiation due to shot peening was reported. The cracks initiated and propagated very slowly until the number of cycles for a rapid stable growth was reached. The interval between crack

initiation and fracture was found to be longer than the period for crack initiation. Similar observations were made by Hammond and Meguid [66] who performed rotating bending fatigue on medium carbon 080M40 steel peened at 16A. De los Rios et al. [1] investigated the effect of peening in unpolished A316 stainless steel specimens peened at 17.1A and subjected to bending fatigue at R = -0.8. Polishing the peened specimens reduced their fatigue lives due to removal of 20-25 % of the CRS layer. Surface fatigue cracks initiating from the edge of the unpolished peened specimen in the shape of quarter of a circle were observed. These cracks appeared to initiate quickly along the edge of the peening dimple and were arrested on reaching the end of the dimple for a period of time before propagating again. Optical microscopy and Scanning Electron Microscopy (SEM) analysis revealed that the cracks grew faster in depth than in width, suggesting the beneficial effect of surface CRS. Shot peening in all cases was found to delay crack initiation and retard short crack propagation. Crack length measurements were made by the replication technique and crack growth rates were calculated using the secant method. The ratio of crack initiation to crack propagation time was also found to reduce with increasing applied stress, suggesting possible relaxation of CRS. Guagliano and Vergani [67] reported the presence of non-propagating cracks in a notched quenched and tempered low alloy steel peened at 12A whose depth (0.15-0.3 mm) coincided with the depth of the peening induced CRS.

Peige et al. [68] conducted rotating bending fatigue tests on unpeened and peened 300M steel specimens at frequency of 50 Hz and inspected the crack initiation sites by SEM analysis. They observed that the cracks always originated on the surface for the unpeened samples. For the peened samples, the cracks initiated beneath the CRS layer, where the residual stresses were tensile. They explained that the critical stress for a crack to initiate in the specimen interior was more than that on the surface for the same material. This shows that shot peening increases the surface resistance to crack initiation. Torres and Voorwald [2] observed subsurface crack initiation for 4340 steel specimens peened at 2.7-14.1A (200% coverage) when subjected to rotating bending fatigue at low (62 % of $\sigma_{y,0.2}$) and medium stress amplitudes (67 % of $\sigma_{y,0.2}$). Most subsurface crack initiations occurred either at non-metallic inclusions (Fig. 2.14) or at unidentified features at varying depths (14-225 μm) beneath the surface. Surface crack initiation was also observed at high stress amplitudes (91 % of $\sigma_{y,0.2}$), especially for specimens peened at 14.1A and unpeened specimens. They correlated the reason for the best fatigue lives obtained for 6.3-8.3A to the low surface roughness coupled with high CRS that caused subsurface crack initiation, and in case of surface

crack initiation, delayed the crack propagation. Similarly, highest fatigue lives were obtained for a quenched and tempered (Q+ T200) 4340 steel peened at 14A (100% coverage) with cut wire shots, due to crack initiation at inclusions [69]. Moreover, these inclusions were located at depths corresponding to the CRS layer depth (240 μm) as shown in Fig. 2.17.

Studies on shot peened powder metallurgy Ni superalloys showed similar effects of peening on crack initiation. Barrie et al. [70] reported that peening with a high intensity (8A) and low coverage (200%) using CW14 shot suppressed crack initiation at surface inclusions in Udimet 720 and resulted in crack initiation at internal inclusions, which significantly improved LCF life by a factor of 2-9. This was however true mostly for fatigue tests performed at the low strain ratios of 0 and -1 for strain ranges of up to 0.8%. Nevertheless, fatigue lives of peened specimens with larger and more inclusions were lower than those of unpeened specimens with smaller and fewer inclusions. This was attributed to the greater accumulation of cyclic damage due to competition at the numerous inclusions in the peened specimens which were larger, more harmfully shaped and oriented than those in the unpeened specimens. Another reason was the higher tensile residual stresses in the interior of peened specimens when compared to those present in the unpeened specimens, that caused a higher stress concentration at inclusions. Another work by Huron and Roth [71] on powder metallurgy Rene'88 DT alloy revealed that shot peening using CW31 shot at an intensity of 7A and 125% coverage did not increase the LCF life significantly, although a slight increase occurred as the crack initiation shifted from surface or near surface inclusions to interior ones. The fatigue life was strongly correlated to the inclusion size. Moreover, the authors [71] used a probabilistic fracture mechanics approach developed for powder metal components to predict fatigue lives of the peened specimens. The model however underestimated the experimental fatigue lives. The authors [71] explained that sharp crack fracture mechanics was not appropriate for estimating fatigue life of the peened specimens when the crack initiated at buried inclusions. They hypothesized that the sharp cracks were formed very late in life and were preceded by a longer incubation period, which was not accounted for by the model. The conventional fatigue threshold did not apply to such small cracks growing in the grains surrounding the stress-concentrating inclusions. The incubation life would increase for smaller inclusion sizes, which explained their high fatigue lives. The authors [71] suggested that shot peening extended the crack incubation as well as propagation life.

From the literature, it can be inferred that shot peening delays crack initiation. Short cracks within the CRS layer induced by peening are decelerated or potentially arrested, thereby increasing the time for crack propagation and improving the fatigue life. Moreover, peening was able to protect the surface and shift the crack initiation to the subsurface, which resulted in the highest fatigue lives.

2.4.3 Effect of peening induced roughness on fatigue life

Roughness is detrimental to fatigue life since it causes premature fatigue crack initiation due to stress concentrations. Ypsilantis et al. [72] demonstrated the importance of considering surface roughness resulting from peening in fatigue life prediction. They compared the fatigue life of a SAE 9254 steel specimen peened at a high intensity of 10C and another peened at 10C followed by a lower intensity of 14A and observed that the latter had three times better fatigue life than the former. The two treatments led to only slight differences in the residual stress profiles that were not sufficient to explain, alone, the significant fatigue life difference experimentally observed. However, the residual stresses were greater in magnitude and deeper in case of 10C intensity, as compared to 14A, which indicates that the enhanced life can be attributed only to the difference in their surface roughness.

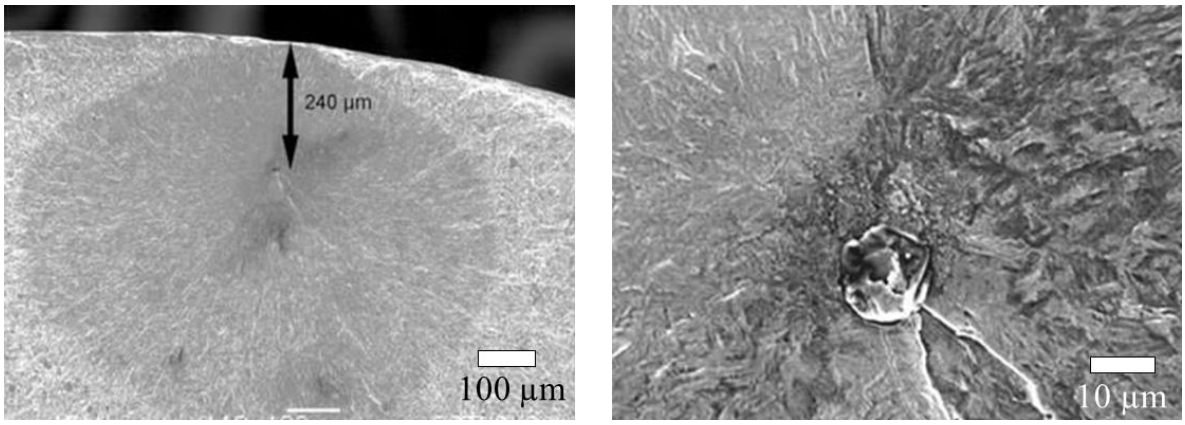

Figure 2.17 Crack initiation in a peened Q+T200 4340 steel at an alumina inclusion located at a depth corresponding to the CRS depth (left), closeup of the inclusion (right) [69]

Torres and Voorwald [2] observed that intermediate peening intensities (6.3A and 8.3A) yielded the best fatigue lives for 4340 steel instead of that with the highest CRS depth (14.1A). This suggests that roughness increases with the peening intensity, and for a threshold intensity, overcomes the beneficial effect of CRS, yielding lower fatigue lives. De los Rios et al. [1] also

found that A 316 steel specimens peened with glass media (12.2N) exhibited better fatigue lives than specimens peened with steel shots (6.3A, 17.1A). Tekeli [73] observed a decrease in fatigue strength in SAE 9245 steel as the peening intensity rose beyond the range of 20-25A. Such a detrimental effect due to high peening intensities is referred to as overpeening. Overpeening causes severe defects such as microcracks, laps, rolled edges or lips and other surface discontinuities that act as crack nucleation sites and lowers fatigue strength [74]. Fig. 2.18 illustrates some peening defects that are detrimental to fatigue life [69, 75].

Surface roughness was also found to increase with the peening coverage, which was detrimental to the fatigue lives of various steels [73, 76, 77].

Shot peened surfaces exhibit a number of dents that can be considered as micro-notches from which shorts crack can initiate. Shot peening micro notches induce stress concentrations that, according to Li et al. [78], are less severe than those induced by a single notch of the same geometry. Li et al. [78] proposed the following relation for stress concentration factor, $K_{t,rough}$ derived from the surface roughness parameters of surfaces with multiple dents by Finite Element Modelling as:

$$K_{t,rough} = 1 + 4.1\left(\frac{R_t}{R_{sm}}\right)^{1.3} \quad \text{for } \left(\frac{R_t}{R_{sm}}\right) < 0.15, \text{ or} \qquad (2.11)$$

$$1 + 2.1\left(\frac{R_t}{R_{sm}}\right) \quad \text{for } \left(\frac{R_t}{R_{sm}}\right) \leq 0.3$$

where R_t is the highest peak to valley height and R_{sm} is the spacing between adjacent peaks in a surface roughness profile. The parameters R_t and R_{sm} represent the peening dimple depth and the dimple width, respectively. This equation has been successfully used by several researchers to quantify the stress concentration effect due to peening [79-82].

Tosha [83] reported, for a medium carbon steel, that the depth (h_{pd}) and width (d) of a peened dimple is a function of the shot diameter (D), shot velocity (V) and the target material Vickers microhardness (H) given by:

$$h_{pd} = k_R * D * V * H^{-1/2} \qquad (2.12)$$

$$d = k_D * D * V^{1/2} * H^{-1/4} \qquad (2.13)$$

where k_D and k_R are target material constants.

According to equations 2.12 and 2.13, for a given target material, the greater is the value of $(D * V)$ and $(D * V^{1/2})$, the higher is the dimple depth (R_t) and width (R_{sm}), respectively. In a physical sense, D and V are related to the shot's kinetic energy through:

$$K.E. = \frac{1}{2} * m_s * V^2 = \frac{1}{2} * \left(\rho * \frac{4}{3} * \pi * \frac{D^3}{8}\right) * V^2 = \frac{\pi}{12}\rho D(D * V)^2 \quad (2.14)$$

where $K.E.$, m_s and ρ are the kinetic energy, mass and density of the shots respectively. Therefore, the higher is the shot's kinetic energy, the greater is the shot's penetration into the target material and hence, the greater is the peened dimple's depth and width.

In summary, peening induced roughness causes surface stress concentrations, which is detrimental to fatigue life, especially for high peening intensities. Therefore, care has to be taken to select peening parameters such that the beneficial effect of CRS and work hardening overcomes the detrimental effect of peening induced roughness. Eqns. (2.11) to (2.13) can be used to optimise the peening parameters such as shot size, shot velocity and shot hardness, for a given material to obtain the desired roughness on the peened parts.

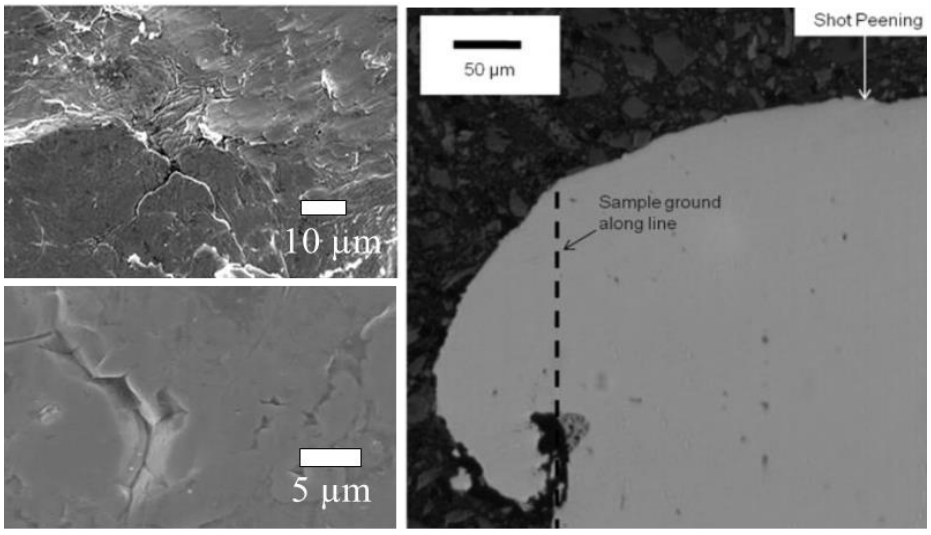

Figure 2.18 Surface defects such as microcracks (top left), micro notches (bottom left) and rolled edges or shear lips (right) caused by peening [69, 75]

2.4.4 CRS relaxation effect on fatigue life

Residual stress relaxation occurs when the shot peened component is subjected to load amplitudes causing plastic strains in the component. Thus, the relaxation can occur at much lower stresses than

the monotonic yield strength, as HSS generally tend to strain soften during cyclic loading [1, 84]. Stabilization of the residual stresses would thus occur when the stresses remain below the cyclic yield strength.

Several researchers have assessed residual stress effects on fatigue life by considering them equivalent to adding a mean stress over the applied mean cyclic stresses. The assumption is based on the observation that a tensile mean stress has a detrimental effect on fatigue strength, whereas a compressive mean stress enhances the fatigue strength [85]. The basis of this was laid by Morrow and Sinclair [86] who performed strain controlled axial fatigue tests on 4340 steel and measured the mean stress relaxation with the increasing number of cycles. Tests were done for 3 types of heat treatment conditions (leading to high, medium and low hardness) with different initial mean stresses (0 to tensile of upto 80% $\sigma_{y,0.2}$ for all hardness conditions and a compressive mean stress of 47% $\sigma_{y,0.2}$ only for low hardness condition) and different strain amplitudes at R = -1. A relaxation of the initial mean stress was observed, which was highest in the first cycle for all conditions at high strain amplitudes, after which the relaxation was mostly linear with increasing number of cycles. Maximum first cycle relaxation occurred for the low hardness (Rockwell C 29) condition at high strain amplitudes while almost no relaxation occurred for medium (Rockwell C 41) and high hardness (Rockwell C 50) conditions. Moreover, no significant relaxation occurred at low strain amplitudes (close to the fatigue limit). Based on the experimental results, they proposed the following empirical relationship for mean stress relaxation:

$$\frac{\sigma_{mN}}{\sigma_{m1}} = \frac{\sigma_{ys} - \sigma_a}{\sigma_{m1}} - \left(\frac{\sigma_a}{\sigma_{ys}}\right)^{b'} \log N \tag{2.15}$$

where σ_{mN} is the mean stress at the Nth cycle, σ_{m1} is the mean stress at the first cycle, σ_a is the alternating stress amplitude, σ_{ys} is the monotonic yield strength, b' is a constant depending on material softening and applied strain range, $\Delta\varepsilon$. When applied to shot peened components, this equation is valid only for R = -1 condition since residual stress is analogous to the initial mean stress only when there is no additional mean stress due to the axial loading. The experimental results for 4340 steel only supported Eqn. (2.15) for N $<10^6$ cycles, as some low hardness specimens showed a steep increase in mean stress relaxation after 10^6 cycles. Jhansale and Topper [87] proposed:

$$\sigma_{mN} = \sigma_{m1}(N)^{b'} \quad (2.16)$$

where b' is the relaxation exponent dependent on material softening and applied strain range $\Delta\varepsilon$.

Kodama [88] observed by X- ray diffraction that shot peening induced surface residual stresses relax more than 50 % during the first fatigue load cycle. This drastic relaxation behaviour in the first cycle however is not explained by Eqn. (2.16) for which no relaxation occurs at N=1. Kodama proposed a relationship similar to Eqn. (2.16) which again supported the relaxation trend after the first load cycle as:

$$\sigma_N^{re} = A' + m'' \log N \quad (2.17)$$

where σ_N^{re} is the surface residual stress after N cycles, A' and m'' are material constants depending on the stress amplitude.

Bergstrom and Ericsson [89] studied residual stress relaxation behavior at R = 0 and -1 in shot peened notched 0.4% C low alloyed steel specimens. They observed that CRS relaxation occurs only when the sample is subjected to a fatigue load that includes a compressive stress/strain (R < 0) and the extent of relaxation is governed by the compressive load level. Significant relaxation was observed for R = -1 while R = 0 showed almost no relaxation. Superimposed compressive overloading was found to be harmful for the compressive residual stress state while tensile overloads resulted in a temporary increase in CRS, which soon relaxed to the level prior to overloading. Torres and Voorwald [2] found that the stress relaxation for shot peened 4340 steel was dependent on the applied stress level and the number of fatigue cycles encountered by the specimens. They observed that, when a specimen shot peened at 14.1A was subjected to low and high stress levels (840MPa and 1130 MPa) at 10^4 cycles at R = -1, the relaxation was more significant to the highest applied stress, both at and below the surface. Stabilization of CRS was also encountered on the same sample when tested for fatigue at 10^3 and 10^4 cycles. Comparing CRS relaxation in shot peened samples at high (14.1A) and medium (6.3A, 8.3A) intensities, and fatigue tested at 840 MPa (R = -1), revealed that CRS relaxation was the smallest for samples peened at an intensity of 6.3A, which supports the best fatigue life found by the authors.

As can be seen from the literature, the relaxation behaviour is mainly affected by the material cyclic stress strain response, applied strain amplitude, load level and degree of cold working, rather than the magnitude of mean (or residual) stress, most of which occurs during the first few fatigue load

cycles. Considering the residual stress relaxation is essential to accurately predict the effects of shot peening on fatigue life.

2.5 Analytical fatigue life prediction for shot-peened materials

A significant contribution towards fatigue life prediction of shot-peened Al alloys was made by Navarro and De los Rios [90]. The authors [91-95] developed a unified model for predicting long and short crack propagation using a Paris law type relationship between CTOD and da/dN. Bilby et al. [96] modeled a freely slipping crack using a dislocation distribution function, tending to infinity in the plastic zone. Navarro and De los Rios [91] improved the model by introducing Taira et al.'s [97] concept of grain boundary barriers interacting with the crack tip plastic zone to explain the short crack deceleration-acceleration behavior. The authors also incorporated the effects of grain orientation and work hardening [98, 99] on short crack growth in their model. The Navarro-Rios model was further modified to include the effects of peening induced CRS, work hardening and surface roughness. The model was experimentally validated for Al 2024-T351 specimens peened at intensities of 6-11A and tested in four-point bending under a stress ratio R = 0.1 by the authors [90]. Additional validation of the model was provided by Solis et al. [100] for the same material peened at 4A intensity, 45° incidence angle and 200% coverage, tested under similar loading conditions. The N-R model however, is a crack propagation-based model and does not account for the time spent in crack initiation, which would affect the high cycle fatigue life prediction as it is crack initiation dominated. Moreover, it does not account for the CRS relaxation during cyclic loading.

A stress-life (S-N) approach based on Crossland and Dan Van multi-axial fatigue criteria was developed by Fathallah et al. [62] to predict the HCF behavior of peened SAE 3415 steel (100% coverage) subjected to 3-point bending at R = 0.1. The approach accounted for the beneficial effects of CRS and work hardening along with the detrimental effects of surface discontinuities caused by peening, except for CRS relaxation. Liu and Pang [101] used the Findley stress criterion for multiaxial fatigue and modified it to account for the effect of CRS and its relaxation upto a stabilized value. The model agreed well with the experimental fatigue results of Torres and Voorwald [2] for 4340 steel shot peened at an intensity of 2.7A, but overestimated the fatigue life of samples peened at an intensity of 8.3A, under LCF conditions. This was attributed to the fact that the model did not account for the peening induced roughness. You et al. [102] used the Smith-

Watson-Topper and Fatemi-Socie multiaxial fatigue criteria to predict the LCF life of a shot peened low-pressure turbine blade steel with different notch geometries. However, the effect of surface roughness was not accounted for, which overestimated the fatigue life for specimens exhibiting peening induced surface damage.

A fracture-mechanics based fatigue life prediction model was introduced by Xiang and Liu [103] for peened 2024-T351 Al alloy specimens subjected to uniaxial constant amplitude high cycle fatigue loading (R = 0.1). The authors used an asymptotic stress intensity factor solution [104] for notch cracks to define the surface roughness created by peening. A time-varying residual stress function was used to account for the changing crack tip stress ratio (due to CRS relaxation) during crack propagation. The model relied on a fictitious initial crack length corresponding to the "intrinsic threshold stress intensity", to preclude the residual stress effects due to pre-cracking during long crack propagation experiments. This was obtained by extrapolating the crack growth curve from Paris-regime log-linearly [105], based on experimental [106] and theoretical observations [107] in literature. Although the model correlated well with experimental results, the initial crack length used for prediction lacked proper experimental evidence. Gao and Wu [108] proposed another fracture mechanics-based approach where they used a plasticity induced crack closure model developed by Newman et al. [109] to predict the axial HCF lives of notched 7475-T7351 Al specimens peened at 8A intensity and 100% coverage tested at R = 0.06. The authors [108] employed the weight function method, suitable to calculate the stress intensity factors for cracks growing in residual stress fields with steep gradients. Only crack propagation was considered since the crack initiation life represented a very small fraction of the total fatigue life. Short crack propagation was monitored by making cellulose acetate replicas of the notch surface at specific intervals. They also defined an initial crack length of 0.02 mm based on their examination of the replicas using SEM. Good agreement between the predicted and the experimental fatigue lives was observed. Bagherifard et al. [110] presented a critical review of the application of two fracture mechanics-based fatigue criteria to calculate the fatigue strength of shot peened notched specimens of a low alloy steel (40NiCrMo7) subjected to rotating bending fatigue tests at R= -1 and axial fatigue tests at R= 0.1. The authors showed that the theory of critical distances (TCD) based on Taylor's Line method, combined with the Sines criterion for equivalent stress calculation, provided better agreement with the experimental fatigue strength than the Atzori approach [111]. According to the TCD approach, notched fatigue limit condition occurs when the

effective stress obtained by averaging the equivalent stress along the notch bisector over a material characteristic length reaches the plain fatigue limit. The Sines criterion considers the peening induced residual stresses as mean stresses superimposed on the applied cyclic load. Bagherifard et al. [112] have also introduced factors for including the effects of peening induced roughness and work hardening. The authors observed that, when the applied stress was uniaxial, considering the biaxial nature of peening induced residual stresses overestimated the fatigue strength, when compared to considering only the residual stress component in the applied load direction. However, this approach requires an accurate determination of the stress distribution in the notch vicinity when subjected to fatigue loading, which calls for costly and time-consuming finite element computations. Moreover, the approach does not consider the impact of shot peening on the notch geometry and the resulting alterations in the stress distributions.

Nevertheless, it is important to point out that the predictive models do not account for the fatigue life dispersion. To account for this dispersion, the aerospace industries typically employ a conservative statistical analysis approach called B-basis [113, 114], which is a measure of the 95% lower confidence interval on the 90% survival of the sample population. Therefore, the use of statistical estimates is needed to prevent premature failures resulting from design based on average fatigue life predictions.

2.6 Summary of literature review

This survey reveals that the influence of shot peening on HSS fatigue life should be determined by considering both the associated beneficial effects (CRS) and the detrimental effects (surface roughness, CRS relaxation).

A component's total fatigue life can be divided into the crack initiation and the short and long crack propagation stages. Crack initiation in HSS is mainly caused by non-metallic inclusions when the specimen is loaded at lower stress amplitudes (HCF regime) and by surface discontinuities when it is loaded at higher stress amplitudes. The difference in the inclusions' and steel matrix mechanical properties promotes the creation of voids prior to fatigue loading or early debonding/cracking within the first few fatigue cycles. Therefore, inclusions are considered as inherent cracks in the material whose propagation govern the component's total fatigue life. The inclusions' size and location are instrumental in determining the stress intensity factor or the driving force for crack growth, which can be determined using Murakami's equation (Eqn. (2.3)).

Similarly, peening dimples can be considered as small notches [78] which cause high surface stress concentrations, that can be estimated using Li et al.'s equation (Eqn. (2.11)). These notches develop into cracks, which propagate until failure. Long crack propagation, quantified by the Paris' equation [53] (Eqn. (2.10)), being a major part of the LCF, can be used for fatigue life predictions. Nevertheless, shot peening primarily lengthens the crack initiation and short crack propagation stages, which cannot be quantified using the above equation. Moreover, the initiation and propagation of short surface cracks in HCF would occupy a significant portion of the fatigue life. Hence, the interaction of peening induced CRS with the material microstructure and closure mechanism, that influence the growth of short cracks, needs to be investigated. The existing fatigue life prediction models for shot peened specimens do not account for this interaction. Most of the models also neglect the CRS relaxation and short crack initiation which are essential for accurate fatigue life predictions. Additionally, while most of the models have been validated for Al-alloys, their application in case of steels has been limited.

For HSS subjected to high cycle fatigue, varying inclusion sizes have been found to be a cause of fatigue life scatter. This scatter is neglected by the fatigue life prediction models, which is an important design consideration for aerospace materials.

Based on the literature survey, the following gaps in knowledge were identified:

- Lack of experimental fatigue data on shot peened high strength steels
- Lack of existing models accounting for the crack initiation and residual stress relaxation in shot peened components subjected to fatigue loading
- Lack of models accounting for the experimental fatigue life scatter for shot-peened specimens

CHAPTER 3 OBJECTIVES

The principal objective of this research project is to study the effect of shot peening on the axial fatigue life of aerospace grade 300M steel.

3.1 Specific objectives

The literature survey identified very specific gaps in the current knowledge that must be addressed:

- ***Insufficient experimental data in case of shot-peened 300M steel (Article 1 & 2)***
  Although shot peening is extensively used on high strength steels that find major applications in aircraft and engine parts, available literature on the axial fatigue life of shot peened high strength steels is scarce. An extensive experimental campaign will be undertaken to obtain axial fatigue data at a stress ratio R = -1 for 300M steel specimens shot peened under different conditions (intensity and coverage) and subjected to 2 stress amplitudes (low and high). Residual stress measurements will also be performed for each of the studied conditions. Such data would be valuable for validating any predictive models developed in the future.

- ***Statistical analysis of fatigue life scatter (Article 1 & 2)***

  The fatigue life scatter obtained from the experimental tests will be analyzed based on statistics. Conservative approaches similar to those used by the aerospace industries such as B-basis will be employed.

- ***Quantification of peening induced CRS relaxation during fatigue loading (Article 1 & 2)***
  As inferred from the literature, CRS relaxation is important to consider while predicting the fatigue life of shot peened steels and depends on the material cyclic yield properties and local deformation. Interrupted axial fatigue tests will be performed to quantify a cycle-based relaxation of the residual stresses in the material at the 2 stress amplitudes.

- ***Quantification of crack initiation and short crack propagation (Article 3)***

  Replication technique will be used to achieve this objective. Silicon replicas of the samples will be made before subjecting them to fatigue loading, and thereafter at predetermined intervals. If the replica is done at proper intervals, the crack can be traced back to the time it initiated [49]. However, this will be possible only for surface cracks. The features responsible for crack initiation will be characterized in terms of size, shape composition and frequency.

CHAPTER 4 METHODOLOGY

This section summarizes the experimental, statistical and modelling techniques used to fulfill the objectives of the research.

4.1 Experimental techniques

4.1.1 Stress-controlled axial fatigue tests

Axial fatigue tests were performed at 2 stress amplitudes: 931 MPa (55% of 0.2% offset yield strength $\sigma_{y,0.2}$) and 1089 MPa (64% of $\sigma_{y,0.2}$) with a stress ratio, R = -1 and a frequency of 10 Hz, in agreement with ASTM E466 standard [119]. Uniform gage cylindrical specimens as shown in Fig. 4.1 were used. The specimens were extracted from 25.4 mm diameter 300M steel bars, quenched and tempered in accordance with the AMS 6257E standard. The tests were performed at room temperature on an MTS 318.25 servo-hydraulic system equipped with a 250 kN MTS 661.22c-01 load cell with MTS 793 software. SEM was used to observe the features responsible for crack initiation on fractured samples. A qualitative compositional analysis of these features by EDS was also accomplished.

At first, 2 stress amplitudes of 862 MPa (51% of $\sigma_{y,0.2}$) and 1089 MPa (64% of $\sigma_{y,0.2}$) were chosen to obtain target N_f of 10^4 and 10^6 cycles (using polished specimens) to account for the low and high cycle fatigue behavior of the material. However, fretting problems were encountered at 862 MPa which resulted in the specimens breaking at the grip section instead of the gage section. Increasing the stress amplitude to 931 MPa alleviated this problem and was thus chosen for the experiments.

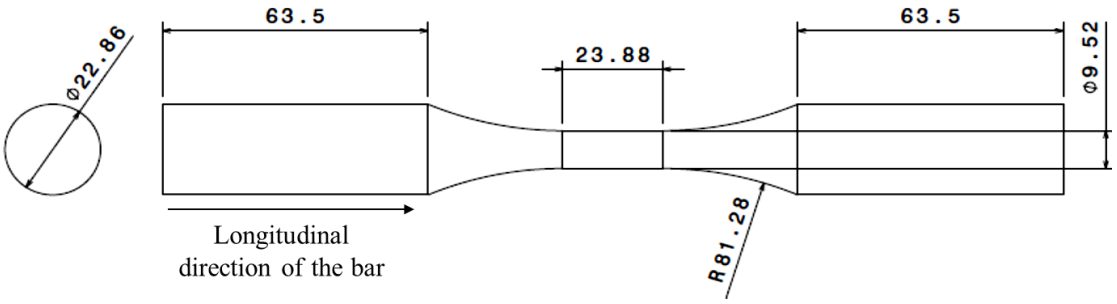

Figure 4.1 Uniform gage cylindrical specimen dimensions (in mm) for stress-controlled fatigue tests

4.1.2 Strain- controlled axial fatigue tests

These tests were performed using the uniform gage cylindrical specimens with a gage length of 28.575 mm according to the ASTM E606 standard. The specimens were extracted from 25.4 mm diameter heat treated 300M steel bars. A strain ratio, R_ε = 0 was used to perform the tests at 6 strain amplitudes, $\Delta\varepsilon/2$ = 0.3%, 0.4% 0.5%, 0.7%, 0.8% and 1%. The tests were performed at room temperature on an MTS 318.25 servo-hydraulic system equipped with a 250 kN MTS 661.22c-01 load cell with MTS 793 software.

4.1.3 Monotonic tensile tests

Tensile tests were performed on cylindrical specimens of 6.1 mm diameter and 25.4 mm gage length according to ASTM E8 standard. The specimens were extracted from 82.6 mm diameter heat treated 300M steel bars. Three tests were performed on a 100 KN capacity MTS servo-hydraulic machine at a strain rate of 0.005 min^{-1}. Two types of extensometers were used – axial (to record the longitudinal strain) and transverse (to record the lateral strain). The setup for the tensile test is shown in Fig. 4.2.

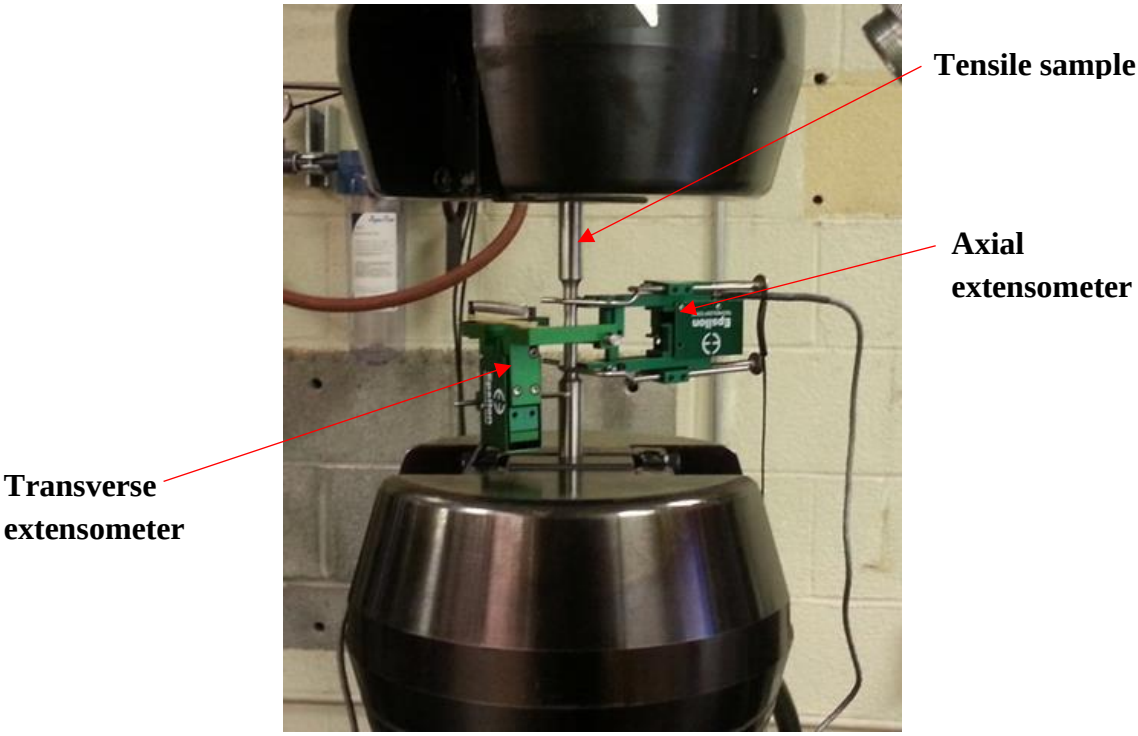

Figure 4.2 Tensile test setup for cylindrical 300M steel samples with axial and transverse extensometers

4.1.4 Shot peening

Shot peening was performed at 100% coverage using an air pressured shot peening machine provided by Canablast and equipped with 6 axis M-20iA Fanuc robot and a rotating table. Two shot types, namely conditioned cut wire CW14 (average diameter = 0.35 mm) and cast steel S230 (average diameter = 0.58 mm) were used. A standoff distance of 305 mm and 90° angle was maintained during the peening process to yield Almen intensities of 4 A and 8 A. The speed of the rotating table and the robot were also maintained at 22 rpm and 22 mm/s respectively. The 3 studied shot type-intensity combinations will be henceforth referred to as S230-4A, S230-8A and CW14-8A. Average shot velocities measured using ShotMeter G3 (a particle velocity sensor from Progressive Surface & Tecnar Automation) for S230-4A, S230-8A and CW14-8A conditions were 12 m/s, 26 m/s and 76 m/s, respectively. The pressure and mass flow rates used to obtain the above-mentioned velocities are tabulated in Table 4.1.

Table 4.1 Shot peening parameters used

Shot peening conditions	Pressure (psi)	Mass flow rate (lb/ min)
S230-4A	8.1	30
S230-8A	15.6	28
CW14-8A	39	15

4.1.5 Surface roughness measurement

Surface roughness profiles were measured with a Mitutoyo Formtracer SV-C3200 contact profilometer for 3 specimens for each surface condition, except for the polished specimens. Three measurements along the longitudinal direction were made for each specimen over a total evaluation length of 20 mm and sampling (or cutoff) lengths of 0.8 mm for the as-machined specimens and those peened using the S230-4A condition. A sampling length of 2.5 mm for specimens peened with S230-8A and CW14-8A conditions was used.

4.1.6 Quantification of peening induced CRS and their relaxation during fatigue loading

Through thickness residual stress profiles were obtained by the X-ray Diffraction (XRD) technique for the hourglass specimens used. A Pulstec μ-X360n apparatus equipped with a Cr-tube was used, allowing the use of $K\alpha$-lines for the measurements on the {211} family of planes. Diffraction peaks were fit by the Lorentzian method [115] and residual stresses were calculated using the $cos\ \alpha$ method [116]. The X-ray elastic constant (XEC), ½ S_2, was previously determined for the {211} family of planes, as described in the work of Delbergue et al. [117]. The XRD measurements were made assuming a non-textured material having an equi-bi-axial stress state after shot peening. Measurements were performed in the loading direction, where most of the stress relaxation occurs in axial fatigue. The XRD conditions used for all residual stress measurements are summarized in Table 4.2.

A layer removal technique was combined with the XRD measurements to obtain the in-depth residual stress profiles. Thin layers of material were removed by electropolishing with a perchloric acid-based solution. The thickness of the removed layer was measured using a Mitutoyo SJ-400 profilometer. The Moore and Evans correction [118] was used to correct the stress redistribution due to the layer removal process.

Interrupted fatigue tests were performed on peened rectangular hourglass specimens (shown in Fig. 4.3), to quantify the residual stress relaxation during cyclic loading. Rectangular specimens were chosen to simplify the XRD measurements. Measurements were performed after: 1 cycle, 200 cycles and 80% of fatigue life for only 2 shot peening conditions (S230-8A and CW14-8A) due to budget constraints. The 80% fatigue life was determined based on the mean fatigue life obtained from 2 hourglass specimens subjected to fatigue at each of the 2 stress amplitudes. The choice of intervals was influenced by the mean stress relaxation results observed in the strain-controlled fatigue tests discussed in Section 8.

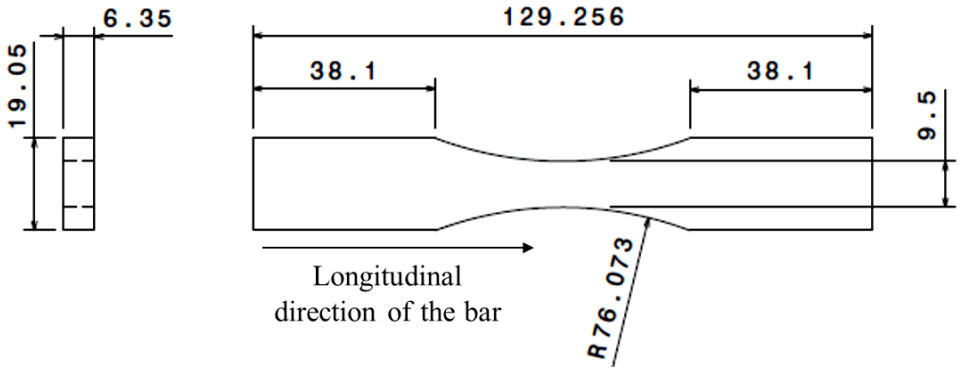

Figure 4.3 Hourglass specimen dimensions (in mm) for short fatigue crack growth tests [119]

Table 4.2 X-ray diffraction conditions used for residual stress measurements

Detectors	Tube target	Diffraction planes	Bragg angle
2D	Cr (λ = 2.291 Å)	{211}	2θ = 156.4°
XEC (½ S_2)	Nb. of inclination	Aperture size	Exposure time
5.68 E-6 MPa^{-1}	1	1 mm	30 s

4.1.7 Full width half maximum (FWHM) and microhardness measurements

The X-ray diffraction peaks were recorded and fit using the Lorentzian method [156] to extract peak width at half of the diffraction maximum intensity or the Full Width at Half the Maximum (FWHM). The FWHM has been correlated to the plastic strain or the degree of cold work in shot peened materials by several researchers [157-159]

Additionally, microhardness has been used as a measure of the amount of cold work in shot peened materials due to the strong similarity between microhardness vs. depth profiles and FWHM vs. depth profiles [157]. Therefore, microhardness vs depth profiles were obtained on the peened hourglass specimens to compare with the FWHM measurements. Vickers microhardness tests were done using a diamond pyramid indenter with a load of 0.5 kgf. For each peening condition, two specimens were used- one prior to fatigue testing and the other after fatigue testing (fractured specimen). Tests were also performed on unpeened specimens for comparison with peened specimens.

4.1.8 Quantification of crack initiation and short crack propagation

Interrupted axial fatigue tests (stress ratio, R = -1) were performed by the authors [119] at room temperature under 2 stress amplitudes: 1089 MPa (64% of $\sigma_{y,0.2}$) and 931 MPa (55% of $\sigma_{y,0.2}$) at a frequency of 10 Hz, in accordance with the ASTM E466 standard [120]. The hourglass specimens, as shown in Fig. 4.3, were extracted from a heat treated 300M steel bar of 31.8 mm diameter. Three surface conditions, namely as-machined, polished and shot peened, were studied. The polished specimens were prepared by mechanically polishing as-machined specimens down to 1 μm surface finish. The peening was done using two types of shots: CW14 (conditioned cut wire) and S230 (cast steel). The peening intensity was 8A and full coverage was reached. A total of 16 samples were tested; 2 samples per surface condition, for each stress amplitude.

Fast curing two-part silicon rubber replicas were used to backtrack the initiation and monitor the propagation of short surface cracks (≤ 0.8 mm), in flat hourglass specimens. Silicon replicas of the samples were made before subjecting them to fatigue loading, and thereafter at predetermined intervals. By observing the replicas, the crack was traced back to the time it initiated. However, this was possible only for surface cracks. The replicas

were observed using optical microscopy. The fracture surfaces were analysed using scanning electron microscopy (SEM). The features responsible for crack initiation were characterized in terms of size, shape composition and frequency. along with energy dispersive spectroscopy (EDS) to qualitatively identify the features responsible for fatigue crack initiation [119].

4.1.9 Long crack propagation and plain-strain fracture toughness tests

Long crack propagation tests were performed at R = 0.1 using 2 12.7mm thick compact tension C(T) specimens with chevron notch according to the ASTM E647 standard [121]. The tests were performed at room temperature on an MTS 318.25 servo-hydraulic system equipped with a 250 kN MTS 661.22c-01 load cell. The crack displacement was measured using MTS 632.02B-20 COD gage. Crack closure was determined according to the 2% compliance offset criterion in the ASTM E647 standard [121]. The purpose of the long crack propagation tests was to compare the crack growth rates of the closure-free short cracks and that of the long cracks.

Plain-strain fracture toughness (K_{IC}) tests were performed using 2 compact tension C(T) specimens (having the same geometry as the LCP tests) according to the ASTM E399 standard [121]. The tests were performed on an MTS 318.10 servo-hydraulic system equipped with a 100 kN MTS load cell.

4.2 Statistical analysis

4.2.1 Fatigue life dispersion

A conservative estimate of 90% survival at 95% confidence interval was chosen for this analysis to compare the fatigue performance of specimens with varied surface treatments. A measure of the lower bound on this estimate, called B-Basis, is typically used in aerospace to set design allowables [122]. The statistical analysis was carried out through the following steps:

a) The Anderson-Darling goodness of fit test [123] was used to identify the best fitting distribution for each condition.

b) The maximum likelihood fitting parameters at 95 % confidence interval were obtained for the distribution. The log-likelihood maximization was achieved by assuming a chi-squared approximation.
c) The number of cycles leading to 90% survival was finally calculated by inserting the maximum likelihood estimates into the inverse cumulative distribution function.

B-basis is defined by the number of cycles to failure corresponding to the lower bound of the 95% confidence interval on 90% survival of specimens.

The statistical analysis was performed using MATLAB R2013a.

Another statistical analysis was performed using a survival of 99%, at 95% confidence interval, using the conventional Weibull and Log normal distributions to fit the fatigue life data. The analysis was performed using a commercial statistical analysis software Minitab. This approach is akin to the conventional statistical analysis of fatigue data more commonly used for steels in aerospace companies.

4.2.1.1 Studied distribution models

4.2.1.1.1 Weibull model

Weibull's distribution is usually used to represent fatigue life data as it is associated with the weakest link theory [124-126]. The probability density function of a Weibull distribution $f^W(x)$ is given by:

$$f^W(x) = \frac{k}{\sigma}\left(\frac{x}{\sigma}\right)^{k-1} e^{-(\frac{x}{\sigma})^k} \quad \text{for } x \geq 0, \tag{4.1}$$

where $k > 0$ is the shape parameter, while $\sigma > 0$ is the distribution's scale parameter.

4.2.1.1.2 Generalized Extreme value or GEV model

The GEV is generally used to model the maxima or minima of a sequence of random variables. Its probability density function, $f^{GEV}(x)$ is:

$$f^{GEV}(x) = \left(\frac{1}{\sigma}\right) \exp\left(-\left(1 + k\frac{(x-\mu)}{\sigma}\right)^{-\frac{1}{k}}\right) (1 + k\frac{(x-\mu)}{\sigma})^{-1-\frac{1}{k}}, \tag{4.2}$$

where k is the shape parameter, μ is the location parameter and σ is the scale parameter.

The GEV combines a family of 3 related distributions that are categorized by their k values (governs the distribution tail) as:

- Type I (Gumbel type), $k = 0$: corresponds to logarithm of the Weibull distribution
- Type II (Fréchet type), $k > 0$: corresponds to inverse of the Weibull distribution [127]
- Type III (Reversed Weibull type), $k < 0$: corresponds to opposite of the Weibull distribution [127] (In Type III, k helps to predict maxima with a finite upper bound, as opposed to Weibull which predicts minima with a known finite lower bound of 0)

Therefore, the GEV distribution is unbounded for Type I, has a finite lower bound for Type II and has a finite upper bound for Type III.

4.2.1.1.3 Log-normal model

The log-normal distribution has been used to characterize the fatigue life data for notched, unnotched 2024-T3 Alclad sheet specimens by Schijve [128, 129]. The probability density function, $f^{Ln}(x)$ for a random variable x following the log-normal distribution is given by:

$$f^{Ln}(x) = \frac{1}{x} \cdot \frac{1}{\sigma\sqrt{2\pi}} \exp\left(-\frac{(lnx-\mu)^2}{2\sigma^2}\right), \quad (4.3)$$

where μ (scale parameter) and σ (shape parameter) are the mean and standard deviation of the variable's natural logarithm, respectively.

4.2.2 Inclusion size

A statistical approach to characterize the inclusion size distribution in a large volume of steel, V_{ref}, from a smaller observation volume, V_o, based on ASTM E2283 standard [130] was undertaken. Inspired from the original work of Murakami [131], the $\sqrt{area}$ parameter was used to define the characteristic inclusion size instead of the maximum feret diameter proposed in the ASTM procedure. The ASTM method consists in examining 4 sections per specimen, from 6 different cylindrical fatigue specimens, in the plane normal to the loading direction. The average inspection area, A_o, was equal to the specimen's reduced section cross-sectional area, which was 71.5 mm^2. Optical microscopy was used to identify the inclusions. The size of the largest observed inclusion was recorded for each inspection area. The inspection volume was given by $V_o = h\,A_o$, where h

was the average largest inclusion size ($\sqrt{area}$). In total, 24 largest inclusions were documented for the 6 specimens.

The obtained inclusion size results were then fit to Gumbel extreme value distribution using the method of maximum likelihood. The largest inclusion size, x_{max}, in the reference volume V_{ref} was obtained as a function of the scale parameter δ and the location parameter λ given by:

$$x_{max} = \delta\, y + \lambda \qquad \text{reduced variate } y = -\ln\left(-\ln\big(F(y)\big)\right) = -\ln\left(-\ln(P)\right), \tag{4.4}$$

where $F(y)$ is the cumulative distribution function. P is the cumulative probability of the observations and can be defined as:

$$P_i = \frac{i}{n+1}, \tag{4.5}$$

where i is the rank of an individual observation when all the observations are arranged in an ascending order and n is the total number of observations.

Two different values of V_{ref} were used. According to ASTM E2283 standard [130], a fixed return value $T = V_{ref}/V_o$ of 1000 should be used, meaning that V_{ref} should be 1000 times V_o. In addition to the ASTM recommended value, a V_{ref} equal to the volume of the cylindrical fatigue specimen's reduced section was used. This was done to compare the predicted value with the largest inclusion experimentally observed at the fatigue crack initiation sites.

4.2.2.1 Inclusion count

An inclusion count was performed on an area of 128.46 mm^2 prepared from a longitudinal slice of the reduced section of a cylindrical fatigue specimen. SEM and EDS were used to identify the inclusions and determine their shape, size and composition.

4.3 Modelling techniques

4.3.1 Fatigue life prediction based on maximum stress intensity factor

Murakami [25] calculated the equivalent discontinuity size $\sqrt{area_R}$ of a periodic artificially introduced surface roughness feature (defined by the profile height R_t and profile width R_{Sm}) by

equating the stress intensity factor obtained for the roughness features with the stress intensity factor for a small surface crack. The proposed equation to calculate $\sqrt{area_R}$ is given as:

$$\frac{\sqrt{area_R}}{R_{Sm}} \cong 2.97\left(\frac{R_t}{R_{Sm}}\right) - 3.51\left(\frac{R_t}{R_{Sm}}\right)^2 - 9.4, \qquad \text{for} \qquad \frac{R_t}{R_{Sm}} < 0.195 \tag{4.6}$$

The fatigue life characterizing the propagation of the main crack from its initial size (size of discontinuity) to its final size (based on material toughness) was considered.

Residual stress and crack closure effects were neglected. Only the tensile part of the stress cycle was considered to account for the crack growth, and hence $\Delta K \approx K_{Imax}$ was assumed to be the crack growth driving force, where K_{Imax} is the maximum stress intensity factor in opening mode I.

Murakami [25] computed K_{Imax} as:

$$K_{Imax} = f\sigma_{max}(\pi\sqrt{area})^{1/2}, \tag{4.7}$$

where the $\sqrt{area}$ parameter can be replaced by the critical roughness size $\sqrt{area_R}$ or inclusion size $\sqrt{area_i}$, depending on the type of discontinuity. σ_{max} is the maximum applied stress, and f is a constant that takes on the values of 0.65 for surface discontinuities (including those which are subsurface but in touch with the free surface), and 0.5 for interior discontinuities. The $area_i$ for interior inclusions is calculated by taking a smooth contour around the inclusion, as shown in Fig. 4.4 a. For inclusions in touch with the surface (Fig. 4.4 b), the $area_i$ parameter is considered as 1.137 times that of an interior inclusion to account for larger critically stressed region, as proposed by Murakami et al. [15, 16]. This proposition is based on the maximum stress intensity factor numerical solution characterizing irregularly shaped surface cracks obtained by Murakami and Nemat-Nasser [132].

The calculated stress intensity factor values (from Eqn. (4.7)) can be used to predict fatigue life based on the integration of Paris' equation from the initial discontinuity size ($\sqrt{area}$) to a final crack size a_c, estimated with the assumption of plain strain fracture toughness K_{Ic}. The number of cycles to failure N_f is then given by:

$$N_f = \frac{2\sqrt{area}}{(m-2)C\,(K_{Imax})^m}\,\left(1 - 1/\left(\frac{a_c}{\sqrt{area}}\right)^{\frac{m}{2}-1}\right), \tag{4.8}$$

Since a_c is much greater than the initial discontinuity size $\sqrt{area}$, Eqn. (4.8) can be further simplified as:

$$N_f = \frac{2\sqrt{area}}{(m-2)C\,(K_{Imax})^m}\,, \tag{4.9}$$

To incorporate the effect of CRS in the fatigue life of peened specimens, a Paris law type relation was also used to represent short crack growth behavior affected by peening.

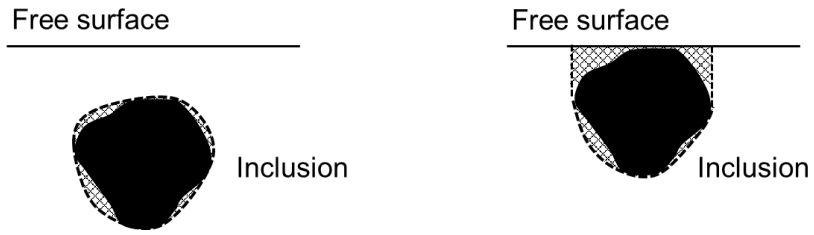

a. b.

Figure 4.4 Critically stressed area, $area_i$ (region enclosed within a smooth contour around the inclusion) for a. an interior inclusion, b. an inclusion in touch with the free surface (based on [15, 16]). Note that the $area_i$ is considered to be bigger for an inclusion in touch with the free surface than an interior inclusion of the same size

4.3.2 Finite Element Analysis (FEA) of residual stress redistribution in rectangular and cylindrical fatigue specimens

A FE model using ANSYS was developed to simulate the residual stress relaxation during fatigue loading (1 fatigue cycle). Firstly, a rectangular specimen with one eighth of the reduced section of the actual rectangular hourglass specimens (used for experimental residual stress analysis) with symmetric boundary conditions was developed. The hexahedral 3D linear solid element SOLID185 was applied in the model, as illustrated in Fig. 4.5a [133]. Since no influence of the cold work on the residual stress relaxation was observed in this work, it was not included into the FE simulation. The main considerations of the FEA are as follows:

a. The kinematic hardening model was used to define the material's yield behavior. True stress- plastic strain data of the studied 300M steel extracted from the monotonic tensile curve (as shown in Fig. 4.6) was used as input parameters since the relaxation of residual stresses after only one fatigue cycle was considered for simulation.

b. Residual stress profiles from experimental tests performed on the peened untested rectangular hourglass specimens were used as initial stress. A least squares approximation was used to fit the residual stress data to be used as input parameter for the FE model.

c. One cyclic fatigue loading at R=-1, σ_a = 931MPa and 1089MPa was simulated. (One cycle was chosen since no significant residual stress relaxation occurred after 1 fatigue cycle for the given stress amplitudes.)

Using the rectangular FE model, the residual stress relaxation was calculated and validated with experimental measurement made on the rectangular hourglass specimens subjected to 1 fatigue cycle.

After the validation of the rectangular model, the cylindrical FE model shown in Fig. 4.5b [133] was built with 2D linear rectangular PLANE 183 elements to model half of the uniform gage cylindrical specimen's reduced section (used for the stress controlled axial fatigue tests). The same loading conditions were applied and the relaxed residual stress under the two loading conditions were obtained for cylindrical specimens peened as per the S230-8A and CW14-8A peening conditions.

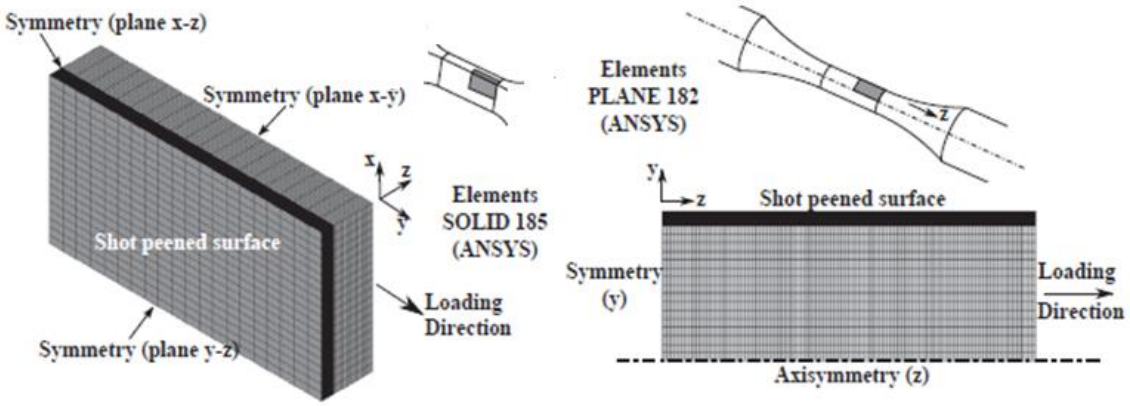

a. b.

Figure 4.5 Finite element models used for the redistribution of the residual stress and cold work profiles, a. one eighth of the rectangular specimen's reduced section is simulated with solid elements and b. a half of the cylindrical specimen's reduced section is simulated with axisymmetric solid elements (adapted from [133])

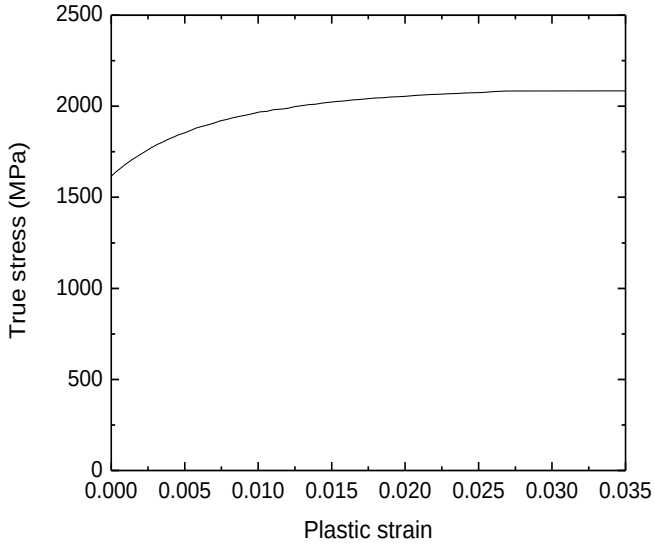

Figure 4.6 True stress-plastic strain curve (extracted from monotonic tensile curve) used as parameters for kinematic hardening model for the FEA

CHAPTER 5 SCIENTIFIC APPROACH AND COHERENCE WITH RESEARCH OBJECTIVES

The main body of this thesis is organized into three chapters, consisting of 1 published and 1 accepted and 1 submitted research article to fulfill the specific objectives listed in the previous chapter. Each of these chapters have their separate introduction, methodology, results, discussions and conclusions. Additional results that have not been included in the aforementioned chapters are summarized in additional sections after Chapters 7 and 8.

5.1 Article 1: Statistical analysis of high cycle fatigue life and inclusion size distribution in shot peened 300M steel

This article presents the effects of shot peening on the axial high cycle fatigue life (R = -1) of 300M steel, based on the quantification of peening induced roughness and residual stresses, as well as residual stress relaxation. Fatigue life of different peening treatments were compared based on a statistical analysis similar to that used in aerospace design for the first time. A thorough analysis of the fatigue crack initiation sites was also done to reveal the effects of peening on a microstructural scale. Features promoting crack initiation were characterized in terms of shape, size, position, and composition. The size of the largest crack initiating feature was predicted using statistical methods.

The main original contributions of this paper are as follows:

- Statistical analysis of fatigue life based on the Weibull and Generalized Extreme Value distribution models.
- Experimental evaluation of roughness, CRS and CRS relaxation for different peening conditions.
- Characterization of the crack initiating features in peened and unpeened specimens and prediction of largest crack initiating feature for the material using Gumbel Extreme Value analysis.

- Establishing an empirical relationship between size of the dominant crack initiating feature and fatigue life.

This article was published in the International Journal of Fatigue in January 2019.

5.2 Article 2: Effect of different shot peening conditions on the fatigue life of 300M steel submitted to high stress amplitudes

This article presents the shot peening influence on the axial fatigue life (R = -1) of 300M steel at a high stress amplitude (leading to a N_f $<10^5$ cycles for baseline polished specimens) by analysing the effects of CRS and its relaxation on the crack initiation phenomena. Statistical analysis by B-basis approach (used in aerospace industries) was used to compare the fatigue lives of unpeened and peened conditions for the first time. Competition between beneficial (CRS) and detrimental effects (roughness) was correlated to the dominant crack initiation feature for all studied surface conditions based on fracture mechanics concepts. A lower bound for fatigue lives were predicted by taking this competition into account. A simplified prediction approach was adopted using only long crack propagation and neglecting short crack effects.

The main original contributions of this paper are as follows:

- Statistical analysis of fatigue lives by B-basis.
- Quantification of CRS relaxation at high stress amplitude by XRD measurements.
- Quantification of long crack propagation at R= 0.1 upto threshold.
- Implementation of a stress-intensity factor-based model to predict the dominant features responsible for crack initiation and a lower bound for fatigue lives for different shot peening conditions.
- Correlation of analytically predicted fatigue life with statistical predictions (B-basis).

This article was accepted in the International Journal of Fatigue on 13th September 2019.

5.3 Article 3: Effect of shot peening on short crack propagation in 300M steel

This article investigates the coupled effect of peening induced CRS and microstructure on short crack propagation in 300M steel under the two tested stress amplitudes (low and high). The analytical model used in Article 2 was improved to account for this effect. The proposed model improved the fatigue life predictions for the peened specimens. A possible difference in short crack growth characteristics caused by a change in specimen geometry was also indicated.

The main original contributions of this chapter are as follows:

- Experimental $da/dN - \Delta K$ results for peened and unpeened conditions at R = -1.
- Correlating the effect of microstructure (prior austenite grains) and CRS with short crack deceleration.
- Establishing an improved fatigue life prediction model incorporating the CRS and microstructure effect on short crack growth in peened specimen.

This article was submitted to the International Journal of Fatigue on 19th May 2019.

CHAPTER 6 ARTICLE 1: STATISTICAL ANALYSIS OF HIGH CYCLE FATIGUE LIFE AND INCLUSION SIZE DISTRIBUTION IN SHOT PEENED 300M STEEL

Bag, A., Delbergue, D., Bocher, P., Lévesque, M., & Brochu, M. (2019). Statistical analysis of high cycle fatigue life and inclusion size distribution in shot peened 300M steel. International Journal of Fatigue, 118, 126-138. https://doi.org/10.1016/j.ijfatigue.2018.08.009

Keywords: shot peening; fatigue; high strength steel; statistical analysis; inclusion

6.1 Introduction

Shot peening consists in bombarding a metal surface with high velocity particles, which induces compressive residual stresses (CRS) and strain hardening in the surface layer (usually up to a few hundred micrometers). The induced CRS and strain hardening can arrest, or delay, the propagation of short surface cracks that initiate within the shot peened layer. As a result, peening is extensively applied in the aerospace and automotive industries to improve fatigue life. Nevertheless, a negative aspect of peening is the associated surface roughness which has, in some cases, been proven to be detrimental to fatigue life [73, 76, 134].

For a given shot type, shot peening is controlled mainly by two parameters:

i) The Almen intensity [135], which is related to the energy transferred to the work piece. For a given target material, higher peening intensities lead to deeper CRS. The magnitude of peening induced CRS is usually governed by the target material Young's modulus, yield stress and hardness. [1, 57, 58]

ii) The peening coverage [136] (percentage of the surface of the material covered by peening dimples) which is related to the peening time. Coverage values higher than 100% correspond to a multiple of the peening time required to reach full coverage (e.g., a coverage of 120% corresponds to peening a part 1.2 times the time required to reach 100% coverage). Surface roughness tends to increase with the peening coverage [73, 76, 134] until reaching saturation at a certain value of coverage [137].

This work focuses on 300M steel, which is a modified high strength version of AISI 4340 steel (a hard martensitic steel) used primarily in aircraft landing gears and rotor shafts. The fatigue life of

peened 4340 steels is mainly governed by the CRS and roughness induced by peening [2]. Therefore, the proper choice of peening conditions yielding sufficiently compressive residual stresses while maintaining optimum surface roughness is crucial.

Torres and Voorwald [2] observed that peening 4340 steel at intensities of 6.3-8.3 A using S230 shots and 200% coverage resulted in the longest rotating bending fatigue life at a low stress amplitude of 931MPa (62 % of the 0.2% offset yield strength, $\sigma_{y,0.2}$). Peening at lower or higher intensities decreased fatigue life by as much as 2-7 times [2]. Other studies on similar steels demonstrated that specimens subjected to 100% coverage had longer fatigue lives than those shot peened with a higher or lower coverage when subjected to low cycle rotating bending fatigue [60] and high cycle bending fatigue [61, 62]. Therefore, based on this somewhat limited literature, it seems that peening at 100% coverage and intensities of 6-8 A maximizes the fatigue life of the studied material loaded at low stress amplitude.

Torres and Voorwald [2] also demonstrated that the fatigue life improvement of peened 4340 steel specimens was influenced by residual stress relaxation. According to Dieter [85], the presence of CRS in a specimen is comparable to the presence of a mean stress in a specimen subjected to fatigue loading. Morrow and Sinclair [86] conducted strain-controlled axial fatigue tests on SAE 4340 steel with 50 HR_c to study mean stress evolution. A cycle-dependant mean stress relaxation was observed with most of the relaxation occurring in the 1st fatigue cycle. Similar observations have been made in case of peening induced CRS, with more than 50% relaxation occurring during the 1st load cycle when subjected to monotonic tensile (95% of the 0.1% offset yield strength, $\sigma_{y,0.1}$) or compressive (30% of $\sigma_{y,0.1}$) loading [138], or completely reversed high cycle axial fatigue loading [88]. The stress relaxation magnitude in the peened specimens was however influenced by the material cyclic stress strain response and the applied stress level. Correspondingly, Morrow and Sinclair [86] observed no significant relaxation in the mean stresses for low alternating stresses (~ 6-59% of $\sigma_{y,0.2}$), especially those closer to the material's fatigue limit. Similar CRS relaxation is therefore expected for hard steels at comparable applied stresses.

In high cycle fatigue regimes, fatigue cracks in most high strength steels tend to initiate at inclusions (i.e., unwanted non-metallic chemical compounds that occur during manufacturing). According to the review of Zhang [19], inclusions in steels may be the products of deoxidation, or

precipitation, during cooling and solidification; for example, Al_2O_3 and SiO_2 inclusions come from the addition of Al and Si deoxidisers. Sometimes, inclusions may form due to chemical and mechanical interactions of molten steel with its surroundings such as reoxidation, slag entrainment, and erosion of refractory lining, which typically yields CaO and MgO inclusions. The above mentioned inclusions are typical of high strength steels and have been documented as potent fracture initiation sites in high cycle fatigue [18, 21, 139]. Inclusion size distribution and composition vary depending on the type of steel and the manufacturing process. According to the weakest link theory, fatigue failure is expected to occur at the largest inclusion present in the material. The occurrence of such large inclusions should therefore be prevented. “Clean” steels can be manufactured by vacuum arc remelting (VAR), in which the probability of finding large inclusions is usually small.

Murakami [131] applied the statistics of extreme values (SEV) to rationalise the fatigue performance of various high strength “clean” steels. The author [131] obtained an empirical equation to predict fatigue strength by calculating the largest inclusion that could be encountered in a specified tested steel volume. For the analysis, Murakami et al. [26] measured the sizes of the largest inclusions observed on optical metallographies in a small volume (~1.53×10^{-4} mm^3), described the inclusion size distribution using the Gumbel extreme value model and successfully predicted the largest inclusion sizes in a much larger volume (~90 mm^3). Murakami [131] also predicted the scatter bands of fatigue strength for various high strength steels.

This work investigates the effect of specific shot peening conditions on the fatigue behaviour of aerospace grade 300M steel. The peening induced roughness, residual stress profiles and their relaxation under cyclic loading were considered. The features observed at crack initiating sites were presented in terms of type, size, position and composition. A statistical analysis of the fatigue results using an estimate of 90% survival life at 95% confidence was achieved for the unpeened and peened surface conditions to compare their fatigue performances. Moreover, a statistical distribution of defect sizes was performed using Gumbel extreme value analysis to identify the largest inclusion that can be found in a given volume of steel.

The paper is organized as follows: Section 6.2 elaborates on the material and studied surface conditions, as well as the experimental methodology used for fatigue tests, peening induced roughness and residual stress measurements. This is followed by Section 6.3 which presents the

results obtained from the experimental campaign. Section 6.4 comes with the discussion of the results. Finally, Section 6.5 concludes the work.

6.2 Material and experimental methods

6.2.1 Material

The studied material is the 300M steel, a modified version of AISI 4340 steel with a higher content of Si and V. Specimens for metallography and mechanical tests were extracted from the longitudinal direction of bars having a diameter of 82.6 mm. The specimens for the axial fatigue tests and residual stress relaxation tests were extracted from bars having diameters of 25.4 and 31.8 mm, respectively. The steel was heat treated according to the following schedule: i) Normalization at 1200 K for 1 h followed by air cooling, ii) Austenitization at 1144 K for 1 h followed by oil quenching, iii) Double tempering at 575 K for 2 h followed by air cooling. The heat treatment schedule conforms to the AMS 6257E standard which is applicable to aerospace landing gears. The chemical composition (average of 82.6 mm and 25.4 mm bars) and mechanical properties of the steel (average of 3 tests performed on samples extracted from 82.6 mm bars according to ASTM E8 standard [140]) are listed in Tables 6.1 and 6.2, respectively. Both the chemical composition and mechanical properties complied with the AMS 6257E standard.

Metallographic samples were prepared from the heat treated material and polished using SiC paper followed by colloidal diamond suspension up to 1µm surface finish. The samples were etched using Vilella's reagent (1 g Picric acid, 5 ml HCl, 100 ml Ethanol) for 20 s, which revealed a typical tempered martensitic microstructure under optical microscopy. A higher resolution on the microstructure was obtained using electron channeling contrast imaging (ECCI) which showed a mixture of lath and plate martensite. Both OM and ECCI images are presented in Fig. 6.1a. This type of microstructure is typical of 300M steel [3, 4]. The microstructure was homogeneous in the rolling or longitudinal (LT), long transverse (LS) and short transverse (TS) directions. The prior austenite grain size was obtained by Kohn's method of controlled oxidation [141] which causes preferential oxidation of the grain boundaries during austenitization. No difference in microstructure was observed in the samples from different bars, the average grain size being 23 µm, as shown in Fig. 6.1b. The average Rockwell hardness (HRc) measured using a 120° diamond

spheroconical indenter at 150 kgf was 54 HRc, which is within the range specified by the AMS 6257E standard.

Table 6.1 Chemical composition (wt. %) of the 300M steel (average of 82.6 mm and 25.4 mm bars)

C	Mn	Si	P	S	Cr	Ni	Mo	V	Cu	Al	Fe
0.40	0.77	1.61	0.006	0.001	0.80	1.92	0.37	0.08	0.10	0.04	Balance

Table 6.2 Mechanical properties of the studied 300M steel (average of 3 tests using 86.2 mm diameter bar) along with their standard deviations (in brackets)

Material	$\sigma_{y,0.2}$(MPa)	σ_{UTS} (MPa)	E (GPa)	υ	$\%El$
300M steel	1693 (±6)	2020 (±10)	197 (±1)	0.28 (±0.03)	11.7 (±0.4)

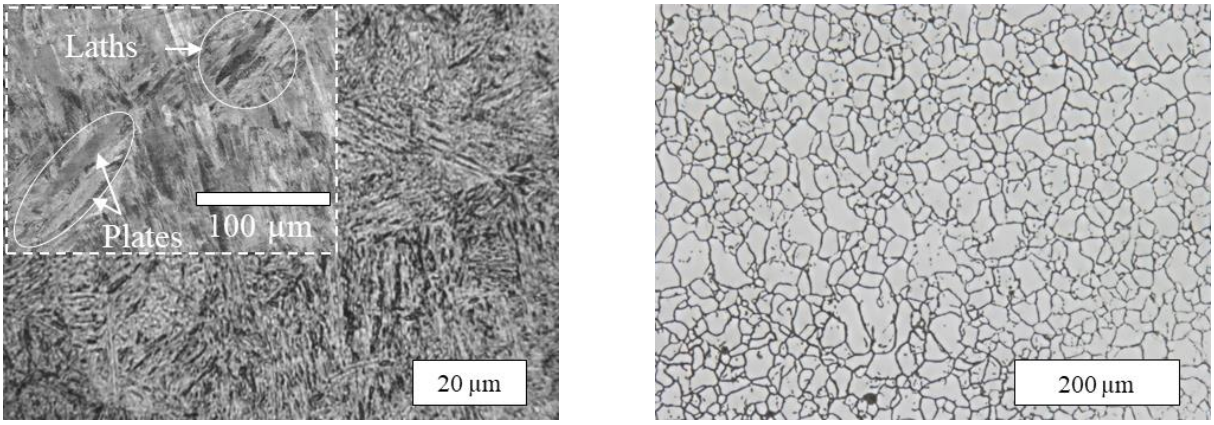

a. b.

Figure 6.1 a. Optical microstructure of 300M steel etched with Vilella's reagent for 20 s, Closeup: ECCI image showing tempered martensite laths and plates, b. Optical image showing prior austenite grain boundaries of 300M steel revealed by Kohn's method

A JEOL JSM-7600F scanning electron microscope (SEM) was used to identify the inclusions in a metallographic sample prepared from the heat-treated 25.4 mm bar. Energy dispersive spectroscopy (EDS) using an Oxford X-Max 80 Silicon Drift Detector was used to qualitatively identify their compositions. The shape, size, elemental composition and frequency of occurrence (%), for a total of 33 observed inclusions, are presented in Table 6.3. These types of inclusions are commonly observed in high strength steels [18, 20, 21, 139]. The inclusion size was calculated using the $\sqrt{area}$ parameter proposed by Murakami [131]. This parameter is defined as the square root of the area of the defect projected onto a surface normal to the longitudinal axis.

Table 6.3 Shape, size, composition and frequency of occurrence (%) for a total of 33 inclusions observed on a metallographic sample of 300M steel

Inclusion shape	Size (µm)	Composition	Frequency (%)
Globular	3-23	Mg, Al, Ca, O, Mn, S	46
Cubic	4-11	Ti, C, N	21
Globular	5-8	Mg, Al, O, Mn, S	12
Globular	3-18	Mg, O, Al	9
Globular	5-8	Mg, Mn, S	6
Cubic	9-13	Ti, C, N, Mg, O	6

6.2.2 Surface conditions

Three surface conditions, namely as-machined, polished and shot peened, have been studied. The as-machined specimens reflect the surface condition of real parts prior to peening. These specimens exhibited surface roughness and surface CRS representative of the machining process they underwent. Polished specimens without the underlying effects of roughness or residual stresses were produced to better represent the baseline material fatigue performance. The specimens were thus prepared by mechanically polishing some as-machined specimens down to 1 µm surface finish. The amount of removed material and the pressure applied during polishing were controlled to produce specimens with low surface residual stresses. The minimum compressive surface residual stress of polished specimens was around -230 MPa, after a 380 µm thick layer was removed.

Shot peening was performed at 100% coverage using an air pressured shot peening machine provided by Canablast and equipped with 6 axis M-20iA Fanuc robot and a rotating table. Two shot types, namely conditioned cut wire CW14 (average diameter = 0.35 mm) and cast steel S230 (average diameter = 0.58 mm) were used. A standoff distance of 305 mm and 90° angle was maintained during the peening process to yield Almen intensities of 4 A and 8 A. Average shot velocities measured using ShotMeter G3 (a particle velocity sensor from Progressive Surface & Tecnar Automation) for S230-4A, S230-8A and CW14-8A conditions were 12 m/s, 26 m/s and 76 m/s, respectively.

Surface roughness profiles were measured with a Mitutoyo Formtracer SV-C3200 contact profilometer for 3 specimens for each surface condition, except for the polished specimens. Three

measurements along the longitudinal direction were made for each specimen over a total evaluation length of 20 mm and sampling (or cutoff) lengths of 0.8 mm for the as-machined and S230-4A peened specimens. A sampling length of 2.5 mm for S230-8A and CW14-8A peened specimens was used.

6.2.3 Stress-controlled axial fatigue tests

Axial fatigue tests were performed at a stress amplitude of 931 MPa (55% of $\sigma_{y,0.2}$**)** with a stress ratio, R = -1 and a frequency of 10 Hz, in agreement with ASTM E466 standard [120]. Uniform gage cylindrical specimens were used, as illustrated in Fig. 6.2a. A total of 5 as-machined, 5 polished, 8 S230-4A peened, 9 S230-8A peened and 7 CW14-8A peened specimens were tested. The tests were performed at room temperature on a MTS 318.25 servo-hydraulic system equipped with a 250 kN MTS 661.22c-01 load cell with MTS 793 software. SEM was used to observe the features responsible for crack initiation on fractured samples. A qualitative compositional analysis of these features by EDS was also accomplished.

6.2.4 Residual stress measurement

Through thickness residual stress profiles were obtained by the X-ray Diffraction (XRD) technique for the hourglass specimens used in the interrupted fatigue tests (Section 6.2.5), as well as for untested specimens (0 fatigue cycle) for each surface condition. Each profile characterizes a specific specimen since measurement of residual stress profiles implies destroying the specimen. A Pulstec µ-X360n apparatus equipped with a Cr-tube was used, allowing the use of $K\alpha$-lines for the measurements on the {211} family of planes. Diffraction peaks were fit by the Lorentzian method [115] and residual stresses were calculated using the $cos\ \alpha$ method [116]. The X-ray elastic constant (XEC), ½ S_2, was previously determined for the {211} family of planes, as described in the work of Delbergue et al. [117]. The XRD measurements were made assuming a non-textured material having an equi-bi-axial stress state after shot peening. Measurements were performed in the loading direction, where most of the stress relaxation occurs in axial fatigue. The XRD conditions used for all residual stress measurements are summarized in Table 6.4.

A layer removal technique was combined with the XRD measurements to obtain the in-depth residual stress profiles. Thin layers of material were removed by electropolishing with a perchloric acid-based solution. The thickness of the removed layer was measured using a Mitutoyo SJ-400

profilometer. The Moore and Evans correction [118] was used to correct the stress redistribution due to the layer removal process.

Table 6.4 X-ray diffraction conditions used for residual stress measurements

Detectors	Tube target	Diffraction planes	Bragg angle
2D	Cr (λ = 2.291 Å)	{211}	2θ = 156.4°
XEC (½ S_2)	Nb. of inclination	Aperture size	Exposure time
5.68 E-6 MPa^{-1}	1	1 mm	30 s

6.2.5 Residual stress relaxation tests

Interrupted fatigue tests were performed on peened rectangular hourglass specimens (shown in Fig. 6.2b), to quantify the residual stress relaxation during cyclic loading. Rectangular specimens were chosen to simplify the XRD measurements. Two peening conditions, which yielded the best performance in terms of fatigue life, (i.e., CW14-8A and S230-8A) were studied. Measurements were performed after: 1 cycle, 200 cycles and 80% of fatigue life. The testing conditions were identical to those described in Section 6.2.3.

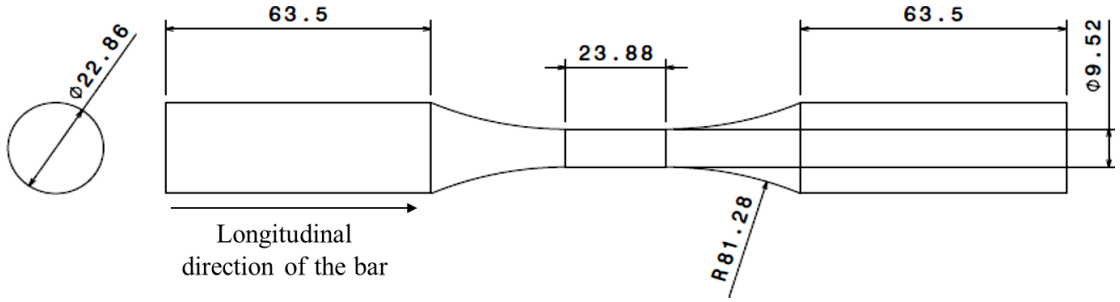

a.

Figure 6.2 Specimen dimensions (mm) a. axial fatigue test specimen, b. residual stress relaxation specimen

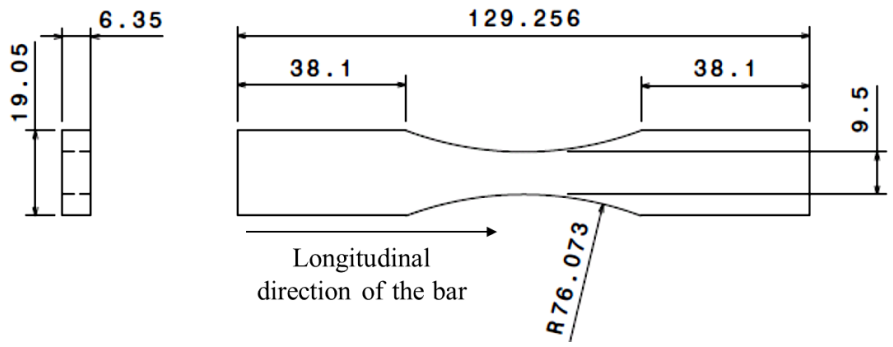

b.

Figure 6.2 Specimen dimensions (mm) a. axial fatigue test specimen, b. residual stress relaxation specimen (cont'd)

6.2.6 Statistical analyses

6.2.6.1 Fatigue life dispersion

Significant scatter is often observed in the fatigue life results due to the stochastic nature of the phenomenon and accounting for this variability rather than using the average value is essential to ensure safety. Statistical analysis is one way of quantifying and predicting this variability.

A conservative estimate of 90% survival at 95% confidence interval was chosen for this analysis to compare the fatigue performance of specimens with varied surface treatments. A measure of the lower bound on this estimate, called B-Basis, is typically used in aerospace to set design allowables [122]. The statistical analysis was carried out through the following steps:

d) The Anderson-Darling goodness of fit test [123] was used to identify the best fitting distribution for each condition.
e) The maximum likelihood fitting parameters at 95 % confidence interval were obtained for the distribution. The log-likelihood maximization was achieved by assuming a chi-squared approximation.
f) The number of cycles leading to 90% survival was finally calculated by inserting the maximum likelihood estimates into the inverse cumulative distribution function.

The statistical analysis was performed using MATLAB R2013a. The following section provides more details.

6.2.6.1.1 Studied distribution models

Weibull model

Weibull's distribution is usually used to represent fatigue life data as it is associated with the weakest link theory [124-126]. The probability density function of a Weibull distribution $f^W(x)$ is given by:

$$f^W(x) = \frac{k}{\sigma}\left(\frac{x}{\sigma}\right)^{k-1} e^{-(\frac{x}{\sigma})^k} \quad \text{for } x \geq 0, \tag{6.1}$$

where $k > 0$ is the shape parameter, while $\sigma > 0$ is the distribution's scale parameter.

Generalized Extreme value or GEV model

The GEV is generally used to model the maxima or minima of a sequence of random variables. Its probability density function, $f^{GEV}(x)$ is:

$$f^{GEV}(x) = \left(\frac{1}{\sigma}\right) \exp\left(-\left(1 + k\frac{(x-\mu)}{\sigma}\right)^{-\frac{1}{k}}\right) (1 + k\frac{(x-\mu)}{\sigma})^{-1-\frac{1}{k}} \tag{6.2}$$

where k is the shape parameter, μ is the location parameter and σ is the scale parameter.

The GEV combines a family of 3 related distributions that are categorized by their k values (governs the distribution tail) as:

- Type I (Gumbel type), $k = 0$: corresponds to logarithm of the Weibull distribution
- Type II (Fréchet type), $k > 0$: corresponds to inverse of the Weibull distribution [127]
- Type III (Reversed Weibull type), $k < 0$: corresponds to opposite of the Weibull distribution [127] (In Type III, k helps to predict maxima with a finite upper bound, as opposed to Weibull which predicts minima with a known finite lower bound of 0)

Therefore, the GEV distribution is unbounded for Type I, has a finite lower bound for Type II and has a finite upper bound for Type III.

6.2.6.2 Inclusion distribution

A statistical approach to characterize the inclusion size distribution in a large volume of steel, V_{ref}, from a smaller observation volume, V_o, based on ASTM E2283 standard [130] was undertaken. Inspired from the original work of Murakami [131], the $\sqrt{area}$ parameter was used to define the characteristic inclusion size instead of the maximum feret diameter proposed in the ASTM procedure. The ASTM method consists in examining 4 sections per specimen, from 6 different cylindrical fatigue specimens, in the plane normal to the loading direction. The average inspection area, A_o, was equal to the specimen's reduced section cross-sectional area, which was 71.5 mm^2. The size of the largest observed inclusion was recorded for each inspection area. The inspection volume was given by $V_o = h\, A_o$, where h was the average largest inclusion size ($\sqrt{area}$). In total, 24 largest inclusions were documented for the 6 specimens.

The obtained inclusion size results were then fit to Gumbel extreme value distribution using the method of maximum likelihood. The largest inclusion size, x_{max}, in the reference volume V_{ref} was obtained as a function of the scale parameter δ and the location parameter λ given by:

$$x_{max} = \delta\, y + \lambda\,, \quad \text{reduced variate} \quad y = -\ln\left(-\ln\left(F(y)\right)\right) = -\ln\left(-\ln(P)\right), \tag{6.3}$$

where $F(y)$ is the cumulative distribution function. P is the cumulative probability of the observations and can be defined as:

$$P_i = \frac{i}{n+1} \tag{6.4}$$

where i is the rank of an individual observation when all the observations are arranged in an ascending order and n is the total number of observations.

Two different values of V_{ref} were used. According to ASTM E2283 standard [130], a fixed return value $T = V_{ref}/V_o$ of 1000 should be used, meaning that V_{ref} should be 1000 times V_o. In addition to the ASTM recommended value, a V_{ref} equal to the volume of the cylindrical fatigue specimen's reduced section was used. This was done to compare the predicted value with the largest inclusion experimentally observed at the fatigue crack initiation sites.

6.3 Results

6.3.1 Surface characteristics

Figs. 6.3a-d illustrate the typical surface of as-machined, S230-4A, S230-8A and CW14-8A peened specimens as observed under the SEM. The as-machined specimens exhibit several lines across their surface, oriented mainly at 45° or aligned with the longitudinal direction. Such marks are not typical of a machining operation, which indicates that subsequent grinding operations were performed on the received specimens. These grinding marks are still prominent in the S230-4A specimens (Fig. 6.3b), whereas, they are overshadowed by the peening dimples on the S230-8A specimens (Fig. 6.3c). CW14-8A specimens (Fig. 6.3d) exhibit large dimples and the grinding marks are hardly visible and have been mostly, if not completely, eliminated by peening.

The arithmetic mean roughness, R_a, the distance between highest peak and deepest valley in the total evaluation length, R_t, and the mean spacing between successive peaks within the sampling length, R_{Sm}, have been used to quantify the resulting roughness. The parameter R_a is studied since it is the most widely used parameter in general engineering practice. The parameters, R_t and R_{Sm} were chosen as they have been successfully used by Li et al. [78] to represent dimple depth and the dimple width in the calculation of stress concentration arising from shot peening dimples, as discussed below. Li et al. [78] derived the stress concentration factor due to surface roughness, $K_{t,rough}$ from Finite Element simulation of surfaces with multiple indentations, as:

$$K_{t,rough} = 1 + 4.1\left(\frac{R_t}{R_{Sm}}\right)^{1.3} \quad \text{for} \quad \left(\frac{R_t}{R_{Sm}}\right) < 0.15 \tag{6.5}$$

The stress concentration factor due to surface roughness for all peening conditions was calculated using Eqn. (6.5) and is listed in Table 6.5.

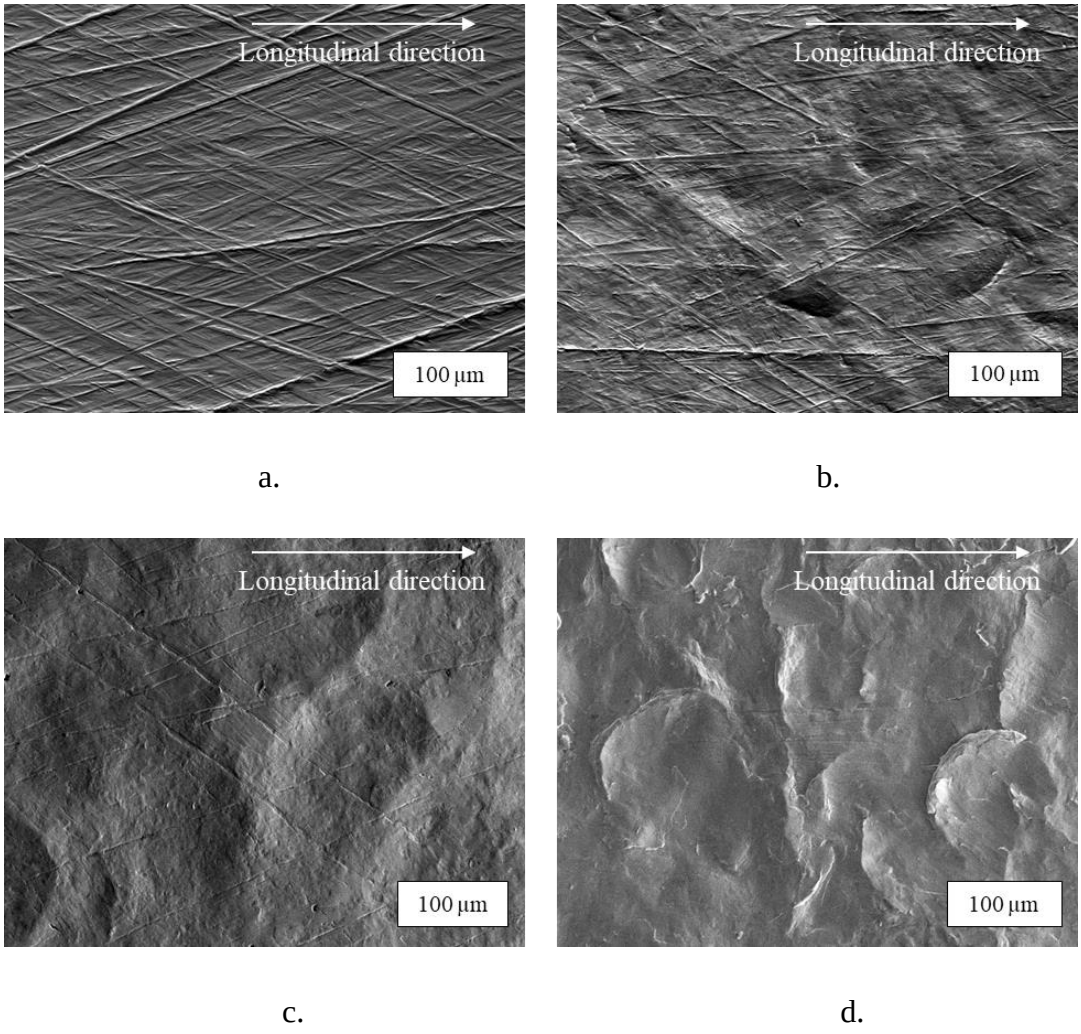

Figure 6.3 SEM image of the surface for a. as-machined condition showing grinding marks mostly oriented at 45° to the longitudinal direction, b. S230-4A condition still showing grinding marks, c. S230-8A condition showing dimples and a few grinding marks and d. CW14-8A condition showing large dimples and no grinding marks

Table 6.5 lists the average values of R_a, R_a, R_{Sm}, and $K_{t,rough}$ for the as-machined and the 3 peening conditions. Table 6.5 shows that increasing the peening intensity increases the resulting roughness. The CW14-8A condition seems to be the harshest, followed by S230-8A and S230-4A (reflected by the increasing R_a and R_t values). This is further corroborated by the surface stress concentration factor values calculated by Eqn. (6.5), which is highest for CW14-8A ($K_{t,rough}$=1.10) followed by S230-8A ($K_{t,rough}$=1.05) and S230-4A ($K_{t,rough}$ =1.04) conditions.

When the shot diameter (listed in Table 6.5) is considered, Table 6.5 suggests that the larger S230 medium generates lower R_t and R_{Sm} values than the smaller CW14 shots.

These observations suggest that CW14 8A causes the most damage to the surface in terms of surface roughness, resulting in higher stress concentrations at the surface than S230-8A and S230-4A peening.

Table 6.5 Average roughness parameter values along with the 95% confidence interval (in brackets) and surface stress concentration factor for all surface conditions (D = average shot diameter, V = average shot velocity)

Surface treatment	As-machined	S230-4A (D = 0.58 mm) V =12 m/s	S230-8A (D = 0.58 mm) V =26 m/s	CW14-8A (D = 0.35 mm) V =76 m/s
R_a, µm (95% CI)	0.31 (0.07)	0.75 (0.18)	1.18 (0.17)	1.44 (0.07)
R_t, µm (95% CI)	2.36 (1.55)	3.94 (0.54)	7.79 (0.85)	15.51 (2.11)
R_{Sm}, µm (95% CI)	113 (18)	135 (46)	230 (79)	279 (37)
$K_{t,rough}$	--	1.04	1.05	1.10

6.3.2 Fatigue test results and their statistical analysis

The results of the axial fatigue tests at a stress amplitude of 931 MPa (R = -1) are presented in Fig. 6.4. The abscissa represents the total number of cycles to failure, N_f, for the corresponding surface condition listed on the ordinate. The amount of scatter in the fatigue life results for all the conditions ranges over an order of magnitude and no significant improvement in fatigue life due to peening can be observed at first glance. A fatigue life of 1.96 x 10^6 cycles for the single runout specimen for the CW14-8A condition (Fig. 6.4) was also included in the statistical analysis since the specimen could not be tested until failure due to the damage of its grip section.

Table 6.6 shows the average fatigue life, the fitted distributions, their Anderson-Darling goodness of fit test coefficients (h, p), and the maximum likelihood parameters along with 90% survival life at 95% confidence interval for each surface condition. The closer the value of (h, p) is to (0,1) the better is the fitting. In this case, the best fit distribution for all surface conditions was the GEV

distribution. The fatigue data for each condition was also fit using the Weibull model to compare the two distributions. The Weibull fit is good for the as-machined and polished specimen data having a p value of around 0.95 and 0.82 respectively, when compared to the Weibull fit for the peened specimens. However, the GEV distribution seems to always fit the data better than the Weibull for all conditions, as reflected by the higher p values. The improved fit obtained for the GEV over the Weibull model can be attributed to the use of an additional third parameter (or the location parameter, μ). Hence, using the Weibull model to fit the fatigue data is not a practical choice as it tends to either overestimate (in case of as-machined and polished condition) or underestimate (in case of peened conditions) the 90% survival life at 95% confidence interval, when compared to the values provided by the GEV fit.

It is also evident from Table 6.6 that the 90% survival life of all the conditions lie very close to each other, the difference between the highest (CW14-8A) and the lowest (polished) being only a factor of 3. It can therefore be said that peening does not cause a significant improvement in the fatigue life for the studied material and testing conditions. Interestingly, when comparing the performance of the polished specimens with the as-machined specimens, one can see that polishing decreases the 90% survival life by half as it removes the material affected by the machining process. This shows that the CRS and surface hardening resulting from the machining process can improve the fatigue life.

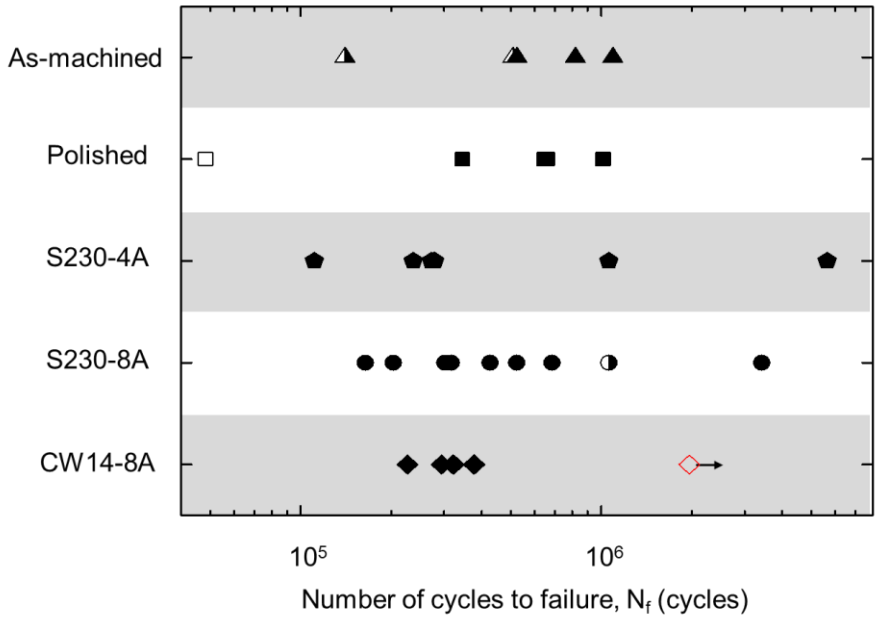

Figure 6.4 Total fatigue life N_f from axial fatigue tests at 931 MPa /R = -1 for all surface conditions. Each symbol type represents N_f for the corresponding surface condition in the ordinate axis (open symbol with arrow represents the single runout specimen, open symbol without arrow represents crack initiation at an inclusion in touch with the surface, half-filled symbols represent surface crack initiation and fully-filled symbols represent subsurface crack initiation at inclusions)

Table 6.6 Details for axial fatigue results (931 MPa/ R = -1) statistical analysis showing average fatigue life, best fit distribution for the data, (h, p)-value of Anderson Darling test, maximum likelihood estimates of fitting parameters and 90% survival life at 95% Confidence Interval

Surface condition	Average fatigue life (x 10^5 cycles)	Best fit distribution	(h, p) value	Fitting parameters (MLE)			90% Survival life at 95% CI (x 10^5 cycles)
				k	μ (x 10^5)	σ (x 10^5)	
As-machined	6.18	GEV	(0,0.97)	-0.42	5.26	3.35	1.92
		Weibull	(0,0.95)	1.98	--	6.95	2.24
Polished	5.42	GEV	(0,0.95)	-0.54	4.69	3.58	0.92
		Weibull	(0,0.82)	1.47	--	5.91	1.27
S230-4A	10.2	GEV	(0,0.59)	1.01	3.28	1.78	1.37
		Weibull	(0,0.31)	0.73	--	7.87	0.37
S230-8A	7.89	GEV	(0,0.99)	0.93	3.06	1.96	1.92
		Weibull	(0,0.65)	1.01	--	7.93	0.86
CW14-8A	5.55	GEV	(0,0.77)	0.78	0.91	2.98	2.42
		Weibull	(0,0.24)	1.20	--	5.98	0.92

6.3.3 Peening induced residual stresses and their relaxation

The experimentally obtained residual stress profiles for the as-machined, polished, S230-8A and CW14-8A rectangular specimens prior to fatigue testing (0 cycle) are depicted in Fig. 6.5a. The figure clearly identifies the surface residual stress, σ_s, maximum CRS, σ_{mc}, depth at which maximum CRS occurs, x_{mc}, and the depth at which the residual stresses become tensile, x_0, for all tested conditions.

In general, the surface and maximum CRS in as-machined specimens are about -404 MPa and -441 MPa, respectively, while for polished specimens they are about -341 MPa. Both S230-8A and CW14-8A conditions exhibited similar maximum CRS values of -1170 MPa. Moreover, the CRS

in the as-machined and polished specimens fade out within a depth of about 24 µm and 8 µm respectively, while the CRS in S230-8A and CW14-8A specimens are about 161 µm and 142 µm deep, respectively.

The residual stress profiles for S230-8A peened specimens after 0 cycle, 1 cycle, 200 cycles and after 80% fatigue life are shown in Fig. 6.5b, and those for CW14-8A specimens after 0 cycle and 80% fatigue life are displayed in Fig. 6.5c. The residual stress profile characteristics for each surface and testing condition are also summarised in Table 6.7.

Analysing the stress relaxation data for the peened specimens (Fig. 6.5b, c / Table 6.7) reveals that S230-8A condition's σ_s and σ_{mc} relaxed by about 11% and 14% of their original value, respectively, at 80% fatigue life, of which 9% and 10% relaxation occurs during the 1st cycle. A total relaxation of 8% and 13% is recorded at 80% fatigue life for σ_s and σ_{mc} in the CW14-8A specimens, respectively, which is quite similar to the S230-8A condition. Nevertheless, the x_{mc} and x_0 values in neither peening condition is affected by the stress relaxation phenomenon.

It should be noted that little residual stress relaxation was expected for a stress amplitude of 931 MPa (55% of $\sigma_{y,0.2}$) since it is very close to a 4340 steel fatigue limit of 965 MPa at 10^7 cycles [142]. This might be attributed to the fact that no significant plastic deformation would occur at this load level, thus preventing relaxation of the residual stresses.

In summary, the magnitude of the maximum compressive residual stresses and the depth of residual stresses for the peened specimens were about 2.7 times and 6.4 times that of as-machined specimens prior to fatigue testing. This is expected to provide a significant improvement in fatigue life. Residual stress relaxation in peened specimens due to fatigue cycling at R = -1 and a maximum stress of 55% of $\sigma_{y,0.2}$ caused little relaxation of stresses, not more than 163 MPa. Since the tested stress amplitude of 931 MPa (55 % of the 0.2% offset yield strength) was close to the fatigue limit of the material (830 MPa), it was not able to cause enough plastic deformation that would lead to significant relaxation of the high compressive residual stresses induced by the peening treatments. Moreover, most of the relaxation occurred during the 1st fatigue cycle while the depth of the compressive residual stress profile remained unchanged. It is most likely that the relaxation at the surface was caused by dislocation rearrangements and cyclic softening [143]. Based on these observations, for this specific testing condition, quantification of the residual stress profile before

fatigue testing would provide important information for the interpretation of fatigue results since the stresses did not relax significantly during fatigue testing.

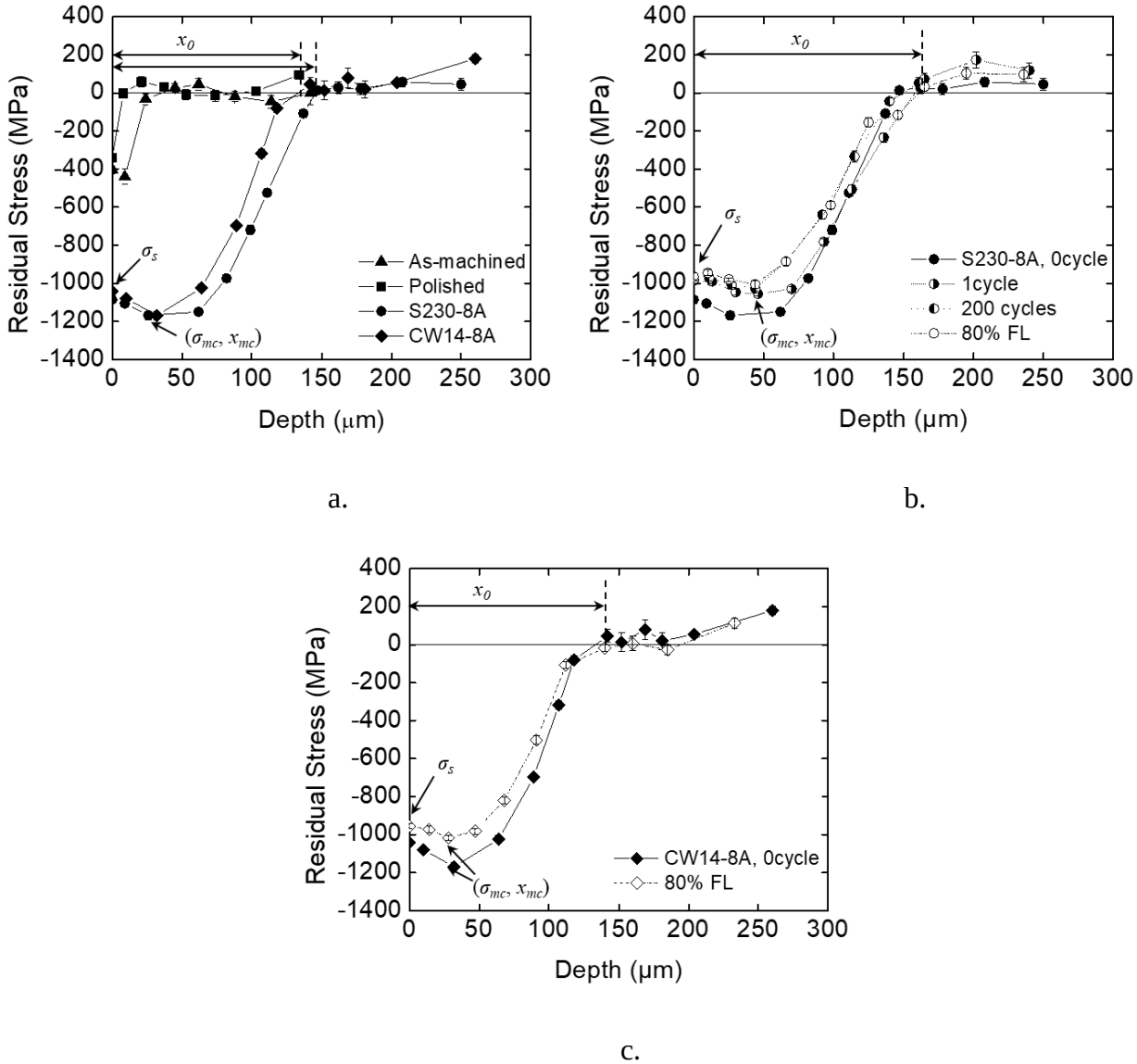

Figure 6.5 XRD Residual stress profiles for a. all surface conditions prior to fatigue testing, b. S230-8A condition at 0 cycle, 1 cycle, 200 cycles and 80% fatigue life, c. CW14-8A condition at 0 cycle and 80% fatigue life (broken lines have been used to connect the experimental points to better represent the evolution of residual stresses with depth)

Table 6.7 Summary of residual stress data for all surface conditions

Parameter	As-machined	Polished	S230-8A				CW14-8A	
Cycles	0	0	0	1	200	80% FL	0	80% FL
σ_s, MPa	-404	-341	-1086	-987	-983	-965	-1044	-956
σ_{mc}, MPa	-441	-341	-1169	-1056	-1029	-1006	-1170	-1018
x_{mc}, µm	9	0	~46	46	44	44	32	28
x_0, µm	24	8	161	165	161	165	142	140

6.3.4 Crack initiating features

Examination of the fracture surfaces under the SEM revealed the features responsible for fatigue crack initiation. It was found that, out of a total of 33 tested specimens, main cracks initiated from the surface in only 4 specimens: 3 from grinding marks (Fig. 6.6a) (2 as-machined and 1 S230-8A peened specimen) and 1 from a non-metallic inclusion in a polished specimen in contact with the surface. In the remaining specimens, failure was caused by non-metallic inclusions of varying sizes located at different depths within the specimen's cross section. Compositional analysis by EDS indicated that two main types of inclusions were mainly responsible for crack initiation:

a. Globular/ellipsoidal/irregular shaped inclusions consisting of Al, Mg, O, Ca elements (in varying proportions) and sometimes small amounts of Si and S. These inclusions shown in Fig. 6.6b will be referred to as Type A.
b. Cubic inclusions composed of Ti, N, C and sometimes MgO inclusions embedded in them. These inclusions shown in Fig. 6.6c will be referred to as Type B.

Type A inclusions were the most common and usually bigger in size, when compared to the Type B inclusions. The conventional fisheye morphology, which is characteristic of the fracture surface due to failure at an interior or subsurface inclusion, was observed for most specimens, as depicted in Fig. 6.6d. Another feature known as the fine granular area (FGA) (Fig. 6.6c) was also observed. The occurrence of FGA is often associated with the coupled effect of hydrogen embrittlement (caused by hydrogen trapped in the inclusion vicinity) and fatigue [144, 145]. This kind of feature

is usually found on fracture surfaces when failure is caused by inclusions, in very high cycle fatigue (VHCF) regimes ($>10^8$ cycles). It has been claimed by several researchers [9, 146, 147] that crack growth in FGA accounts for more than 90% of the total fatigue life in VHCF regime. In this work, FGA was observed for all specimens which had a total fatigue life of 1 million cycles, or more.

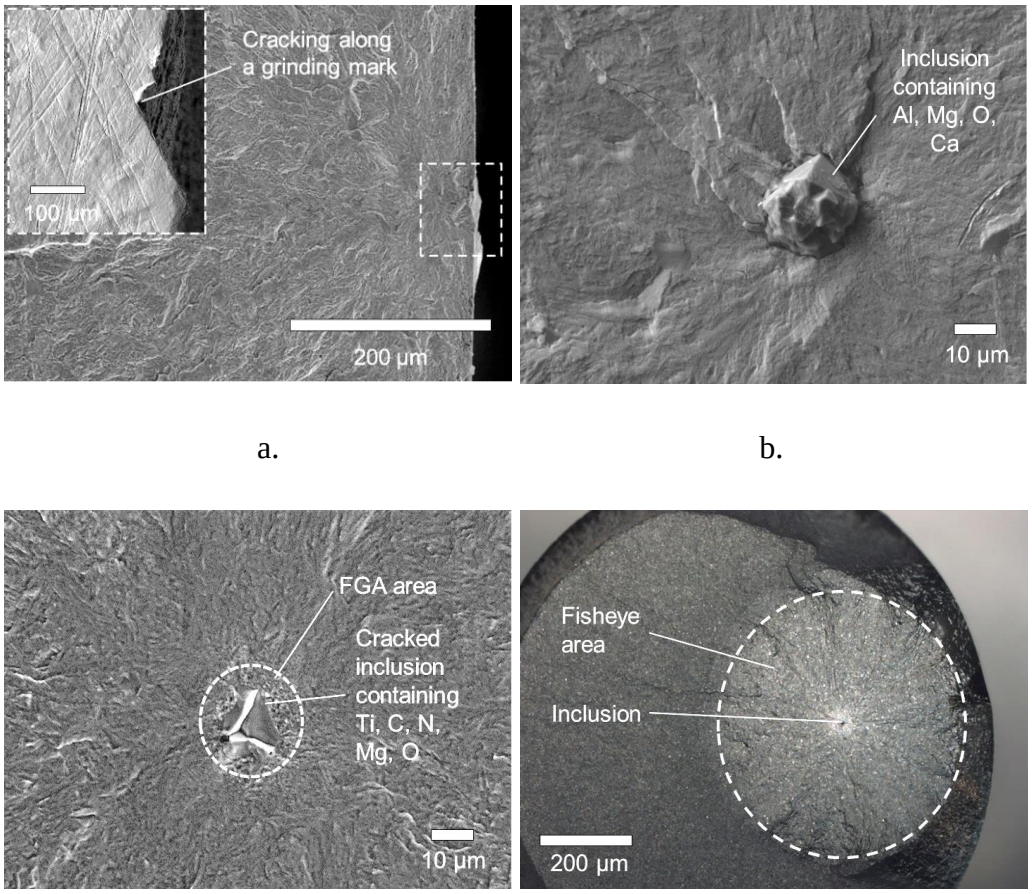

a. b.

c. d.

Figure 6.6 Crack initiation sites in fractured fatigue specimens observed under SEM namely a. grinding mark, b. an un-cracked, embedded Type A inclusion, c. a cracked Type B cubic inclusion with surrounding FGA area, d. fisheye morphology for a crack initiating at an interior inclusion

In Fig. 6.4, the fatigue lives of the specimens with surface crack initiation and those with subsurface crack initiation at inclusions are represented by half-filled and fully-filled symbols, respectively. The fatigue life of the polished specimen with crack initiation at an inclusion in touch with the surface is represented by an open symbol. The 2 specimens for which the crack initiated at surface

grinding marks, in as-machined condition, had lower fatigue lives than those for which the crack initiated at inclusions. However, the fatigue life for the S230-8A peened specimen where the crack initiated at the grinding mark was relatively high (1.06 x 10^6 cycles) and only one other S230-8A specimen had a higher fatigue life (3.42 x 10^6 cycles), which failed due to a small inclusion (12.7 μm). This might indicate a possible benefit of peening on the fatigue life of as machined specimens since the S230-8A peened specimen with a surface crack initiation has 2-8 times higher fatigue life than the as-machined specimens with a surface initiation.

The effect of inclusion characteristics on the fatigue life for all surface conditions was investigated. The number of cycles to failure (N_f) vs. the inclusion size ($\sqrt{area}$), is illustrated in Fig. 6.7a. Note that for an inclusion in touch with the free surface, the $\sqrt{area}$ parameter is 1.07 times that of an interior inclusion [131], which accounts for surface effects. Fig. 6.7a suggests that the larger the inclusion present at the crack initiation site, the lower is the resulting fatigue life; with the exception of a small inclusion of 21 μm (open symbol in Figs. 6.7a, b) located just beneath the surface in a polished specimen. In fact, the N_f of this specimen (4.83 x 10^4 cycles) was about 3.4 times lower than that of the S230-8A specimen with the largest inclusion of 51 μm, located in the specimen interior. It is important to note that this is an exclusive case that occurred in a polished specimen which is characterised by low surface CRS. No such occurrences were found in case of the peened specimens with high surface CRS.

The inclusions' position found at the crack initiation sites was defined as the distance from the center of the inclusion to the specimen surface. Fig. 6.7b reveals that plotting the fatigue life vs. inclusion position for all surface conditions exhibits no clear trend.

These observations point to the fact that the inclusion size has a significant influence on the fatigue life of the material under the given testing conditions. The worst possible fatigue life would therefore result from a specimen having a large inclusion at the surface. Therefore, an estimate of the largest inclusion that can occur in the studied 300M steel would be of utmost importance.

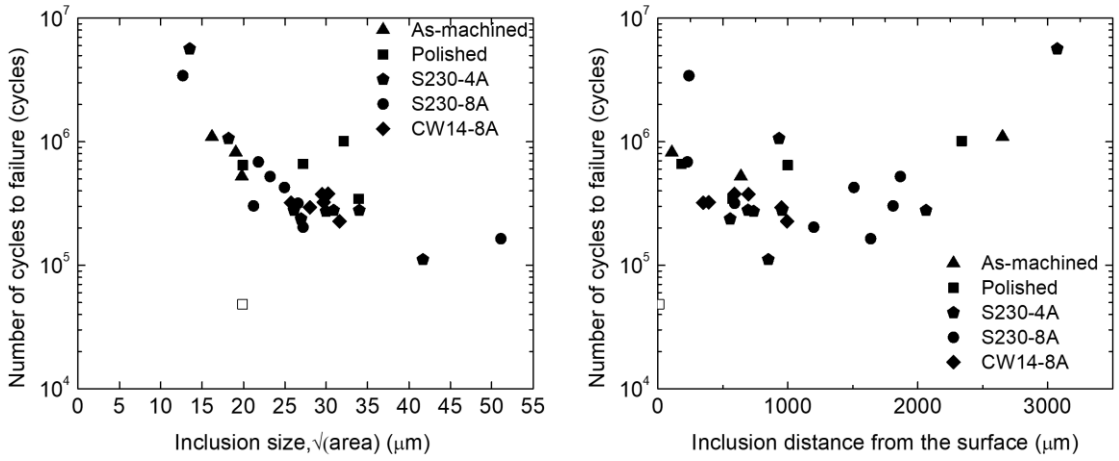

a. b.

Figure 6.7 Plots showing the relationship between: a. inclusion size and total fatigue life, b. inclusion position and total fatigue life for all surface conditions (open symbol represents the polished specimen which showed an exception to the general trend in Fig. 6.7a)

6.3.5 Inclusion analysis

The results of the statistical analysis using Gumbel extreme value model (Section 6.2.6.2) to determine the largest inclusion size in 2 different reference volumes are shown in Table 6.8. The average inclusion size h was around 11.28 μm and the original inspected volume was, $V_o = h\,A_o$ = 0.8 mm^3. A reference volume V_{ref} = A_o x 23.88 mm (length of reduced section) =1707 mm^3 corresponds to the volume of the reduced section of the cylindrical fatigue specimen. The predicted maximum inclusion size, x_{max}, in this volume is about 53 μm. The other V_{ref} of 805 mm^3 is 1000 times the inspected area as recommended in the ASTM procedure [130] , and the x_{max} is around 49 μm. Therefore, the maximum inclusion sizes predicted in both these volumes using the current analyses are consistent with the largest inclusion size of 51 μm observed at a fatigue fracture site. Moreover, no significant change in the x_{max} value, or its associated error and confidence interval, is observed, even when the V_{ref} corresponding to the critically stressed volume in the fatigue specimens is double that of the value recommended by the ASTM standard [130].

Thus, the conventional method for inclusion analysis using statistics of extremes is adequate for estimating the maximum inclusion size for the given batch of 300M steel.

In addition, a comparison between the frequency distributions of the inclusion sizes found by optical microscopy in the metallographic specimens used for the Gumbel analysis, and those found at fatigue crack initiation sites, is made in Figs. 6.8a and 6.8b, respectively. It can be seen that the majority of the inclusions observed in the metallographic specimens are < 15 µm. However, the fatigue cracks seem to initiate mostly at inclusions in the range of 15-35 µm. This indicates that even though smaller inclusions may be present in the material, fatigue crack initiation tends to occur always at biggest inclusions. Moreover, Fig. 6.7a shows that the lowest fatigue lives are obtained when the inclusions are about 45-50 µm. Hence, relying solely on metallographic observations could underestimate the size of the largest inclusion present in the material. This difference between the apparent and the real inclusion size could be drastic in case of large components and could lead to lower fatigue lives than expected. This supports the fact the Gumbel extreme value model would be the optimal choice for identifying the largest inclusions present in the material.

Table 6.8 Results from the Gumbel Extreme value analysis for prediction of largest inclusion size in a given reference volume of steel

(V_o= inspection volume, h = average inclusion size, V_{ref}= reference volume, T = return period, δ, λ = Scale and location parameter of the Gumbel distribution, SE = Standard error, CI_{95} = 95% Confidence interval at 99.9% probability, x_{exp} = experimentally observed largest inclusion size)

V_o (mm^3)	h (µm)	V_{ref} (mm^3)	T (V_{ref}/V_o)	δ	λ	x_{max} (µm)	SE	CI_{95}	x_{exp} (µm)
0.8	11.28	1707	2120	5.09	13.54	53	1.23	2.46	51
		805	1000			49	1.35	2.71	

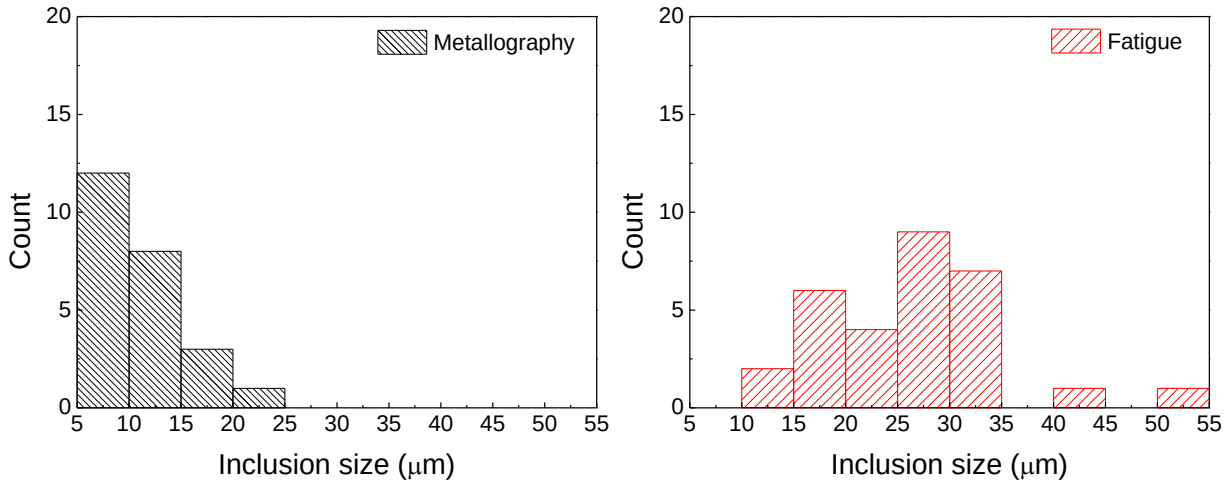

a. b.

Figure 6.8 Frequency distribution for inclusion sizes observed a. in metallography specimens, b. at crack initiation sites in fatigue specimens

6.4 Discussion

6.4.1 Effect of peening on fatigue life

A significant scatter was observed in axial fatigue life results for the given 300M steel for both unpeened and peened conditions. Such scatter is typical for high strength steels where failure is dictated by inclusions, especially in the high and very high cycle fatigue regimes [21, 25, 148] . Since very little difference was observed in the 90% survival life at 95% confidence for all the surface conditions, the fatigue life for all conditions were assimilated and statistically analyzed. It was found that the fatigue life for all surface conditions together could be best fit using the GEV model (k = 0.54, μ = 3.15 x 10^5, σ = 2.43 x 10^5), supported by a high (h, p) value of (0, 0.9) from the Anderson-Darling goodness of fit test. Fig. 6.9 represents the empirical cumulative distribution function (cdf) based on the experimental fatigue life data along with the cdf for GEV. It is evident that a single distribution represents well the fatigue life data for both peened and unpeened specimens. This indicates that shot peening does not provide a significant benefit in terms of fatigue life for the given testing conditions.

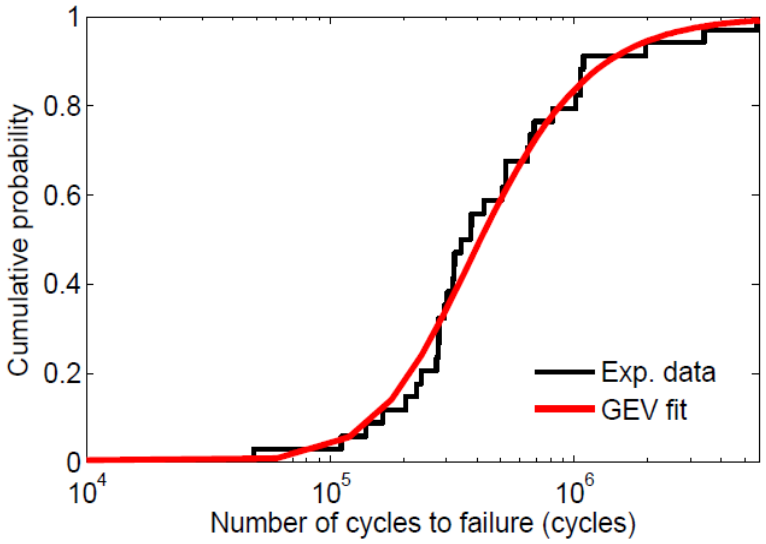

Figure 6.9 Cumulative distribution function for the experimental fatigue life data and for the GEV fit to the fatigue life data

Also, a difference in crack initiation position was observed when comparing the cdf (normal) for peened and unpeened specimens as shown in Fig. 6.10. Peening seems to lower the probability of a crack initiating at the surface or within the CRS layer, when compared to the unpeened specimens. This is consistent with the fact that all the cracks in peened specimens (except one), were initiated at inclusions located much deeper than the effective layer of CRS induced by peening, which is only around 140-160 µm. The CRS can reduce the local stress ratio (R) seen by the material within the effective layer, which prevents early crack initiation and fast short crack propagation as shown by the authors [119]. This difference in the position of the crack initiation site caused by peening, nevertheless, does not significantly influence fatigue life, as shown in Fig. 6.7b.

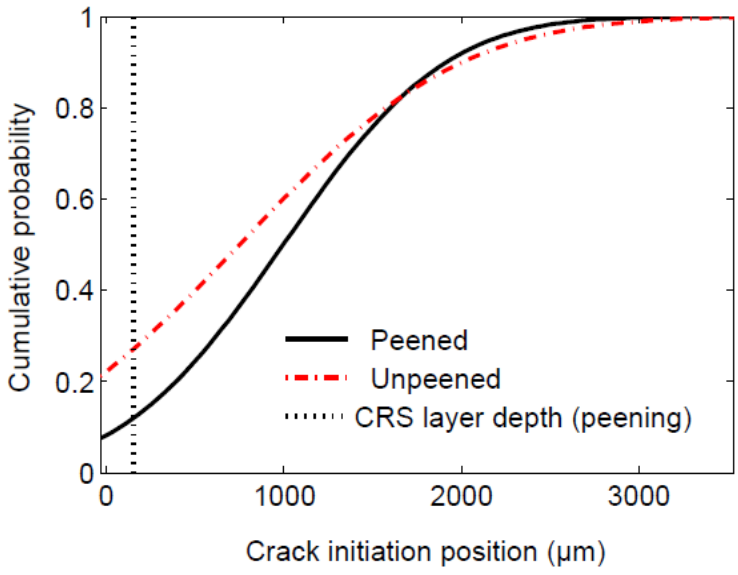

Figure 6.10 Cumulative distribution function for the crack initiation position in unpeened and peened specimens (dotted line at 150 μm represents the average depth of the CRS layer induced by peening)

The slight difference in fatigue lives between the unpeened and peened conditions could be explained based on the fact that the stress concentration caused by the surface roughness is similar to that caused by subsurface inclusions, for the given testing conditions. As a result, there exists a competition between the 2 crack initiation mechanisms (one caused by surface roughness and the other by subsurface inclusions). This is evident in as-machined specimens where surface crack initiation occurs for 2 out of 5 specimens. In these 2 specimens, a smaller inclusion size or a higher surface roughness would have triggered surface initiation, while for the remaining 3 specimens, a larger inclusion size or lower surface roughness would have caused a subsurface initiation. Consequently, in polished specimens, with very low surface roughness, cracks are initiated either at subsurface inclusions or an inclusion in touch with the surface.

Similarly, in peened specimens, inclusions are the most frequent crack initiation sites (22 out of 23 cases). However, the effect of peening induced CRS protecting the surface is not that significant to the fatigue life, unless: i) the size of the inclusion is very small (close to the critical inclusion size required to initiate a crack), or ii) the surface roughness is sufficiently high to cause a surface crack initiation.

This is supported by the following observations. Firstly, the longest fatigue lives (5.65 x 10^6 cycles, 3.42 x 10^6 cycles) were obtained for a S230-4A and S230-8A peened specimen, respectively, where the crack initiated at small inclusions (13.5 µm, 12.7 µm). These inclusion sizes are consistent with the critical inclusion size range of 6-10 µm required to initiate a crack in high strength steels subjected to rotating-bending fatigue in the high cycle fatigue (HCF) regime [9]. Moreover, a high fatigue life (1.06 x 10^6 cycles) was obtained for a S230-8A peened specimen where the crack initiated at a surface grinding mark. In this specific case, shot peening was found to increase the fatigue life by about 2-8 times, when compared to the as-machined specimens with surface crack initiation.

Hence, it can be said that peening could be beneficial in HCF when the crack initiates within the layer affected by CRS. Most of the industrial parts that require shot peening are subjected to bending fatigue, where the part experiences maximum stresses at the surface rather than in the whole volume. In such cases, peening could improve fatigue life. However, experimental tests under bending loads are necessary to explore this hypothesis.

6.4.2 Effect of inclusion size on fatigue life

As shown in Fig. 6.7a, the fatigue life for the tested material at the given stress amplitude was mostly influenced by the size of non-metallic inclusions, irrespective of the surface condition. Therefore, based on all the experimental data obtained, an empirical relationship between inclusion size and the axial fatigue life of 300M steel at 931 MPa (R= -1) is proposed, as schematized in Fig. 6.11. Only the fatigue life corresponding to an inclusion at the surface was removed as it would experience a different local stress (due to the effect of CRS) than the interior inclusions. A power law fit was obtained by non-linear regression, which shows a good correlation of R^2 = 0.78. The fitting coefficient, A = 5.22 x 10^{10} and fitting exponent, b = -3.68 was obtained. The value of the fitting exponent was consistent with those found in literature [9] for similar relationships between fatigue life and inclusion size in high strength steels in the HCF regime.

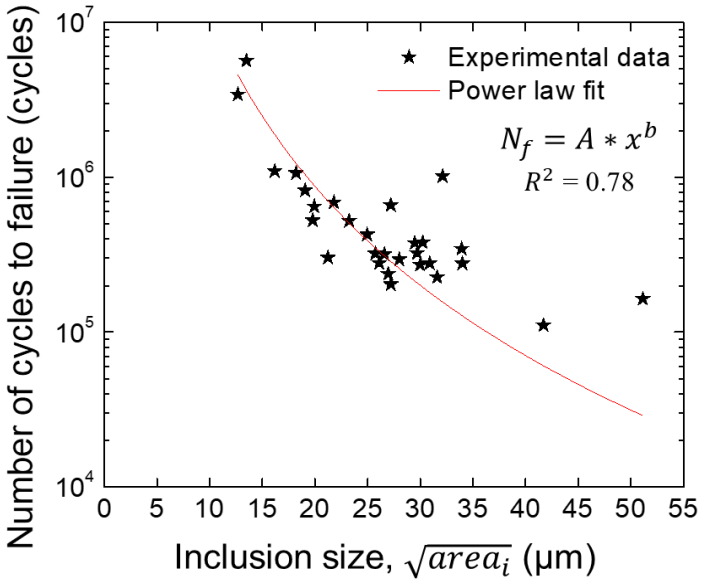

Figure 6.11 Power law fit of fatigue life as a function of inclusion size for all specimens where failure was caused by inclusions

6.5 Conclusions

The effect of shot peening on the axial fatigue life of 300M steel specimens was investigated at a stress amplitude of 931MPa (R = -1). As-machined, polished, S230-4A, S230-8A and CW14-8A peened specimens were used. The peening induced roughness, residual stress profiles and their relaxation due to fatigue loading, were studied with a view to understand and quantify their influence on the material fatigue performance. Features observed at crack initiation sites were also analyzed. In addition, statistical analyses were accomplished to characterize the fatigue life dispersion and inclusion distribution in the given steel. The main findings of this work can be summarized as follows:

Fatigue life results demonstrate similar average values and large scatter in all conditions, irrespective of the surface treatment. The fatigue lives are better fit by the Generalized Extreme Value model, when compared to that obtained from the Weibull model. A more conservative estimate of 90% survival life at 95% confidence interval revealed that the fatigue life for all surface conditions are very similar.

Both S230-8A and CW14-8A conditions have similar residual stress profiles, which are relaxed in average by only up to 12% during fatigue loading.

CW14-8A condition produces the highest R_t and R_{Sm}, and consequently the highest stress concentration ($K_{t,rough}$ =1.1), due to a more severe surface deformation than S230-8A and S230-4A peening conditions.

In the range of the tested conditions, the stress concentration due to surface roughness for all conditions is, however, very close to the stress concentration due to subsurface inclusions. As a result, no significant difference in fatigue life is observed for most of the peened specimens, even when a surface layer of 150 µm is protected by peening induced CRS.

Nevertheless, in a situation where surface roughness is higher, or the inclusion sizes are smaller, shot peening would probably have a beneficial effect on the fatigue life. This is corroborated by the high fatigue lives obtained when the crack initiated at small inclusions (~13 µm) or a surface grinding mark.

Non-metallic inclusions are primarily responsible for crack initiation in all surface conditions at this stress amplitude. An empirical relationship was proposed to predict fatigue life based on inclusion size for the studied conditions.

The Gumbel Extreme Value analysis is able to predict the largest inclusion (53 µm) in the critically stressed volume of a fatigue specimen, which is in good agreement with the experimentally obtained inclusion size (51 µm).

In summary, at the tested low stress amplitude, the fatigue life of 300M steel is governed mainly by inclusions, while peening seems to prevent early crack nucleation due to surface inclusions and grinding marks. Therefore, in order to improve fatigue life at this stress amplitude, steps should be taken to improve the steel cleanliness. Nevertheless, for rougher components or components where a stress gradient exists, shot peening could have a more significant beneficial effect.

6.6 Acknowledgements

This work was financially supported by the Consortium of Research and Innovation in Aerospace Québec (CRIAQ), the Natural Sciences and Engineering Research Council of Canada (NSERC), Pratt & Whitney Canada, Bell Helicopter Textron Canada, L3-Communications MAS, Héroux Devtek and the Mathematics of Information Technology and Complex Systems (MITACS) (Grant No.: RDC 435539-12). The authors would also like to acknowledge the assistance received from

Mr. Arnaud Divialle and Ms. Cristina Del Vasto of Héroux Devtek, and Mr. Nicolas Brodusch of McGill University, Canada during the realization of the work.

CHAPTER 7 ARTICLE 2: EFFECT OF DIFFERENT SHOT PEENING CONDITIONS ON THE FATIGUE LIFE OF 300M STEEL SUBMITTED TO HIGH STRESS AMPLITUDES

Amrita Bag[a], Dorian Delbergue[b], Jihane Ajaja[a], Philippe Bocher[b], Martin Lévesque[a], Myriam Brochu[a]

[a] Département de génie mécanique, École Polytechnique de Montréal, QC H3T 1J4, Montréal, Canada

[b] Département de génie mécanique, École de technologie supérieure, QC H3C 1K3, Montréal, Canada

Article accepted in the International Journal of Fatigue on 13th September 2019.

Abstract: Shot peening may not always be beneficial to fatigue performance. It is therefore necessary to carefully analyse both beneficial and detrimental aspects of peening and their interactions with the properties of the target material. In this study, the axial fatigue life of high strength 300M steel (modified AISI 4340) tested at a high stress amplitude (< 2 x 10^5 cycles) was investigated for 3 different peening conditions. Peening induced roughness, initial residual stresses and their relaxation during cyclic loading were quantified. B-basis analysis, a conservative approach used for design in aerospace applications, was employed to compare the peened and unpeened specimens' fatigue lives. It was observed that the combined effect of roughness and compressive residual stresses determines the dominant feature responsible for fatigue crack initiation. A stress-intensity factor-based approach was proposed to predict a lower bound for the fatigue lives of the tested conditions. The cracks initiated at intrinsic material discontinuities (inclusions) and peening or machining induced surface discontinuities. The analytical fatigue life predictions agreed with the statistical B-basis values for conditions exhibiting a low fatigue life scatter.

Keywords: shot peening; fatigue; 300M; statistical analysis; inclusion

7.1 Introduction

300 M steel is a high strength steel, similar to AISI 4340 steel in composition, but with a higher Si and V contents that confers its improved strength and fracture toughness. It is widely used in aircraft landing gear and rotor shaft applications. Such components are susceptible to fatigue damage. Therefore, surface treatments that induce beneficial compressive residual stresses are widely used to enhance the treated parts' fatigue life. One such technique is shot peening, a cold working process in which a metal surface subjected to a stream of high velocity spherical particles,

referred to as ‘shot’, plastically deforms the material surface layer, creating compressive residual stresses (CRS) and strain hardening. These stresses contribute to short crack arrest or propagation delay. Another aspect of shot peening is the associated surface roughness which can sometimes reduce fatigue life. Severe peening conditions can give rise to surface discontinuities in the form of burrs, microcracks and material folds, as shown by Higounenc [1]. Tekeli [2] observed a decrease in the rotating bending fatigue strength of SAE 9245 spring steel when subjected to a peening intensity above 20-25A using S230 steel shot (0.58 mm diameter) and 100% coverage. He attributed this behavior to microcrack initiation resulting from peening induced surface roughness. In addition, He et al. [3] reported a similar reduction in the bending fatigue life of a 11Cr-Mo-V martensitic steel peened with similar sized shots at a much lower intensity of 13A and 200% coverage, due to formation of peening lips or rolled edges as a result of surface deformation.

The fatigue strength of hard materials, such as quenched steels, is highly sensitive to the presence of micro-sized defects, as demonstrated by the early work of Murakami and Endo [4]. They performed rotating bending fatigue tests on steels having hardness above 500 HV (~50 HRc) with artificial holes whose diameters ranged from 40 to 200 μm. They observed that even the smallest hole of 40 μm diameter could cause a significant decrease in fatigue strength. Hence, for some sensitive materials, the surface discontinuities induced by conventional shot peening may prove detrimental to fatigue resistance. Therefore, to make a proper choice of peening conditions for a particular material (in terms of fatigue performance), it is essential to understand how the material is affected by peening treatments under a given set of mechanical testing conditions.

Several researchers have reported that, in hard martensitic steels, peening induced CRS tend to shift the fatigue crack initiation position from the specimen’s surface to its interior, typically beneath the CRS layer. Such interior crack initiation is usually triggered by non-metallic inclusions or martensitic packet boundaries. Iwata et al. [5] observed by transmission electron microscopy that, for a quenched martensitic steel subjected to rotating bending fatigue, the cracks initiated at martensite packets near the surface due to dislocation slip. For specimens peened with 0.6 mm diameter steel shots at 300% coverage (the intensity was not specified), crack initiation occurred at slip bands ~500 μm beneath the surface, which corresponded to the depth of the CRS layer induced by peening. Similar crack initiation beneath the CRS affected layer was reported by Peige et al. [6] for a shot peened quenched and tempered 300M steel subjected to rotating bending fatigue in the high cycle fatigue (HCF) regime (the shot peening conditions were not specified). Other

works supporting these claims include those of Gao et al. [7] for a quenched and tempered 40CrNi2Si2Mo2V steel peened at an intensity of 12A and 120% coverage, and those of Wang et al. [8] for several heat treated high and medium strength steels peened with 0.8 mm diameter cast steel shot for a range of intensities (12-24 A) and coverages (100-500%), and subjected to 3-point bending fatigue under HCF conditions. Since interior cracks are characterized by lower propagation rates, when compared to surface cracks, as explained by Grad and Kerscher [9], shot peening can significantly improve fatigue life.

During cyclic loading (especially involving compressive loads), however, CRS relaxation may occur, depending on the applied stress amplitude and the material's cyclic stress-strain behaviour, as shown in the early work by Morrow and Sinclair [10]. The authors studied the relaxation of superimposed compressive mean stresses on the fully reversed strain controlled axial fatigue testing of SAE 4340 steel specimens of varying hardness, for different applied strain amplitudes. They observed that the highest stress relaxation occurred in the first cycle under high strain amplitudes (inducing stresses close to the material's yield), after which the relaxation was mostly linear with the increasing number of cycles. In the case of peening induced CRS, Kodama [11] and Hanagarth et al. [12] reported more than 50% relaxation during the 1st load cycle when a steel sample was subjected to completely reversed high cycle axial fatigue loading. Torres and Voorwald [13] observed that, when a quenched and tempered 4340 steel specimen shot peened at an intensity of 14.1A was subjected to low and high stress levels (840MPa and 1130 MPa) at 10^4 cycles (R = -1), the stress relaxation was more significant for the highest applied stress, both at and below the surface. Stabilization of CRS was encountered on the same sample after 10^3 cycles.

Such residual stress relaxation phenomena must be accounted for when evaluating the peened components' fatigue life to avoid fatigue life overestimation. Similarly, the debit in fatigue life due to the introduction of peening induced roughness also needs to be considered.

This work focuses on the effect of specific shot peening conditions on the axial fatigue life of aerospace grade 300M steel, for a stress amplitude corresponding to 64% of the material's 0.2% offset yield strength $\sigma_{y,0.2}$, causing failure in the range of 2 x 10^5 cycles. It is expected that, under the given stress amplitude, higher plastic deformation would lead to a short crack initiation life, and most of the fatigue life would be spent in crack propagation [14]. The crack initiation features (i.e., surface discontinuities, inclusions) could therefore be considered as small inherent cracks [15]

and their growth would govern the component's total fatigue life. The driving force for such crack growth can be represented by the stress intensity factor range as proposed by linear elastic fracture mechanics outlined in the book of Dowling [14]. Hence, a stress intensity factor-based approach was adopted in this paper to identify the feature from which a crack would favorably propagate for each of the peening conditions, as well as for unpeened conditions.

Moreover, in the aerospace sector, stringent design allowables are imposed to ensure the safety of the engineering structures, which takes into account the fatigue life dispersion. Therefore, fatigue life results were analyzed as per the B-basis (95% confidence on the 90% survival estimate) to predict a lower bound for the treated specimens' fatigue life, for each surface condition.

Experimental investigation of peening induced roughness and residual stresses, along with residual stress relaxation during cyclic loading, was performed. Crack initiating features were characterized in terms of type, size, position and composition. Crack propagation in the material was also quantified using long crack propagation tests. The material, the studied surface conditions and the experimental methodology are described in Section 2. Thereafter, the results obtained from the experimental campaign are presented in Section 3. In Section 4, the long crack propagation data along with the calculated stress intensity factor ranges were used to predict fatigue life. The statistically predicted fatigue lives using B-basis were compared to those predicted using the analytical stress intensity factor-based model. The gathered information was used to draw conclusions regarding the most suitable peening condition for 300M steel for the given testing conditions.

7.2 Material and experimental methods

7.2.1 Material

The investigated material is a heat treated 300M steel. The material's chemical composition and monotonic mechanical properties (extracted from the authors' previous work [16]) are tabulated in Tables 7.1 and 7.2, respectively. The microstructure consists of tempered martensite and the average prior austenite grain size is 23 µm [16]. The material's average macro-hardness is about 54 HRc, which is in accordance with the AMS6257E standard that specifies a minimum hardness of 52 HRc.

Table 7.1 Chemical composition (wt. %) of the 300M steel [16]

C	Mn	Si	P	S	Cr	Ni	Mo	V	Cu	Al	Fe
0.40	0.77	1.61	0.006	0.001	0.80	1.92	0.37	0.08	0.10	0.04	Balance

Table 7.2 Mechanical properties of the studied 300M steel (average of 3 tests using 86.2 mm diameter bars) along with their standard deviations (in brackets) [16]

Material	$\sigma_{y,0.2}$ (MPa)	σ_{UTS} (MPa)	E (GPa)	υ	$\%El$
300M steel	1693 (±6)	2020 (±10)	197 (±1)	0.28 (±0.03)	11.7 (±0.4)

7.2.2 Surface conditions

As-machined, polished and 3 shot peened conditions were studied. Peening was performed at 100% coverage using: i) S230 shot at an intensity of 4A (S230-4A), ii) S230 shot at an intensity of 8A (S230-8A), and iii) CW14 shot at an intensity of 8A (CW14-8A). As described previously by the authors [16], the as-machined specimens possessed non uniform grinding marks on the surface oriented in different directions, most of which were oriented at 45° with respect to the longitudinal direction. While these grinding marks were still visible after peening with the S230-4A or S340-8A conditions, most of them were eliminated due to the surface deformation caused by peening with the CW14-8A condition.

Table 7.3 (extracted from [16]) depicts the measured values (average of 9 measurements) of the surface roughness parameters R_a, R_t and R_{Sm}, where R_a is the arithmetic mean roughness, R_t is the distance between highest peak and deepest valley in the total evaluation length, and R_{Sm} is the mean spacing between successive peaks within the sampling length. The corresponding stress concentration factor $K_{t,rough}$ was calculated using the equation from the finite element simulation of Li et al. [17] for multiple shot indentations, as:

$$K_{t,rough} = 1 + 4.1\left(\frac{R_t}{R_{Sm}}\right)^{1.3} \quad \text{for} \quad \left(\frac{R_t}{R_{Sm}}\right) < 0.15 \tag{7.1}$$

Table 7.3 shows that the CW14-8A condition induces the highest surface roughness and stress concentration factor, followed by the S230-8A and the S230-4A conditions.

Table 7.3 Average roughness parameter values along with their 95% confidence intervals (in brackets) and surface stress concentration factors for all surface conditions (D = average shot diameter, V = average shot velocity) [16]

Surface treatment	As-machined	S230-4A (D = 0.58 mm) V = 12 m/s	S230-8A (D = 0.58 mm) V = 26 m/s	CW14-8A (D = 0.35 mm) V = 76 m/s
R_a, µm (95% CI)	0.31 ($\pm$0.07)	0.75 ($\pm$0.18)	1.18 ($\pm$0.17)	1.44 ($\pm$0.07)
R_t, µm (95% CI)	2.36 ($\pm$1.55)	3.94 ($\pm$0.54)	7.79 ($\pm$0.85)	15.51 ($\pm$2.11)
R_{Sm}, µm (95% CI)	113 ($\pm$18)	135 ($\pm$46)	230 ($\pm$79)	279 ($\pm$37)
$K_{t,rough}$	--	1.04	1.05	1.10

7.2.3 Stress-controlled axial fatigue tests

Room temperature axial fatigue tests were performed at a stress amplitude of 1089 MPa (64% of $\sigma_{y,0.2}$) with a stress ratio R = -1 and a frequency of 10 Hz, in agreement with ASTM E466 standard [18], using uniform gage cylindrical specimens (Fig. 7.1a). An MTS 318.25 servo-hydraulic system equipped with a 250 kN MTS 661.22c-01 load cell was used to perform the tests. A total of 8 specimens for as-machined and each of the 3 peening conditions, and 5 specimens for the polished condition, were mechanically tested. Fractography analyses were performed using JEOL JSM-7600F Scanning Electron Microscope (SEM). Oxford X-Max 80 Silicon Drift Detector was used for Energy Dispersive Spectroscopy (EDS) to qualitatively analyze the features responsible for fatigue crack initiation.

7.2.4 Residual stress measurement and residual stress relaxation tests

The X-Ray Diffraction (XRD) technique, coupled with layer removal by electropolishing, was used to obtain in-depth residual stress profiles. Details regarding the residual stress measurement technique have been discussed in the authors' previous work [16].

Interrupted axial fatigue tests were performed on 300M steel hourglass specimens (Fig. 7.1b) to quantify residual stress relaxation under the fatigue testing conditions described in Section 7.2.3. Two peening conditions that yielded the best (S230-8A) and the worst (CW14-8A) fatigue lives were studied. Measurements were performed after 1 cycle and 80% of fatigue life for the CW14-8A condition, and after 80% of fatigue life for the S230-8A condition. These residual stress profiles are compared to the initial stress profiles (0 cycle) [16] in Section 7.3.2.

7.2.5 Long crack propagation test

Long crack propagation tests were performed at R = 0.1 and at a frequency of 20 Hz using 2 compact tension C(T) specimens (Fig. 7.1c), as per the ASTM E647 standard [19]. The tests were performed in ambient atmosphere at room temperature using a clevis and pin assembly supported by an MTS 318.25-250 kN load frame. The decreasing K method by load shedding was adopted to reach the fatigue crack growth threshold corresponding to crack growth rates of about 10^{-10} m/cycle. The test was then continued at constant force amplitude to obtain comparison data under K-increasing conditions upto a crack growth rate of 2 x 10^{-7} m/cycle. The crack opening displacement (COD) was recorded using an MTS 632.02B-20 clip-on displacement gage. The MTS Test Suite Elite software was employed to calculate the crack size a, using the compliance method [19]. The crack growth rate da/dN was calculated using the secant method [19] from the $a - N$ curves.

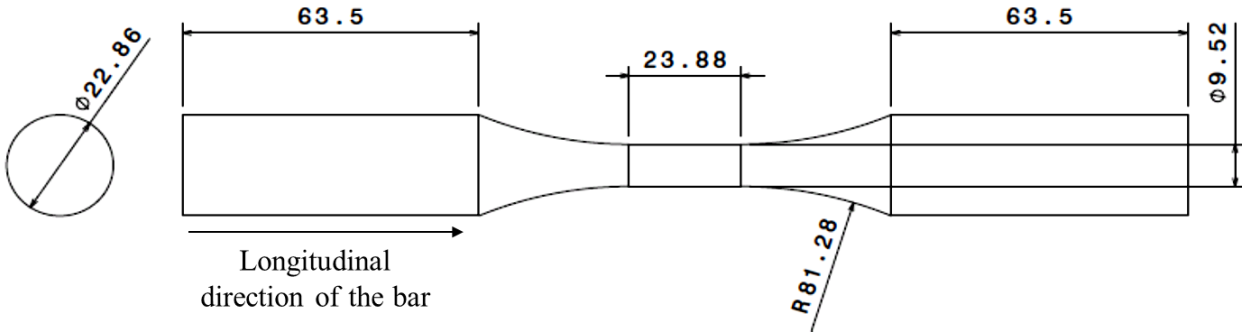

a.

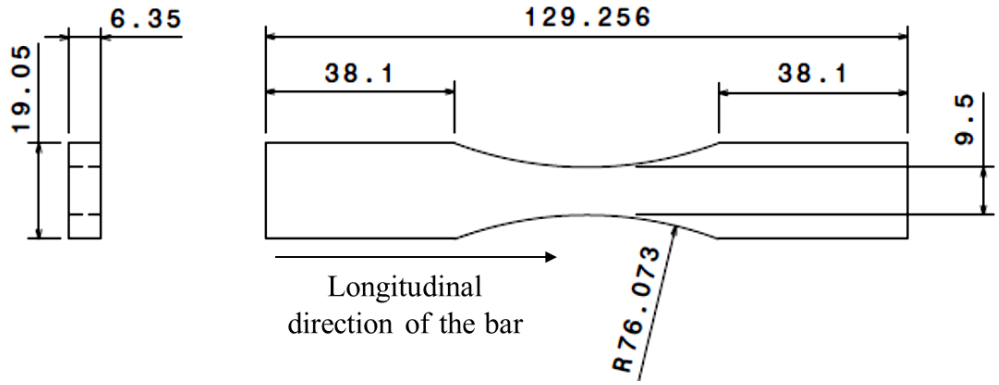

b.

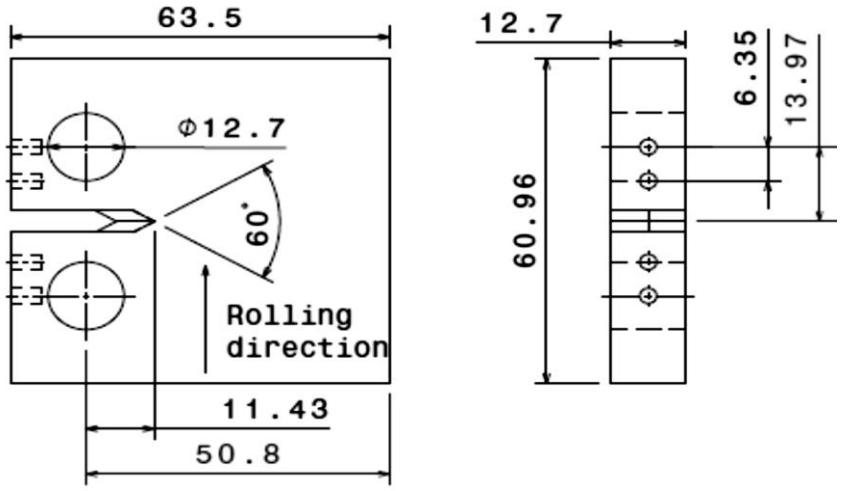

c.

Figure 7.1 a. Axial fatigue test specimen, b. residual stress relaxation specimen, and c. long crack propagation test specimen dimensions (mm)

7.2.6 Statistical analysis of fatigue life dispersion

The B-basis analysis adopted by the aerospace industry, as outlined in the works of Rice et al. [20] and Jackson [21], was chosen to compare the fatigue lives resulting from the tested conditions. The B-basis represents a statistical prediction of the lower bound for the observed fatigue life characterizing a population and is defined by the number of cycles to failure corresponding to the lower bound of the 95% confidence interval on 90% of the specimens surviving to the applied load.

Best fit statistical distributions for the fatigue data were identified using the Anderson-Darling goodness of fit test [22]. The goodness of fit was determined by the Anderson-Darling coefficients h and p. The closer the (h, p) value is to (0, 1), the better is the fit, while a (h, p) value of (1, 0) represents that the data does not follow the given distribution. Two distribution models that best described the specimens' fatigue lives were chosen among the Weibull, the log-normal and the Generalized Extreme Value (GEV) models.

The log-normal distribution has been used to characterize the fatigue life data for notched, unnotched 2024-T3 Alclad sheet specimens by Schijve [23, 24]. The probability density function, $f^{Ln}(x)$ for a random variable x following the log-normal distribution is given by:

$$f^{Ln}(x) = \frac{1}{x} \cdot \frac{1}{\sigma\sqrt{2\pi}} \exp\left(-\frac{(lnx-\mu)^2}{2\sigma^2}\right), \tag{7.2}$$

where μ (scale parameter) and σ (shape parameter) are the mean and standard deviation of the variable's natural logarithm, respectively.

The GEV is generally used to model the minima or maxima of a sequence of random variables. Its probability density function, $f^{GEV}(x)$, is:

$$f^{GEV}(x) = \left(\frac{1}{\sigma}\right) \exp\left(-\left(1 + k\frac{(x-\mu)}{\sigma}\right)^{-\frac{1}{k}}\right) \left(1 + k\frac{(x-\mu)}{\sigma}\right)^{-1-\frac{1}{k}}, \tag{7.3}$$

where k is the shape parameter, μ is the location parameter and σ is the scale parameter.

Details regarding the GEV distribution and its applicability to represent fatigue life data for the studied material have been discussed elsewhere [16].

The 90% survival life at 95% confidence interval was calculated from the fitted statistical distributions. The statistical analysis was done using MATLAB R2013a.

7.3 **Results**

7.3.1 Fatigue test results and statistical analysis

Fig. 7.2 shows the axial fatigue test results at a stress amplitude of 1089 MPa (R = -1). The total number of cycles to failure, N_f, is displayed on the abscissa for the corresponding surface condition presented on the ordinate axis. The open, half-filled and fully filled symbols represent different types of crack initiation features, which are elaborated in Section 7.3.3.

The average fatigue lives of all tested conditions presented in Table 4 reveal that the polished specimens sustain the least cycle count to failure, when compared to the other conditions. The highest average fatigue life was obtained for the S230-4A condition, while the as-machined specimens and specimens treated as per conditions, S230-8A and CW14-8A yielded similar average fatigue lives.

Table 7.4 presents the best fit distribution (lognormal or GEV), the Anderson-Darling goodness of fit test coefficients (h, p), the maximum likelihood parameters and the B-basis values for each surface condition. The Generalized Extreme Value distribution is generally used to represent an extreme event. Therefore, in the context of fatigue life data, failures triggered by an extreme discontinuity, close to the upper bound of its size range may be represented by the GEV distribution. As shown in the work of Bianchetti et al. [25], the lognormal distribution represents fatigue failure due to the multiplicative effect of more than one potential crack initiating sources, which results in cumulative damage of the component. Table 7.4 shows that for the as-machined and all the peening conditions, where two types of crack initiation features are active, the GEV distribution provides a good fit to the fatigue life data. This indicates that the fatigue failures are triggered by large discontinuities of either type that serve as the weakest link. However, for the as-machined specimens, the lognormal distribution provides a slightly better fit to the fatigue life data. For polished specimens, the lognormal distribution provides a good fit to the fatigue life data, but fatigue life data cannot be fit using the GEV distribution.

The highest B-basis value is obtained for the specimens treated as per the S230-8A condition (3.34 x 10^4 cycles), and it is also the most reliable peening condition. It is closely followed by the S230-4A condition (2.62 x 10^4 cycles) while the lowest B-Basis value is given by the CW14-8A condition (-16.3 x 10^4 cycles). Although physically impossible, a negative B-basis value for the specimens

treated as per the CW14-8A condition relates to the fact that the condition is highly unreliable due to a larger predicted scatter in terms of the scale parameter or the standard deviation (σ) and may lead to very low fatigue lives. It also indicates that additional tests are required to obtain a finite B-basis value at 1089 MPa. Similar observations were made in the case of as-machined specimens where the GEV distribution predicts a higher scatter than the lognormal distribution and hence, yielded a negative B-basis value. When compared to the as-machined condition (0.58×10^4 cycles), the polished, the S230-4A and the S230-8A conditions yielded 2.6, 4.5, 5.8 times higher B-basis values. This suggests that, while polishing and certain peening conditions (S230-4A and S230-8A) can improve the fatigue lives of a given as-machined specimen, other peening conditions such as CW14-8A may be detrimental.

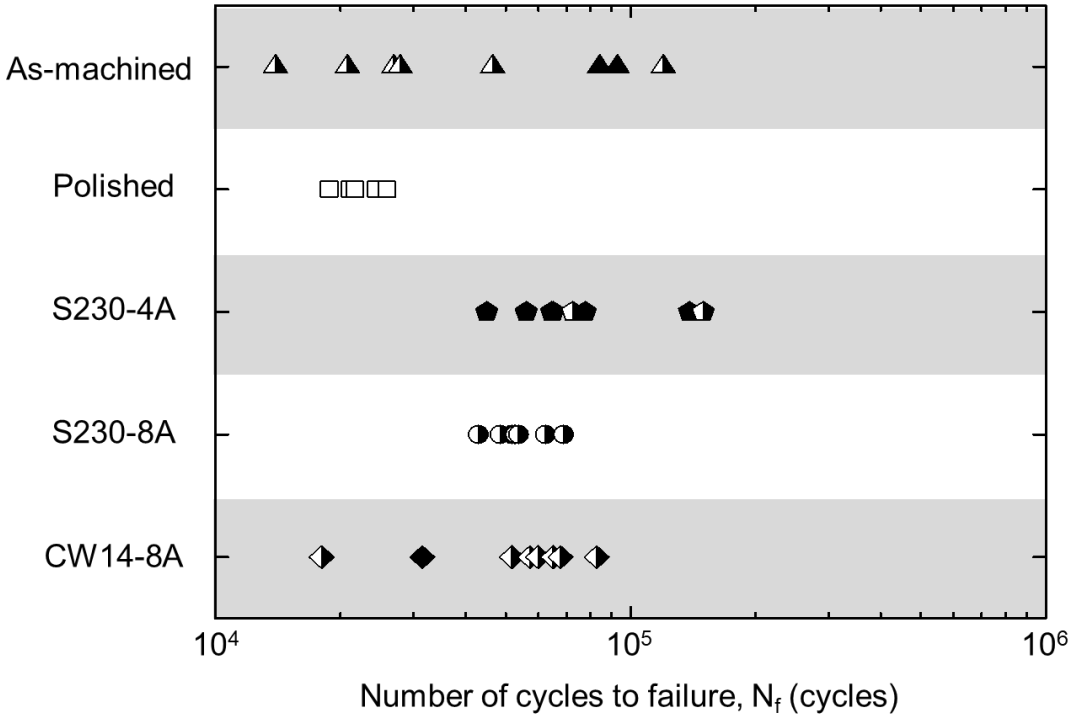

Figure 7.2 Total fatigue life N_f from axial fatigue tests submitted to a stress amplitude of 1089 MPa and R = -1. Each symbol type represents N_f for the corresponding surface condition in the ordinate axis (half-filled symbols represent surface crack initiation at grinding marks/peening induced discontinuities, fully-filled symbols represent crack initiation at interior inclusions, open symbols represent crack initiation at surface inclusions)

Table 7.4 Statistical analysis details for axial fatigue results (1089 MPa and R = -1) showing average fatigue life, best fit distributions for the data, (h, p)-value of Anderson Darling test, Maximum Likelihood Estimates (MLEs) of fitting parameters and B-basis values

Surface condition	Average N_f (x 10^4 cycles)	Best fit distribution	(h,p) value	Fitting parameters (MLE)			B-basis (x 10^4 cycles)
				k	μ	σ	
As-machined	5.42	Lognormal	(0,0.95)	--	10.64	0.78	0.58
		GEV	(0,0.94)	0.65	2.91 x 10^4	1.88 x 10^4	-2.03
Polished	2.24	Lognormal	(0,0.99)	--	10.01	0.13	1.52
		GEV	(1,0)	--	--	--	--
S230-4A	8.36	Lognormal	(0,0.78)	--	11.25	0.42	--
		GEV	(0,0.95)	0.39	6.34 x 10^4	1.92 x 10^4	2.62
S230-8A	5.42	Lognormal	(0,0.90)	--	10.89	0.14	3.73
		GEV	(0,0.91)	-0.07	5.09 x 10^4	0.63 x 10^4	3.34
CW14-8A	5.42	Lognormal	(0,0.63)	--	10.81	0.5	--
		GEV	(0,0.97)	-0.59	5.04 x 10^4	2.15 x 10^4	-16.3

7.3.2 Peening induced residual stresses and their relaxation

Fig. 7.3 illustrates the residual stress profiles after 80% of the fatigue life for specimens peened with the S230-8A condition, and after 1 cycle and 80% fatigue life for those peened with the CW14-8A condition. The residual stress profiles for all surface conditions prior to fatigue testing (0 cycles) [16] were also included for comparison. The figure clearly identifies the surface residual stress (σ_s), the maximum CRS (σ_{mc}), the depth at which the maximum CRS occurs (x_{mc}) and the depth

at which the residual stresses become tensile (x_0), for all tested conditions. Table 7.5 summarizes the residual stress profile characteristics for each surface and testing condition.

Analysing the peened specimens' residual stress relaxation data revealed that the S230-8A condition's σ_s and σ_{mc} values relaxed by about 22% and 26% after 80% of the fatigue life. Similar relaxation of σ_s and σ_{mc}values were observed for the CW14-8A condition (16% and 25%, respectively). About 73% and 76% of the total stress relaxation occurred during the 1st cycle for the σ_s and σ_{mc}, respectively. Moreover, the maximum CRS after the 1st cycle was located at 39 µm depth below the surface. After 80% of the fatigue life, the σ_{mc} for both peening conditions was nearly constant, from the surface down to 45 µm. In addition, x_0 was not significantly affected by the loading cycles.

At the chosen stress amplitude of 1089 MPa (64% of $\sigma_{y,0.2}$), the amount of surface stress relaxation was no more than 237 MPa, which represents about ~22% of the initial surface residual stresses induced by the peening process. The depth of the CRS was similar for the S230-8A and CW14-8A peening conditions (~150 µm) and did not undergo significant change due to cyclic loading.

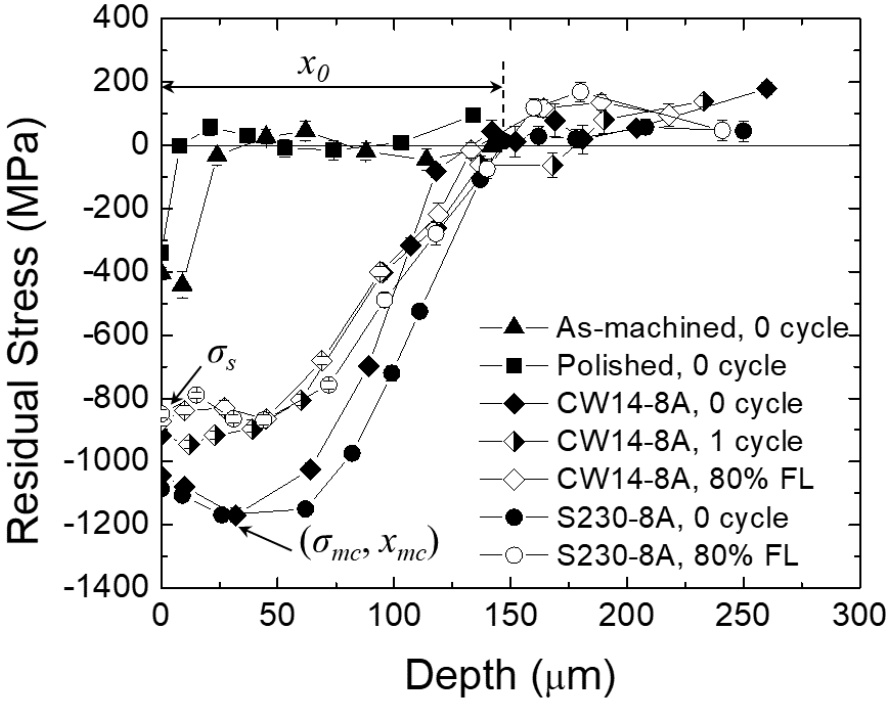

Figure 7.3 XRD residual stress profiles in specimens treated as per the S230-8A condition after 80% of fatigue life, those treated as per the CW14-8A condition at 1 cycle and 80% of the fatigue life, and specimens having all the other surface conditions prior to fatigue testing (0 cycle) [16]. Broken lines have been used to connect the experimental points to better represent the residual stresses' evolution. The CRS profiles are similar for the specimens treated as per the S230-8A and CW14-8A conditions, both at 0 cycle and after 80% of the fatigue life. For the specimens treated as per CW14-8A condition, the maximum CRS relaxation occurs after 1 fatigue cycle, after which it stabilizes. The depth of CRS for both peening conditions remains unchanged

Table 7.5 Summary of residual stress data for all surface conditions

Parameter	As-machined	Polished	S230-8A		CW14-8A		
Cycles	0*	0*	0*	80% FL	0*	1	80% FL
σ_s, MPa	-404	-341	-1086	-849	-1044	-919	-872
σ_{mc}, MPa	-441	-341	-1169	-869	-1170	-946	-872
x_{mc}, µm	9	0	~46	0-44	32	~39	0-45
x_0, µm	24	8	161	150	142	137	133

*Data from Bag et al. [16]

7.3.3 Features responsible for crack initiation

The features responsible for fatigue crack initiation were investigated using SEM. Three types of crack initiating features were observed, namely: grinding marks or peening induced discontinuities and non-metallic inclusions. Some examples are presented in Figures 7.4a-c. Table 7.6 lists the nature of the discontinuities responsible for the main crack initiation for each surface condition, and the number of specimens showing this discontinuity along with their size range and location. Inclusion size was determined as the square root of the area of the discontinuity projected onto a surface normal to the loading axis. This quantity is defined as the effective inclusion area, $\sqrt{area_i}$, by Murakami and Endo [27], based on their detailed investigation of the effect of the size, geometry and location of small surface defects on the rotating bending and axial fatigue strength of more than 15 high strength steels. The inclusions' position was defined as the distance from the center of the inclusion to the nearest specimen surface.

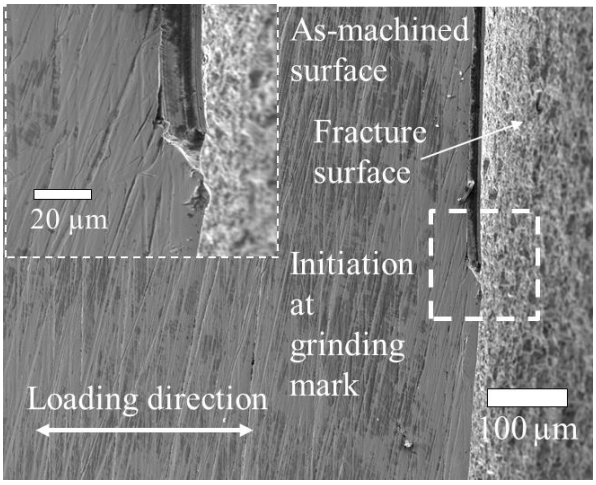

a.

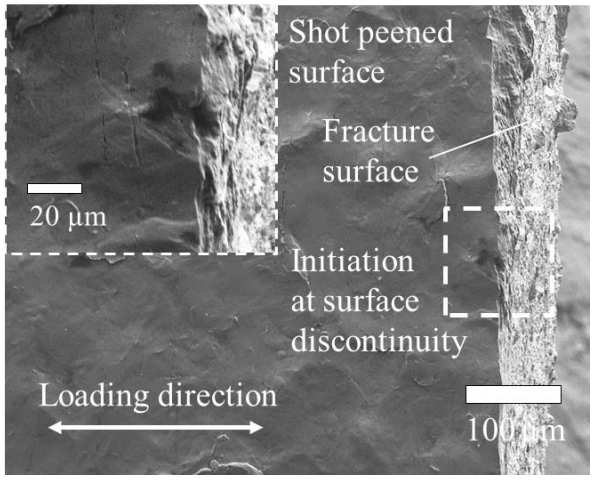

b.

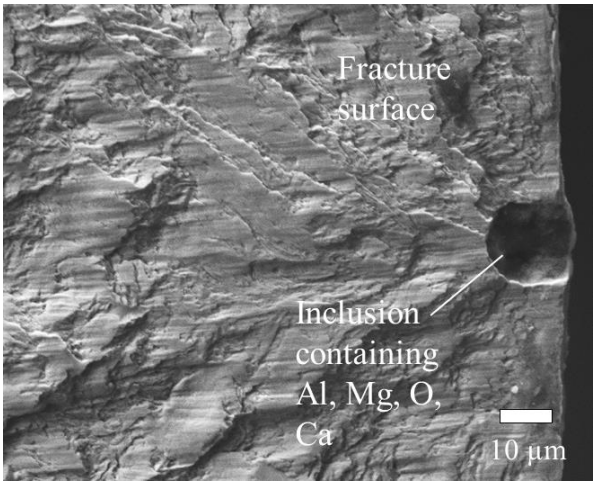

c.

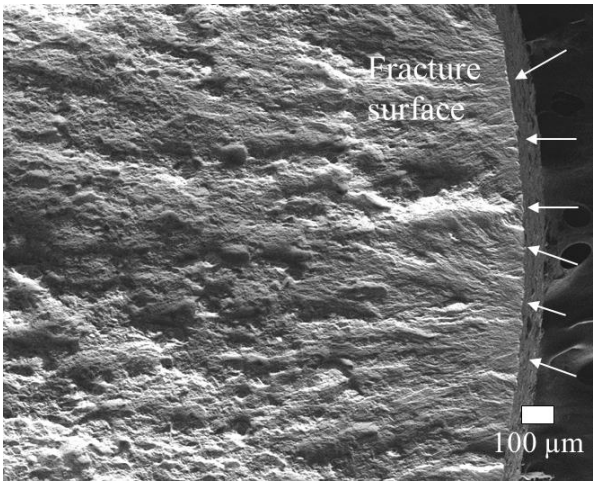

d.

Figure 7.4 SEM images of fatigue specimens' fracture surfaces showing crack initiating from, a. grinding mark (in an as-machined specimen), b. surface discontinuity (in a specimen treated as per the CW14-8A condition), c. an inclusion just below the specimen surface (in a polished specimen), d. several surface discontinuities in a specimen treated as per the CW14-8A condition and having the lowest fatigue life (arrows represent multiple crack initiation sites)

Fatigue cracks in as-machined specimens initiated at a surface grinding mark 6 times out of 8, while the remaining 2 specimens failed at inclusions located deep (>2000 µm) inside the specimen, after a relatively high number of cycles (Fig. 7.2). For polished specimens, the crack initiation always occurred at inclusions (even as small as 9 µm) located at, or just below, the surface. For the specimens treated as per the S230-4A condition, 6 out of 8 failures were caused by interior

inclusions with large sizes (21-42 μm) located beneath the shot peening affected layer. The remaining 2 specimens with surface-initiated cracks have a relatively high fatigue life (Fig. 7.2). For specimens treated as per S230-8A and CW14-8A conditions, cracks initiated at peening induced discontinuities or surface grinding marks 7 out of 8 times. The remaining one failed due to a large interior inclusion. Multiple crack initiation sites were observed for all peened specimens when cracks were triggered by surface discontinuities. The lowest fatigue life for peened specimens (1.8×10^4 cycles) was observed for a specimen peened with the CW14-8A condition, whose fracture surface revealed the largest number of multiple crack initiation sites (Fig. 7.4d) spread over a large proportion of its circumference.

Table 7.6 Summary of features observed at crack initiation sites and their characteristics for all tested surface conditions. The number of specimens of each case is written in brackets

Surface condition	Total number of specimens tested	Crack initiating feature	Size (μm)	Position (μm)
As-machined	8	Grinding marks (6)	--	0 (Surface)
		Interior inclusions (2)	22-25	>2000
Polished	5	Inclusions near the surface (5)	9-30	5-15
S230-4A	8	Grinding marks (2)	--	0 (Surface)
		Interior inclusions (6)	21-42	292-1753
S230-8A	8	Grinding marks/ Peening induced discontinuities (7)	--	0 (Surface)
		Interior inclusions (1)	31	>2000
CW14-8A	8	Grinding marks/ Peening induced discontinuities (7)	--	0 (Surface)
		Interior inclusions (1)	30	>2000

The inclusions responsible for crack initiation were globular or ellipsoidal in shape (Fig. 7.4c) and were composed of Al, Mg, O, Ca (in varying amounts) and sometimes small amounts of Si and S. Similar inclusion compositions were reported by Yang et al. [26] for commercial 42CrMo steel specimens and Saberifar et al. [27] for 30MnVS6 steel subjected to fully reversed rotating bending

fatigue, and by Spriestersbach et al. [28] for high carbon–chromium bearing steel 100Cr6 subjected to fully reversed axial fatigue in the very high cycle fatigue regime ($>10^8$ cycles).

The number of cycles to failure N_f vs. the crack initiating inclusion size for all tested conditions is illustrated in Fig. 7.5a. The figure shows that the N_f decreases for all surface conditions when the inclusion size increases. The N_f of polished specimens, which are characterized by surface crack nucleation, was less sensitive to the inclusion sizes, when compared to the other conditions.

The plot of inclusion distance from the surface vs. N_f in Fig. 7.5b shows that all polished specimens failed from an inclusion in touch with the surface. In comparison, for the other surface conditions, the inclusions triggering crack initiation were found deeper in the material, beneath the CRS affected layer of 150 µm. This unique behavior of the polished specimens can be explained by the absence of significant CRS at the surface. Sufficiently compressive residual stresses counterbalance the stress concentration created by inclusions in touch with the surface. CRS have a beneficial effect on the fatigue life, as can be seen by the results presented in Fig. 7.5. For a comparable inclusion size of ~30 µm, the polished specimens where the crack initiation was triggered by an inclusion at the surface had significantly shorter fatigue lives, when compared to the specimens peened as per the S230-8A and CW14-8A conditions, where the crack was initiated at a subsurface inclusion. These results indicate that, in the presence of CRS at the surface, surface and interior discontinuities are competing to trigger crack initiation.

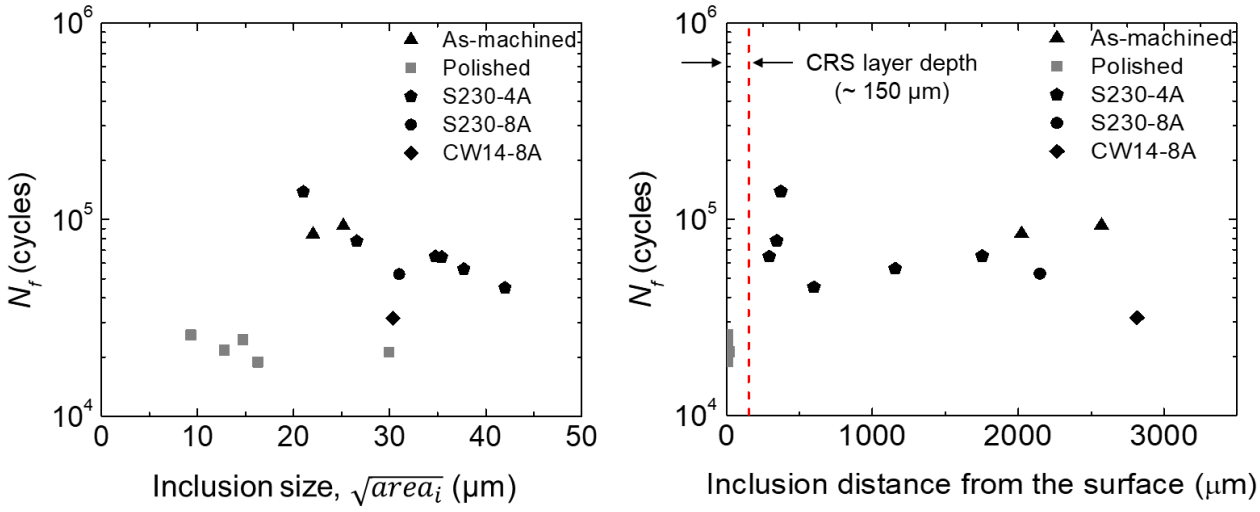

a. b.

Figure 7.5 Plots showing a. inclusion size $\sqrt{area_i}$ vs. total fatigue life N_f, b. inclusion position vs. N_f for all tested surface conditions (the dashed line at 150 μm represents the maximum depth of CRS induced by peening). The fatigue life decreases when the inclusion size increases; the trend is more gradual for polished specimens (grey) than other surface conditions (black). No correlation is observed between the fatigue life and the inclusion position

7.3.4 Long crack propagation test results

The material long crack growth behavior was characterized to attempt predicting the fatigue life using LEFM. Fig. 7.6 plots the average crack growth rate da/dN vs. the stress intensity factor range ΔK (log scale) for the 2 C(T) specimens. The threshold stress intensity factor range, ΔK_{th}, was found to be around 4.2 MPa$\sqrt{m}$, which lies in the range of 5 MPa$\sqrt{m}$, an average value reported for steels [29]. The linear portion of the log $(\frac{da}{dN})$ − log (ΔK) plot of a long LEFM crack is fitted by Paris' equation:

$$\frac{da}{dN} = C(\Delta K)^m, \tag{7.4}$$

where m and C are material constants. The average Paris law coefficient C and exponent m were found to be around 2.27 x 10^{-11} m/(cycle. MPa$\sqrt{m}$) and 2.79, respectively.

A small amount of crack closure was observed for a ΔK of 7 MPa$\sqrt{m}$, as depicted in Fig. 7.7. The slope of the solid line represents the compliance value (slope of the linear fit of the crack opening

displacement vs. load curve) for a fully open crack during a load cycle unloading. The solid points represent the compliance values obtained from the cycle loading part. The small compliance deviation from the fully open crack compliance during the loading part is represented by the value of $U = \frac{\Delta P_{eff}}{\Delta P} = \frac{P_{max} - P_O}{P_{max} - P_{min}} = 0.9$, where P_{max} and P_{min} are the maximum and minimum load, and P_O is the opening load calculated according to the 2% compliance offset criterion in the ASTM E647 standard [19]. The U value that best characterizes our results is 0.9, a fully open crack being characterized by U = 1. The ΔK_{th} of closure free cracks could be slightly smaller than 4.2 MPa$\sqrt{m}$.

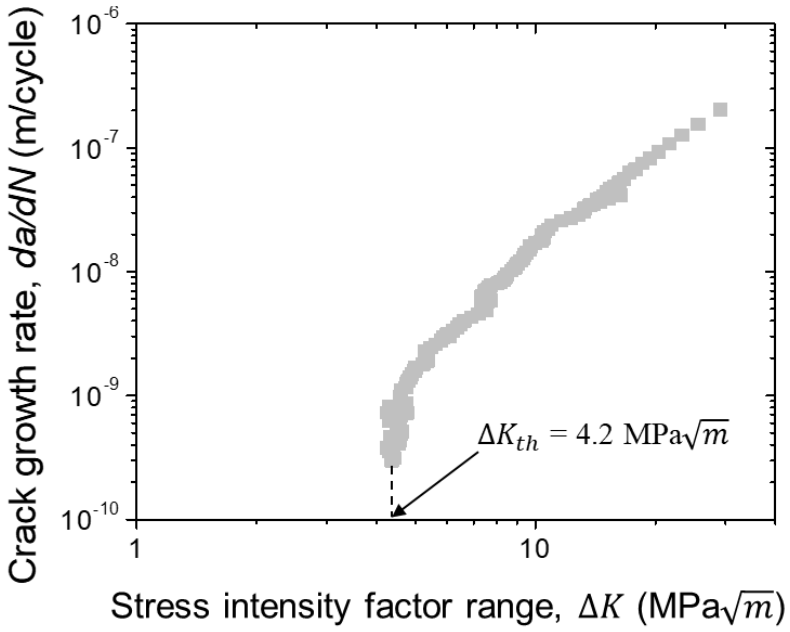

Figure 7.6 Log-log plot of crack growth rate da/dN vs. stress intensity factor range ΔK depicting the long crack propagation behavior of 300M steel C-T specimens tested at R = 0.1 (ΔK_{th} is the threshold stress intensity factor range)

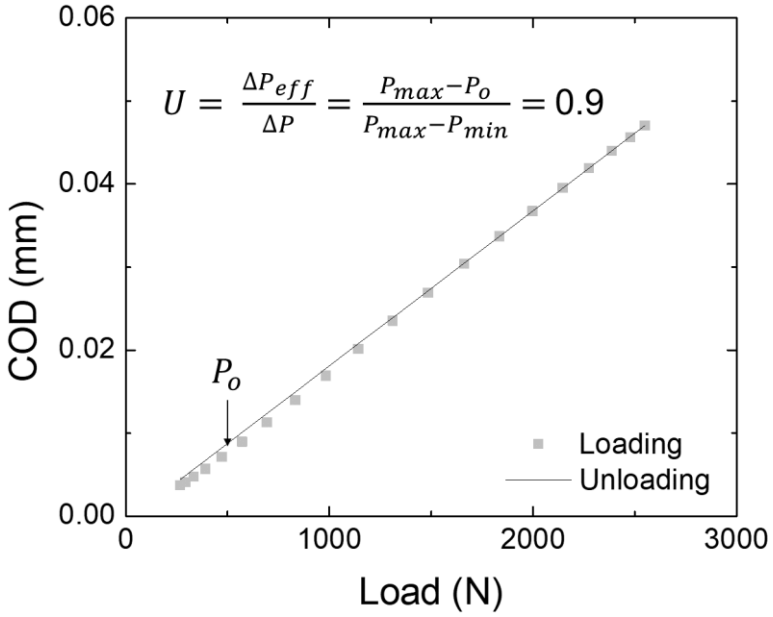

Figure 7.7 Crack opening displacement (COD) vs. load curve for the loading and unloading part of a cycle (ΔP_{eff} is the effective load range free of crack closure, ΔP is the closure affected load range, P_{max} and P_{min} are the maximum and minimum load, and P_O is the opening load estimated according to the 2% compliance offset criterion in the ASTM E647 standard). A fully open crack is characterized by U of 1. A U of 0.9 indicates a small amount of closure for the specimen tested at R = 0.1 for a ΔK of 7 MPa$\sqrt{m}$

7.4 Results analysis and discussion

7.4.1 Equivalent size and stress intensity factor range calculation for surface and interior discontinuities

Murakami [15] calculated the equivalent discontinuity size $\sqrt{area_R}$ of a periodic artificially introduced surface roughness feature (defined by the profile height R_t and profile width R_{Sm}) by equating the stress intensity factor obtained for the roughness features with the stress intensity factor for a small surface crack. The proposed equation to calculate $\sqrt{area_R}$ is given by:

$$\frac{\sqrt{area_R}}{R_{Sm}} \cong 2.97\left(\frac{R_t}{R_{Sm}}\right) - 3.51\left(\frac{R_t}{R_{Sm}}\right)^2 - 9.47\left(\frac{R_t}{R_{Sm}}\right)^3, \qquad \text{for } \frac{R_t}{R_{Sm}} < 0.195 \tag{7.5}$$

Residual stress and crack closure effects were neglected. Only the tensile part of the stress cycle was considered to account for the crack growth, and hence $\Delta K \approx K_{Imax}$ was assumed to be the

crack growth driving force, where K_{Imax} is the maximum stress intensity factor in opening mode I.

Murakami [15] computed K_{Imax} as:

$$K_{Imax} = f\sigma_{max}(\pi\sqrt{area})^{1/2}, \tag{7.6}$$

where the $\sqrt{area}$ parameter can be replaced by the critical roughness size $\sqrt{area_R}$ or inclusion size $\sqrt{area_i}$, depending on the type of discontinuity. σ_{max} is the maximum applied stress, and f is a constant that takes on the values of 0.65 for surface discontinuities (including those which are subsurface but in touch with the free surface), and 0.5 for interior discontinuities. The $area_i$ for interior inclusions is calculated by taking a smooth contour around the inclusion, as shown in Fig. 7.8a. For inclusions in touch with the surface (Fig. 7.8b), the $area_i$ parameter is considered as 1.137 times that of an interior inclusion to account for larger critically stressed region, as proposed by Murakami et al. [30, 31]. This proposition is based on the maximum stress intensity factor numerical solution characterizing irregularly shaped surface cracks obtained by Murakami and Nemat-Nasser [32].

Eqn. (7.6) suggests that, for a discontinuity of the same size, the magnitude of stress intensity factor would increase by 34% for inclusions in contact with the free surface, and therefore yield lower fatigue lives.

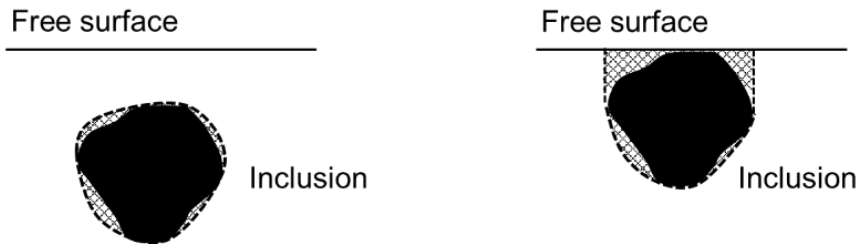

a. b.

Figure 7.8 Critically stressed area, $area_i$ (region enclosed within a smooth contour around the inclusion) for a. an interior inclusion, b. an inclusion in touch with the free surface (based on [30, 31]). Note that the $area_i$ is considered to be bigger for an inclusion in touch with the free surface than an interior inclusion of the same size

The crack growth will be favoured at the feature characterized by the highest stress intensity factor range, which will in turn govern the specimen's fatigue life. By comparing the stress intensity

factor range from surface roughness and inclusions, it should be possible to predict the critical feature from which a fatigue crack will propagate. Table 7.7 depicts the calculated values of the maximum stress intensity factor for surface roughness K_{Imax,R_t} using Eqn. (7.6), along with the maximum stress intensity factor for surface or interior inclusions $K_{Imax,i}$ observed at crack initiation sites. It should be noted that the $K_{Imax,i}$ are represented by single values for the S230-8A and CW14-8A peening conditions since crack initiation from an inclusion occurred only once in each case. For all other conditions where the inclusion-initiated failures occurred more than once, a range of $K_{Imax,i}$ values are reported. The range of inclusion sizes ($\sqrt{area_i}$) present in the material was reported as 7 to 51 µm [16].

The K_{Imax,R_t} values were calculated from an average of 3 specimens. Although no surface roughness measurement was performed on polished specimens, it is expected that the stress intensity factor characterizing roughness is much lower than that of the as-machined specimens. Therefore, a K_{Imax,R_t} value of 1.6 MPa$\sqrt{m}$ was assumed, which is half that of the as-machined specimens (3.3 MPa$\sqrt{m}$). To complete the analysis, the feature most frequently observed at the crack initiation site is reported in the last column of the table.

The results presented in Table 7.7 indicate that cracks initiated at inclusions, in general, when the $K_{Imax,i}$ was higher than the K_{Imax,R_t} and at surface roughness features when the $K_{Imax,i}$ was lower than the K_{Imax,R_t}. The only batch of specimens that makes an exception to this statement are the as-machined specimens for which 75% of the ruptures occurred from grinding marks, although its estimated K_{Imax,R_t} is small (3.3 MPa$\sqrt{m}$), when compared to its $K_{Imax,i}$. In the case of the as-machined condition, the sharpness and linearity of the grinding marks may have increased the K_{Imax,R_t}, when compared to the more uniform and round shape of dimples created by shot peening. Since the estimation of $\sqrt{area_R}$ in Eqn. 7.5 is based on uniform and periodic roughness features, it may have underestimated the actual K_{Imax,R_t} of the as-machined specimens that had non-uniform grinding marks oriented in different directions.

For specimens treated as per the S230-4A condition, most of the cracks initiated at subsurface inclusions. Table 7.7 shows that the K_{Imax,R_t} of 4.2 MPa$\sqrt{m}$ for this condition is lower than the $K_{Imax,i}$ values ranging from 4.4 to 6.3 MPa$\sqrt{m}$. This suggests that statistically, the inherent material discontinuities (inclusions) are more detrimental to fatigue life than the surface roughness

features produced by peening with S230-4A condition. It means that for S230-4A condition, there is a high probability of finding large inclusions (21-42 μm) located in the tensile residual stress region within the material that produce higher stress intensities than the smaller surface discontinuities (11.27 μm) located within the CRS region. As a consequence, higher experimental fatigue lives were obtained for the specimens where crack initiated at the surface roughness features. The inherent scatter in inclusion sizes could result in low fatigue lives, increasing the fatigue life scatter and lowering the B basis values.

For the specimens treated as per S230-8A and CW14-8A conditions, the surface discontinuities exhibit K_{Imax,R_t} values of 5.9 and 8.2 MPa$\sqrt{m}$, respectively, and only one specimen for each condition failed at a subsurface inclusion yielding a $K_{Imax,i}$ value of about 5.3 MPa$\sqrt{m}$. Considering the largest inclusion of 51 μm in the specimen subsurface [16], a $K_{Imax,i}$ of 7 MPa$\sqrt{m}$ is obtained, which is close to the high stress intensity values associated with the surface roughness features. Therefore, under these conditions, it is more probable that surface roughness discontinuities will initiate fatigue cracks rather than large inclusions located in the subsurface region. As a large number of surface roughness discontinuities are present at the material surface, a lower dispersion of the fatigue lives and highly predictable fatigue lives was obtained as quantified by a high B basis value (3.34 x 10^4 cycles) close to the average value (5.42 x 10^4 cycles) for the S230-8A condition. For specimens treated as per the CW14-8A condition, the fatigue life scatter was increased due to the presence of a single critical surface discontinuity (since all other specimens treated as per the CW14-8A condition had similar fatigue lives), which indicates a greater surface damage caused by peening with CW14-8A condition, when compared to that induced by the S230-8A condition.

The comparison of the K_{Imax} values with the material ΔK_{th} is coherent. The majority of features observed at crack initiation sites have K_{Imax} equal to, or higher than, the material ΔK_{th}. This indicates that Murakami's approach is suitable to explain the crack growth for the tested material and conditions.

Table 7.7 Maximum stress intensity factor values due to inclusions ($K_{Imax,i}$) and surface roughness (K_{Imax,R_t}) for all surface conditions calculated based on experimental results for $\sigma_{max} = 1089$ MPa

Surface condition	$K_{Imax,i}$ (MPa$\sqrt{m}$) *(calculated from inclusions at crack initiation sites)*	K_{Imax,R_t} (MPa$\sqrt{m}$) *(calculated from surface roughness profiles)*	Crack initiation site (SEM observation)
As-machined	4.5-4.8	3.3	75% Roughness
Polished	3.8-6.9	1.6	100% Inclusion
S230-4A	4.4-6.3	4.2	75% Inclusion
S230-8A	5.4	5.9	87.5% Roughness
CW14-8A	5.3	8.2	87.5% Roughness

7.4.2 Fatigue life prediction based on maximum stress intensity factor

The fatigue life characterizing the propagation of the main crack from its initial size (size of discontinuity) to its final size (based on material toughness) was considered.

The calculated stress intensity factor values (from Eqn. (7.6)) can be used to predict fatigue life based on the integration of Paris' equation (Eqn. (7.4)) from the initial discontinuity size ($\sqrt{area}$) to a final crack size a_c, estimated with the assumption of plain strain fracture toughness K_{Ic}. The number of cycles to failure N_f is then given by:

$$N_f = \frac{2\sqrt{area}}{(m-2)C\,(K_{Imax})^m}\,\left(1 - 1/\left(\frac{a_c}{\sqrt{area}}\right)^{\frac{m}{2}-1}\right) \tag{7.7}$$

Since a_c is much greater than the initial discontinuity size $\sqrt{area}$, Eqn. (7.7) can be further simplified as:

$$N_f = \frac{2\sqrt{area}}{(m-2)C\,(K_{Imax})^m} \tag{7.8}$$

The fatigue life predictions are based on 2 values of $\sqrt{area}$: i) the size of the actual surface discontinuities such as grinding mark/ peening induced roughness associated with the surface preparation process, represented by $\sqrt{area_R}$, and ii) the largest inclusion size ($\sqrt{area_i}$ = 51 μm) that can be encountered in the fatigue specimen volume according to a previous statistical analysis of inclusions by the authors [16] using metallographic samples. For inclusion-initiated failures, the fatigue life prediction also considers the location of the largest inclusion (surface or subsurface) based on the K_{Imax} calculated from Eqn. (7.6). For each surface condition, the shorter life predicted by one or the other $\sqrt{area}$ is expected to reflect the worst-case fatigue life scenario.

Fig. 7.9 illustrates the predicted fatigue life results obtained from Eqn. (7.8). The half-filled star symbols represent the minimum predicted fatigue life resulting from crack propagation from a grinding mark (GM) or a peening induced discontinuity (PD). The experimental fatigue life data (same symbols as in Fig. 7.2) for all tested surface conditions are also presented.

The predictions using $\sqrt{area_R}$ (half-filled stars) for the as-machined condition is about 2.8 x 10^4 cycles, which is twice higher than the lowest fatigue life obtained experimentally. A possible reason for the fatigue life overestimation is that the non-uniform and linear grinding marks were not appropriately characterized by Eqn. (7.5) as explained previously.

For S230-4A, S230-8A and CW14-8A surface treatments, the predictions are 3.1, 2.4 and 1.3 times lower than their experimental lowest fatigue lives for crack initiation due to surface roughness, respectively. A possible reason for this fatigue life underestimation in peened specimens could be related to the effects of CRS. The CRS were not considered when predicting crack growth. The CRS can lower the stresses acting on the surface discontinuities, thereby reducing the stress intensity factor range, which will delay or slow down short crack propagation. Such phenomenon was observed by the authors in a previous work using similar material and testing conditions [33].

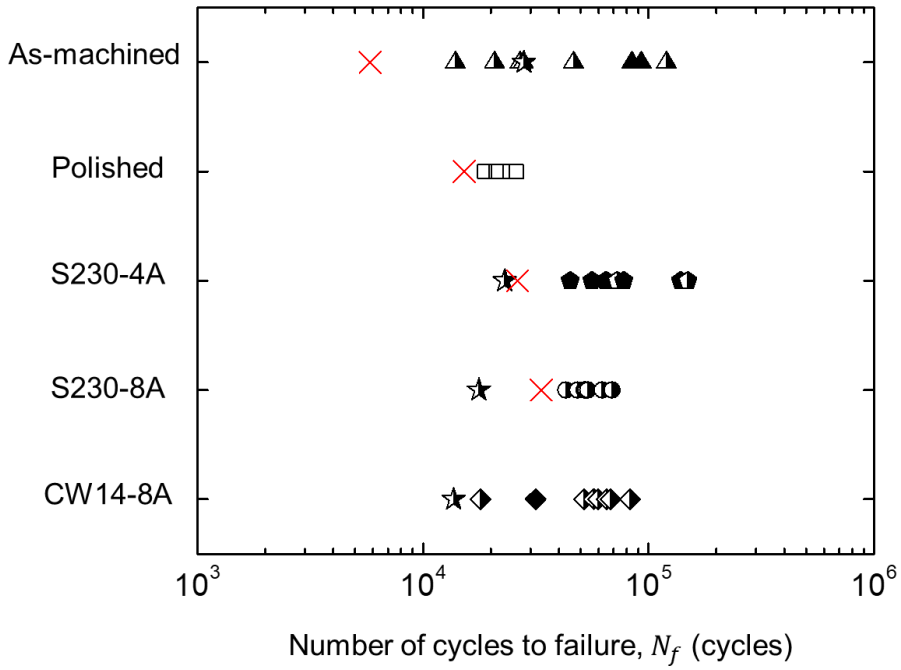

Figure 7.9 Plot showing number of cycles to failure N_f for all tested surface conditions at a 1089 MPa stress amplitude and R = -1. Half-filled symbols represent N_f for specimens where cracks initiated at surface discontinuities (GM = grinding marks, PD = peening induced discontinuities). Fully-filled and open symbols represent N_f for specimens where crack initiation occurred at subsurface and surface inclusions, respectively. Half-filled star symbols represent the fatigue life predicted using the largest surface roughness discontinuity size ($\sqrt{area_R}$). Red cross symbols represent the B-basis estimates

7.4.3 Effect of CRS on crack initiating features: surface roughness vs. inclusions

Fig. 7.10 presents the percentage of cracks that initiated at surface roughness features for all tested conditions vs. the stress intensity factor due to surface roughness K_{Imax,R_t}. The figure shows that the competition between the crack initiation features (surface or subsurface inclusions and the surface roughness discontinuities) can be understood using the $K_{Imax,i}$ range for the inclusions represented by the shaded region, and K_{Imax,R_t} values represented by the symbols.

Looking at the crack initiation for as-machined specimens in Fig. 10, which was triggered by grinding marks in 75% of the tested specimens, one should expect a higher stress intensity factor

for the surface features than the inclusions. The calculation proposed for K_{Imax,R_t} (Table 7.7) predicts the opposite: $K_{Imax,R_t} < K_{Imax,i}$. To obtain the experimentally measured lowest fatigue life of 1.4 x 10^4 cycles, the actual K_{Imax,R_t} characterizing the ground surface should be in the range of 4.2 MPa$\sqrt{m}$ according to Eqn. (7.8) which is coherent with the measured ΔK_{th} for the bulk material.

For the polished specimens, the detrimental effect of surface roughness was eliminated due to a K_{Imax,R_t} < 3.3 MPa$\sqrt{m}$. In absence of high CRS, the crack initiation site was shifted to the largest material discontinuities occurring close to the surface. It was observed that inclusions as small as 9 μm had a detrimental effect on fatigue life.

In the case of specimens peened with the S230-4A condition, only 25% of the cracks initiated from the surface. The surface roughness was characterized by a K_{Imax,R_t} of 4.2 MPa$\sqrt{m}$. Since the K_{Imax,R_t} is near the lower bound of the $K_{Imax,i}$ range, the probability of finding an inclusion with a higher $K_{Imax,i}$ than the $K_{Imax,R_t}$is higher. Nevertheless, the K_{Imax,R_t} for the S230-4A condition is similar to the true K_{Imax,R_t} predicted for the as-machined condition. This suggests that the high CRS conferred by the S230-4A condition prevents surface crack initiation and causes the crack to initiate at an internal feature instead.

For specimens peened as per S230-8A and CW14-8A conditions, 87.5% of cracks initiated at the features created by the shot impacts on the surface. The proposed K_{Imax,R_t} are in accordance with these observations. Since the K_{Imax,R_t} are close to the upper bound of the $K_{Imax,i}$ range, the probability of finding a sufficiently large inclusion with a $K_{Imax,i}$ higher than the K_{Imax,R_t} is much lower in these cases, when compared to those resulting from S230-4A condition.

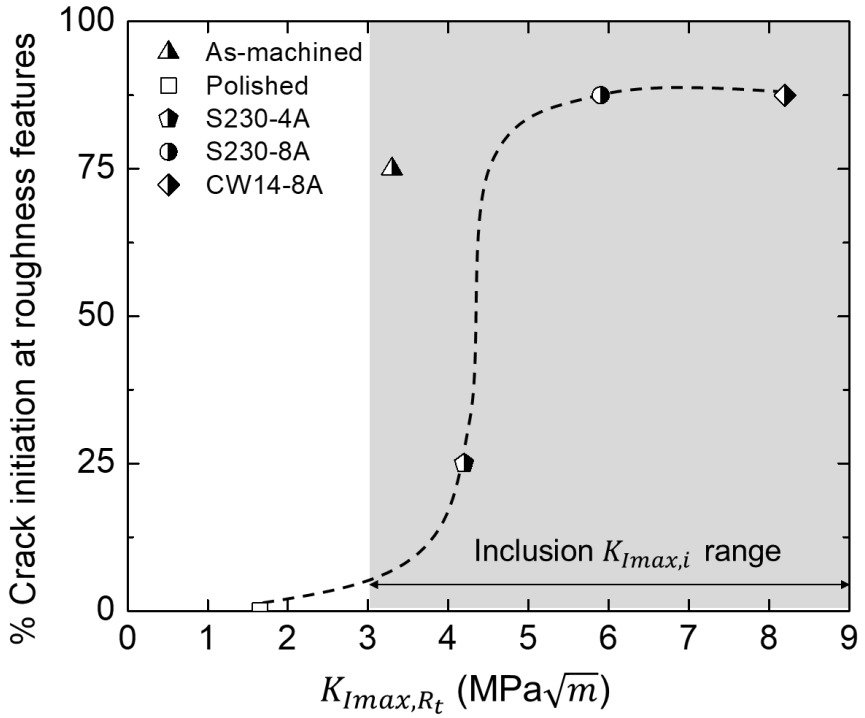

Figure 7.10 Plot showing the relationship between the stress intensity factor due to surface roughness K_{Imax,R_t} and the percentage of crack initiation occurring at roughness features for all surface conditions. The range of stress intensity factors for inclusions in the material is depicted by $K_{Imax,i}$ (shaded region). The % of crack initiation at roughness features decreases when K_{Imax,R_t} is lower than, or close to, the lower bound of $K_{Imax,i}$ range and vice-versa. The dotted line has been added to ease the understanding of the demonstrated trend

7.4.4 Analytical vs. experimental fatigue lives for surface roughness and inclusion-initiated failures

Fig. 7.11 depicts the analytically predicted fatigue lives for individual cases of surface roughness and inclusion-initiated failures obtained for each surface condition using Eqn. (7.8) vs. the corresponding experimental fatigue lives. The diagonal line in the figure represents a predicted to experimental fatigue life ratio of 1. For surface roughness-initiated failures, the predicted fatigue lives are based on the average roughness parameter R_t for each surface condition reported in Table 7.3.

For surface roughness-initiated failures, the predicted fatigue life to experimental fatigue life ratio in the case of the as-machined specimens varies from 0.2-2, which reflects the fact that the model is not suitable to predict the fatigue life of as-machined specimens.

For all the shot peened specimens with surface roughness-initiated failures, the experimental fatigue lives are higher than the corresponding predicted fatigue lives indicating the beneficial effect of peening induced CRS on short crack propagation. S230-4A condition shows the maximum benefit followed by the S230-8A and the CW14-8A conditions.

In the case of inclusion-initiated failures, based on the assumption that the CRS affect only crack initiation, the maximum fatigue life improvement should be a factor of 2 (ratio of the surface to subsurface intrinsic fatigue life prediction). Interestingly, the polished specimens and the specimen peened using CW14-8A condition lie on the diagonal line, showing that the fatigue behavior of these conditions can be properly explained by long crack propagation. For as-machined, S230-4A and S230-8A conditions, the experimental fatigue lives are higher than the predicted ones, by a factor of ~2. The analytical model assumes the internal inclusion of 51 μm to be an existing crack and calculates the fatigue life spent in its propagation. On calculating the initial crack size that would yield the experimental fatigue lives obtained for the as-machined, S230-4A and S230-8A conditions, it is found that the initial crack size should be 3 to 21 times smaller than the actual size of the inclusion. The initial discontinuity sizes that could account for these high fatigue lives are in the range of 1 to 13 um, sizes that are too small to be accurately described by LEFM. The fatigue results suggest that some crack nucleation mechanisms are active at the early stage of fatigue to generate local irreversible structural changes that results in a long enough crack for propagation described by Paris' law.

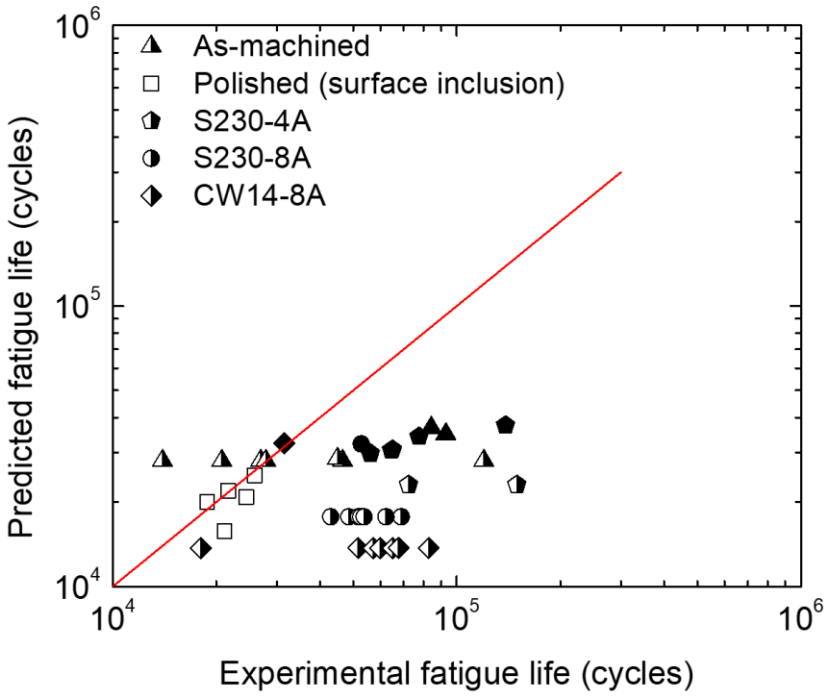

Figure 7.11 Analytically predicted fatigue life vs. experimental fatigue life for surface roughness-initiated and inclusion-initiated failures for each surface condition. The half filled, open and filled symbols represent crack initiation from surface roughness features, surface inclusions and subsurface inclusions, respectively. The diagonal line depicts a predicted to experimental fatigue life ratio of 1

7.4.5 Effect of CRS and roughness on fatigue life

Fig. 7.12 summarizes the combined effect of CRS and roughness on fatigue life. In this figure, the process conditions (ordinate axis) are ordered by increasing roughness (R_t) and surface CRS (σ_s). The dashed and the solid lines correspond to the number of cycles for crack propagation from a 51 μm inclusion located at the specimen surface and interior, respectively. Both predictions are for residual stress-free and smooth specimens and were obtained by applying Eqns. (7.6) and (7.8). The symbols are the shortest fatigue lives experimentally obtained for each tested surface condition. For the S230-4A condition, the lowest fatigue life caused by a surface roughness feature (half-filled) is also depicted, for comparison with other peening conditions where the majority of the cracks initiated at similar surface discontinuities.

Fig. 7.12 shows that, for polished specimens with low CRS of -341 MPa and an $R_t < 2.4$ µm, crack initiation is favoured at surface inclusions. The lowest experimental fatigue life (1.9 x 10^4 cycles)

was obtained for a 15 µm surface inclusion. The lowest possible fatigue life for the polished condition would correspond to the fatigue life obtained for crack initiating from a 51 μm surface inclusion given by the dashed line.

For as-machined specimens with slightly higher surface CRS than the polished specimens and a $R_t \geq 2.4$ µm, the crack initiation site occurred systematically at grinding marks, with some samples reaching fatigue lives significantly higher than that for the polished samples (about 5 times higher). The compressive region of the residual stress of 24 µm (as shown in Fig. 7.3) seems to be sufficiently deep to neutralise the role of surface inclusions in the crack initiation process. It is interesting to observe that the lowest experimental fatigue life for this condition (1.4 x 10^4 cycles) is close to the dashed line in Fig. 7.12, indicating that the grinding mark in this sample is a discontinuity comparable in size to the largest possible inclusion expected in this material (51 µm).

For the S230-4A condition, the surface CRS is expected to have a similar magnitude as that of the other two peening conditions. This is because the surface CRS magnitude is usually dependent on the target material's mechanical properties and hardness, and is independent of the shot peening conditions, as observed in the experimental study by Miao et al. [34]. Therefore, an average value of -1065 MPa is depicted in Fig. 7.12. When looking at the lowest experimental fatigue life in a specimen peened with the S230-4A condition, it is observed that the shot peened surface roughness is less detrimental to fatigue life than subsurface inclusions (continuous line). The effect of CRS on the crack initiation phenomenon can be seen by comparing the experimental minimum fatigue life obtained for surface crack initiation (7.3 x 10^4 cycles) and the predicted fatigue life for equivalent surface roughness discontinuity (2.3 x 10^4 cycles).

Fig. 7.12 shows that, for the S230-8A condition, a high R_t of 7.8 µm leads to systematic crack initiations at surface roughness features with very reproducible results, resulting in the highest B basis values for the condition. The experimentally obtained minimum fatigue life (4.3 x 10^4 cycles) for the S230-8A condition is comparable to the lowest life resulting from the S230-4A condition, although the crack initiated at a subsurface inclusion in the latter case. Although the range of fatigue lives are similar for the specimens peened with S230-4A and S230-8A conditions (due to similar K_{Imax} values for inclusions and peening induced surface discontinuities), the S230-8A condition shows the best statistical behavior due to its systematic crack initiation features.

Nevertheless, when comparing minimum fatigue life (4.3 x 104 cycles) for the S230-8A condition with the minimum fatigue life obtained for crack initiation triggered by surface discontinuities (half-filled symbol in Fig. 7.12) resulting from the S230-4A condition (7.3 x 10^4 cycles), the fatigue life is found to be twice lower. This can be attributed to the higher roughness associated to the S230-8A condition, as compared to the S230-4A condition. This indicates that the CRS is not sufficient to counter the stress intensification caused by the surface roughness features in case of the S230-8A condition and therefore, results in surface crack initiation.

The still higher R_t of 15.5 µm produced by peening with CW14 shot at 8A leads to the lowest minimum fatigue life (1.8 x 10^4 cycles), when compared to those obtained for the other 2 peening conditions. The debit in fatigue life due to the detrimental effect of surface roughness for the CW14-8A condition is depicted by the shaded region with a '−' sign in Fig. 7.12.

Recent work by Klotz et al. [35] on Inconel718 Ni superalloy peened with S230-4A, CW14-4A and CW14-8A conditions subjected to low cycle axial fatigue at R= 0.1, showed that the S230-4A condition yielded the highest average fatigue life. The fatigue crack initiation for the specimens peened with S230-4A condition was pushed to interior material discontinuities such as large grains due to the beneficial effect of CRS (σ_s = -859 MPa) and surface cold work, despite the associated surface roughness (R_t = 8.65 µm). This is similar to the observation made for the S230-4A condition in this work, where cracks initiated mostly at internal inclusions.

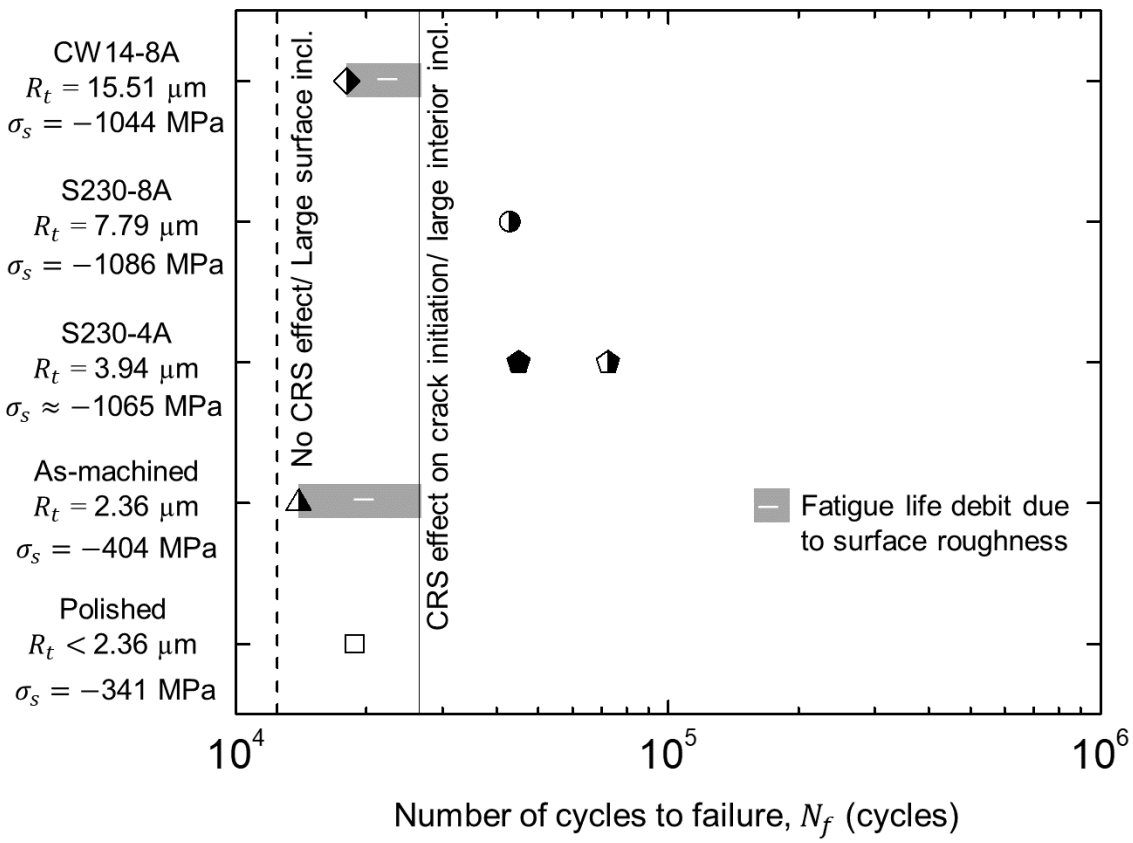

Figure 7.12 Plot depicting the combined effect of CRS (σ_s) and roughness (R_t) presented in the ordinate axis on the fatigue life of the conditions presented in the abscissa. The dashed and solid vertical lines represent the analytically predicted fatigue lives for surface and subsurface crack initiation at the largest inclusion size of 51 μm predicted to be present in the material (without incorporating CRS effect). These two lines depict the minimum fatigue life for smooth and rough residual stress free specimens, respectively. The symbols represent the experimentally observed lowest fatigue lives for crack initiation at surface inclusions (open), surface roughness features (half-filled) or interior inclusions (filled)

Choice of the best peening condition for fatigue life improvement

In the case of the given material and testing conditions, S230-4A and S230-8A conditions produce higher fatigue lives than the CW14-8A condition in terms of both B-basis and analytical fatigue life predictions. The S230-8A condition has a B-basis which is 1.3 times that of the S230-4A condition, mainly due to the lower fatigue life scatter of the former. This lower scatter results is explained by the specimens peened using the S230-8A condition present regular surface roughness

features that cause a smaller dispersion and hence a higher B-basis. The equivalent discontinuity size associated with the surface roughness of the S230-8A condition is actually of the same order as the largest possible internal discontinuity expected to be present in the material (51 μm). On the other hand, the S230-4A condition is governed by two crack initiating features, related to the maximum subsurface inclusion sizes and relatively small surface roughness features. The lower B-basis of the S230-4A condition is then related to the specimens with higher fatigue lives due to the absence of specific severe surface discontinuities, resulting in specimens surviving high number of cycles when no large inclusion is present.

The minimum experimental fatigue lives and B-basis values for both the S230-4A and S230-8A conditions are higher than the analytically predicted fatigue life due to failure triggered by the largest inclusion, and the only way to improve the fatigue behavior for these conditions is to improve the material cleanliness. More specifically, the S230-4A condition is the only present peening process that is sufficiently severe to prevent initiation from surface inclusion while generating surface discontinuities with equivalent sizes smaller than the largest possible inclusion found in the material. Hence, it can be said that the S230-4A condition represents the optimal trade-off between the detrimental effect related to increased surface roughness and the beneficial effect of CRS on the material's fatigue life. For this peening condition, the minimum fatigue life can be calculated using the analytical model based on stress intensity factor considering the largest possible internal discontinuity of 51 μm expected to be present in the material (2.65×10^4 cycles).

7.5 Conclusions

The effect of peening on the axial fatigue life of 300M steel for R = -1, at a stress amplitude of 1089 MPa (64% of $\sigma_{y,0.2}$) was studied. Surface roughness, residual stress and fractography analyses were performed. Statistical analysis to estimate the lowest fatigue life expected from a sample population (B-basis) was performed. In addition, worst case fatigue lives were predicted for each surface condition using the stress intensity factor calculated with the estimated size of the largest crack-initiating discontinuity. The following conclusions can be drawn:

- Shot peening or machining induced compressive residual stresses can be sufficiently high to prevent crack initiation at small surface inclusions, thereby increasing fatigue life.

- For peening conditions with lower roughness (S230-4A), the CRS was able to prevent surface crack initiation and caused subsurface crack initiation at inclusions. For peening conditions with higher roughness and similar CRS (S230-8A and CW14-8A), although surface crack initiation was prevalent, the CRS was able to delay short crack propagation to yield higher fatigue lives than the unpeened conditions.
- Under the given loading conditions (N_f < 2 x 10^5 cycles), the peening induced surface CRS undergo only ~22% relaxation in magnitude while the depth of CRS remains constant at ~150 μm.
- An analytical model based on Murakami's equations for maximum stress intensity factor and LEFM was used to predict the minimum fatigue lives for the tested conditions. For inclusion-initiated failures, the inclusion's location (surface or subsurface) was considered by Murakami's equation. The model did not account for the effect of CRS on short crack propagation, but the comparison between calculations and experimental results allows this effect to be quantified. The experimental fatigue lives of the shot peened specimens initiating at surface discontinuities are systematically about 3 times higher than those predicted by the model. In the case of subsurface inclusion-initiated failures, the model systematically underestimates the experimental fatigue lives by a factor of about 2; suggesting that other mechanisms have to be taken into consideration at the early stage of crack propagation.
- The competition between the crack initiation features (subsurface or surface inclusions and the surface roughness discontinuities) can be understood using the stress intensity factors characterizing the features. When K_{Imax,R_t} for surface roughness is near the lower bound of the $K_{Imax,i}$ range for inclusions, the crack is more likely to initiate at an inclusion due to probability. Similarly, when K_{Imax,R_t} is near the upper bound of the $K_{Imax,i}$ range, the crack is more likely to initiate at a surface roughness feature.
- Based on B-basis results, S230-8A is the best peening condition, however relying solely on B-basis can be misleading. The reason for high B-basis values obtained for the S230-8A condition is attributed to the surface roughness features with regular topography which act as crack initiating sites, reducing the fatigue life dispersion.

7.6 Acknowledgements

This work was financially supported by the Consortium of Research and Innovation in Aerospace Québec (CRIAQ), the Natural Sciences and Engineering Research Council of Canada (NSERC), Pratt & Whitney Canada, Bell Helicopter Textron Canada, L3-Communications MAS, Héroux Devtek and the Mathematics of Information Technology and Complex Systems (MITACS) (Grant No.: RDC 435539-12).

7.7 Additional results- Strain-controlled fatigue, FWHM and microhardness & statistical analysis of fatigue life data

This section summarizes the results of the strain-controlled fatigue tests, FWHM profiles and the microhardness profiles that were obtained experimentally as part of the study. The statistical analysis of the stress-controlled fatigue life data at the stress amplitudes of 931 MPa and 1089 MPa based on a survival of 99%, at 95% confidence interval using Minitab software is also presented.

As discussed in Section 2.4.4, CRS relaxation in shot peened specimens is affected by local plasticity, the material cyclic behaviour, applied strain amplitude, load level and degree of cold working. Therefore, strain-controlled axial fatigue tests were conducted to understand the cyclic yield behavior of 300M steel. Moreover, it was discussed that residual stresses can be considered equivalent to mean stresses. Hence, mean stress relaxation occurring during the strain-controlled fatigue tests was correlated to the residual stress relaxation and the material's local deformation behaviour during peening. The evolution of the degree of cold work and its relation to the CRS relaxation was studied by analysing the FWHM vs depth profiles. Microhardness vs. depth profiles were also obtained to find a correlation between the material local yield state (reflected by microhardness) and degree of cold work (reflected by FWHM).

7.7.1 Strain-controlled axial fatigue test results

Fig. 7.13 a depicts the true stress ($\Delta\sigma/2$) vs true strain ($\Delta\varepsilon/2$) plot constructed using the stabilized cyclic stress amplitudes at each of the 6 tested strain amplitudes, along with monotonic tensile test curve. The cyclic stress-strain curve lies below the monotonic curve, which means that the material undergoes cyclic softening. The softening is well observed in Fig. 7.13 b, displayed by the progressive narrowing of the hysteresis loops for the specimen subjected to a cyclic strain amplitude of 0.1%. The 0.2% offset cyclic yield strength is estimated to be 1377 MPa for a strain amplitude $\Delta\varepsilon/2$ of 0.0094. The cyclic elastic limit is 570 MPa for a strain amplitude of 0.003. From Fig. 7.13, the corresponding strain amplitudes for applied stress amplitudes of 931MPa and 1089 MPa are 0.0051 and 0.0062, respectively, and lie below the 0.2% offset cyclic yield strain. Fig. 7.14 displays the true stress ($\Delta\sigma/2$) vs true plastic strain amplitude ($\Delta\varepsilon_p/2$) plot. The solid line represents the relation $\Delta\sigma/2 = K'\left(\Delta\varepsilon_p/2\right)^n$, where K' and n are the strain hardening coefficient

and strain hardening exponent, respectively. The calculated plastic strain amplitudes at 931 MPa and 1089 MPa are about 0.0001 and 0.0005 respectively.

In in Fig. 7.13 b, the downward shift of the hysteresis loops due to fatigue loading is caused by the combined effect of softening and mean stress relaxation. Mean stress relaxation is observed for all tested strain amplitudes, as shown in Fig. 7.14. As expected, the degree of mean stress relaxation increases with an increase in strain amplitude. Irrespective of the strain amplitude, most of the relaxation occurs during the first cycle. For lower strain amplitudes (0.003 to 0.007), the mean stresses gradually decrease within the first 200 cycles to reach a stabilized value and remain unchanged until failure. For the specimen tested at a strain amplitude of 0.008, the mean stresses decrease during the first 300 cycles, then increase gradually before stabilizing at around 600 cycles. The behaviour of this particular specimen however could not be explained. For the specimen tested at a strain amplitude of 0.01, the mean stresses do not stabilize and continue to relax until failure.

Residual stresses can be considered equivalent to mean stresses, as discussed in Section 2.4.4. Therefore, based on the mean stress relaxation trends for low strain amplitudes of 0.005 and 0.007, it can be expected that the residual stresses will relax by about 50% within 1 cycle, and reach a stabilized value within 200 cycles. Hence, residual stress relaxation tests were performed at 1 cycle, 200 cycles and 80% fatigue life for the axial fatigue testing at 931 MPa and 1089 MPa.

Fig. 7.15 shows that the extent of mean stress relaxation is only about 1% at $\Delta\varepsilon/2$= 0.003, 26% at $\Delta\varepsilon/2$= 0.004, 30% at $\Delta\varepsilon/2$= 0.007, 52% at $\Delta\varepsilon/2$= 0.008, 58% at $\Delta\varepsilon/2$= 0.01.

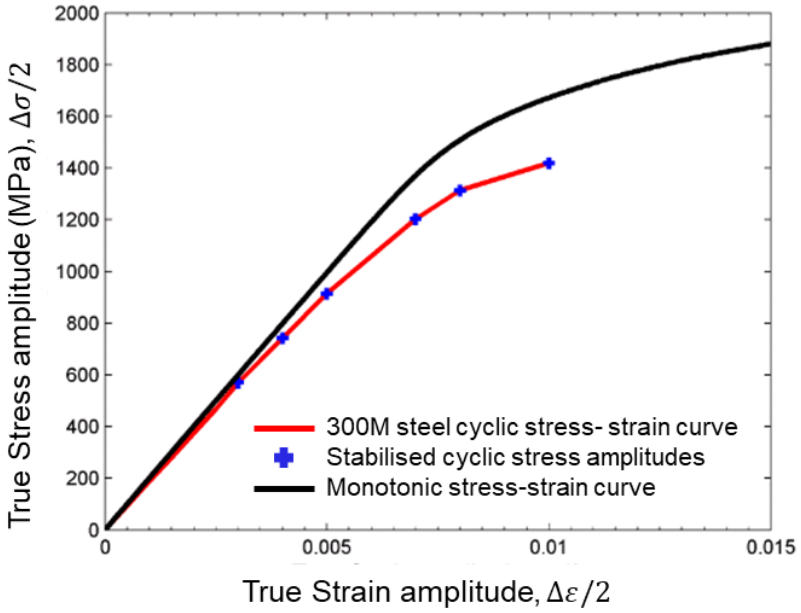

a.

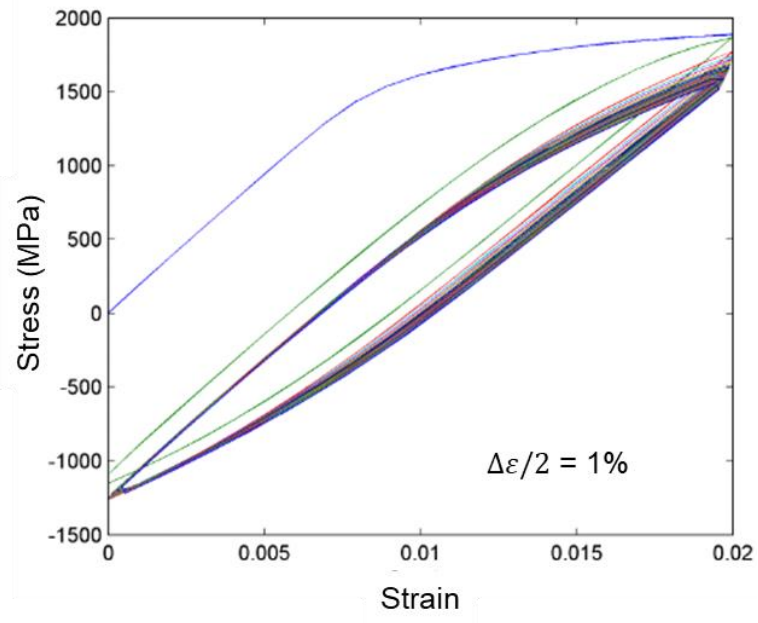

b.

Figure 7.13 a. Cyclic and monotonic stress strain curves for the studied 300M steel ('+' symbols depict the stabilized cyclic stresses obtained for each tested strain amplitude), b. Hysteresis loops for strain-controlled fatigue testing at strain amplitude of 0.01 (The progressive downward shift of the loops is due to mean stress relaxation while the narrowing of the loops is due to cyclic softening)

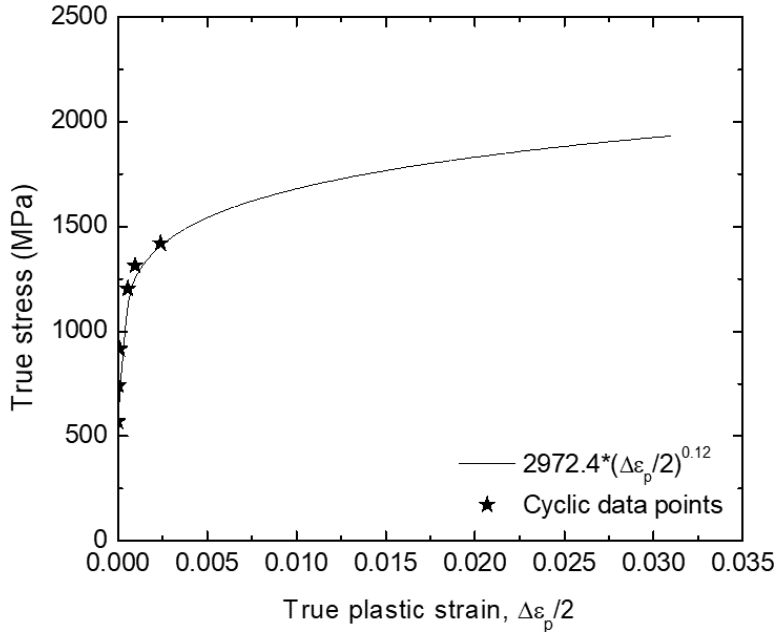

Figure 7.14 True stress vs. true plastic strain amplitude curve (The solid line represents the relation $\Delta\sigma/2 = K'\left(\Delta\varepsilon_p/2\right)^n$, where K' and n are the strain hardening coefficient and strain hardening exponent, respectively. The stars represent the experimental data points)

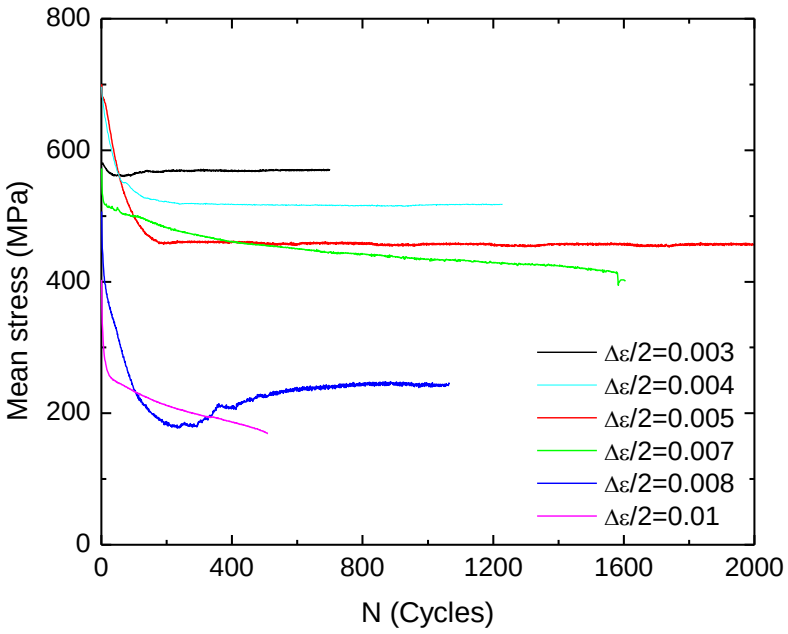

Figure 7.15 Mean stress vs. number of cycles (N) plot for all tested strain amplitudes (Maximum mean stress relaxation occurs during the first fatigue cycle; mean stresses gradually decrease and stabilize after 200 cycles for all stress amplitudes except at higher strain amplitudes of 0.008 and 0.01)

7.7.2 Full width half maximum (FWHM) and microhardness test results

Fig. 7.16 a illustrates the FWHM vs depth plots for the as-machined, polished, and specimens treated as per the S230-8A and CW14-8A conditions, prior to fatigue testing (0 cycle). Figs. 7.16 b and c depict the FWHM vs depth plots for the specimens treated as per the S230-8A and CW14-8A conditions subjected to interrupted axial fatigue at stress amplitudes of 931 MPa and 1089 MPa, respectively.

The figures show that the FWHM vs depth plots resemble the corresponding CRS vs depth curves (Figs. 6.5 and 7.3). The FWHM values are lower at the surface for both peened and unpeened specimens than in the bulk. For unpeened specimens, the values recover within the first 20 µm (equivalent to the size of 1 grain) to about 6 degrees, which is representative of the bulk material FWHM value. For the peened specimens, the FWHM decreases to a minimum at a depth of around 50 µm prior to fatigue tests (0 fatigue cycle). The values finally stabilize at a depth of around 150 µm (the depth at which the CRS become zero). Negligible changes are observed when the peened specimens are subjected to fatigue loading at the two stress amplitudes, as shown in Figs. 7.16 b and c. The lower value of FWHM at the surface is supported by the fact that the 300M steel undergoes cyclic softening under strain-controlled fatigue conditions which may be applicable to locally plasticized areas at the material surface resulting from high peening-induced deformation. This may also be one of the factors responsible for the relaxation of CRS observed during fatigue loading. It is expected that with lower shot peening intensity such as 4A, the effect of cyclic softening could be diminished due to reduced local plastic deformation.

Microhardness vs. depth profiles obtained for peened and unpeened specimens are presented in Fig 7.17. The unpeened specimens show an average microhardness value of about 580HV. A high standard deviation (±20HV) is observed for both untested and fractured ($\sigma_a = 931$ MPa, $N_f = 6.53$ x 10^4 cycles) specimens treated as per the CW14-8A condition and no clear conclusion can be drawn from the results. For the specimens treated as per the S230-8A condition, the standard deviation is smaller (±5HV). The specimen treated as per the S230-8A condition prior to fatigue test exhibits an average microhardness of 600HV, up to 200 µm, that gradually decreases to the base value of 580HV. The fractured specimen treated as per the S230-8A condition (σ_a =1089 MPa, $N_f = 2.71$ x 10^4 cycles) however, shows similar microhardness as that of the unpeened untested specimen. This may indicate the role of residual stresses in influencing the microhardness

measurements, leading to slightly lower values as the stresses relax during fatigue loading. It should be noted that near surface measurements could not be performed as the indent had a diagonal size of around 40 µm.

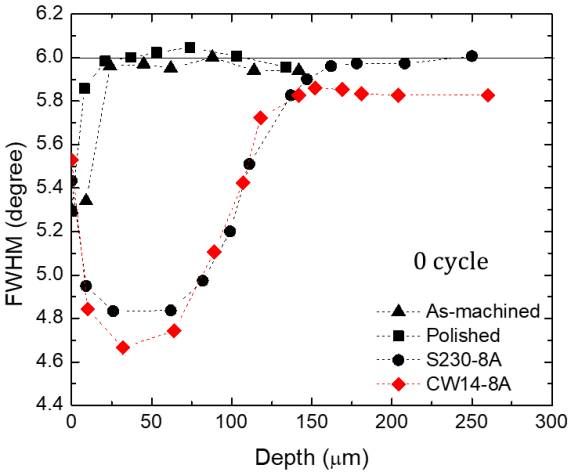

a.

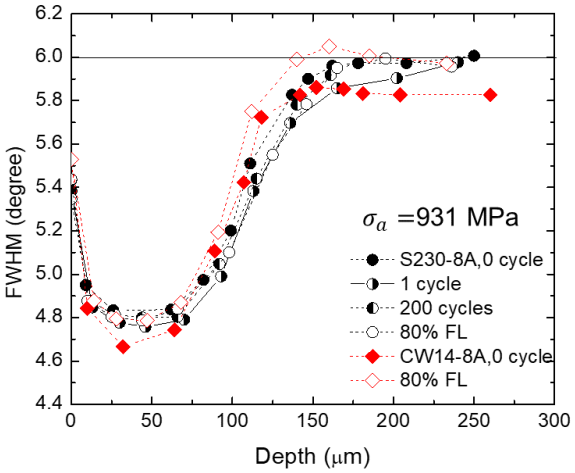

b.

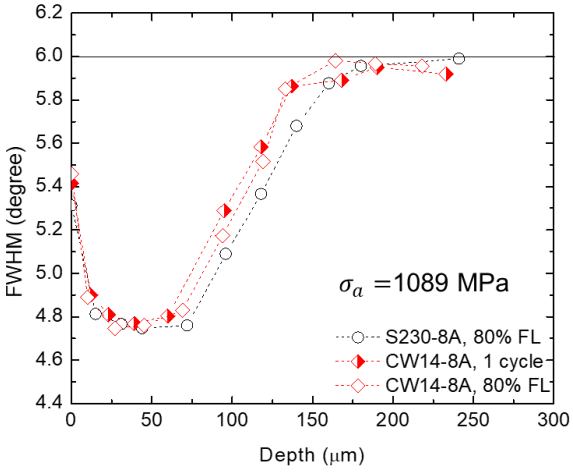

c.

Figure 7.16 FWHM vs. depth profiles for a. all surface conditions prior to fatigue loading (0 cycle), b. specimens treated as per the S230-8A and CW14-8A conditions subjected to a fatigue stress amplitude of 931 MPa for various number of applied stress controlled fatigue tests. (0 cycle, 1 cycle, 200 cycles, 80% fatigue life), c. specimens treated as per the S230-8A and CW14-8A conditions subjected to a fatigue stress amplitude of 931 MPa after 1 cycle and 80% fatigue life. The lower value of FWHM at the surface than in the bulk material indicates process-induced strain softening. No significant change in FWHM was observed as a result of fatigue loading at 931 MPa and 1089 MPa

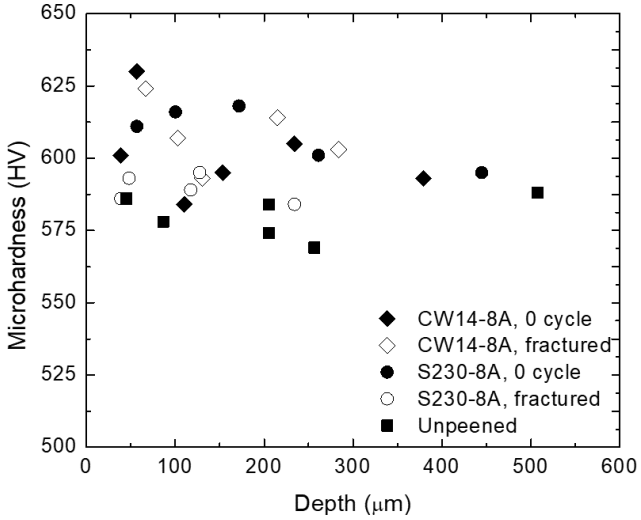

Figure 7.17 Microhardness vs. depth profiles for an unpeened untested specimen, and specimens treated as per the S230-8A and CW14-8A conditions prior to fatigue testing (0 cycle) and after fracture

7.7.3 Statistical analysis (Minitab) results

Tables 7.8 and 7.9 show the statistical analysis results for comparing the 99% survival fatigue life at 95 % confidence interval of the unpeened and peened cylindrical fatigue specimens subjected to axial fatigue (R= -1). Only Weibull and lognormal distributions were used to characterise the fatigue lives as they are more commonly used for steels in aerospace companies. The Anderson - Darling goodness of fit coefficient is represented as $AD*$ instead of the (h, p) values in Minitab as it is adjusted to handle censored (or runout) data and different plot-point methods (apart from the traditional Kaplan-Meier method). The lower the value of $AD*$, the better is the fit. For the specimen treated as per the CW14-8A condition, the analysis was performed both by censoring (considering the fatigue life of the runout specimen as an upper limit for the data) and un-censoring (considering the runout specimen fatigue life as just another failure data) the fatigue life data to compare the results.

Table 7.8 shows that the Weibull distribution provides a better fit to the unpeened specimens' fatigue life tested for a maximum stress of 931 MPa, while the lognormal distribution better represents the peened specimens' fatigue life data. The specimen treated as per the CW14-8A condition exhibits the highest 99% survival life. It is also observed that censoring the fatigue life data of the specimens treated as per the CW14-8A condition yields a lower survival life than the

uncensored approach due to the absence of a defined upper limit in the case of the latter. The next highest survival life is given by the as-machined specimens (6.83 x 10^4 cycles) closely followed by the specimens treated as per the S230-8A condition (6.45 x 10^4 cycles). Next comes the specimens treated as per the S230-4A condition (2.94 x 10^4 cycles) and finally, the polished specimens (2.55 x 10^4 cycles). The trend is the same as that observed for the 90% survival life at 95% confidence interval using GEV and Weibull distributions.

Table 7.9 shows that, except for the specimens peened using the CW14-8A condition, for all other specimens (peened and unpeened), the fatigue data follow the lognormal distribution. The highest 99% survival life at 95% confidence interval is obtained for the specimens treated as per the S230-8A condition (3.92 x 10^4 cycles), followed by the S230-4A (3.08 x 10^4 cycles), polished (1.71 x 10^4 cycles), CW14-8A (1.47 x 10^4 cycles) and finally the as-machined conditions (0.76 x 10^4 cycles). The obtained trend is very similar to that obtained using the B-basis analysis. The only difference is that, choosing the Weibull distribution over GEV for the specimens treated as per the CW14-8A condition, leads to a higher 99% survival life for these specimens when compared to the as-machined specimens. In this regard, more fatigue data should be generated and used for the statistical analysis to determine the most suitable distribution and thereafter draw conclusions regarding the best surface condition with respect to fatigue life. The need for a larger data input is also supported by the fact that the 99% survival life at 95% confidence interval is higher than the B-basis values (the lower 95% confidence limit on the 90% survival life). This is due to the high standard deviation resulting from the small number of tested fatigue specimens.

Table 7.8 Details of axial fatigue results (931 MPa, R = -1) statistical analysis showing average fatigue life, best fit distribution for the data, Anderson Darling test coefficient ($AD*$), maximum likelihood estimates of fitting parameters and 99% survival life at 95% Confidence Interval (CI)

Surface condition	Average N_f (x 10^5 cycles)	Best fit distribution	$AD*$	Fitting parameters (MLE)			99% Survival life at 95% CI (x 10^4 cycles)
				k	μ	σ	
As-machined	6.18	Lognormal	2.628	--	13.14	13.14	9.88
		Weibull	2.534	1.98	--	6.95 x 10^5	**6.83**
Polished	5.42	Lognormal	2.755	--	12.83	1.20	3.03
		Weibull	2.640	1.47	--	5.91 x 10^5	**2.55**
S230-4A	10.2	**Lognormal**	2.416	--	12.94	1.22	**2.94**
		Weibull	2.467	0.73	--	7.87 x 10^5	0.15
S230-8A	7.89	**Lognormal**	1.650	--	13.11	0.93	**6.45**
		Weibull	1.863	1.01	--	7.93 x 10^5	0.83
CW14-8A (uncensored)	5.55	**Lognormal**	2.729	--	12.92	0.71	**8.83**
		Weibull	2.770	1.20	--	5.98 x 10^5	0.13
CW14-8A (censored)	5.55	**Lognormal**	8.410	--	12.92	0.71	**7.23**
		Weibull	8.571	1.20	--	5.98 x 10^5	0.76

Table 7.9 Details for axial fatigue results (1089 MPa, R = -1) statistical analysis showing average fatigue life, best fit distribution for the data, Anderson Darling test coefficient (AD^*), maximum likelihood estimates of fitting parameters and 99% survival life at 95% Confidence Interval (CI)

Surface condition	Average N_f (x 10^4 cycles)	Best fit distribution	AD^*	Fitting parameters (MLE)			99% Survival at 95% CI (x 10^4 cycles)
				k	μ	σ	
As-machined	5.42	**Lognormal**	1.822	--	10.64	0.78	**0.76**
		Weibull	1.839	1.52	--	6.05 x 10^4	0.30
Polished	2.24	**Lognormal**	2.497	--	10.01	0.13	**1.71**
		Weibull	2.500	10.10	--	2.35 x 10^4	1.49
S230-4A	8.36	**Lognormal**	1.990	--	11.25	0.42	**3.08**
		Weibull	2.101	2.48	--	9.48 x 10^4	1.48
S230-8A	5.42	**Lognormal**	1.872	--	10.89	0.14	**3.92**
		Weibull	1.984	7.28	--	5.76 x 10^4	3.06
CW14-8A	5.42	Lognormal	2.060	--	10.81	0.5	1.68
		Weibull	1.843	3.25	--	6.06 x 10^4	**1.47**

CHAPTER 8 ARTICLE 3: EFFECT OF SHOT PEENING ON SHORT CRACK PROPAGATION IN 300M STEEL

Amrita Bag[a], Martin Lévesque[a], Myriam Brochu[a]

[a] Département de génie mécanique, École Polytechnique de Montréal, QC H3T 1J4, Montréal, Canada

[b] Département de génie mécanique, École de technologie supérieure, QC H3C 1K3, Montréal, Canada

Article submitted to the International Journal of Fatigue on 19th May 2019.

Keywords: short crack, long crack, crack propagation, shot peening, fatigue, high strength steel, 300M steel

Abstract: The short crack growth behaviour of high strength martensitic 300M steel was studied for as-machined, polished and 2 peening conditions subjected to axial fatigue at both high (64% of 0.2% offset yield strength $\sigma_{y,0.2}$) and low (55% of $\sigma_{y,0.2}$) stress amplitudes at a stress ratio R = -1. It was observed that prior austenite grain boundaries acted as barriers to short crack propagation in peened specimens within the peening induced compressive residual stress layer, causing crack decelerations within the first 6 grains. Using the $da/dN - \Delta K$ trend of the short cracks, fatigue lives of the peened specimens were predicted at both the stress amplitudes. These analytical predictions (which reflect the effect of microstructure and compressive residual stresses) were within 15% of the experimental fatigue lives.

8.1 Introduction

Shot peening is a cold working treatment where high velocity spherical particles, called shots, bombard ductile metallic surfaces. The process induces near surface compressive residual stresses (CRS) and strain hardening. Both the peening induced CRS and strain hardening are responsible for delaying the initiation and hindering the propagation of short surface cracks (< 0.5-1 mm).

Typically, short cracks grow at a faster rate than the long Linear Elastic Fracture Mechanics (LEFM) cracks at the same stress intensity factor range, ΔK, which has often been attributed to the negligible crack closure effect in short cracks [33, 50]. These short cracks are characterised by low crack-size to -plastic-zone-size ratios and their crack tip plastic zones are blocked by microstructural features, such as grain boundaries, inclusions, precipitates etc. As the crack-size to -plastic-zone-size ratio increases, the cracks encompass grains more easily and the effect of

microstructure on the short crack growth rate diminishes. Gradually, the crack size (a) becomes sufficiently large to satisfy the small scale yielding criterion (a > 25 times the crack tip plastic zone size r_p) after traversing about 10 grains [33] and behaves according to LEFM principles. The stable crack growth region of a LEFM crack is then represented by the well-known Paris' equation [53] as:

$$\frac{da}{dN} = C(\Delta K)^m, \tag{8.1}$$

where $\frac{da}{dN}$ is the long crack propagation rate and m and C are material- and loading-condition dependent constants.

Prior-austenite grain boundaries can act as barriers to short crack propagation in AISI4340 steel by constraining the crack tip plastic zone, until the stress concentration at the barrier reaches a critical value to induce plasticity in the next grain [46]. Peening induced CRS, usually extending upto a few hundred micrometers, delay this phenomenon by lowering the local stress ratio near the crack tip. This situation hinders short crack propagation, thus lowering their growth rates. Such phenomena were reported for various steels subjected to axial fatigue under a stress ratio R = -1 and rotating bending fatigue at R = -1 and -2 [42]. It was found that the microstructural barriers were more effective at negative stress ratios than positive ones (R = 0), causing crack growth decelerations until the crack reached a length corresponding to 8 times the microstructural unit size [42]. The occurrence of plasticity-induced closure due to the increase in the crack tip's plastic zone wake has also been identified as a potential cause for short crack growth decelerations [95].

This delay in short crack growth enhances fatigue life. However, little research has been done to fully understand how different peening conditions affect the short crack growth in high strength 300M steel (modified AISI 4340 steel typically used in aircraft landing gears). Such information could help to better optimise the peening process and use it more judiciously to enhance aircraft components' fatigue lives.

This paper deals with the effect of machining, polishing and 2 shot peening conditions on the short fatigue crack growth of aerospace grade 300M steel samples submitted to high and low stress amplitudes. Previous works by the authors [119, 156] demonstrated the effect of peening induced CRS and roughness on the material's overall fatigue life when it is submitted to high and low stress amplitudes. The competition between roughness and CRS in the determination of crack initiation

sites [156] and the effects of the individual peening conditions on crack initiation and short crack propagation stages [119] were studied. This work completes the previous by discussing the combined effect of microstructure and CRS on the short crack growth with the help of $da/dN - \Delta K$ plots. Finally, a comparison is made between the fatigue lives predicted using the short crack and long crack growth parameters.

8.2 Background

8.2.1 Material

Specimens for short crack propagation (SCP) tests were extracted from 31.8 mm diameter heat-treated 300M steel bars. Details regarding the material's heat treatment, composition and mechanical properties are available in the authors' previous work [154]. The size distribution of the prior austenite grains is depicted in Fig. 8.1. The mean grain size computed from 101 measured grains is 23 µm and complies with the requirements of the AMS6257E standard. The grain size distribution is homogeneous, according to the ASTM E112 standard [157].

8.2.2 Methodology

8.2.2.1 Short crack propagation (SCP) test

Interrupted axial fatigue tests (stress ratio, R = -1) were performed by the authors [119] at room temperature under 2 stress amplitudes: 1089 MPa (64% of 0.2% offset yield strength $\sigma_{y,0.2}$) and 931 MPa (55% of $\sigma_{y,0.2}$) at a frequency of 10 Hz, in accordance with the ASTM E466 standard [120]. Hourglass specimens, as shown in Fig. 8.2, were used. Three surface conditions, namely as-machined, polished and shot peened, were studied. The polished specimens were prepared by mechanically polishing as-machined specimens down to 1 µm surface finish. The peening was done using two types of shots: CW14 (conditioned cut wire) and S230 (cast steel). The peening intensity was 8A and full coverage was reached. The two peening conditions are hereafter referred to as CW14-8A and S230-8A. Details regarding the peening treatments and the surface conditions can be found in the authors' previous work [154]. A total of 16 samples were tested; 2 samples per surface condition, for each stress amplitude. Fast curing two-part silicon rubber replicas were used to backtrack the initiation and monitor the propagation of short surface cracks (≤ 0.8 mm), in every

specimen. The replicas were observed using optical microscopy. The fracture surfaces were analysed using scanning electron microscopy (SEM) along with energy dispersive spectroscopy (EDS) to qualitatively identify the features responsible for fatigue crack initiation [119].

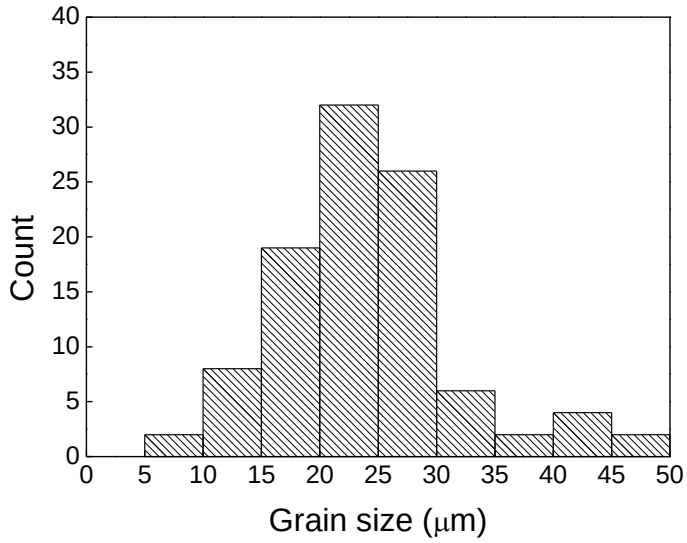

Figure 8.1 Prior austenite grain size distribution in the 300M steel (Mean = 23 μm, Standard deviation = 8 μm, Total number of grains measured =101). The grain size distribution is homogeneous, in accordance with the ASTM E112 standard [157]

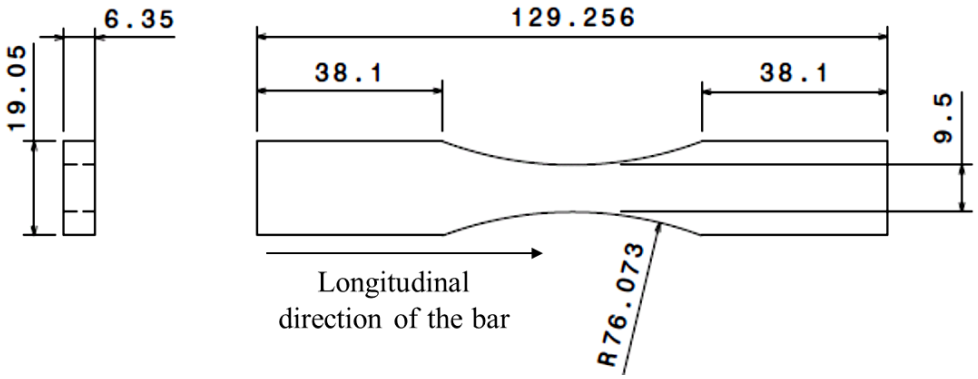

Figure 8.2 Hourglass specimen dimensions (in mm) for short fatigue crack growth tests [119]

The aspect ratio (a/c), where a is the crack depth and c is half the surface crack width, was determined to be 1 for cracks up to 0.8 mm in length, irrespectively of the surface condition. The calculation of a/c was based on measurements from semi/quarter elliptical secondary cracks found on the tested specimens' fractured surfaces shown in Fig. 8.3a and 8.3b. The stress intensity factor

range ΔK for these short surface cracks were estimated using Newman's empirical equation [158] as:

$$\Delta K = \Delta\sigma \sqrt{\frac{\pi a}{Q}}\, F\left(\frac{a}{t}, \frac{a}{c}, \frac{c}{b}, \varphi\right) \tag{7.2}$$

where $\Delta\sigma$ is the nominal stress range, a is the crack depth, c is half the surface crack width, and t and b are the thickness and width of the specimen's reduced section, respectively. φ is the parametric angle, which is 90° for quarter elliptical and 180° for semi-elliptical cracks. The procedure for obtaining the values of Q and F are detailed in the work of Newman [158].

The secant method [121] was used to calculate the crack growth rates (da/dN) from the crack size measured on the replicas.

8.2.2.2 Residual stress profiles

In-depth residual stress profiles for the tested surface conditions were obtained by the X-ray diffraction method coupled with subsequent layer removal by electropolishing. Details regarding the measurement can be found in the authors' previous work [154]. The authors [154] also quantified the CRS relaxation after 1 cycle, 200 cycles and 80% of fatigue life when submitted to an axial stress amplitude of 931 MPa. It was observed that more than 70% of the relaxation (150 MPa) occurred after 1 cycle and the relaxation reached a stabilized value within 200 cycles. It was also observed that this value remained unchanged up to 80% of the fatigue life. Similar trends were observed for an applied stress of 1089 MPa, with the maximum relaxation occurring after the first cycle [156]. The total CRS relaxation was however twice that occurring for a stress level of 931 MPa. CRS relaxation was not quantified for the unpeened specimens. Therefore, CRS profiles of unpeened and peened specimens prior to fatigue testing, and after 80% of the fatigue life for peened specimens, were used to explain the short crack propagation behavior. Fig. 8.4 represents the CRS data for unpeened specimens prior to fatigue loading (0 cycle), for specimens submitted to the S230-8A and CW14-8A peening conditions after 80% of the fatigue life, for a stress amplitude of 1089 MPa and the data obtained from samples submitted to the S230-8A peening condition after 80% of the fatigue life for a stress amplitude of 931 MPa.

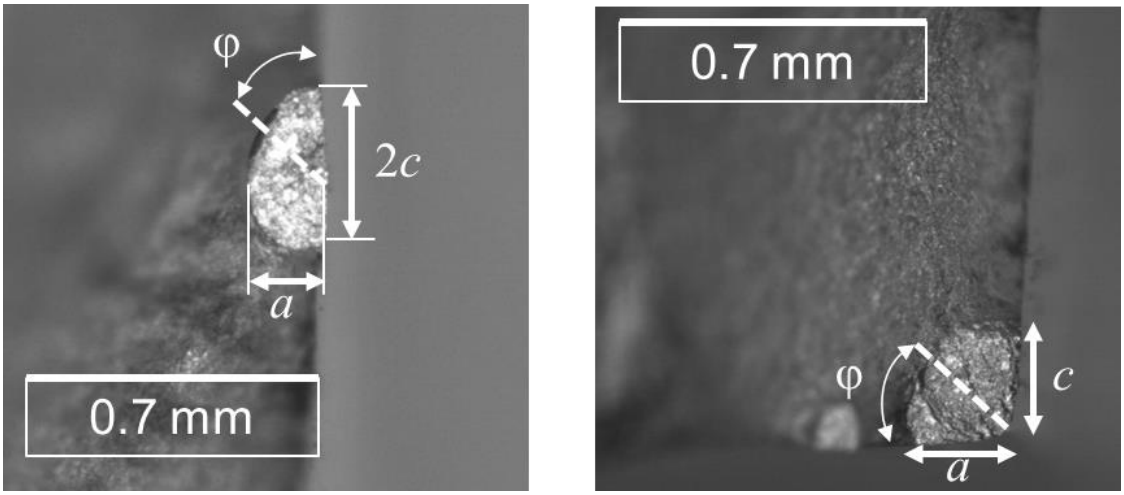

a. b.

Figure 8.3 Optical microscope image of a. a semi-elliptical crack and b. a quarter-elliptical cracks on hourglass specimens used for calculation of the short crack's aspect ratio (a/c) (a = crack depth, c = half the surface crack width, φ = parametric angle). The images were obtained from the mechanical tests carried out in [119]

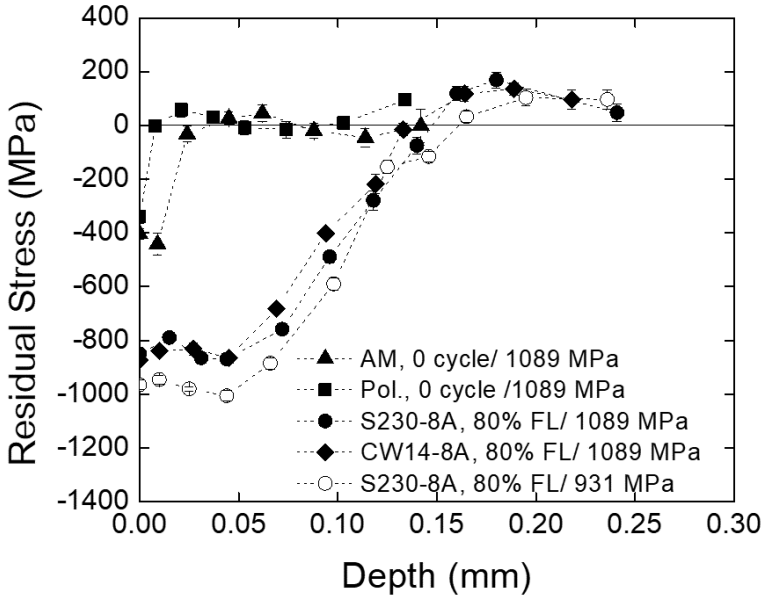

Figure 8.4 Residual stress profiles for the specimens peened with S230-8A and CW14-8A conditions after 80% of the fatigue life (FL) when subjected to a stress amplitude of 1089 MPa [156], and for the specimen peened with S230-8A condition when subjected to a stress amplitude of 931 MPa [154]. Residual stress profiles for the as-machined and polished specimens are also depicted (broken lines have been used to connect the experimental points to better represent the evolution of residual stresses). Similar residual stress profiles are observed for both peening conditions for a stress amplitude of 1089 MPa; the CRS is slightly deeper for the specimen peened with S230-8A condition. The maximum CRS for the specimen peened with S230-8A condition and submitted to a fatigue stress amplitude of 1089 MPa is relaxed by a small amount when compared to that obtained when the sample is submitted to 931 MPa. The CRS depth remains the same for all peening conditions at both stress amplitudes

8.2.2.3 Long crack propagation test

Fig. 8.5 presents the long crack propagation test results [7] for 300M steel (R = 0.1) using compact tension C(T) specimens according to the ASTM E647 standard [121]. The long crack propagation Paris' law constants C and m are presented in Table 8.1 (Section 8.3.3). The closure free (ΔP_{eff}) to closure affected (ΔP) load range ratio ($U = \Delta P_{eff}/\Delta P$) of 0.9 reported in Fig. 8.6 [7] depicts the small amount of crack closure observed for the long cracks. The closure was determined according to the 2% compliance offset criterion in the ASTM E647 standard [121].

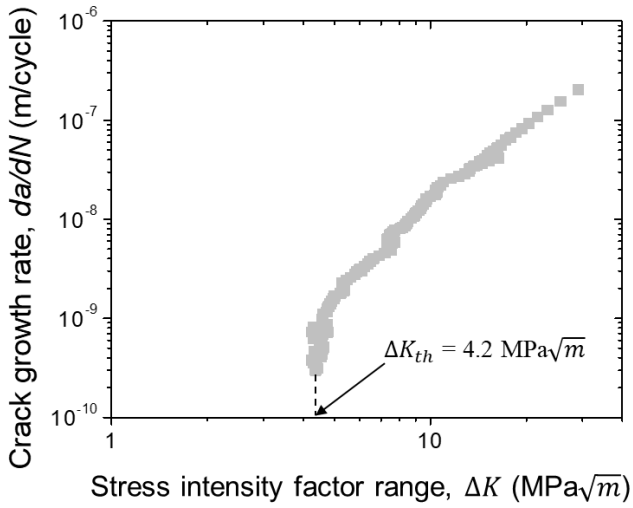

Figure 8.5 Log-log plot of crack growth rate da/dN vs. stress intensity factor range ΔK depicting the long crack propagation behavior of 300M steel C-T specimens tested at R = 0.1 (ΔK_{th} is the threshold stress intensity factor range) [7]

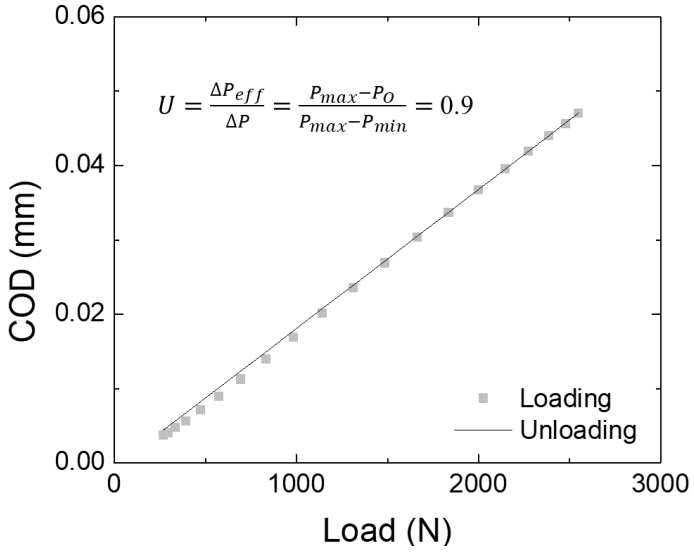

Figure 8.6 Crack opening displacement (COD) vs. load curve for loading and unloading part of a cycle (ΔP_{eff} is the effective load range free of crack closure, ΔP is the closure affected load range, P_{max} and P_{min} are the maximum and minimum load, and P_O is the opening load estimated according to the 2% compliance offset criterion in the ASTM E647 standard). A fully open crack is characterized by U of 1. A U of 0.9 indicates a small amount of closure for the specimen tested at R = 0.1 for a ΔK of 7 MPa$\sqrt{m}$ [7]

8.2.2.4 Stress-intensity factor-based model for fatigue life prediction

The authors [156] have previously used the long crack growth parameters to predict the axial fatigue life (N_f) of the specimens shot peened with S230-8A and CW14-8A conditions when submitted to a stress amplitude of 1089 MPa (R = -1). This was analytically calculated by integrating Paris' equation from the initial discontinuity size $\sqrt{area}$ to a final crack size a_c, corresponding to the material's plain strain fracture toughness K_{Ic}, as:

$$N_f = \frac{2\sqrt{area}}{(m-2)C\,(K_{Imax})^m} \qquad \text{when } a_c >> \sqrt{area} \tag{8.3}$$

Only the tensile part of the stress cycle was considered to account for the crack growth, and hence $\Delta K \approx K_{Imax}$ was assumed to be the crack driving force. K_{Imax} is the maximum stress intensity factor in opening mode I calculated using Murakami's empirical equation [25] as:

$$K_{Imax} = f\sigma_{max}(\pi\sqrt{area})^{1/2} \tag{8.4}$$

where σ_{max} is the maximum applied stress and f = 0.65 for surface discontinuities. For crack initiation at surface grinding marks or peening induced discontinuities, the $\sqrt{area}$ parameter denotes the equivalent size of a periodic roughness feature characterized by the profile height R_t and profile width R_{sm} according to Murakami's approximation [25] given by:

$$\frac{\sqrt{area_R}}{R_{Sm}} \cong 2.97\left(\frac{R_t}{R_{Sm}}\right) - 3.51\left(\frac{R_t}{R_{Sm}}\right)^2 - 9.47\left(\frac{R_t}{R_{Sm}}\right)^3 \qquad \text{for } \frac{R_t}{R_{Sm}} < 0.195 \tag{8.5}$$

The K_{Imax} values thus calculated using Eqn. (8.5) by the authors [156] for the S230-8A and CW14-8A conditions are 5.9 and 8.2 MPa$\sqrt{m}$, respectively.

The fatigue lives calculated using the described model are presented in Section 8.3.3.

8.3 Results analysis and discussion

8.3.1 Short crack propagation: Effect of microstructure and CRS

Figs. 8.7 a-c illustrate the $da/dN - \Delta K$ results from the SCP tests performed at a stress amplitude of 1089 MPa for the two tested as-machined specimens (labelled AM1, AM3) along with polished (Pol) specimens, and those peened with S230-8A (S230-8A-1, S230-8A-3) and CW14-8A (CW14-8A-1, CW14-8A-3) conditions.

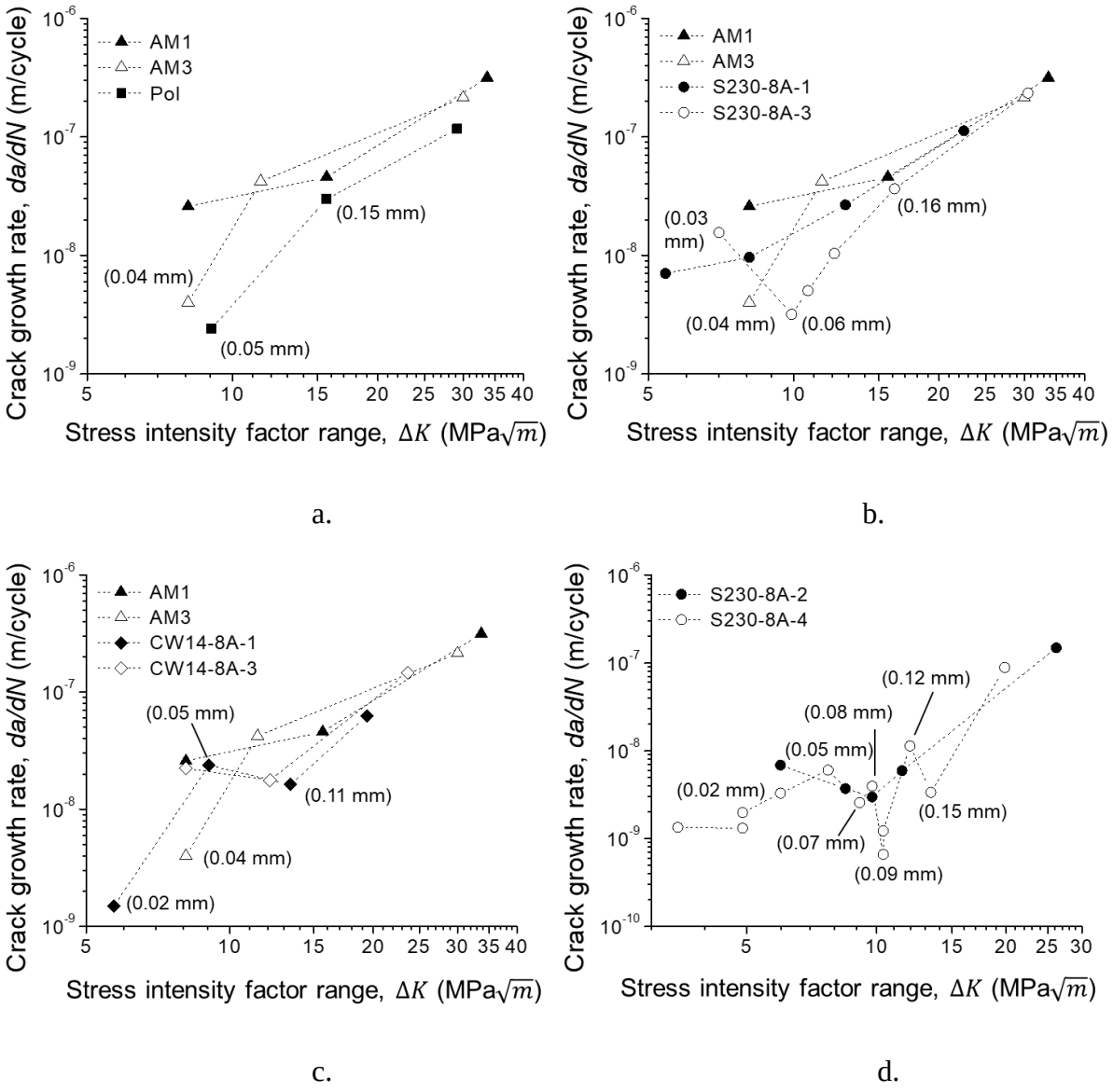

Figure 8.7 Short crack $da/dN - \Delta K$ plots for as-machined (AM) specimens vs. a. polished (Pol.) specimen, b. specimens peened with S230-8A condition, c. CW14-8A specimen submitted to a fatigue stress amplitude of 1089 MPa, and d. specimens peened with S230-8A condition submitted to a fatigue stress amplitude of 931 MPa (broken lines joining experimental points are used to help visualize crack accelerations and decelerations). The crack decelerations are affected by the CRS depth and prior austenite grain boundaries. The corresponding crack lengths for some points are depicted in brackets to ease understanding

Fig. 8.7a shows that the crack growth rates were higher for the as-machined specimens, when compared to those observed on the polished samples for a ΔK of ~16 MPa$\sqrt{m}$ or a crack length of 0.15 mm, which was equivalent to ~7 grain diameters (or 7D).

Fig. 8.7b suggests that the specimens peened with the S230-8A condition had lower crack growth rates for ΔK values for up to 16 MPa$\sqrt{m}$, when compared to the as-machined specimens' short crack growth rate (except the first data point for AM3 specimen). This corresponds to a crack length of 0.16 mm (7D), which is equivalent to the total depth of the S230-8A peening induced CRS (Fig. 8.4). Crack growth rate deceleration was encountered for the S230-8A-3 specimen at a crack length of 0.03 mm (~1D) for a ΔK of 7 MPa$\sqrt{m}$ up to 0.06 mm (~3D) for a ΔK of 10 MPa$\sqrt{m}$, after which the crack growth rate became similar to that of the as-machined specimens. This region of crack deceleration is very close to the depth of maximum CRS, which is around 0.04 mm.

Conversely, Fig 8.7c shows that the crack growth rate (2 x 10^{-9} m/cycle) of the CW14-8A-3 specimen was lower than that of the as-machined specimens and similar to the lowest crack growth rate for the polished specimen. At this time, the crack was about 0.02 mm in length, which is shorter than the first grain. The crack growth decelerated in both the specimens peened with the CW14-8A condition when the crack reached the next barrier at ~0.05 mm (~2D). These low crack growth rates correspond to the regions at which the maximum value of CRS occurred, which is close to the surface and at around 0.045 mm deep in the sample. The crack growth decelerations continued until a ΔK of ~13 MPa$\sqrt{m}$ was applied, when the cracks were about 0.11 mm (~5D) long, which coincides with the total depth of the CRS (0.13 mm or ~6D). Following this, the crack growth rates of both the peened and unpeened specimens became similar again.

Fig. 8.7d displays the $da/dN - \Delta K$ curves for samples peened under the S230-8A condition when submitted to the lower stress amplitude of 931 MPa. It can be clearly seen in Fig. 8.7d that the cracks in the specimens as per the S230-8A condition encounter numerous barriers that slow their propagation down. The crack decelerations are recorded at crack lengths of 0.02 mm (~D), 0.05 mm (~2D), 0.08 mm (~3D) and 0.12 mm (~5D), which may correspond to successive grain boundary barriers. The first 3 crack decelerations occurred at depths where the CRS was within 6% of the maximum CRS (-1006 MPa), as seen in Fig. 8.4. All the crack decelerations occurred within the CRS affected depth.

These observations suggest that most crack decelerations occurred within the first 5 grains (upto a ΔK of 13 MPa$\sqrt{m}$ and a length of ~0.1 mm) in peened specimens. Although the unpeened specimens showed no crack decelerations, crack growth rates as low as 2 x 10^{-9} m/cycle were observed in the first 1 or 2 grains (upto a ΔK of 9 MPa$\sqrt{m}$), where some compressive residual stresses had been measured. This was equivalent to some of the crack growth rates encountered in the peened specimens. The lower crack propagation rates observed in peened specimens might result from more compressive and deeper residual stresses.

8.3.2 Comparison between short crack propagation (SCP) and long crack propagation (LCP)

The $da/dN - \Delta K$ data obtained from SCP tests on as-machined hourglass specimens subjected to both high and low stress amplitudes (R = -1) is plotted along with the $da/dN - \Delta K$ data from the LCP test on C(T) specimens (R = 0.1) [156] in Fig. 8.8. It can be seen that the average short crack growth rate superimposes on the long crack growth rate. No effect of the difference in stress ratios is visible on the results. This can be attributed to the absence of significant crack closure in long cracks, as shown in Fig. 8.5. Therefore, the stable crack growth region for both long and short cracks in the as-machined specimens can be represented by a Paris-type relationship (Eqn. (8.1)).

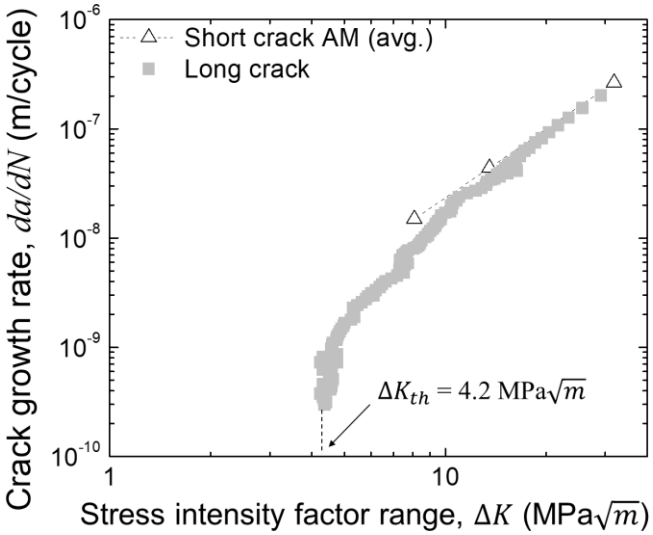

Figure 8.8 Long crack propagation (R = 0.1) [7] and short crack propagation (R = -1) results (average of 2 specimens) for as-machined (AM) 300M steel specimens (ΔK_{th} is the threshold stress intensity factor range). The short crack growth rate coincides with the long crack growth rate which is affected by a small amount of crack closure

It is evident that the short crack deceleration and acceleration behaviour encountered in shot peened specimens cannot be characterized by Eqn. (8.1). A new relationship must therefore be proposed.

8.3.3 Fatigue life prediction incorporating the effect of CRS on SCP

The authors [156] observed that, for the specimens peened with the S230-8A and CW14-8A conditions, the fatigue lives of cylindrical (uniform gage) specimens were underestimated when the long crack growth parameters were input in Eqn. (8.3). It is evident from Figs. 8.7 and 8.8 that the short cracks in shot peened specimens have lower crack growth rates than the long cracks, for ΔK values above the ΔK_{th} of 4.2 MPa$\sqrt{m}$. To incorporate the effect of CRS in the fatigue life prediction of the peened specimens, the LCP constants (C, m) were replaced with those averaging the short crack behavior (C', m'). C' and m' were obtained by fitting Eqn. (8.1) to the $da/dN - \Delta K$ results obtained from replicas taken on the rectangular hourglass specimens. Figs. 8.9a and 8.9b depict the fits performed on the 2 tested specimens for the S230-8A and CW14-8A conditions. It was observed that the specimens with fewer recorded crack deceleration points (S230-8A-1 and CW14-8A-3) had C' and m' values that were closer to the long crack growth constants (C, m) than those with more crack deceleration points (S230-8A-3 and CW14-8A-1). Hence, the fitting constants of the latter were chosen for the fatigue life predictions to represent the short crack trend. The values of C' and m' obtained for the samples peened with the S230-8A and CW14-8A conditions when subjected to a stress amplitude of 1089 MPa are reported in Table 8.1, along with the LCP constants (C, m).

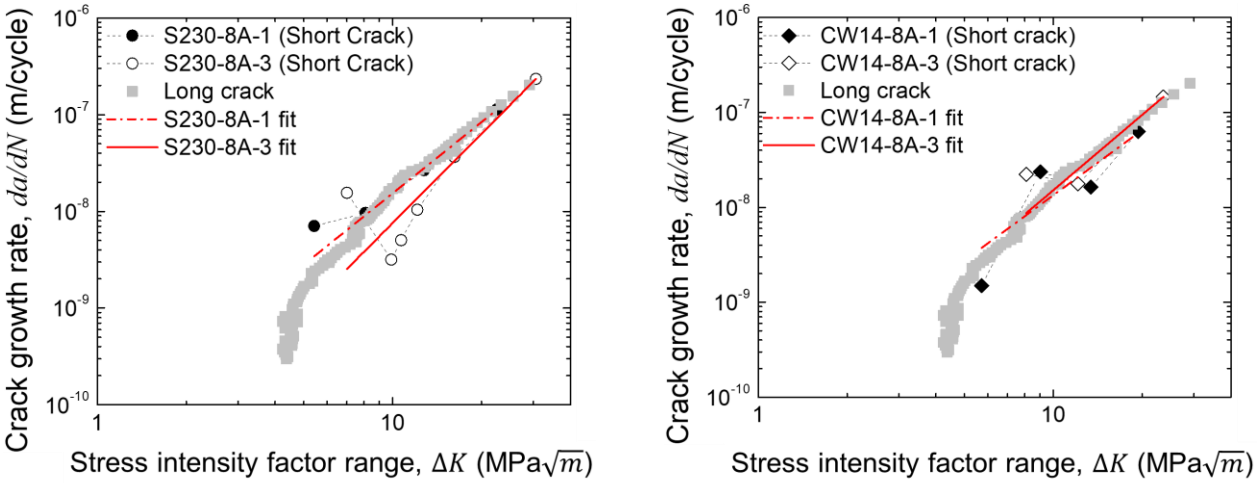

a. b.

Figure 8.9 Power law fit (straight lines) for short crack $da/dN - \Delta K$ results of the specimens peened with the S230-8A and CW14-8A conditions, along with the long crack propagation results [7]. The fits obtained for specimens with more crack deceleration points (S230-8A-3 and CW14-8A-1) better represent average short crack growth

Table 8.1 Short crack growth rate constants (C', m') for samples peened with the S230-8A and CW14-8A conditions when tested at a stress amplitude of 1089 MPa (R = -1), and long crack propagation constants (C, m) tested at R = 0.1

Specimen	C'	m'
S230-8A-1	5.44 x 10^{-11}	2.45
S230-8A-3	6.47 x 10^{-12}	3.07
CW14-8A-1	6.99 x 10^{-11}	2.28
CW14-8A-3	3.52 x 10^{-11}	2.63
	C	m
LCP	2.27 x 10^{-11}	2.79

The fatigue life for the samples peened with the S230-8A and CW14-8A conditions calculated using the short crack growth behavior, $N_{f,SCP}$ as well as the average experimental fatigue lives of the rectangular hourglass specimens are presented in Table 8.2. The fatigue life predictions for samples submitted to a stress amplitude of 1089 MPa made using long crack propagation (LCP) constants, $N_{f,LCP}$ were compared with the average experimental fatigue lives of cylindrical specimens that failed from surface discontinuities, as reported in the authors' previous work [156].

Table 8.2 shows that the $N_{f,SCP}$ are always higher than the $N_{f,LCP}$. For hourglass specimens peened with the S230-8A condition, the $N_{f,SCP}$ is 1.6 times that of the $N_{f,LCP}$, while the average experimental fatigue life coincides with the $N_{f,SCP}$. For hourglass specimens peened with the CW14-8A condition, the $N_{f,SCP}$ is 2.6 and 0.8 times that of the $N_{f,LCP}$ and the average experimental fatigue life, respectively.

Now, by comparing the $N_{f,SCP}$ with the average experimental fatigue lives of the cylindrical fatigue specimens, we can verify the applicability of the short crack growth rate data of the rectangular hourglass specimens in the cylindrical specimens' fatigue life predictions. As shown in Table 8.2, the $N_{f,SCP}$ of the specimens peened with the S230-8A and CW14-8A conditions are underestimated by factors of 2 and 1.6 respectively, as compared to the average experimental fatigue lives.

From the above observations, it is evident that the use of C' and m' improves the fatigue life predictions of peened specimens tested under a stress amplitude of 1089 MPa. It indicates that the contribution of CRS is significant and should therefore be accounted for to accurately predict the crack growth behavior of specimens with surface residual stresses.

Table 8.2 Predicted fatigue lives using SCP and LCP parameters along with the average experimental axial fatigue lives of the hourglass specimens peened with the S230-8A and CW14-8A conditions and the cylindrical fatigue specimens (with surface crack initiation) when subjected to a stress amplitude of 1089 MPa and R = -1 (FL = fatigue life)

Surface condition	Predicted FL using SCP ($N_{f,SCP}$) (x 10^4 cycles)	Predicted FL using LCP ($N_{f,LCP}$) [156] (x 10^4 cycles)	Average experimental FL (Hourglass) (x 10^4 cycles)	Average experimental FL (Cylindrical) [156] (x 10^4 cycles)
S230-8A	2.76	1.77	2.64	5.44
CW14-8A	3.55	1.37	4.18	5.75

Nevertheless, despite using SCP parameters, the fatigue lives of the cylindrical specimens are underestimated by upto a factor of 2. This reflects a probable effect of the specimen geometry on the fatigue life. The presence of edges in the hourglass specimens is known to produce a stress state more favourable to local plastic deformation [159] which favours crack initiation, when compared to the continuous surface of the cylindrical specimens. Similar observations were made by Nogami et al. [160] for reduced activation ferritic/martensitic steels, where sub-standard size hourglass specimens produced lower fatigue lives than similar size cylindrical specimens at strain amplitudes < 1% (R = -1).

8.4 Conclusions

The short fatigue crack growth behavior of 300M steel as-machined specimens, polished specimens and specimens peened with S230-8A and CW14-8A conditions when submitted to 2 stress amplitudes: 1089 MPa (64% of $\sigma_{y,0.2}$) and 931 MPa (55% of $\sigma_{y,0.2}$) at R = -1, was studied. Silicon replicas were used to capture the short crack growth rates. Fatigue lives of peened specimens tested at the stress amplitude of 1089 MPa were predicted using a stress-intensity factor-based model by accounting for the effect of CRS through a characterization of the short crack growth behavior. The key conclusions drawn are as follows:

- The region of crack deceleration in peened specimens and low crack growth rates in unpeened specimens occurs within the region affected by compressive residual stresses. Moreover, the distance between the successive crack growth decelerations in shot peened specimens corresponds to the average size of the prior-austenite grains.
- Crack deceleration was observed for crack lengths corresponding to 3 and 5 grain diameters for the specimens peened with the S230-8A and CW14-8A conditions, respectively, when subjected to the higher stress amplitude (1089 MPa). At the lower stress amplitude (931 MPa), the short cracks in the S230-8A specimens decelerated upto twice the size (5 grain diameters) observed at 1089 MPa.
- The average short crack growth rate of the as-machined specimens is well represented by the closure free long crack growth rates.
- The average short crack growth behavior in the peened specimens was quantified by fitting the $da/dN - \Delta K$ results for the short cracks to a Paris' type equation. The short cracks for which the maximum number of crack decelerations were recorded experimentally, better represented the short crack growth behavior. Therefore, with more experimental data, more accurate values for the fitting constants could be achieved.
- Use of short crack growth parameters (C', m') instead of long crack growth parameters (C, m) improved the fatigue life prediction for shot-peened rectangular hourglass specimens by upto a factor of 3. The predicted fatigue lives were within 15% of the experimental lives.
- Using the same short crack growth parameters calibrated from the hourglass specimens to predict the fatigue lives of the uniform gage cylindrical specimens, underestimated the predicted fatigue life (by a factor of 2). An effect of specimen geometry on the crack initiation life is expected to have caused this underestimation.

8.5 Additional results- Finite element analysis of residual stress distribution in rectangular and cylindrical fatigue specimens

This section presents the simulation of residual stress evolution subjected to the studied fatigue stress amplitudes in cylindrical and rectangular specimens as described in Section 4.3.2. A comparison is made to ascertain whether lower fatigue lives obtained for the cylindrical specimens when compared to the rectangular specimens, is caused by a difference in CRS and their evolution during fatigue loading.

Figs. 8.10 and 8.11 illustrate the FEA results for the residual stress distribution in the rectangular fatigue specimens treated as per the S230-8A and CW14-8A conditions subjected to stress amplitudes of 931 MPa and 1089 MPa respectively, along with their experimental results. Figs. 8.12 and 8.13 illustrate the predicted residual stress relaxation for the cylindrical specimens vs. experimentally measured residual stress relaxation for the rectangular fatigue specimens for the same conditions. Note that there were no CRS relaxation experiments performed after 1 fatigue cycle for the rectangular specimens treated with S230 shot at 8A intensity subjected to 1089 MPa and CW14 shot at 8A intensity subjected to 931 MPa. Instead the residual stress relaxation was measured after 80% of their fatigue life had elapsed. As discussed previously (Section 6.3.3 and Section 7.3.2), maximum residual stress relaxation at the given stress amplitudes occur during the first fatigue cycle with no significant change thereafter. Therefore, CRS relaxation obtained experimentally after 80% fatigue life for these two conditions is very close to the FEA results obtained after 1 cycle.

The figures show that the FEA results obtained for both rectangular and cylindrical specimens are similar to each other as well as to those obtained experimentally on the rectangular fatigue specimens for comparable conditions. In fact, the FEA results for the two specimen geometries are so similar that the Figs. 8.10 and 8.12, and Figs. 8.11 and 8.13 seem identical. This could suggest that factors other than the local residual stress distribution affects the fatigue life for different specimen geometries shot peened using the same conditions.

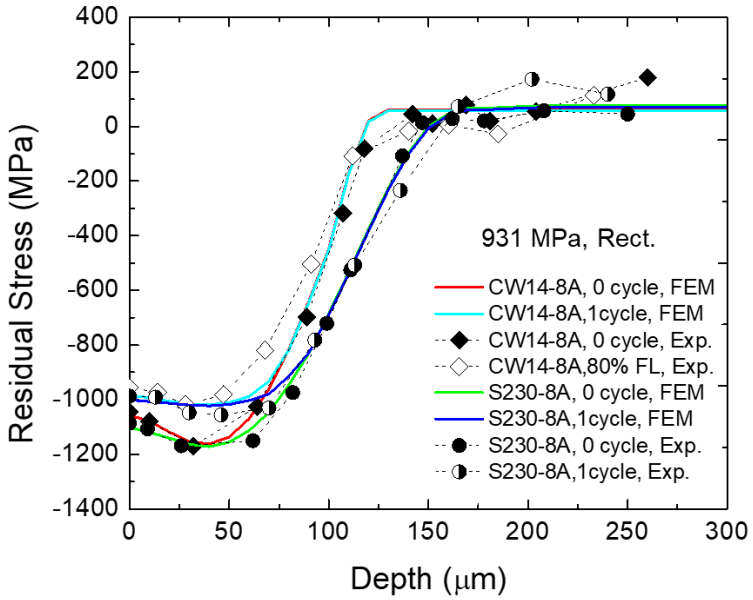

Figure 8.10 Predicted and experimentally measured residual stress profiles for the specimens treated as per the CW14-8A and S230-8A conditions subjected to a fatigue stress amplitude of 931 MPa prior to fatigue loading (0 cycle), after 1 cycle and after 80% of fatigue life. The predicted residual stress relaxation for the rectangular fatigue specimens are similar to those experimentally measured on rectangular fatigue specimens

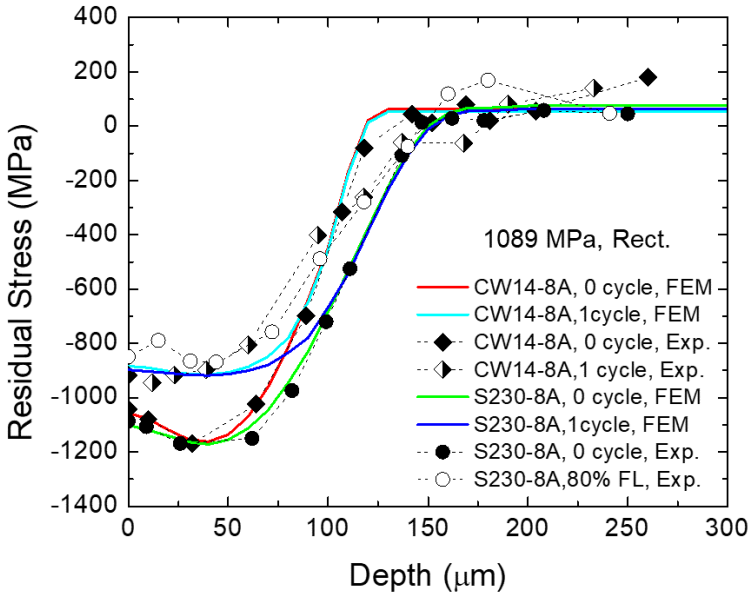

Figure 8.11 Predicted and experimentally measured residual stress profiles for the specimens treated as per the CW14-8A and S230-8A conditions subjected to a fatigue stress amplitude of 1089 MPa prior to fatigue loading (0 cycle), after 1 cycle and after 80% of fatigue life. The predicted residual stress relaxation for the rectangular fatigue specimens are similar to those experimentally measured

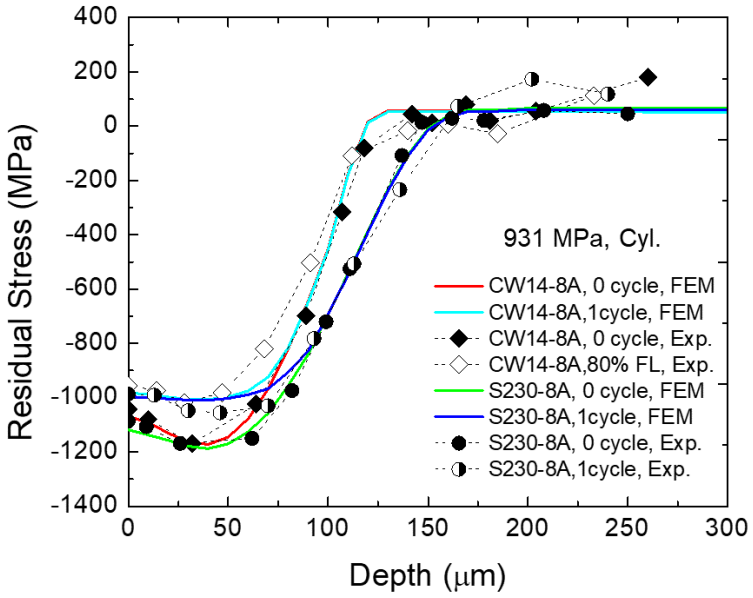

Figure 8.12 Predicted and experimentally measured residual stress profiles for the specimens treated as per the CW14-8A and S230-8A conditions subjected to a fatigue stress amplitude of 931 MPa prior to fatigue loading (0 cycle), after 1 cycle and after 80% of fatigue life. The predicted residual stress relaxation for the cylindrical fatigue specimens are similar to those experimentally measured on rectangular fatigue specimens

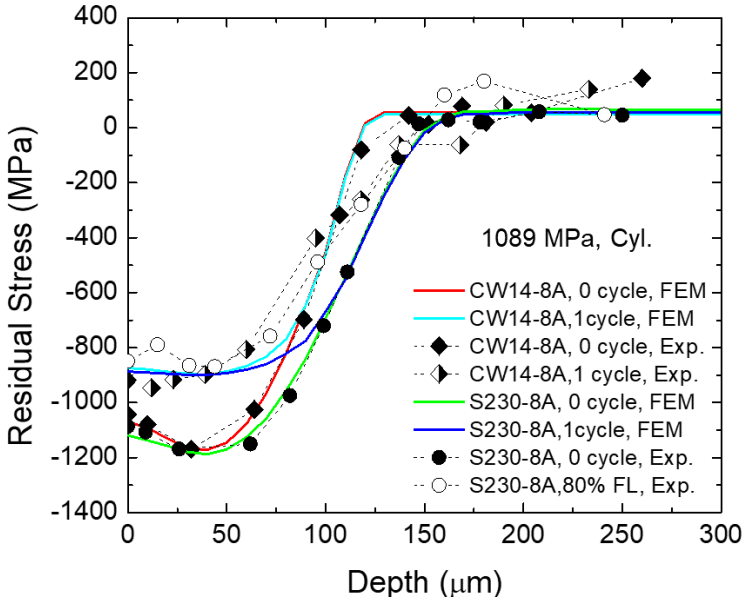

Figure 8.13 Predicted and experimentally measured residual stress profiles for the specimens treated as per the CW14-8A and S230-8A conditions subjected to a fatigue stress amplitude of 1089 MPa prior to fatigue loading (0 cycle), after 1 cycle and after 80% of fatigue life. The predicted residual stress relaxation for the cylindrical fatigue specimens are similar to those experimentally measured

CHAPTER 9 GENERAL DISCUSSION

This section presents a summary of the key findings of the present work, followed by an overall discussion, applicable to 300M steel for the studied loading and shot peening conditions.

9.1 Key findings

9.1.1 Peening induced CRS undergo small amount of relaxation during cyclic loading

In the 1st article, it was observed that fully reversed axial fatigue loading relaxed the surface CRS induced by peening with S230 shot and CW14 shot at an intensity of 8A by 11% and 8%, respectively, when tested in HCF condition at $\sigma_a = 55\%$ of $\sigma_{y,0.2}$. In the 2nd article, the surface CRS relaxed by 22% and 16% for the specimens peened as per the S230-8A and CW14-8A conditions, respectively, when tested at a higher $\sigma_a = 65\%$ of $\sigma_{y,0.2}$. The depth of CRS remained unaffected for the lower stress amplitude while it decreased by only 7% at the higher stress amplitude. Moreover, more than 70% of the total relaxation occurred after the 1st fatigue cycle at both stress amplitudes. Therefore, it is expected that the observed magnitude of residual stress relaxation would not affect the fatigue life for 300M steel considerably for the studied conditions. This is supported by the findings of Torres and Voorwald [2] and Morrow and Sinclair [86] who observed that low applied stresses or strains (close to the fatigue limit) in the case of 4340 steels resulted in very little relaxation of compressive residual (or mean) stresses.

9.1.2 Fatigue crack initiation occurs at material discontinuities or process related discontinuities based on the induced roughness and CRS

From the 1st and 2nd articles, the discontinuities responsible for triggering crack initiation can be classified into: material discontinuities (inclusions) and process related discontinuities (grinding marks or peening induced discontinuities). The coupled effect of CRS and roughness of the corresponding surface condition determines which discontinuity will trigger crack initiation.

Table 10.1 summarizes the initial surface CRS, roughness (R_t) and % of cracks initiating at inclusions or surface roughness features for each surface condition. At the lower fatigue stress amplitude, cracks initiated at internal inclusions most of the time, as the beneficial effect of CRS

overcame the stress concentrations caused by surface roughness for all surface conditions. For the higher fatigue stress amplitude, crack initiation was favoured at surface roughness features. Nevertheless, crack initiation at surface inclusions was preferred in conditions with low CRS coupled with low roughness in case of polished specimens, or at interior inclusions for those with a high CRS and low roughness in case of peened specimens (S230-4A condition).

Table 9.1 Summary of initial surface CRS, roughness roughness (R_t) and % of cracks initiating at inclusions (incl.) or surface roughness features (rough.) for each surface condition tested at $\sigma_a =$ 931 MPa and 1089 MPa

	Polished	As-machined	S230-4A	S230-8A	CW14-8A
Initial surface CRS (MPa)	-341	-404	-1065	-1086	-1044
Roughness, R_t (µm)	$<$ 2.36	2.36	3.94	7.79	15.51
Crack initiation site (931 MPa)	100% incl.	60% incl.	100% incl.	89% incl.	89% incl.
Crack initiation site (1089 MPa)	0% rough.	75% rough.	25% rough.	88% rough.	88% rough.

9.1.3 Shot peening does not have a significant effect on the HCF life (for the tested conditions)

The 1st article showed that shot peening prevented cracks from initiating at inclusions and surface roughness discontinuities located within the CRS affected depth of 150 µm from the surface. However, this did not improve the peened specimens' fatigue lives significantly, which was governed mainly by the size of the inclusions located deeper than the CRS affected layer. The preferred crack initiation at inclusions was attributed to the possibility that the stress concentration caused by inclusions were similar to, or higher than, those caused by surface roughness features. Using equations from the 2nd article, it is observed that the stress intensity factor range for the

subsurface inclusions of sizes 13-51 μm encountered for this steel based on the fractographic observations is 3-6 MPa√m. For surface roughness features, the stress intensity factor is around 3 MPa√m.

Nevertheless, for a specimen treated as per the S230-8A condition where the cracks initiated at surface discontinuities, a fatigue life of more than a million cycles was obtained. This value was about thrice the average fatigue life of the two as-machined specimens with surface crack initiation. This indicates that shot peening may show a greater improvement in fatigue life of components tested with a stress gradient high enough to have a ΔK lower than ΔK_{th} beneath the peening induced compressive residual stress layer.

9.1.4 Gumbel extreme value model can predict the largest inclusion size in a given steel volume

In the 1st article, the largest inclusion size (51 μm) in the fatigue specimen's reduced section volume was accurately predicted by the Gumbel extreme value statistical model. It was shown that conventional methods of evaluating material cleanliness solely based on examination of metallographic cross sections could not detect inclusion sizes larger than 25 μm that were mainly responsible for fatigue crack initiation.

9.1.5 Shot peening can sometimes have a detrimental effect on the fatigue life at high stress amplitudes

The 2nd article showed that shot peening sometimes resulted in lower fatigue lives than the average fatigue life of the as-machined specimens by upto a factor of 3 in the case of the most detrimental peening condition or the CW14-8A condition, which produced the highest surface roughness. Statistical analysis by B-basis also demonstrated the higher fatigue life dispersion shown by the condition, when compared to the as-machined specimens.

9.1.6 Considering the CRS and grain boundaries affected short crack propagation improves the fatigue life prediction for shot peened specimens

The short crack growth behavior in peened specimens was found to be affected by the CRS and microstructure in Chapter 8. The distance between successive short crack decelerations could be correlated to the average diameter of the prior austenite grains (23 µm). Using short crack propagation data instead of the long crack propagation improved the average fatigue life predictions for S230-8A and CW14-8A peened rectangular hourglass specimens by factors of 2 and 3, respectively.

9.1.7 Peening and/or machining may result in work softening

FWHM vs depth profiles presented in Section 7.7.2 indicate that work softening rather than hardening takes place in the near surface layers of the given steel. As observed from the strain-controlled fatigue tests, the material undergoes cyclic softening when subjected to axial strains which causes mean stress relaxation. The mean stress relaxation is equivalent to CRS relaxation in case of the peened specimens. Nevertheless, microhardness tests on peened specimens were inconclusive due to the similar size of work hardened/softened layer as the indent size, which prevented near surface measurements. Nanohardness measurements should be performed to further investigate the true nature of the shot peened layer.

9.2 Discussion

9.2.1 Choice of the best peening condition in terms of fatigue life

In general, peening at a lower intensity of 4A resulted in lower roughness than at a higher intensity of 8A. Peening with smaller CW14 shot at 8A intensity produced deeper dents (higher R_a), yielding higher stress concentration factors than obtained by peening with larger S230 shot at the same intensity. Similar observations were made by Bianchetti et al. [155] for the same peening conditions on AA7050-T7451. This is attributed to the higher velocity (or energy) of the CW14 shots required to produce 8A intensity than the S230 shot, which is in accordance with the experimental study by Miao et al. [137] on aluminium 2024.

Similar CRS and CRS relaxation profiles were obtained for the specimens treated using CW14 and S230 shot at an intensity of 8A. Although no CRS profiles were measured for the specimens peened using S230 shot at an intensity of 4A, a higher % of inclusion-initiated cracks for this condition, especially at higher stress amplitudes suggests that the CRS was sufficiently high to overcome the stress concentration produced by peening induced roughness.

In HCF, no clear conclusion could be drawn regarding the best peening condition as the specimens' fatigue lives were dictated by material cleanliness. Improving the material cleanliness would result in crack initiation at the process induced surface roughness features, which would help to better visualize the fatigue life improvement for each peening condition. In presence of lower applied stresses (low plastic deformation) in HCF, crack initiation constitutes most of the component fatigue life. Therefore, it is expected that the peening with S230 shot at 4A intensity which produces lower roughness and high CRS, would yield higher fatigue lives than the other peening conditions. Additionally, 52-87% lower fatigue lives were obtained for the as-machined specimens with surface crack initiation, when compared to the specimen peened using S230 shot at 8A intensity with surface crack initiation. This indicates that shot peening may show a greater improvement in fatigue life of components subjected to a stress gradient sufficiently high to cause surface crack initiations.

Improvements in fatigue life of specimens peened with S230 shot at 4A intensity subjected to higher stress amplitudes were observed when cracks initiated at surface features. In fact, for these specimens with surface crack initiation, fatigue lives were higher than all the specimens peened using S230 shot at 8A intensity and all but one specimen specimens peened using CW14 shot at 8A intensity. It is expected that at higher stress amplitudes too, shot peened specimens may show a greater beneficial effect on fatigue life of specimens submitted to stresses with a gradient, as in case of bending.

All in all, it can be inferred that peening with larger S230 shot at a low intensity of 4A provides optimum fatigue life for the 300M steel tested at $\sigma_a = 64\%$ of $\sigma_{y,0.2}$ and $\sigma_a = 55\%$ of $\sigma_{y,0.2}$.

9.2.2 Scope of the proposed fatigue life prediction models

Three types of fatigue life prediction models were proposed in the current work: empirical, statistical and analytical.

The empirical model was proposed to predict the fatigue lives of all specimens in HCF, irrespective of their surface conditions. It was based on a power law relationship of fatigue life with the equivalent inclusion size represented by Murakami's [15] $\sqrt{area}$ parameter. Although the relationship predicted the general trend very well, it was unable to account for the high fatigue life dispersion which sometimes led to an underestimation of the fatigue life by a factor as large as 10. This suggests that parameters other than just the inclusion size affect the fatigue lives and should be further investigated to improve fatigue life prediction in HCF.

For higher stress amplitudes, the statistical model (B-basis) was employed to estimate the lowest fatigue life that could be obtained for a given surface condition while accounting for the fatigue life dispersion. The analytical model assumed propagation of a critical discontinuity from an initial size (represented by the $\sqrt{area}$ parameter) to a final size corresponding to failure, according to LEFM criterion, and calculated a lower limit for the fatigue life. The analytical predictions supported the B-basis values for the polished specimens and the specimens peened using S230 shot at 4A intensity which exhibited crack initiation at surface and subsurface inclusions, respectively, but not for those peened using S230 and CW14 shot at an intensity of 8A. For the specimens peened using S230 shot at 8A intensity, systematic surface roughness features generated by peening resulted in a low fatigue life dispersion and hence, higher B-basis than the analytical prediction which did not consider the effect of CRS. For the specimens peened using CW14 shot at 8A intensity, one specimen with a very low N_f of 1.8 x 10^4 cycles increased the overall fatigue life dispersion, resulting in a negative B-basis value.

Hence, it can be said that the statistical model estimates are based on the combined fatigue life dispersion resulting from multiple crack initiation features, while the analytical model offers individual fatigue life predictions for each discontinuity type. Additionally, the analytical model is able to predict the dominant crack initiating feature in case of multiple discontinuities in the material by using the stress intensity factor corresponding to the limiting size of the crack initiating feature. Therefore, solely relying on the B-basis values could lead to an erroneous choice of the optimum peening condition as is evident in case of the highest B-basis predicted for S230-8A condition, which is not the best peening condition, as shown in the 2nd article.

The analytical model successfully predicted the average fatigue lives at the higher stress amplitude by implementing the short crack behavior. However, the predictions were applicable only to the

rectangular hourglass specimens on which the short crack propagation tests were performed. The fatigue life predictions were underestimated (by a factor of 2) for uniform gage cylindrical specimens which exhibited higher fatigue lives due to absence of edges. Moreover, it is expected that the underestimation of fatigue life due to the specimen geometry would be more significant at the lower stress amplitude of 931 MPa. This is reflected by the fact that at 931 MPa, the experimental fatigue life of a cylindrical specimen peened using S230 shot at 8A intensity (1.06 x 10^6 cycles) was 17 times higher than that of average life of the rectangular specimens, as compared to 2 times for an applied stress of 1089 MPa.

Therefore, to improve the predictions, the short crack growth behavior should be validated for cylindrical specimens or specimens with geometries producing similar stress concentration factors as the cylindrical specimens. In addition, the replica analysis should be performed at closer intervals to record more crack deceleration points. This would help to obtain a better estimate for the short crack growth parameters (C', m') used for the fatigue life predictions.

CHAPTER 10 CONCLUSIONS AND RECOMMENDATIONS

The principal objective of this work was to investigate the effect of 3 shot peening conditions (using S230 shot at intensities of 4A and 8A, and CW14 shot at an intensity of 8A) on the fully reversed axial fatigue life of aerospace grade 300M steel at 2 stress amplitudes: 55% of $\sigma_{y,0.2}$ and 65% of $\sigma_{y,0.2}$.

300M steel's microstructural (grain size) and macro structural characteristics (static and cyclic mechanical property testing) as well as its long crack propagation behavior were characterized. The fatigue and short crack propagation behavior were studied for both unpeened and peened specimens. Shot peened surface characteristics and crack initiating features were examined using SEM and roughness profilometer, while XRD was used to quantify the residual stresses induced by peening. The residual stress relaxation during cyclic loading was also quantified.

A high fatigue life scatter (one order of a magnitude on a log scale) was observed in HCF, where the fatigue cracks initiated at inclusions for 91% of the time. Based on the experimental results, an empirical relationship was used to predict the HCF lives of the peened and unpeened specimens as a function of the equivalent inclusion size ($\sqrt{area}$). Statistical analysis using Gumbel extreme value model was used to predict the largest inclusion size present in the highly stressed volume of the tested specimens.

At the higher fatigue stress amplitude, the percentage of cracks initiating at inclusions reduced to 41%. Majority of the cracks initiated at the surface discontinuities induced by the grinding or the peening process. However, similar fatigue life scatter as in HCF was observed for as-machined condition, due to the random nature of the surface features produced by the subsequent grinding process. This scatter was reduced by conditions which produced more systematic roughness features (peening with S230 shot at an intensity of 8A), and also by those exhibiting low surface roughness where crack initiation was governed by surface (polished) and subsurface inclusions (peening with S230 shot at an intensity of 8A). A statistical model (based on fatigue life dispersion analysis using B-basis) and an analytical model (based on stress intensity factor and long crack propagation) were used to estimate the worst-case fatigue lives for each peening condition at the higher stress amplitude. The analytical model was improved by incorporating short crack propagation.

The main conclusions derived from the analyses of the experimental and modelling results are as follows:

- Shot peening does not have a significant effect on fatigue life at lower stress amplitudes while it can be detrimental to fatigue life at higher stress amplitudes. Significant fatigue life improvement is however expected in case of components experiencing a stress gradient (bending fatigue).
- Shot peening performed using larger shots (S230) and at low intensity (4A) gives the best trade-off between the beneficial effect of CRS and the detrimental effect of peening induced roughness.
- Peening with CW14 shots at 8A intensity causes higher fatigue life dispersion than the as-machined specimens tested at higher stress amplitudes and therefore, is highly unreliable.
- Material cleanliness is the limiting factor for fatigue life of all peening conditions tested at lower stress amplitudes and for the specimens treated using S230 shot at intensities of 4A and 8A tested at higher stress amplitudes.
- Gumbel extreme value statistical analysis should be used to determine the material cleanliness combined with the conventional metallographic approach.
- Analytically predicted fatigue lives agreed well with the B-basis values for conditions where crack initiation was triggered by surface or subsurface inclusions. For peening conditions where crack initiation was triggered by surface roughness features, the effect of CRS in delaying crack initiation and short crack propagation need to be considered in the analytical model to prevent underestimation of fatigue life.
- The analytical model accounts for the individual size dispersion for each discontinuity type to estimate the corresponding maximum stress intensity factor (calculated using Murakami's approximations [15]) and therefore, predict the crack initiation sites corresponding to the worst-case scenarios. The B-basis analysis lacks in this regard as a single distribution model is used to characterise fatigue lives resulting from failures due to multiple discontinuity types.
- Prior austenite grain boundaries were identified as the barriers to short crack propagation within the region of peening induced CRS based on the short crack propagation tests.

Therefore, the analytical model was further improved to account for short crack propagation affected by the material microstructure and CRS. The improved model was able to accurately predict the average fatigue lives of shot peened rectangular hourglass specimens tested at the higher stress amplitude (within 15% of the experimental fatigue lives). The predictions were, however, underestimated by upto a factor of 2 when compared to the cylindrical specimens. The presence of edges in the rectangular specimens is expected to have favored local plastic deformation when compared to the continuous surface of the cylindrical specimens, which led to higher experimental fatigue lives in case of the latter.

Recommendations for future work

- **Study the effect of shot peening on the fatigue life of 300M steel specimens subjected to bending fatigue**

  Although the fatigue lives of the peened specimens were limited by the material cleanliness, it was observed that in HCF, a single specimen treated using S230 shot at 8A intensity where the cracks initiated at surface discontinuities, had a fatigue life of more than a million cycles (34% higher than the average fatigue life for the condition). Similarly, at the higher stress amplitude, the specimen treated using S230 shot at 4A intensity yielded the highest fatigue life when crack initiation occurred at surface roughness discontinuities. Therefore, to evaluate the improvement in fatigue life due to peening, specimens could be subjected to bending fatigue as it would lead to surface crack initiation due to the higher stress concentration at the surface. Rotating bending conditions are relevant to most of the parts in aerospace applications. Greater influence of compressive residual stresses on the rotating bending fatigue life of high strength steels have been reported in the works of several authors ([2], [66], [68]).

- **Reduce the surface roughness of the peened specimens**

  It was observed that the peening induced roughness was detrimental to fatigue life for some conditions. Therefore, a reduction of the roughness is desirable to achieve better fatigue lives. As reported by Segurado et al. [161], a second low intensity peening treatment using ceramic shots improved the rotating bending fatigue life of heat treated 4340 steel. The second treatment reduced the surface roughness induced by a prior treatment using cut wire

shots of 0.7 mm diameter at 19A intensity and 100% coverage. Single peening treatments using ceramic shot at 8A and 100% coverage were also reported to produce similar results.

- **Quantify crack initiation life for peened cylindrical specimens**

  The proposed analytical model underestimated the fatigue life of peened cylindrical specimens when CRS effect on short crack propagation based on experiments using rectangular hourglass specimens were considered. This underestimation was more pronounced for specimens tested at the lower stress amplitudes than at the higher stress amplitude. Indeed, at low stress amplitudes, the crack initiation life would occupy a major portion of the specimens' fatigue life. A difference in stress concentration produced by the specimen geometry would drastically affect the crack initiation life and hence the total fatigue life. The incorporation of crack initiation life in HCF is therefore necessary for accurate fatigue life predictions when the crack initiates at surface discontinuities.

- **Investigate crack initiation from inclusions and its implementation in fatigue life models**

  It was observed that the analytical model underestimated the fatigue life of shot peened specimens where cracks initiated at interior inclusions. The model assumes that the fatigue crack grows to the size of the inclusion in a few cycles and therefore considers the inclusion size to be the initial crack size during fatigue life estimation. However, it is hypothesized that the crack is of the size of a grain and takes a considerable number of cycles to grow to the size described by LEFM. Similar hypothesis has been proposed by Huron and Roth [71] in their work on a shot peened powder metallurgy Ni superalloy. Finite element analysis could be used to model the crack formation from inclusions and its early growth. Factors other than inclusion size such as inclusion shape, inclusion roughness [162], and the state of the inclusions after shot peening (intact, cracked or debonded) [163] may also affect the fatigue life of the material and should be considered.

- **Investigate CRS profiles and short crack propagation for S230-4A peening condition**

  In this work, peening with S230 shot at 4A intensity was found to have the most beneficial effect on the fatigue life of specimens tested at the higher stress amplitude. Therefore, it would be interesting to quantify the CRS, CRS relaxation and study the effect of short crack

propagation for this condition. The high fatigue lives and reduced number of cycles to crack initiation at surface roughness for this condition may be related to a reduced cyclic softening effect. Therefore, the FWHM vs depth profiles for the S230-4A condition should also be investigated.

- **Perform nanoindentation to investigate the work hardening/softening induced by peening**

  Since the microhardness vs depth profiles performed on the peened specimens were inconclusive, nanoindentation could be used to gather information regarding the properties of the work hardened/softened layer induced by peening. Such information would be helpful to corroborate or contradict the trends obtained from FWHM vs depth profiles.

BIBLIOGRAPHY

1. De los Rios, E.R., et al., *Fatigue crack initiation and propagation on shot-peened surfaces in A316 stainless steel.* International Journal of Fatigue, 1995. **17**(7): p. 493-499.
2. Torres, M.A.S. and H.J.C. Voorwald, *An evaluation of shot peening, residual stress and stress relaxation on the fatigue life of AISI 4340 steel.* International Journal of Fatigue, 2002. **24**(8): p. 877-886.
3. Youngblood, J. and M. Raghavan, *Correlation of microstructure with mechanical properties of 300M steel.* Metallurgical Transactions A, 1977. **8**(9): p. 1439-1448.
4. Figueroa-Gordon, D.J., *Hydrogen re-embrittlement susceptibility of ultra high strength steels,* 2005, Cranfield University.
5. Military Handbook, S., *Metallic materials and elements for aerospace vehicle structures.* Department of Defense, Washington DC (Nov. 1990), 1972: p. 9.16-9.20.
6. Suresh, S., *Fatigue of Materials* Cambridge Solid State Science Series1991, Cambridge: Cambridge University Press.
7. Kendall, J., M. James, and J. Knott. *The behaviour of physically short fatigue cracks in steels*. in *The Behaviour of Short Fatigue Cracks, EGF Pub.1*. 1986. Mechanical Engineering Publications.
8. Furuya, Y., *Notable size effects on very high cycle fatigue properties of high-strength steel.* Materials Science and Engineering: A, 2011. **528**(15): p. 5234-5240.
9. Li, S., *Effects of inclusions on very high cycle fatigue properties of high strength steels.* International Materials Reviews, 2012. **57**(2): p. 92-114.
10. Sakai, T., H. Harada, and N. Oguma, *Crack initiation mechanism of bearing steel in very high cycle fatigue*, in *Fracture of Nano and Engineering Materials and Structures*2006, Springer. p. 1129-1130.
11. Shiozawa, K., et al., *Subsurface crack initiation and propagation mechanism in high-strength steel in a very high cycle fatigue regime.* International Journal of Fatigue, 2006. **28**(11): p. 1521-1532.

12. Zhou, C., et al., *Influence of Hydrogen on GBF in Very High Cycle Fatigue of High Strength Steel.* Journal of Iron and Steel Research, International, 2013. **20**(12): p. 92-97.

13. Weijun, H., et al., *High-cycle Fatigue Fracture Behavior of Ultrahigh Strength Steels.* Journal of Materials Science & Technology 2008. **24**(5): p. 787-792.

14. Murakami, Y. and T. Endo, *Effects of small defects on fatigue strength of metals.* International Journal of Fatigue, 1980. **2**(1): p. 23-30.

15. Murakami, Y., S. Kodama, and S. Konuma, *Quantitative evaluation of effects of non-metallic inclusions on fatigue strength of high strength steels. I: Basic fatigue mechanism and evaluation of correlation between the fatigue fracture stress and the size and location of non-metallic inclusions.* International Journal of Fatigue, 1989. **11**(5): p. 291-298.

16. Murakami, Y. and H. Usuki, *Quantitative evaluation of effects of non-metallic inclusions on fatigue strength of high strength steels. II: Fatigue limit evaluation based on statistics for extreme values of inclusion size.* International Journal of Fatigue, 1989. **11**(5): p. 299-307.

17. Zhang, J., et al., *Influence of inclusion size on fatigue behavior of high strength steels in the gigacycle fatigue regime.* International Journal of Fatigue, 2007. **29**(4): p. 765-771.

18. Yang, Z., et al., *On the critical inclusion size of high strength steels under ultra-high cycle fatigue.* Materials Science and Engineering: A, 2006. **427**(1): p. 167-174.

19. Zhang, L.-f., *Inclusion and Bubble in Steel—A Review.* Journal of Iron and Steel Research, International, 2006. **13**(3): p. 1-8.

20. Van Den Avyle, J.A., *Correlation of Fractography, Microstructure, and Fracture Toughness Behavior of High Strength Alloys,* in *Department of Metallurgy and Materials Science*1975, Massachusetts Institute of Technology, Cambridge.

21. Spriestersbach, D., P. Grad, and E. Kerscher, *Influence of different non-metallic inclusion types on the crack initiation in high-strength steels in the VHCF regime.* International Journal of Fatigue, 2014. **64**: p. 114-120.

22. Liu, Y., et al., *Dependence of fatigue strength on inclusion size for high-strength steels in very high cycle fatigue regime.* Materials Science and Engineering: A, 2009. **517**(1-2): p. 180-184.

23. Kiessling, R., *Non-metallic inclusions in steel, Part III*1978, London, The Metals Society. 87-94.

24. Tanaka, K. and T. Mura, *A theory of fatigue crack initiation at inclusions.* Metallurgical Transactions A, 1982. **13**(1): p. 117-123.

25. Murakami, Y., *Metal fatigue: effects of small defects and nonmetallic inclusions*2002: Elsevier.

26. Murakami, Y., T. Toriyama, and E. Coudert, *Instructions for a new method of inclusion rating and correlations with the fatigue limit.* Journal of Testing and Evaluation, 1994. **22**(4): p. 318-326.

27. Miller, K.J., *The behaviour of short fatigue cracks and their initiation Part I—A review of two recent books.* Fatigue & Fracture of Engineering Materials & Structures, 1987. **10**(1): p. 75-91.

28. Dowling, N.E., *Mechanical behavior of materials: engineering methods for deformation, fracture, and fatigue*2012: Pearson.

29. Pearson, S., *Initiation of fatigue cracks in commercial aluminium alloys and the subsequent propagation of very short cracks.* Engineering Fracture Mechanics, 1975. **7**(2): p. 235-247.

30. Morris, W.L., *The noncontinuum crack tip deformation behavior of surface microcracks.* Metallurgical Transactions A, 1980. **11**(7): p. 1117-1123.

31. Miller, K., *The short crack problem.* Fatigue & Fracture of Engineering Materials & Structures, 1982. **5**(3): p. 223-232.

32. Kaynak, C., A. Ankara, and T. Baker, *Effects of short cracks on fatigue life calculations.* International journal of fatigue, 1996. **18**(1): p. 25-31.

33. Taylor, D. and J. Knott, *Fatigue crack propagation behaviour of short cracks; the effect of microstructure.* Fatigue & Fracture of Engineering Materials & Structures, 1981. **4**(2): p. 147-155.

34. Kitagawa, H. and S. Takahashi. *Applicability of fracture mechanics to very small cracks or the cracks in the early stage*. in *Second International Conference on Mechanical Behavior of Materials. ASM, Metals Park, Ohio. 1976, 627-631*. 1976.

35. E1820, A., *Standard Test Method for Measurement of Fracture Toughness*, 2017: West Conshohocken, PA.

36. Anderson, T.L., *Fracture mechanics: fundamentals and applications*2005: CRC press.

37. Lankford, J., *The growth of small fatigue cracks in 7075–T6 aluminum.* Fatigue & Fracture of Engineering Materials & Structures, 1982. **5**(3): p. 233-248.

38. Suresh, S. and R.O. Ritchie, *Propagation of short fatigue cracks.* International Metals Reviews, 1984. **29**(1): p. 445-475.

39. Ritchie, R.O. and J. Lankford, *Small fatigue cracks: A statement of the problem and potential solutions.* Materials Science and Engineering, 1986. **84**: p. 11-16.

40. Brown, M. *Interfaces between short, long, and non-propagating cracks*. in *EGF Pub.1*. 1986. Mechanical Engineering Publications.

41. Hobson, P., M. Brown, and E. de Los Rios. *Two phases of short crack growth in a medium carbon steel*. in *Behaviour of short fatigue cracks*. 1986.

42. Tokaji, K. and T. Ogawa, *The growth behaviour of microstructurally small fatigue cracks in metals.* Short fatigue cracks, ESIS, 1992. **13**: p. 85-99.

43. Miller, K., *The behaviour of short fatigue cracks and their initiation part II -a general summary.* Fatigue & Fracture of Engineering Materials & Structures, 1987. **10**(2): p. 93-113.

44. McEvily, A.J., *The Growth of Short Fatigue Cracks.* Journal of the Society of Materials Science, Japan, 1998. **47**(3): p. 3-11.

45. Miller, K.J., *Materials science perspective of metal fatigue resistance.* Materials science and technology, 1993. **9**(6): p. 453-462.

46. Lankford, J., *Initiation and early growth of fatigue cracks in high strength steel.* Engineering Fracture Mechanics, 1977. **9**(3): p. 617-624.

47. Tanaka, K. *Mechanics and micromechanics of fatigue crack propagation*. in *Fracture Mechanics: Perspectives and Directions Twentieth Symposium*. 1989.

48. Hussain, K., *Short fatigue crack behaviour and analytical models: a review.* Engineering Fracture Mechanics, 1997. **58**(4): p. 327-354.

49. De Los Rios, E., Z. Tang, and K. Miller, *Short crack fatigue behaviour in a medium carbon steel.* Fatigue & Fracture of Engineering Materials & Structures, 1984. **7**(2): p. 97-108.

50. Tanaka, K., Y. Nakai, and M. Yamashita, *Fatigue growth threshold of small cracks.* International Journal of Fracture, 1981. **17**(5): p. 519-533.

51. Dowson, A.L., M.D. Halliday, and C.J. Beevers, *In-situ SEM studies of short crack growth and crack closure in a near-alpha Ti alloy.* Materials & Design, 1993. **14**(1): p. 57-59.

52. Morris, W., *The early stage of fatigue crack propagation in Al 2048.* Metallurgical Transactions A, 1977. **8**(4): p. 589-596.

53. Paris, P. and F. Erdogan, *A critical analysis of crack propagation laws.* Journal of Fluids Engineering, 1963. **85**(4): p. 528-533.

54. Administration, F.A., *Metallic materials properties development and standardization (MMPDS), MMPDS-05*, 2010.

55. Sih, G.C., *Multiscale Fatigue Crack Initiation and Propagation of Engineering Materials: Structural Integrity and Microstructural Worthiness: Fatigue Crack Growth Behaviour of Small and Large Bodies*. Vol. 152. 2008: Springer Science & Business Media.

56. Standard, S., *Procedures for Using Standard Shot Peening Test Strip*, in *J443*2010.

57. Matlock, B.S., D.J. Snoha, and S.M. Grendahl, *Using XRD elastic and plastic strain data to evaluate the effectiveness of different cold-working techniques in aerospace materials.* Powder Diffraction, 2009. **24**(SupplementS1): p. S51-S58.

58. Gao, Y.-K., M. Yao, and J.-K. Li, *An analysis of residual stress fields caused by shot peening.* Metallurgical and Materials Transactions A, 2002. **33**(6): p. 1775-1778.

59. Prevey, P., et al. *Comparison of Mechanical Suppression by Shot Peening and Low Plasticity Burnishing to Mitigate SCC and Corrosion Fatigue Failures in 300M Landing Gear Steel* in *ICSP-9* 2005.

60. Meguid, S.A., *Effect of partial-coverage upon the fatigue fracture behaviour of peened components.* Fatigue & Fracture of Engineering Materials & Structures, 1991. **14**(5): p. 515-530.

61. Prevey, P.S. and J.T. Cammett, *The effect of shot peening coverage on residual stress, cold work and fatigue in a Ni-Cr-Mo low alloy steel*, 2000, Lambda Research Cincinnati OH.

62. Fathallah, R., et al., *High cycle fatigue behavior prediction of shot-peened parts.* International Journal of Fatigue, 2004. **26**(10): p. 1053-1067.

63. Herzog, R., et al., *The significance of Almen intensity for the generation of shot peening residual stresses.* stress, 1996. **10**: p. 11.

64. Robertson, G., *The effects of shot size on the residual stresses resulting from shot peening*, 1971, SAE Technical Paper.

65. Berns, H. and L. Weber. *Crack initiation and growth in shot-peened and prestrained peened high strength steel*. in *ICSP-2*. 1984. Chicago, U.S.A.

66. Meguid, S.A. and D.W. Hammond, *Fatigue Fracture and Residual Stress Relaxation in Shot-Peened Components*, in *International Conference on Residual Stresses*, G. Beck, S. Denis, and A. Simon, Editors. 1989, Springer Netherlands. p. 797-802.

67. Guagliano, M. and L. Vergani, *An approach for prediction of fatigue strength of shot peened components.* Engineering Fracture Mechanics, 2004. **71**(4-6): p. 501-512.

68. Peige, S., et al. *Qualitative Analysis about Effect of Shot Peening on Fatigue Limit of a 300M Steel under the Rotating Bending Condition*. in *ICSP-6*. 1996.

69. Llaneza, V. and F. Belzunce, *Optimal shot peening treatments to maximize the fatigue life of quenched and tempered steels.* Journal of Materials Engineering and Performance, 2015. **24**(7): p. 2806-2815.

70. Barrie, R.L., et al., *Effectiveness of shot peening in suppressing fatigue cracking at non-metallic inclusions in Udimet® 720.* Materials Science and Engineering: A, 2008. **474**(1-2): p. 71-81.

71. Huron, E.S. and P.G. Roth, *The influence of inclusions on low cycle fatigue life in a P/M nickel-base disk superalloy.* Superalloys 1996, 1996: p. 359-368.

72. Ypsilantis, D., C. Mas, and L. Castex. *Shot peening influence on the endurance limit in fatigue of the SAE9254 steel*. in *Groupement frangais pour 1 'analyse des contraintes par dazractometrie X*. 1984. Aix-en provence, France.

73. Tekeli, S., *Enhancement of fatigue strength of SAE 9245 steel by shot peening.* Materials Letters, 2002. **57**(3): p. 604-608.

74. Gray, H., L. Wagner, and G. Lutjering *Influence of shot peening induced surface roughness, residual macro stresses and dislocation density on the elevated temperature HCF properties of Ti alloy*.

75. He, B., et al., *Effects of shot peening on short crack growth rate and resulting low cycle fatigue behaviour in low pressure turbine blade material.* Materials Science and Technology, 2013. **29**(7): p. 788-796.

76. Verpoort, C. and C. Gerdes, *Influence of shot peening on material properties and the controlled shot peening of turbine blades.* Metal Behaviour and Surface Engineering, 1989.

77. Gray, H., L. Wagner, and G. Lutjering, *Influence of Shot Peening Induced Surface Roughness, Residual Macrostresses and Dislocation Density on the Elevated Temperature HCF-Properties of Titanium Alloys.(Retroactive Coverage).* Shot Peening: Science, Technology, 1987: p. 447-457.

78. Li, J., et al., *An analysis of stress concentrations caused by shot peening and its application in predicting fatigue strength.* Fatigue & Fracture of Engineering Materials & Structures, 1992. **15**(12): p. 1271-1279.

79. Curtis, S., et al., *Analysis of the effects of controlled shot peening on fatigue damage of high strength aluminium alloys.* International Journal of Fatigue, 2003. **25**(1): p. 59-66.

80. Rodopoulos, C., et al., *Optimisation of the fatigue resistance of 2024-T351 aluminium alloys by controlled shot peening—methodology, results and analysis.* International Journal of Fatigue, 2004. **26**(8): p. 849-856.

81. Klotz, T., et al., *Surface characteristics and fatigue behavior of shot peened Inconel 718.* International Journal of Fatigue, 2018. **110**: p. 10-21.

82. Wang, Z.-Y., Q.-Y. Wang, and M. Cao, *Experimental Study on Fatigue Behaviour of Shot-Peened Open-Hole Steel Plates.* Materials, 2017. **10**(9): p. 996.

83. Tosha, K. *Characteristics of shot peened surfaces and surface layers*. in *Proceedings of the first Asia-Pacific forum on precision surface finishing and deburring technology*. 2001.

84. Webster, G. and A. Ezeilo, *Residual stress distributions and their influence on fatigue lifetimes.* International Journal of Fatigue, 2001. **23**: p. 375-383.

85. Dieter, G.E. and D. Bacon, *Mechanical metallurgy*. Vol. 3. 1986: McGraw-Hill New York.

86. Morrow, J. and G. Sinclair. *Cycle-dependent stress relaxation*. in *Symposium on basic mechanisms of fatigue, ASTM STP*. 1959.

87. Jhansale, H. and T. Topper, *Engineering analysis of the inelastic stress response of a structural metal under variable cyclic strains.* ASTM STP, 1973. **519**: p. 246-270.

88. Kodama, S. *The behavior of residual stress during fatigue stress cycles*. in *Proceedings of the International Conference on Mechanical Behavior of Metals II, Society of Material Science, Kyoto*. 1972.

89. Bergström, J. and T. Ericsson, *Relaxation of shot peening induced compressive stress during fatigue of notched steel samples.* Surface Engineering, 1986. **2**(2): p. 115-120.

90. De Los Rios, E., M. Trull, and A. Levers, *Modelling fatigue crack growth in shot-peened components of Al 2024-T351.* Fatigue & Fracture of Engineering Materials & Structures, 2000. **23**(8): p. 709-716.

91. Navarro, A. and E. Rios, *A model for short fatigue crack propagation with an interpretation of the short-long crack transition.* Fatigue & Fracture of Engineering Materials & Structures, 1987. **10**(2): p. 169-186.

92. Navarro, A. and E. De Los Rios, *An alternative model of the blocking of dislocations at grain boundaries.* Philosophical Magazine A, 1988. **57**(1): p. 37-42.

93. Navarro, A. and E. De Los Rios, *Compact solution for a multizone BCS crack model with bounded or unbounded end conditions.* Philosophical Magazine A, 1988. **57**(1): p. 43-50.

94. Navarro, A. and E. Rios, *A microstructurally-short fatigue crack growth equation.* Fatigue & Fracture of Engineering Materials & Structures, 1988. **11**(5): p. 383-396.

95. Navarro, A. and E. De Los Rios, *Short and long fatigue crack growth: a unified model.* Philosophical Magazine A, 1988. **57**(1): p. 15-36.

96. Bilby, B., A. Cottrell, and K. Swinden, *The spread of plastic yield from a notch.* Proceedings of the Royal Society of London. Series A. Mathematical and Physical Sciences, 1963. **272**(1350): p. 304-314.

97. Taira, S., K. Tanaka, and Y. Nakai, *A model of crack-tip slip band blocked by grain boundary.* Mechanics Research Communications, 1978. **5**(6): p. 375-381.

98. De los Rios, E. and A. Navarro, *Considerations of grain orientation and work hardening on short-fatigue-crack modelling.* Philosophical Magazine A, 1990. **61**(3): p. 435-449.

99. Navarro, A. and E. De Los Rios, *Fatigue crack growth modelling by successive blocking of dislocations.* Proceedings of the Royal Society of London. Series A: Mathematical and Physical Sciences, 1992. **437**(1900): p. 375-390.

100. Solis, J., J. Oseguera-Peña, and I. Betancourt, *Short Crack Propagation Model Applied to Shot Peened Aluminium Alloys.* Advanced Materials Research, 2009. **65**: p. 53-61.

101. Liu, J. and M. Pang, *Fatigue life prediction of shot-peened steel.* International Journal of Fatigue, 2012. **43**(Supplement C): p. 134-141.

102. You, C., et al., *Low cycle fatigue life prediction in shot-peened components of different geometries–part II: life prediction.* Fatigue & Fracture of Engineering Materials & Structures, 2017. **40**(5): p. 749-760.

103. Xiang, Y. and Y. Liu, *Mechanism modelling of shot peening effect on fatigue life prediction.* Fatigue & Fracture of Engineering Materials & Structures, 2010. **33**(2): p. 116-125.

104. Liu, Y. and S. Mahadevan, *Fatigue limit prediction of notched components using short crack growth theory and an asymptotic interpolation method.* Engineering Fracture Mechanics, 2009. **76**(15): p. 2317-2331.

105. Xiang, Y., Z. Lu, and Y. Liu, *Crack growth-based fatigue life prediction using an equivalent initial flaw model. Part I: Uniaxial loading.* International Journal of Fatigue, 2010. **32**(2): p. 341-349.

106. Cadario, A. and B. Alfredsson, *Fatigue growth of short cracks in Ti-17: experiments and simulations.* Engineering Fracture Mechanics, 2007. **74**(15): p. 2293-2310.

107. Marines-Garcia, I., et al., *Fatigue crack growth from small to large cracks on very high cycle fatigue with fish-eye failures.* Engineering Fracture Mechanics, 2008. **75**(6): p. 1657-1665.

108. Gao, Y. and X. Wu, *Experimental investigation and fatigue life prediction for 7475-T7351 aluminum alloy with and without shot peening-induced residual stresses.* Acta Materialia, 2011. **59**(9): p. 3737-3747.

109. Newman Jr, J., et al., *Small-crack effects in high-strength aluminum alloys.* 1994.

110. Bagherifard, S., C. Colombo, and M. Guagliano, *Application of different fatigue strength criteria to shot peened notched components. Part 1: Fracture Mechanics based approaches.* Applied Surface Science, 2014. **289**: p. 180-187.

111. Atzori, B., P. Lazzarin, and G. Meneghetti, *A unified treatment of the mode I fatigue limit of components containing notches or defects.* International Journal of Fracture, 2005. **133**(1): p. 61-87.

112. Bagherifard, S. and M. Guagliano, *Application of different fatigue strength criteria on shot peened notched parts. Part 2: nominal and local stress approaches.* Applied Surface Science, 2014. **289**: p. 173-179.

113. Rice, R., et al. *Development of MMPDS handbook aircraft design allowables*. in *7th Joint DOD/FAA/NASA Conference on Aging Aircraft*. 2003. New Orleans, LA Citeseer.

114. Jackson, J. *Definition of Design Allowables for Aerospace Metallic Materials*. in *AeroMat Conference and Exposition*. 2007. Baltimore, MD.

115. Noyan, I.C. and J.B. Cohen, *Residual stress: measurement by diffraction and interpretation*2013: Springer.

116. Sasaki, T., et al., *Influence of image processing conditions of debye Scherrer ring images in x-ray stress measurement using an imaging plate.* Advanced X-ray Analysis, 1997. **40**: p. 588-594.

117. Delbergue, D., et al., *Comparison of Two X-Ray Residual Stress Measurement Methods: Sin2 ψ and Cos α, Through the Determination of a Martensitic Steel X-Ray Elastic Constant.* Materials Research Proceedings, 2017. **2**.

118. Moore, M. and W. Evans, *Mathematical correction for stress in removed layers in X-ray diffraction residual stress analysis*, 1958, SAE Technical Paper.

119. Bag, A., et al., *Study of short crack growth in shot peened 300M steel*, in *13th International Conference on Shot Peening*2017: Montréal, Canada.

120. International, A., *ASTM E466-15 Standard Practice for Conducting Force Controlled Constant Amplitude Axial Fatigue Tests of Metallic Materials*, 2015: West Conshohocken, PA.

121. International, A., *ASTM E647-15e1 Standard Test Method for Measurement of Fatigue Crack Growth Rates*, 2015: West Conshohocken, PA.

122. Neal, D.M. and M.G. Vangel, *Statistically Based Material Properties. A Military Handbook-17 Perspective*, 1990, Army Lab command Watertown MA Material Technology lab.

123. Anderson, T.W. and D.A. Darling, *A Test of Goodness of Fit.* Journal of the American Statistical Association, 1954. **49**(268): p. 765-769.

124. Jayatilaka, A.d.S. and K. Trustrum, *Statistical approach to brittle fracture.* Journal of Materials Science, 1977. **12**(7): p. 1426-1430.

125. Delahay, T. and T. Palin-Luc, *Estimation of the fatigue strength distribution in high-cycle multiaxial fatigue taking into account the stress–strain gradient effect.* International Journal of Fatigue, 2006. **28**(5): p. 474-484.

126. Wormsen, A. and G. Härkegård. *A statistical investigation of fatigue behaviour according to Weibull's weakest link theory*. in *ECF15*. 2004. Stockolm.

127. Lai, C.-D., *Generalized Weibull Distributions*, in *Generalized Weibull Distributions*2014, Springer. p. 23-75.

128. Schijve, J., *A normal distribution or a Weibull distribution for fatigue lives.* Fatigue & Fracture of Engineering Materials & Structures, 1993. **16**(8): p. 851-859.

129. Schijve, J., *Statistical distribution functions and fatigue of structures.* International Journal of Fatigue, 2005. **27**(9): p. 1031-1039.

130. International, A., *ASTM E2283-08 Standard Practice for Extreme Value Analysis of Nonmetallic Inclusions in Steel and Other Microstructural Features*, 2014: West Conshohocken, PA.

131. Murakami, Y., *Inclusion rating by statistics of extreme values and its application to fatigue strength prediction and quality control of materials.* Journal of Research-National Institute of Standards and Technology, 1994. **99**: p. 345-345.

132. Murakami, Y. and S. Nemat-Nasser, *Interacting dissimilar semi-elliptical surface flaws under tension and bending.* Engineering Fracture Mechanics, 1982. **16**(3): p. 373-386.

133. Klotz, T., et al., *Analytical fatigue life prediction of shot peened Inconel 718.* International Journal of Fatigue, 2018. **113**: p. 204-221.

134. Qiang, B., et al., *Effect of shot peening coverage on residual stress field and surface roughness.* Surface Engineering, 2017: p. 1-8.

135. International, S., *SAE J443. Procedures for Using Standard Shot Peening Almen Strip*, 2010.

136. SAE, *SAE J2277. Shot Peening Coverage Determination*, 2013.

137. Miao, H., et al., *Experimental study of shot peening and stress peen forming.* Journal of Materials Processing Technology, 2010. **210**(15): p. 2089-2102.

138. Hanagarth, H., O. Vöhringer, and E. Macherauch. *Relaxation of shot peening residual stresses of the steel 42 CrMo 4 by tensile or compressive deformation*. in *Proceedings of the Fourth International Conference on Shot Peening*. 1990. The Japan Society of Precision Engineering, Tokyo, Japan.

139. Saberifar, S., et al., *The interaction between non-metallic inclusions and surface roughness in fatigue failure and their influence on fatigue strength.* Materials & Design, 2012. **35**: p. 720-724.

140. International, A., *ASTM E8/E8M-16a Standard Test Methods for Tension Testing of Metallic Materials*, 2016: West Conshohocken, PA.

141. Standard, B., *Steels—micrographic determination of the apparent grain size*, in *BS EN ISO*2003. p. 44.

142. Philip, T.V. and T.J. Mccaffrey, *Ultrahigh-strength steels.* ASM International, Metals Handbook. Tenth Edition., 1990. **1**: p. 430-448.

143. Sohar, C., et al., *Gigacycle fatigue behavior of a high chromium alloyed cold work tool steel.* International Journal of Fatigue, 2008. **30**(7): p. 1137-1149.

144. Murakami, Y., T. Nomoto, and T. Ueda, *Factors influencing the mechanism of superlong fatigue failure in steels.* Fatigue & fracture of engineering materials & structures, 1999. **22**(7): p. 581-590.

145. Murakami, Y., T. Nomoto, and T. Ueda, *On the mechanism of fatigue failure in the superlong life regime (N> 107 cycles). Part 1: influence of hydrogen trapped by inclusions.* Fatigue & Fracture of Engineering Materials & Structures, 2000. **23**(11): p. 893-902.

146. Chapetti, M.D., T. Tagawa, and T. Miyata, *Ultra-long cycle fatigue of high-strength carbon steels part I: review and analysis of the mechanism of failure.* Materials Science and Engineering: A, 2003. **356**(1–2): p. 227-235.

147. Wang, Q., et al., *Effect of inclusion on subsurface crack initiation and gigacycle fatigue strength.* International Journal of Fatigue, 2002. **24**(12): p. 1269-1274.

148. Furuya, Y., T. Abe, and S. Matsuoka, *Inclusion-controlled fatigue properties of 1800 MPA-class spring steels.* Metallurgical and Materials Transactions A, 2004. **35**(12): p. 3737-3744.

149. Higounenc, O., *Correlation of shot peening parameters to surface characteristic.* ICSP-9, Paris, France, 2005: p. 28-35.

150. Iwata, N., et al., *Effect of shot peening on fatigue fracture for an as quenched martensitic steel.* Materials science and technology, 2002. **18**(6): p. 629-632.

151. Gao, Y.-k., et al., *Another mechanism for fatigue strength improvement of metallic parts by shot peening.* Journal of Materials Engineering and Performance, 2003. **12**(5): p. 507-511.

152. Wang, S., et al., *Fatigue limits of shot-peened metals.* Journal of Materials Processing Technology, 1998. **73**(1): p. 57-63.

153. Grad, P. and E. Kerscher, *Reason for the transition of fatigue crack initiation site from surface to subsurface inclusions in high-strength steels.* Fatigue & Fracture of Engineering Materials & Structures, 2017. **40**(11): p. 1718-1730.

154. Bag, A., et al., *Statistical analysis of high cycle fatigue life and inclusion size distribution in shot peened 300M steel.* International Journal of Fatigue, 2019. **118**: p. 126-138.

155. Bianchetti, C., M. Lévesque, and M. Brochu, *Probabilistic analysis of the effect of shot peening on the high and low cycle fatigue behaviors of AA 7050-T7451*. International Journal of Fatigue, 2018. **111**: p. 289-298.

156. Bag, A., et al., *Effect of different shot peening conditions on the fatigue life of 300M steel submitted to high stress amplitudes.* Submitted to International Journal of Fatigue, 2019.

157. E112, A., *Standard Test Methods for Determining Average Grain Size*, 2013: West Conshohocken, PA.

158. Newman Jr, J. and I. Raju, *An empirical stress-intensity factor equation for the surface crack.* Engineering fracture mechanics, 1981. **15**(1-2): p. 185-192.

159. Brochu, M., et al. *Fatigue testing of a cast aluminum alloy: experimental challenges*. in *12th International Conference on Fracture*. 2009. Ottawa.

160. Nogami, S., et al., *Development of fatigue life evaluation method using small specimen.* Journal of Nuclear Materials, 2013. **441**(1-3): p. 125-132.

161. Segurado, E., F. Belzunce, and I.F. Pariente, *Effects of low intensity shot peening treatments applied with different types of shots on the fatigue performance of a high-strength steel.* Surface and Coatings Technology, 2018. **340**: p. 25-35.

162. Gillner, K., M. Henrich, and S. Münstermann, *Numerical study of inclusion parameters and their influence on fatigue lifetime.* International Journal of Fatigue, 2018. **111**: p. 70-80.

163. Prasannavenkatesan, R., et al., *3D modeling of subsurface fatigue crack nucleation potency of primary inclusions in heat treated and shot peened martensitic gear steels.* International Journal of Fatigue, 2009. **31**(7): p. 1176-1189.

APPENDIX A – ARTICLE 4: STUDY OF SHORT CRACK GROWTH IN SHOT PEENED 300M STEEL

Amrita Bag[a], Dorian Delbergue[b], Martin Lévesque[a], Philippe Bocher[b], Myriam Brochu[a]

[a] École Polytechnique de Montréal, Canada, amrita.bag@polymtl.ca

[b] École de technologie supérieure, Canada

Article presented at 13th International Conference on Shot Peening on 19th September 2017.

Keywords: short crack, fatigue, shot peening, high-strength steel, crack initiation

A.1 Introduction

Shot peening can enhance the fatigue life of metals as a result of strain hardening and induced compressive residual stresses (CRS) which either delay the initiation of short fatigue cracks or cause an arrest of the already existing short cracks within the CRS layer. Some studies show that shot peening does not delay the initiation, but the propagation of micro cracks and that strain hardening contributes very little in arresting cracks, as compared to crack closure by CRS [1][2]. Short crack growth (including crack initiation) has been found to account for more than 70% of the fatigue life of a component [3] and therefore could better reflect the effect of peening on fatigue life. These short cracks are usually of the order of a few micrometres to a millimetre in length and have been found to exhibit crack growth rates which are much higher than conventional long Linear Elastic Fracture Mechanics (LEFM) cracks mainly due to the absence of small scale yielding and closure observed in long cracks [4]. Short cracks can be classified into two broad types based on their size and the applied stress namely: microstructurally short cracks (MSC) or Stage I cracks and physically short cracks (PSC) or Stage II cracks as schematized in Fig. A.1. The MSC are usually of the order of microstructural features such as the grain diameter. They exhibit an initial accelerating–decelerating growth pattern as they advance, and the crack tip plastic zone encounters microstructural barriers. Gradually, the plastic zone size increases, thus increasing the crack's resistance to the barriers. After traversing 2-3 grains [4], the effect of microstructure diminishes and crack transitions to Stage II. Its growth is then governed by Elastic-plastic Fracture Mechanics (EPFM); provided the crack is still smaller than 25 times the plastic zone size. As the crack grows further, its size exceeds this value, and after covering approximately 10 grains [4], the crack

behaviour merges with that of a long LEFM crack. Shot peening has been found to primarily affect Stage I and Stage II EPFM cracks [5].

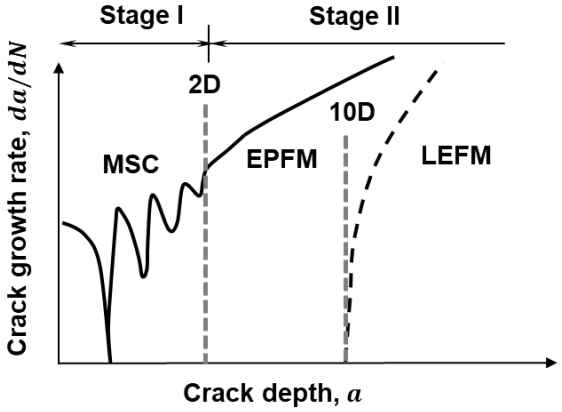

Figure A.1 Crack growth rate vs. crack depth plot (log scale) for short cracks based on [4] (D = grain diameter)

A.2 Objectives

The main objective of the current work was to investigate the effect of shot peening on the short crack initiation and propagation in 300M steel, which is part of a larger objective of modelling the fatigue life of shot peened steel components. Microstructurally and physically short cracks of length ranging from 0.02 mm-0.2 mm have been studied in the current work.

A.3 Methodology

Hourglass specimens (Fig. A.2) of 300M steel have been used to perform interrupted constant stress amplitude axial fatigue tests at R = -1 and 10 Hz for two stress amplitudes: σ_{55} and σ_{64} (55% and 64% of $\sigma_{y,0.2}$ respectively). Three surface conditions have been studied in the present work, namely: polished, as-machined and shot peened. The polished specimens were prepared by mechanically polishing as-machined specimens down to 1 µm surface finish. The peening was achieved by using two types of shots namely CW14 (conditioned cut wire) and S230 (cast steel) at 8A intensity and 100% coverage. A total of 16 samples were tested; 2 samples per stress level for each surface condion. Surface crack length measurements were performed using replica technique to backtrack the initiation and propagation of short cracks in all the specimens. The resulting replicas were analysed by means of optical microscopy. Fractography analysis was performed

using Scanning Electron Microscope (SEM) and Energy Dispersive Spectroscopy (EDS). Moreover, residual stresses for all surface conditions were obtained by X-ray diffraction (XRD) using a Pulstec µ-X360n apparatus equipped with a Cr-tube. To measure the through thickness residual stress profiles, thin layers of material were successively removed by electropolishing using a perchloric acid-based solution. This was performed to study the effect of peening induced residual stresses on short crack growth.

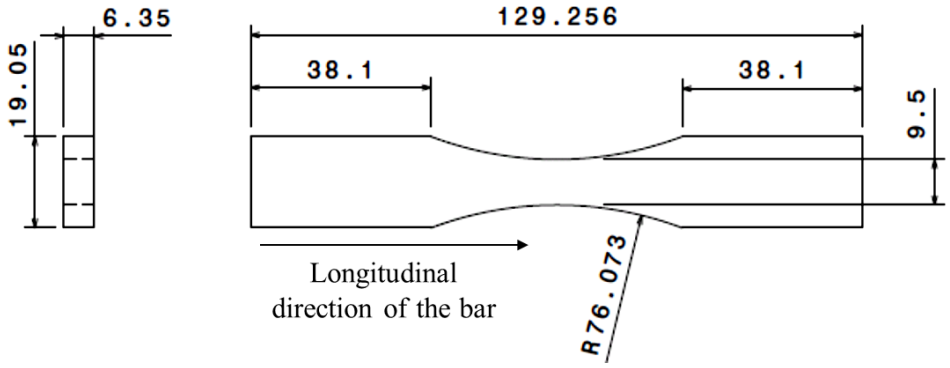

Figure A.2 Hourglass flat specimen dimensions (in mm)

The total fatigue life of a component (N_t) can be divided into three basic stages given by:

$N_t = N_i + N_p + N_{LC}$, where N_i = crack initiation life, N_p = short crack propagation life, N_{LC} = long crack propagation life. In the present study, we will investigate the effects of shot peening on the crack initiation and short crack growth regime durations. Here, crack initiation has been quantified by the number of cycles required to grow a crack of 0.02 mm which is comparable to the average grain diameter of the material, D = 23 µm. Short crack propagation ranges between 0.02 mm to 0.2 mm. The basis of these assumptions will be discussed later in the section "Crack growth rate results".

A.4 Results

A.4.1 Average fatigue life

The average fatigue lives presented in this paper are normalised by the average fatigue life (N_t) of polished specimens as shown by the ordinate legend of Fig. A.3.

At σ_{55}, fatigue life of polished (100%) and as-machined specimens (99%) are similar whereas the fatigue lives of CW14 and S230 peened specimens (84%) are about 16% lower.

At σ_{64}, best fatigue life was given by CW14 peened specimens (117%) which was 17% higher than the baseline polished specimens. The S230 peened (74%) and the as-machined (43%) specimens had 26% and 57% lower lives as compared to the polished specimens respectively.

Thus, shot peening is found to improve fatigue life only in case of the high stress amplitude (σ_{64}) and the CW14 peened specimens showed better life than those with the S230 peening condition. At σ_{55}, both conditions showed similar lives, shorter than the as-machined specimens.

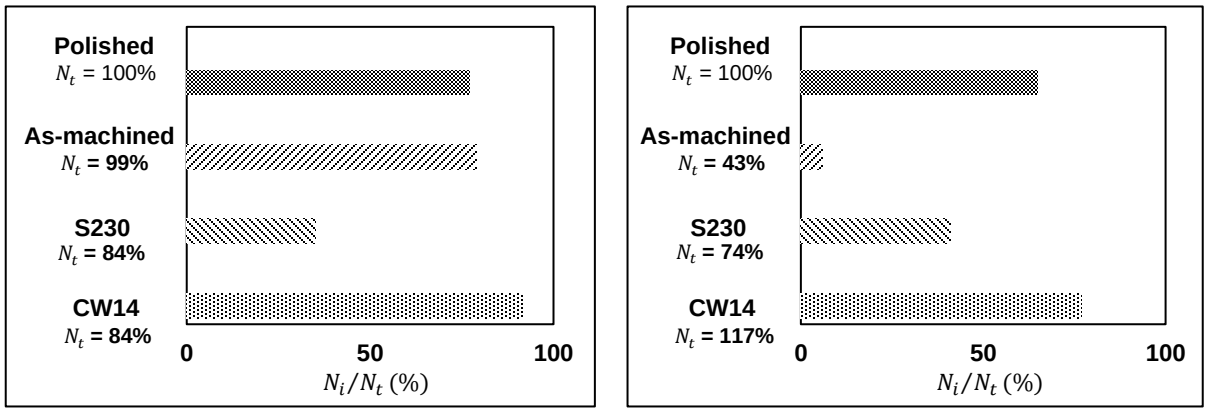

a. b.

Figure A.3 Ratio of crack initiation life (N_i) to total fatigue life (N_t) at a. σ_{55} b. σ_{64}

A.4.2 Effect of peening on crack initiation

For a given surface condition, the abscissa of Fig. A.3 depicts the ratio of crack initiation life to the fatigue life (N_i/N_t), in order to analyze the effect of shot peening on specific damage mechanisms.

Investigating the percentage of total fatigue life (N_t) occupied by crack initiation (N_i), it was observed that it accounts for about 35-92% of N_t at σ_{55}. A higher N_i/N_t ratio resulted in a higher overall fatigue life; except in case of CW14 peened specimens, which in spite of having the highest N_i/N_t, did not have the highest fatigue life (Fig. A.3a). In case of CW14 peened specimens, most of the life was dominated by crack initiation, while in S230 peened specimens, crack initiation occurred relatively early and most of the life was spent in propagation of a short crack. Fatigue lives of both the peening conditions were however very close. At σ_{55}, for both the peening conditions, the cracks initiated at the surface on the specimen edge. The as-machined and the polished specimens were subjected to subsurface crack initiation at non-metallic inclusions mainly composed of Al, Mg, O and Ca (Fig. A.4a). The size of the inclusions (represented as square root

of the inclusion area [6]) was in the range of 1-28 µm and they were situated within a depth of 0.03 mm from the surface.

In case of σ_{64}, N_i/N_t was highest in CW14 peened specimens followed by polished, S230 peened and as-machined specimens (Fig. A.3b) which was consistent with the decreasing order of their fatigue lives. The polished specimens had crack initiation at inclusions similar to the ones tested at σ_{55}. All crack initiations except for polished specimens started at the surface on the specimen edge (Fig. A.4b).

This confirms that shot peening with CW14 delays crack initiation at the higher stress amplitude, σ_{64}. In general, peening with CW14 seems to increase the cycles to crack initiation more than S230 peening at both stress amplitude, reflected by the higher N_i/N_t ratios of CW14 peened specimens compared to S230 peened ones (Fig. A.3).

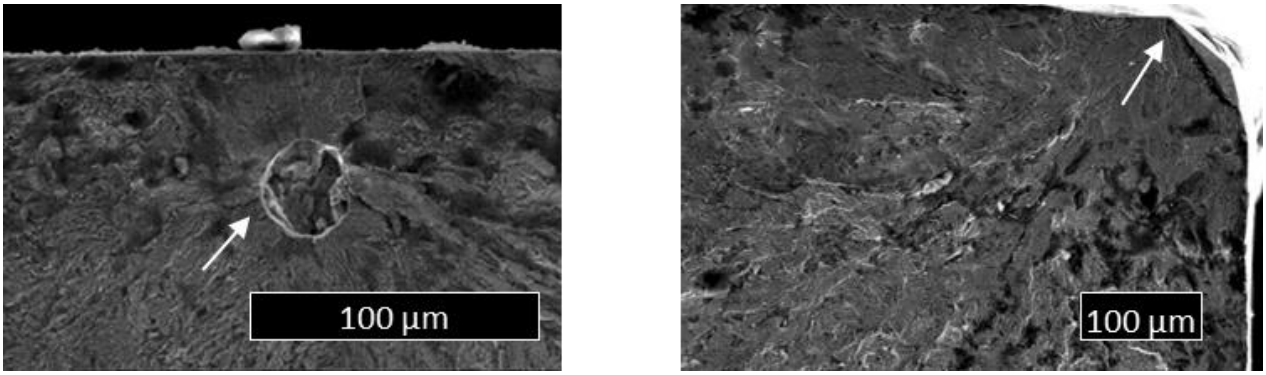

a. b.

Figure A.4 Crack initiation (white arrow) a. at an inclusion in a polished specimen at σ_{55}, b. at the edge in a peened specimen at σ_{64}

A.4.3 Short crack growth rate results

It is evident from the aforementioned results at σ_{55}, that the fatigue lives of both peening conditions are similar although the N_i/N_t ratio of CW14 peened specimens is almost 3 times that of the S230 peened ones. This could indicate that peening with S230 affects the short crack propagation more than crack initiation, contrary to CW14 peening condition. Therefore, it is necessary to investigate how the different peening conditions affect short crack growth as compared to the unpeened conditions.

The aspect ratio (a/c) or the ratio of crack depth, a to surface crack length c has been calculated for cracks upto 0.8 mm in length. Owing to the complex shape of the dominant crack, the calculation of a/c is based on measurements from semi/quarter elliptical shaped secondary cracks that were found on the fracture surface of the specimens tested at σ_{64}. The a/c value was found to be always equal to 1 for $a < 0.8$ mm. No secondary cracks were observed on the fracture surface of specimens tested at σ_{55}. However, the dominant crack morphology of the specimens was similar at both stress amplitudes. Therefore, the same a/c ratio of 1 was used for specimens tested at σ_{55}.

In the current study, the smallest crack depth detected in the replicas corresponds to 0.02 mm. Therefore, N_i was defined as the number of cycles required to reach this size. In case of unpeened specimens, no clear transition from Stage I to stage II was observed due to lack of data. Therefore, based on the predictions of Taylor and Knott [4], the upper limit for Stage I cracks was fixed at 0.05 mm ($2D$) and that for Stage II EPFM cracks at 0.2 mm ($10D$).

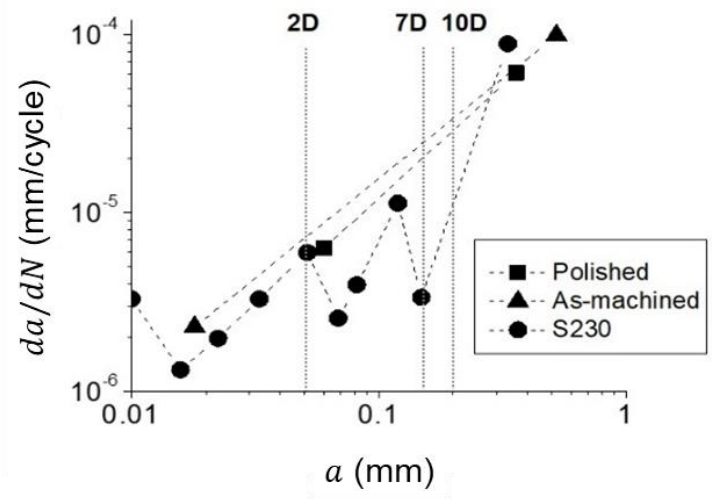

Figure A.5 Crack growth rate vs. crack depth plot (log scale) for polished, as-machined and S230 peened specimen at σ_{55} (Dotted lines are joining experimental points to help visualize acceleration and deceleration)

At σ_{55}, the Stage I propagation rates of polished as-machined and S230-peened specimens were very similar as depicted in Fig. A.5. However, the transition of MSC to EPFM cracks was delayed in S230 peened specimens to $7D$ as compared to unpeened specimens ($2D$). Crack growth was retarded at grain boundary barriers till it reached a size of 0.16 mm ($7D$). As a result, the EPFM

crack propagation rates were 2-4 times lower than the unpeened specimens at the barriers. No observations could be made for CW14 peened specimens due to lack of data.

At σ_{64}, the propagation rates of CW14 peened specimens at the end of Stage I (a = $2D$) were similar to the as-machined specimens and S230 peened specimens as shown in Fig. A.6. However, as the cracks transitioned to Stage II, the crack growth rates in unpeened specimens began to increase monotonically as expected, except for the peened specimens, where the crack growth rates dropped. In CW14 peened specimens, the decrease in crack propagation rates was gradual which delayed the transition of MSC to EPFM cracks. The crack traversed 5 grains instead of 2 grains before switching to Stage II. In S230 peened specimens, crack growth rates after crossing 2 grains decreased by 3-4 times. The growth rates continued to drop until the crack reached a size of 0.07 mm ($3D$) and then accelerated upto 0.12 mm ($5D$). After $5D$, however, the crack growth rates of all conditions were quite similar.

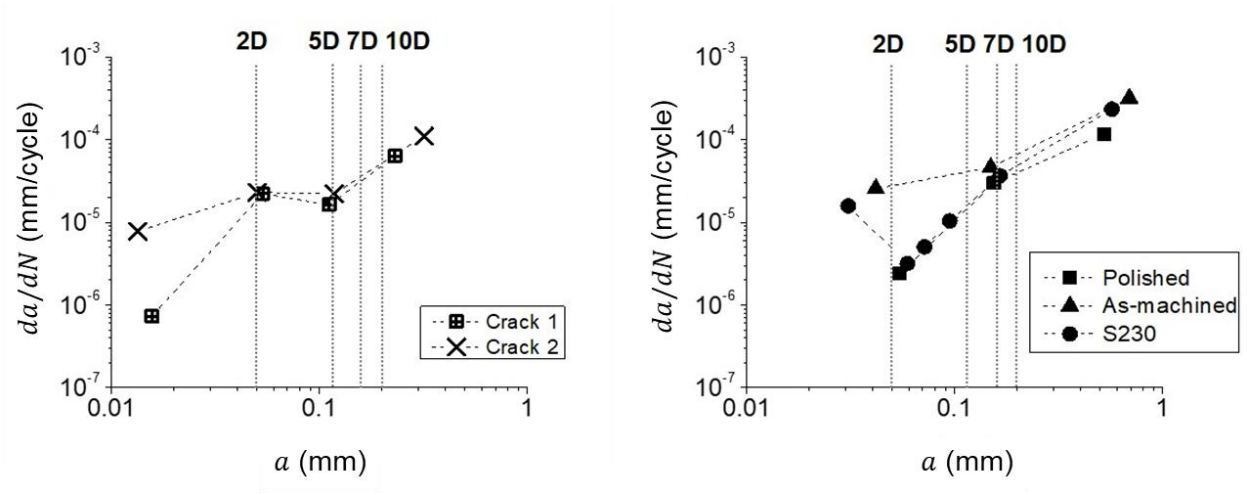

a. b.

Figure A.6 Crack growth rate vs. crack depth plot (log scale) for a. CW14 peened specimen, b. polished, as-machined and S230 peened specimen at σ_{64}

A.4.4 CRS and surface roughness results

The measured residual stress profiles for all surface conditions are presented in Fig. A.7. The surface roughness of all the samples (except polished) was measured using a roughness profilometer. Table A.1 provides the data for surface CRS, depth of CRS, mean roughness parameter R_a, total fatigue life, N_t (%) and the crack initiation sites at σ_{55} and σ_{64} for all tested

conditions. It can be seen that the maximum CRS was same for both S230 and CW14 peened specimens followed by as-machined and finally polished specimens. The CRS was however deeper in S230 peened specimens than the CW14 peened. The surface roughness was highest for the CW14 peening condition, followed by S230 peening condition and finally as-machined. Taking into account all these parameters, the effect of peening on short crack growth and the resulting influence on fatigue life will be discussed below.

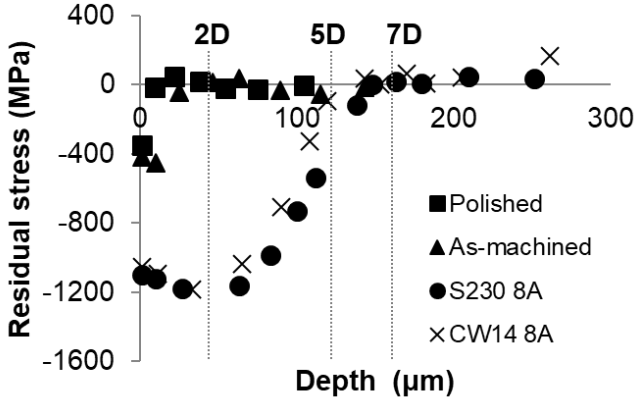

Figure A.7 XRD residual stress profiles for polished, as-machined and peened specimens

Table A.1 Compressive residual stress, roughness, fatigue life and crack initiation site data for all tested conditions

Condition	Surface CRS (MPa)	CRS depth (µm)	R_a (µm)	N_t % (σ_{55})	Crack initiation site (σ_{55})	N_t % (σ_{64})	Crack initiation site (σ_{64})
Polished	-404	8	--	100	Subsurface	100	Subsurface
As- machined	-441	24	0.29 ±0.06	99	Subsurface	43	Surface
S230 8A	-1080	150	0.82 ±0.04	84	Surface	74	Surface
CW14 8A	-1044	125	1.23 ±0.01	84	Surface	117	Surface

A.5 Discussion

In general, a competition between the detrimental effect of roughness and the beneficial effect of CRS was observed and could be related to the resulting trend in fatigue life.

At σ_{55}, highest fatigue life is given by polished and as-machined specimens. The low roughness in the case of polished and as-machined specimens coupled with the CRS resulted in subsurface crack initiation, and hence, a high N_t. In case of peened specimens, the higher roughness overcame the effect of high surface CRS, causing surface rather than subsurface crack initiations. It is however interesting to note that, in spite of having the highest roughness, the CW14 peened specimen had the highest crack initiation life and fatigue life similar to S230-peened ones. Nevertheless, in S230-peened specimens, the in-depth CRS seemed to delay the transition of Stage I to Stage II cracks (Fig. A.5), although it did not improve the overall fatigue life. Therefore, peening did not prove beneficial for fatigue life at the lower stress amplitude (σ_{55}).

At σ_{64}, highest fatigue life is given by CW14 peened specimens followed by polished, S230 peened and as-machined specimens. In polished specimens, in absence of surface defects, crack initiation occurred at subsurface inclusions, and crack initiation was delayed to a greater extent than in as-machined or S230 peened specimens (which were affected by competition between the roughness and CRS). In as-machined specimens, the CRS was not deep enough to affect the short crack propagation rates, therefore the effect of roughness dominated. In S230 peened specimens, the Stage I cracks decelerated while travelling in the region of maximum CRS (1.5D-3D) as shown in Fig. A.6b, which led to a better fatigue life compared to as-machined specimens. On the contrary, in CW14 peened specimens, in spite of the high roughness, crack initiation was delayed. A small amount of crack deceleration occurred between 2D and 5D (Fig. A.6a), which corresponds to the crack growing deeper into the material from a region of maximum CRS to gradually diminishing CRS. Afterwards, crack growth accelerated at around 0.12 mm (or 5D), which corresponds to the end of the CRS layer in CW14 peened specimens (Fig. A.7). It should be noted that, after reaching a length of 0.05 mm (2D), the cracks in CW14 peened specimens had growth rates higher than those of the S230 peening condition which gradually became similar at around 7D. This suggests that S230 peening is more effective in delaying crack propagation compared to CW14 peening, and that the higher fatigue life in CW14 peening condition at σ_{64} is caused primarily by delayed crack initiation.

A.6 Conclusions

Study of short crack behaviour is instrumental in revealing the effect of peening on specific damage mechanisms governing fatigue life. From the present work, the following conclusions can be drawn:

- In general, there seems to be a competition between the detrimental effect of roughness and the beneficial effect of CRS depending on the applied stress. At low stress-high roughness conditions (peened specimens), effect of roughness dominates over CRS, causing surface crack initiation; while in case of low stress-low roughness conditions (unpeened specimens), CRS dominates leading to subsurface crack initiation. At high stress, CRS effect dominates over roughness.
- Higher the N_i/N_t, higher is the fatigue life, irrespective of the stress amplitude (except CW14 at σ_{55}).
- Peening is nevertheless beneficial only for the high stress amplitude (σ_{64}). Of the 2 peening conditions, CW14-8A gave a higher fatigue life at σ_{64} by delaying both crack initiation and short crack propagation. S230-8A condition was found to affect short crack propagation at both σ_{55} and σ_{64} although it did not improve the fatigue life.

A.7 References

[1] Liu, W., Dong, J., Zhang, P., Zhai, C., & Ding, W. (2009). Effect of shot peening on surface characteristics and fatigue properties of T5-treated ZK60 alloy. Materials Transactions, 50(4), 791-798.

[2] Guagliano, M., & Vergani, L. (2004). An approach for prediction of fatigue strength of shot peened components. Engineering Fracture Mechanics, 71(4), 501-512.

[3] Kitagawa, H., & Takahashi, S. (1976). Applicability of fracture mechanics to very small cracks or the cracks in the early stage. In Second International Conference on Mechanical Behavior of Materials. ASM, Metals Park, Ohio. 1976, 627-631.

[4] Taylor, D., & Knott, J. F. (1981). Fatigue crack propagation behaviour of short cracks; the effect of microstructure. Fatigue & Fracture of Engineering Materials & Structures, 4(2), 147-155.

[5] Miller, K. J. (1993). Materials science perspective of metal fatigue resistance. Materials Science and Technology, 9(6), 453-462.

[6] Yukitaka, M., & Masahiro, E. (1983). Quantitative evaluation of fatigue strength of metals containing various small defects or cracks. Engineering Fracture Mechanics, 17(1), 1-15.

APPENDIX B – STATISTICAL ANALYSIS FOR FATIGUE LIFE DATA

B.1 Methodology

We start the analysis by firstly, identifying an appropriate statistical distribution model (for example, lognormal, Weibull, Generalized Extreme Value, etc.) which provides the best fit for the given fatigue life data. In statistics, the probability of a random variable of a continuous distribution (having a probability density function, $f\ (x)$) to acquire a value less than or equal to a value 'k', is defined by the cumulative distribution function:

$$F(a) = \int_{-\infty}^{k} f(x)\, dt \tag{B.1}$$

The parameters for the distribution are then obtained by the principle of maximum likelihood, which works by maximizing the likelihood function given by:

$$\mathcal{L}(\theta; x_1, x_2, \dots, x_n) = \prod_{i=1}^{n} f(x_i|\theta) \tag{B.2}$$

where, θ = parameter set for the distribution, x_i = individual observations made and n = number of observations. Another, more convenient method for achieving the maximum likelihood estimate (mle) for the parameters is by maximizing the natural logarithm of the likelihood function, which has been used for the present work.

The goodness of fit for the model is estimated by means of Anderson-Darling (AD) test which is the best suited for detecting discrepancies between the tail regions of the cumulative distribution function (cdf) of the distribution model and that of the actual data. Reliability estimates are usually measured in the tail regions, which makes it more desirable to evaluate the distributional assumptions near the tail region rather than the mean. The AD test provides an (h, p) value which tends to an ideal value of 0 and 1 respectively provided the data fits perfectly to the model distribution. The h value is the result of a null hypothesis that the particular distribution fits the data provided. An h value of '1' represents the rejection of the null hypothesis while a value of '0' represents an acceptance of the same. The p value represents the probability (at a certain significance level) for which, when the null hypothesis is true, the statistical summary (such as the sample mean difference) for the model would be the same as or of greater magnitude than the actual observed results. Significance level or α denotes the statistical significance of the p value, meaning, the p-value must be greater than a certain critical value of α (usually 0.05) for the p value to be

accepted as statistically significant. The (h, p) value is evaluated for each distribution that is most likely to fit the data until the best fit is obtained.

In case of fatigue life data, survival analysis is commonly used to calculate the probability of an individual surviving a certain minimum number of fatigue cycles by means of a survivor function, $S(x)$ which is related to the cdf given by:

$$S(x) = 1 - F(x) \tag{B.3}$$

The number of cycles leading to 90% survival was back-calculated by feeding the maximum likelihood parameter estimates into the inverse of the cumulative distribution function.

The 95% confidence limits for the parameters were obtained by using maximization of log-likelihood based on a chi-squared (χ^2) approximation. In general, the mle of the parameters have the maximum log-likelihood value, which decreases as we move away from this value. Using χ^2 approximation, we can define a critical value above which the log likelihood is still considered acceptable. This region in parameter space corresponds to the confidence region of the parameters.

B.2 Statistical analysis results for fatigue life data using Minitab (probability plots)

Statistical analyses for the fatigue specimens were performed using Minitab software to determine the 99% survival life at 95% confidence interval. Anderson-Darling test was performed to select the best fit distribution to the fatigue data among Weibull and Lognormal distributions for each surface condition and for both studied stress amplitudes. The resulting plots (Fig. B.1, B.2) showing the fit of the data to the distribution in terms of %probability vs. fatigue life are depicted in this section. The lower the adjusted Anderson Darling coefficient, the better is the fit.

After choosing the best fit distribution, the statistical analysis is performed to estimate 99% survival life at 95% confidence interval. The resulting plots (Fig. B.1, B.2) of probability density function (pdf) vs. fatigue life, survival % vs. fatigue life and hazard function vs. fatigue life are shown. (Hazard function is defined as the instantaneous rate of failure at a given time. An increasing hazard function represents an increasing rate of failure of the component over time.). For the specimens peened using CW14 shot at 8A intensity subjected to a fatigue stress amplitude of 931 MPa, two

sets of analyses have been performed- one treating the runout specimen as a part of the data, and the other by censoring the fatigue life for the runout specimen.

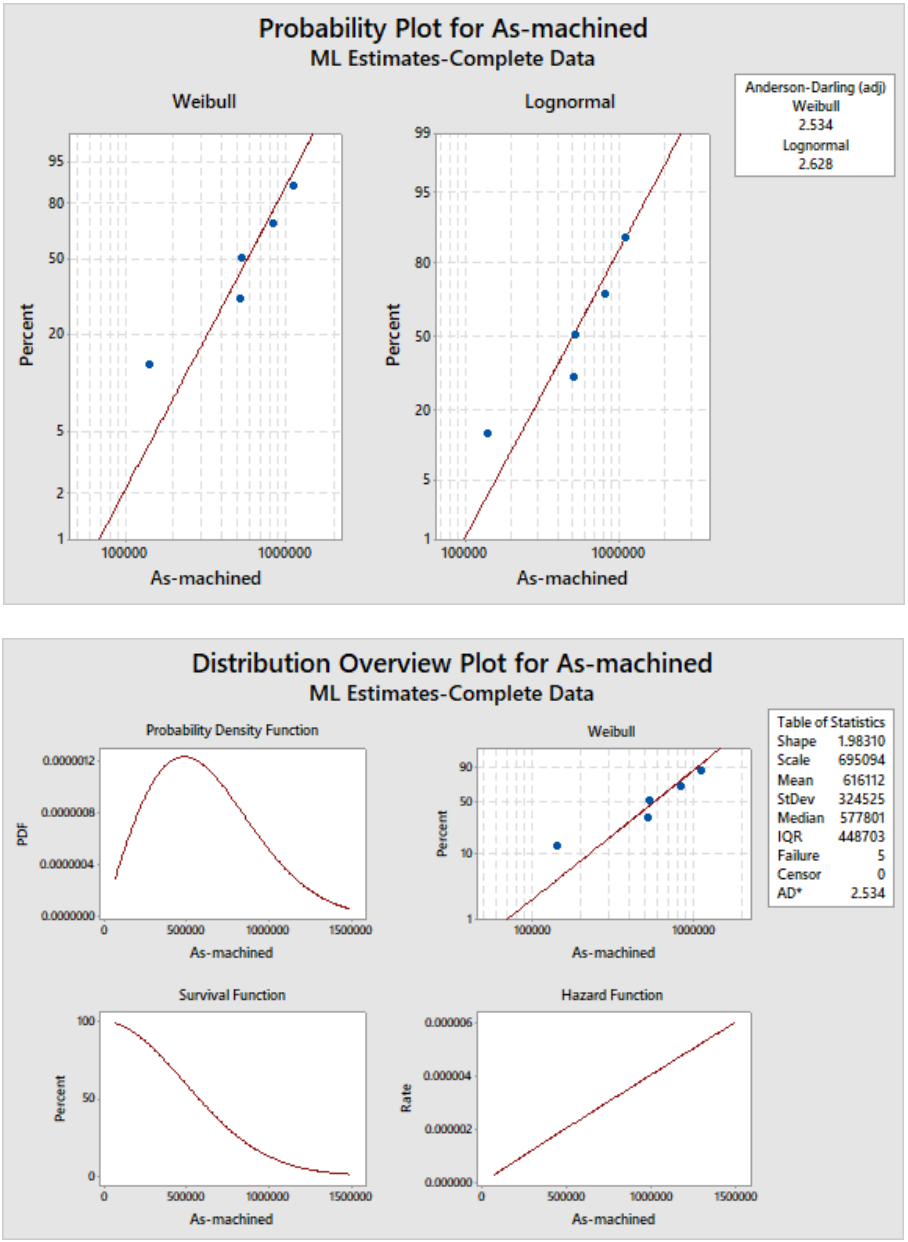

a.

Figure B.1 %Probability vs. fatigue life, probability density function (pdf) vs. fatigue life, survival % vs. fatigue life and hazard function vs. fatigue life plots for a. as-machined specimens, b. polished specimens, c. specimens peened using S230 shot at 4A intensity, d. specimens peened using S230 shot at 8A intensity and e. specimens peened using CW14 shot at 8A intensity subjected to a stress amplitude of 931 MPa (censored & uncensored)

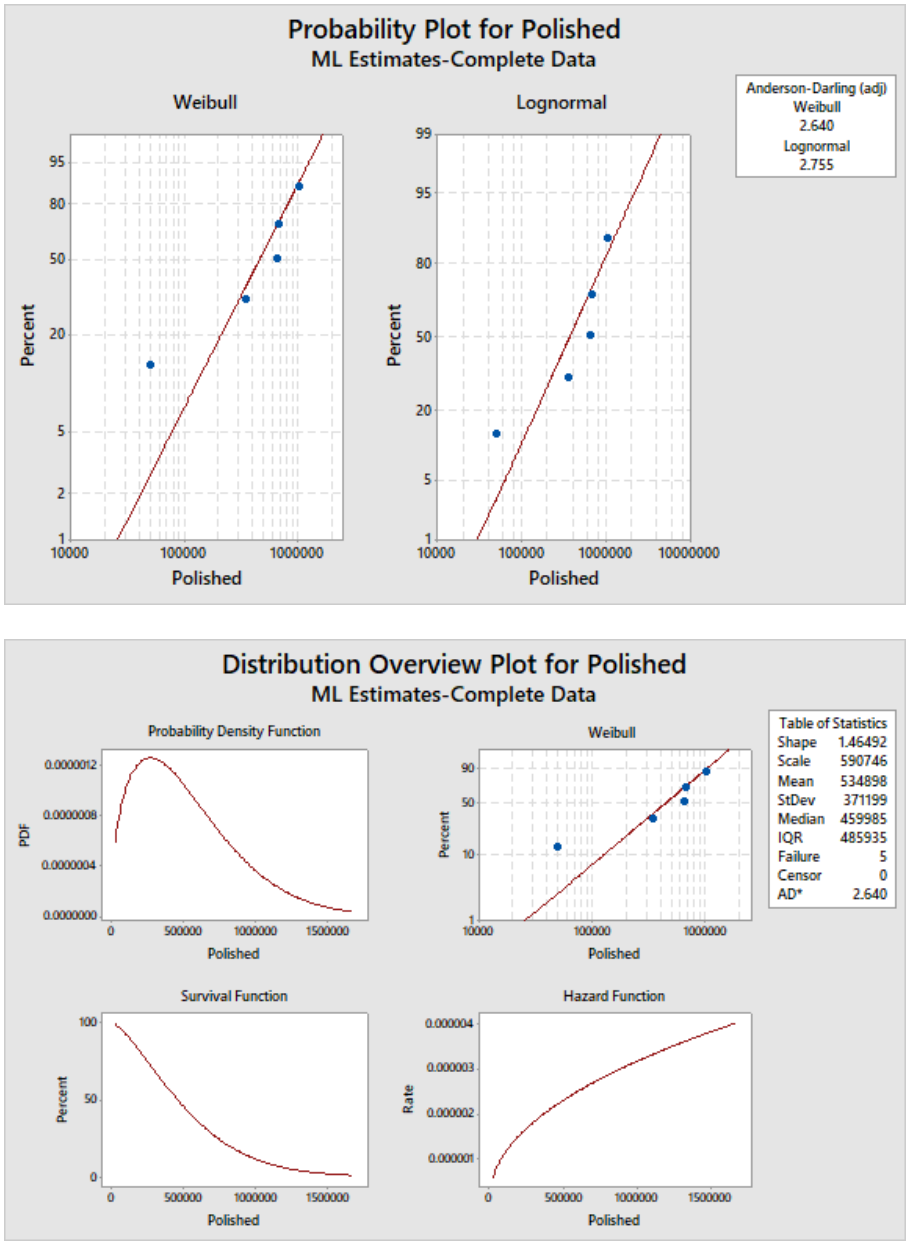

b.

Figure B.1 %Probability vs. fatigue life, probability density function (*pdf*) vs. fatigue life, survival % vs. fatigue life and hazard function vs. fatigue life plots for a. as-machined specimens, b. polished specimens, c. specimens peened using S230 shot at 4A intensity, d. specimens peened using S230 shot at 8A intensity and e. specimens peened using CW14 shot at 8A intensity subjected to a stress amplitude of 931 MPa (censored & uncensored) (cont'd)

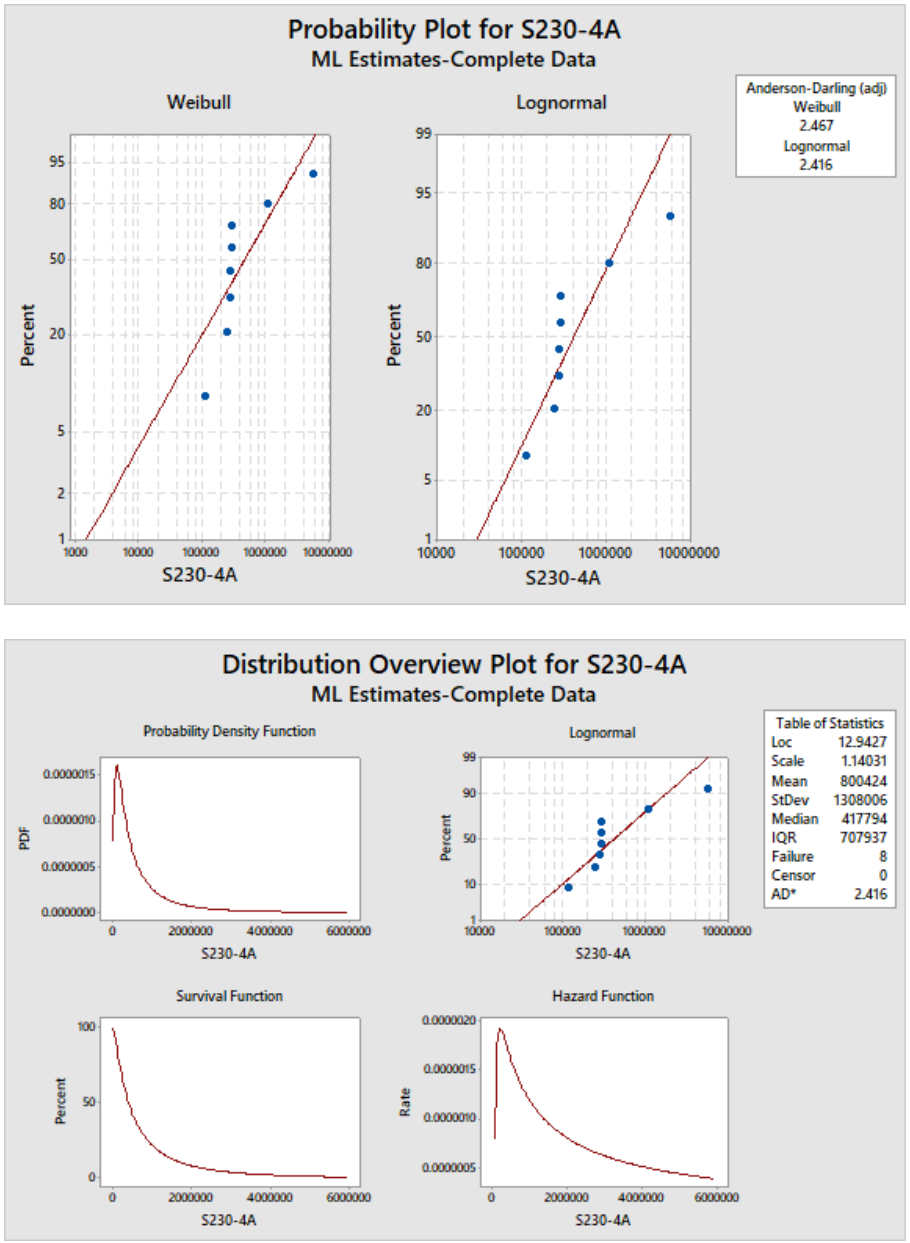

c.

Figure B.1 %Probability vs. fatigue life, probability density function (*pdf*) vs. fatigue life, survival % vs. fatigue life and hazard function vs. fatigue life plots for a. as-machined specimens, b. polished specimens, c. specimens peened using S230 shot at 4A intensity, d. specimens peened using S230 shot at 8A intensity and e. specimens peened using CW14 shot at 8A intensity subjected to a stress amplitude of 931 MPa (censored & uncensored) (cont'd)

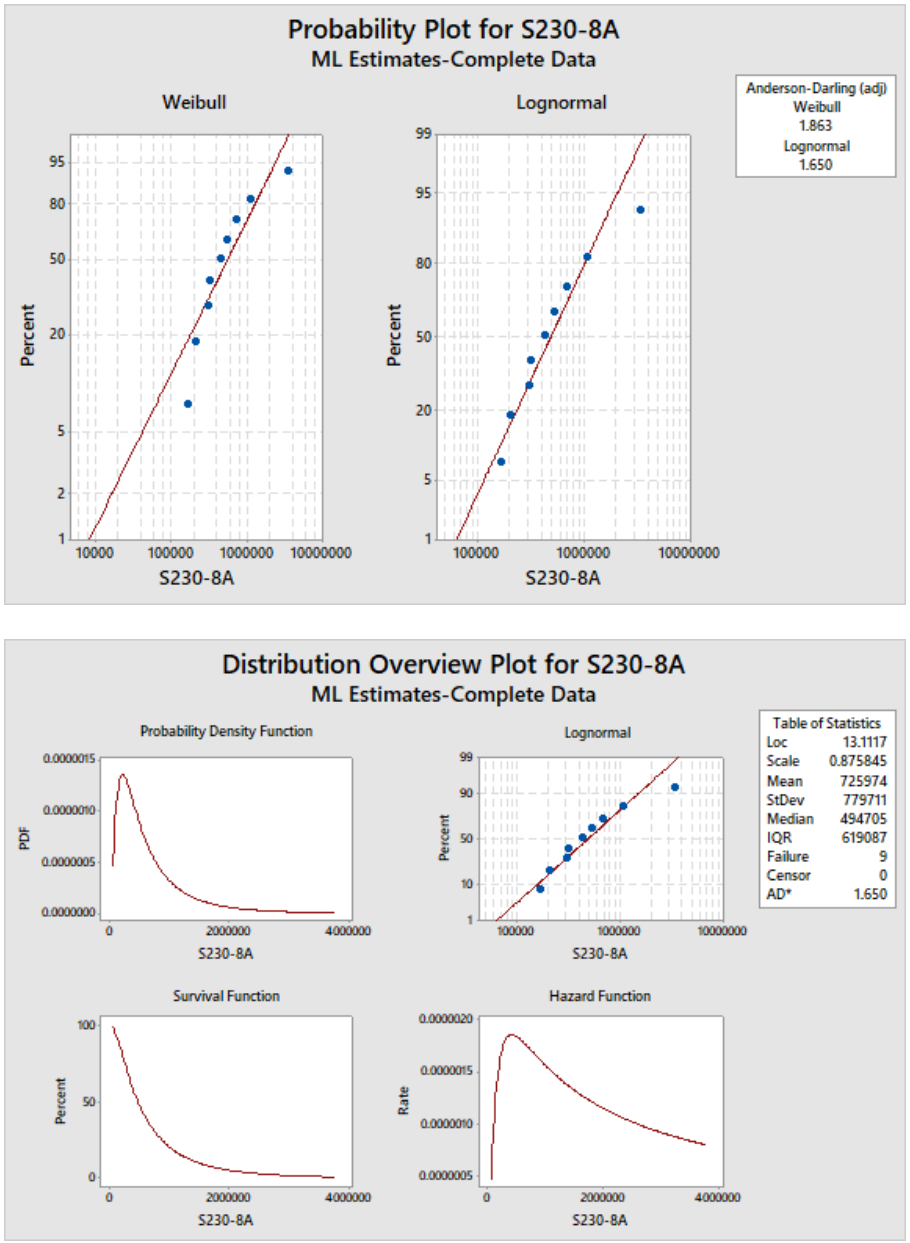

d.

Figure B.1 %Probability vs. fatigue life, probability density function (pdf) vs. fatigue life, survival % vs. fatigue life and hazard function vs. fatigue life plots for a. as-machined specimens, b. polished specimens, c. specimens peened using S230 shot at 4A intensity, d. specimens peened using S230 shot at 8A intensity and e. specimens peened using CW14 shot at 8A intensity subjected to a stress amplitude of 931 MPa (censored & uncensored) (cont'd)

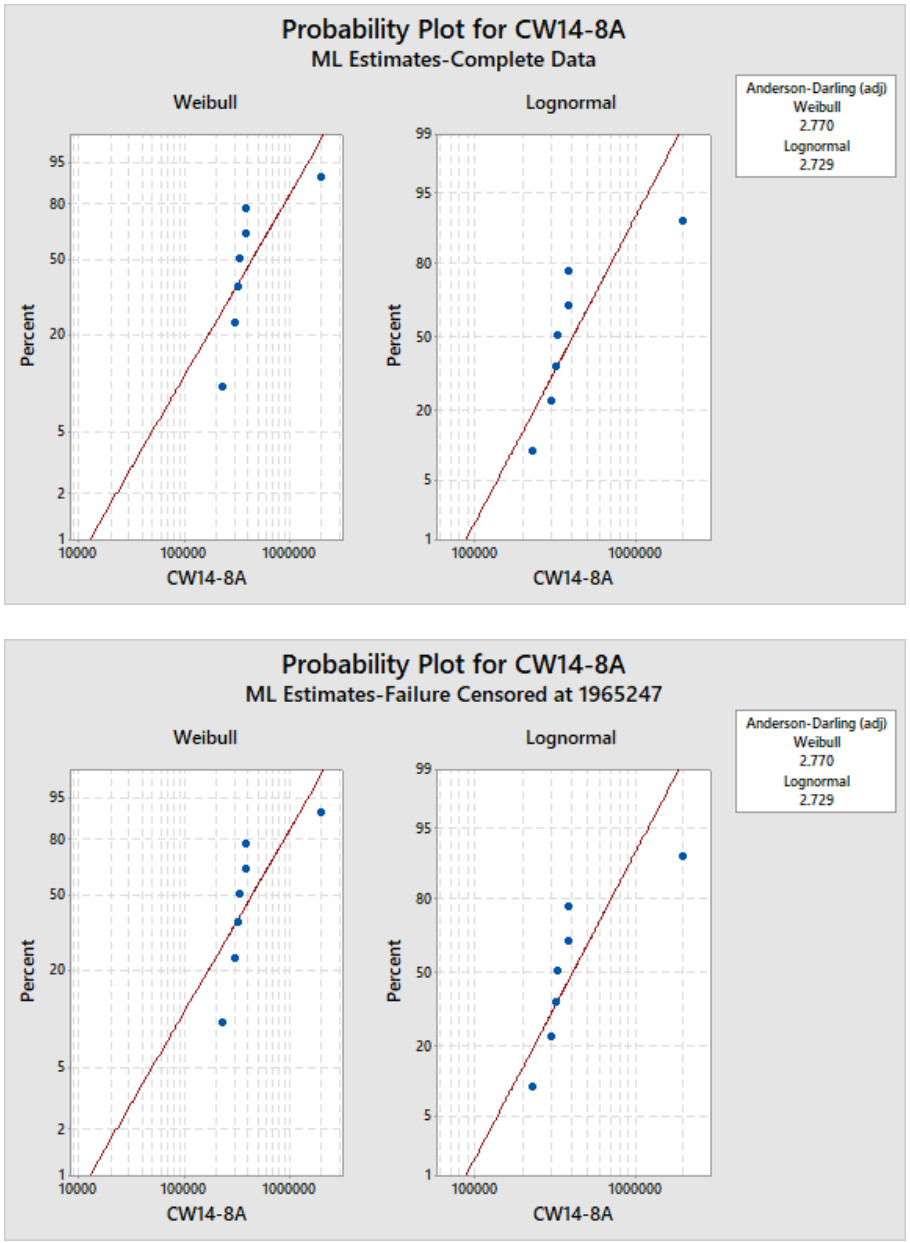

e.

Figure B.1 %Probability vs. fatigue life, probability density function (pdf) vs. fatigue life, survival % vs. fatigue life and hazard function vs. fatigue life plots for a. as-machined specimens, b. polished specimens, c. specimens peened using S230 shot at 4A intensity, d. specimens peened using S230 shot at 8A intensity and e. specimens peened using CW14 shot at 8A intensity subjected to a stress amplitude of 931 MPa (censored & uncensored) (cont'd)

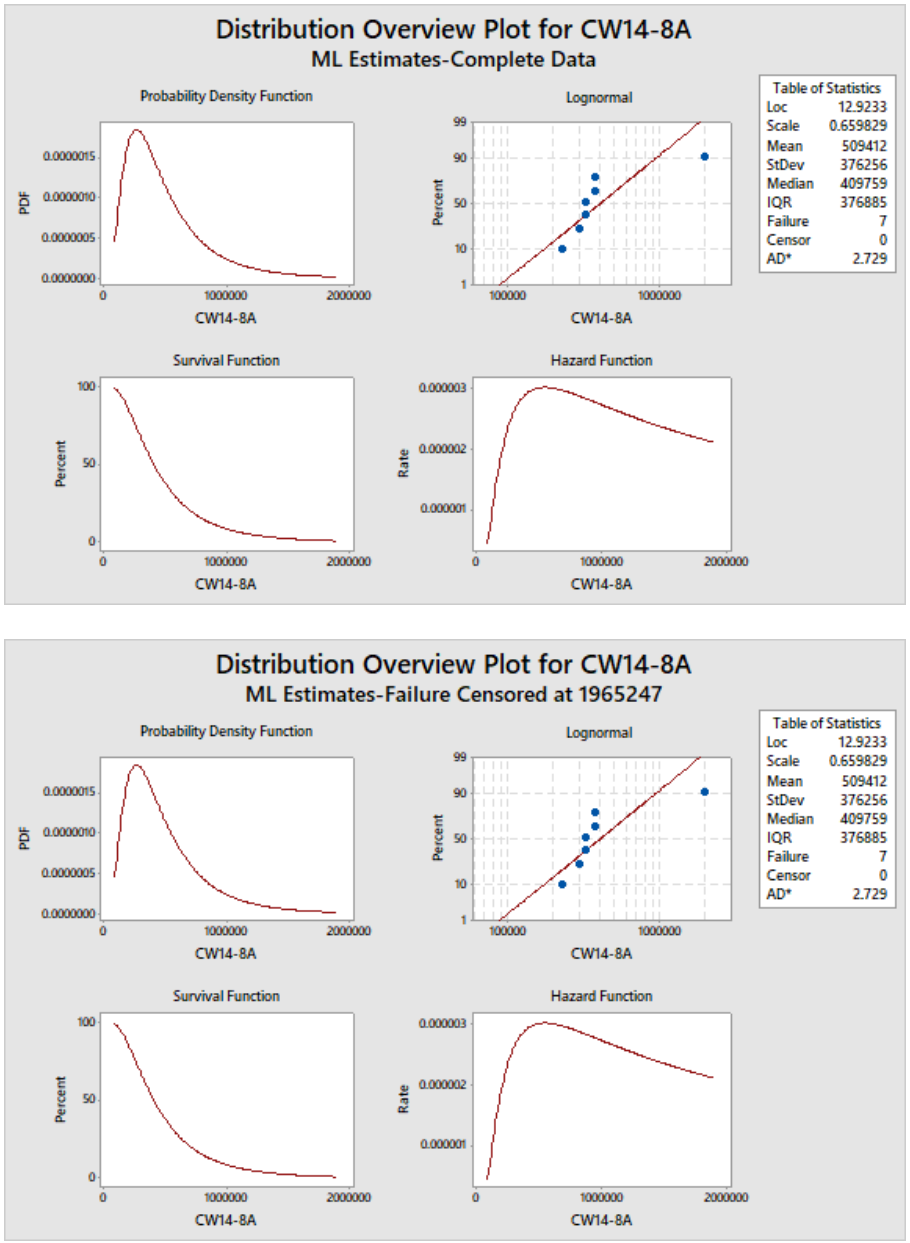

e.

Figure B.1 %Probability vs. fatigue life, probability density function (pdf) vs. fatigue life, survival % vs. fatigue life and hazard function vs. fatigue life plots for a. as-machined specimens, b. polished specimens, c. specimens peened using S230 shot at 4A intensity, d. specimens peened using S230 shot at 8A intensity and e. specimens peened using CW14 shot at 8A intensity subjected to a stress amplitude of 931 MPa (censored & uncensored) (cont'd)

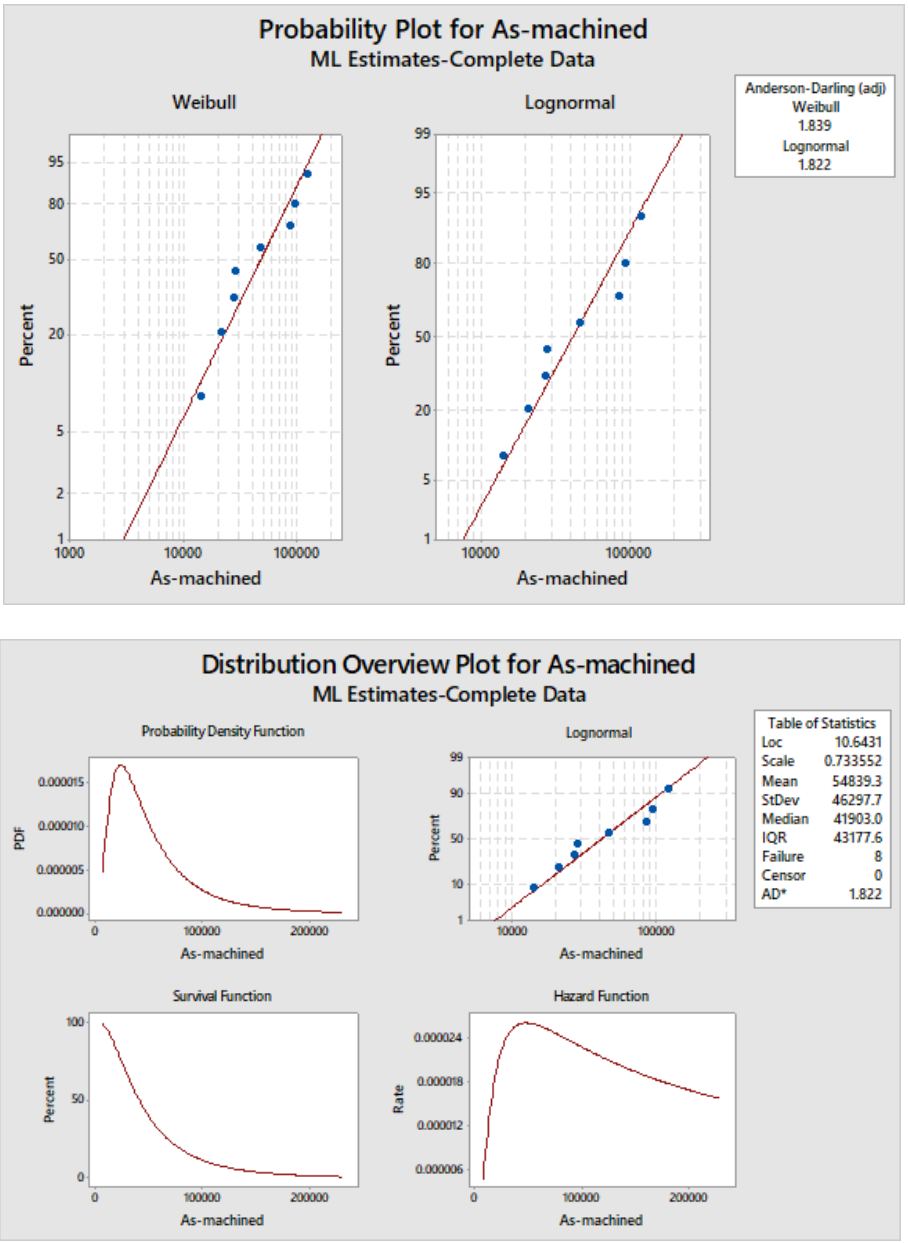

a.

Figure B.2 %Probability vs. fatigue life, probability density function (*pdf*) vs. fatigue life, survival % vs. fatigue life and hazard function vs. fatigue life plots for a. as-machined specimens, b. polished specimens, c. specimens peened using S230 shot at 4A intensity, d. specimens peened using S230 shot at 8A intensity and e. specimens peened using CW14 shot at 8A intensity subjected to a stress amplitude of 1089 MPa

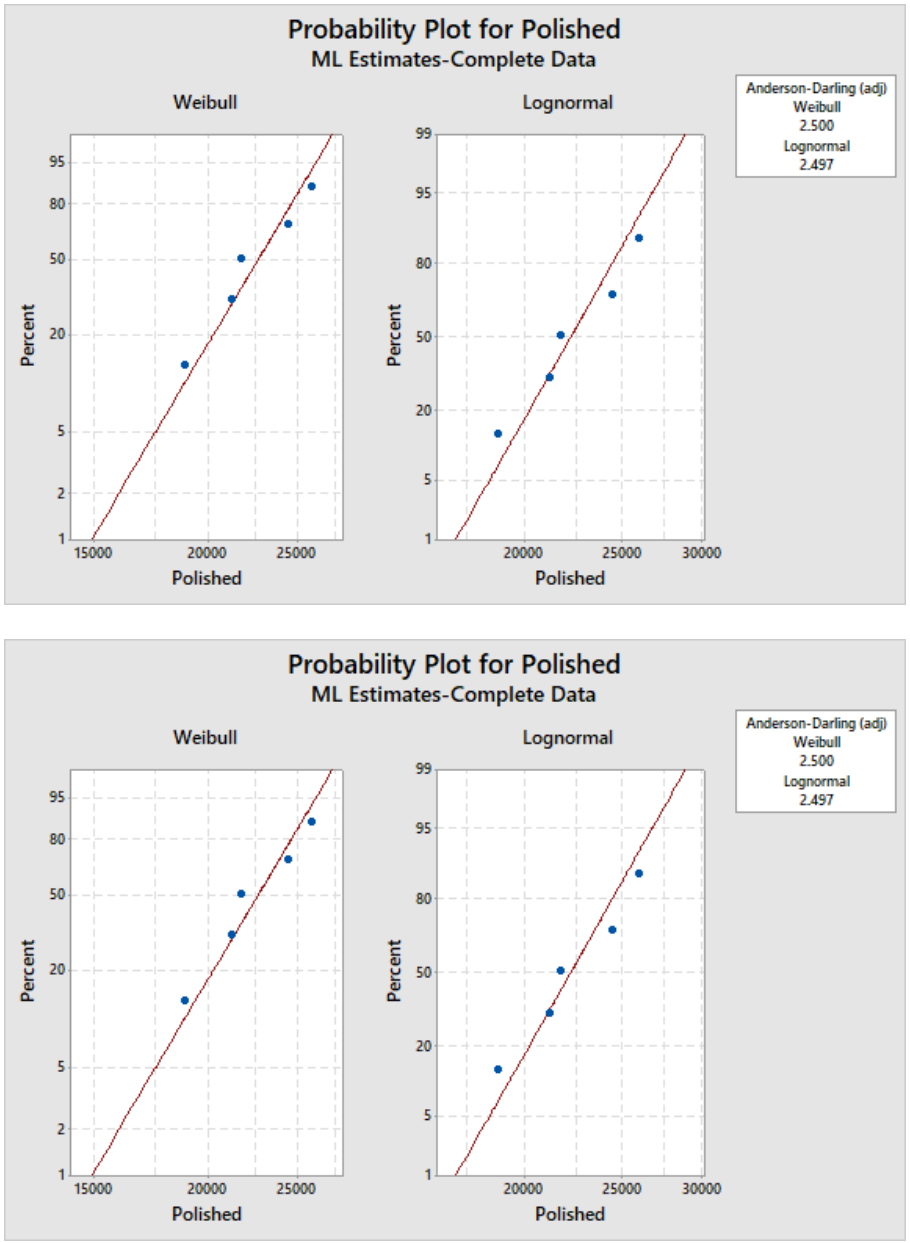

b.

Figure B.2 %Probability vs. fatigue life, probability density function (*pdf*) vs. fatigue life, survival % vs. fatigue life and hazard function vs. fatigue life plots for a. as-machined specimens, b. polished specimens, c. specimens peened using S230 shot at 4A intensity, d. specimens peened using S230 shot at 8A intensity and e. specimens peened using CW14 shot at 8A intensity subjected to a stress amplitude of 1089 MPa (cont'd)

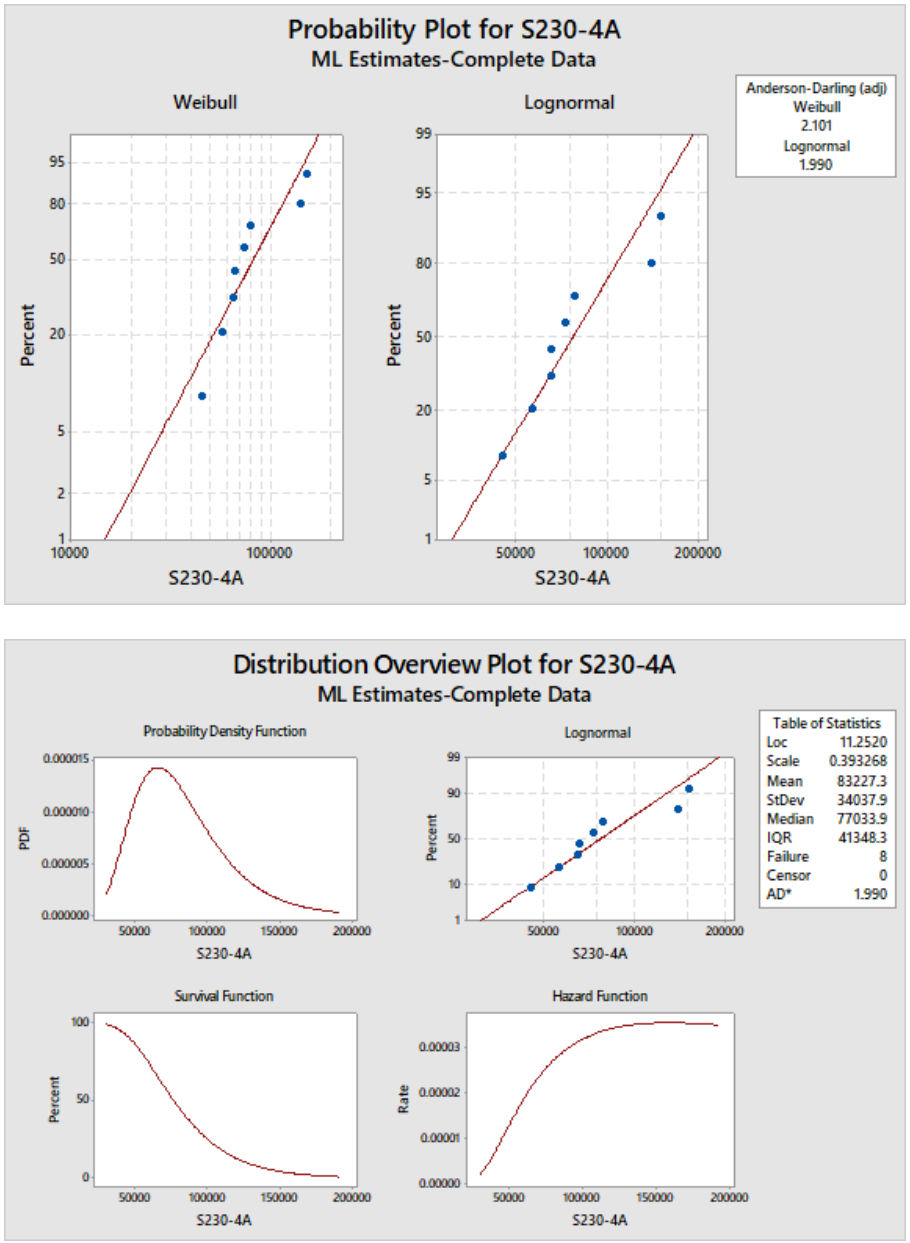

c.

Figure B.2 %Probability vs. fatigue life, probability density function (pdf) vs. fatigue life, survival % vs. fatigue life and hazard function vs. fatigue life plots for a. as-machined specimens, b. polished specimens, c. specimens peened using S230 shot at 4A intensity, d. specimens peened using S230 shot at 8A intensity and e. specimens peened using CW14 shot at 8A intensity subjected to a stress amplitude of 1089 MPa (cont'd)

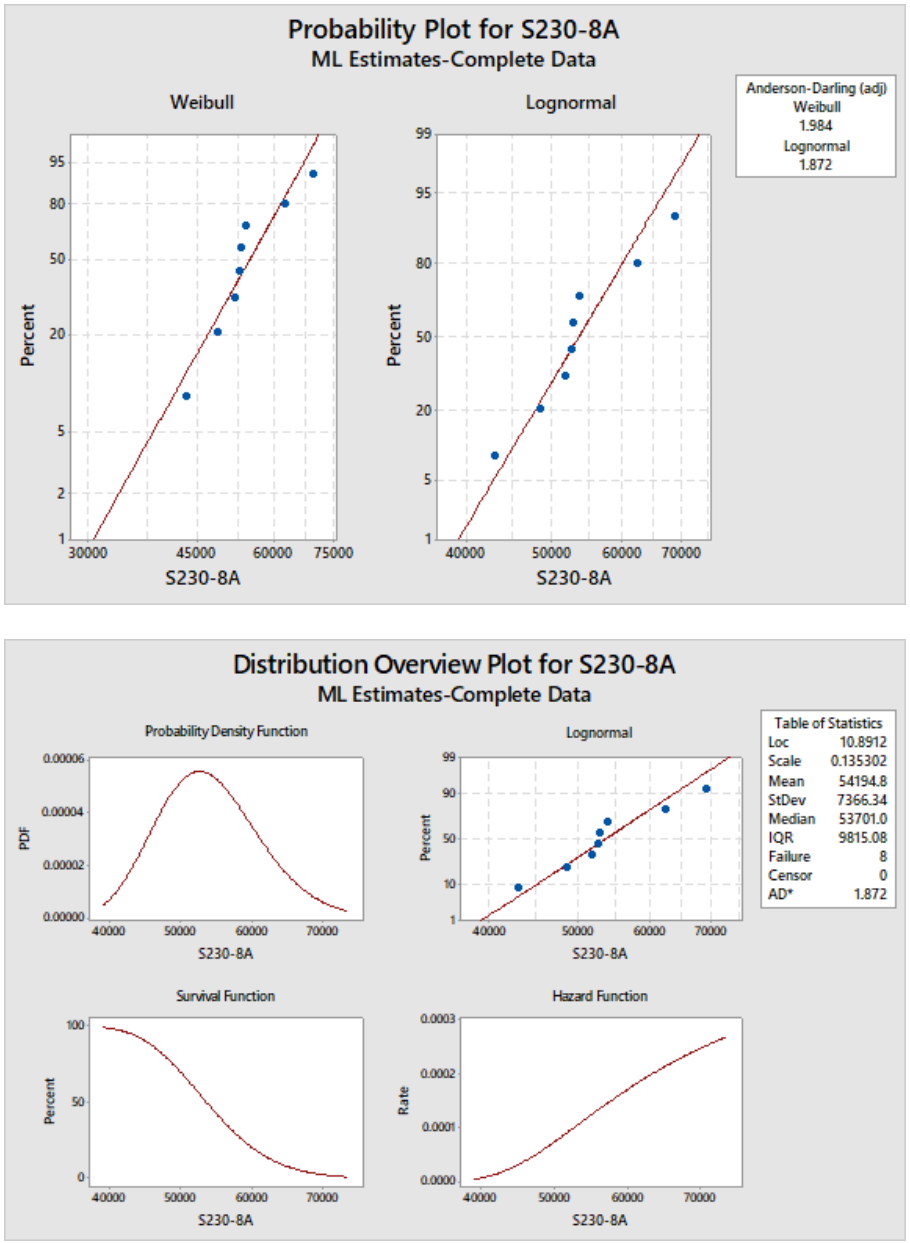

d.

Figure B.2 %Probability vs. fatigue life, probability density function (pdf) vs. fatigue life, survival % vs. fatigue life and hazard function vs. fatigue life plots for a. as-machined specimens, b. polished specimens, c. specimens peened using S230 shot at 4A intensity, d. specimens peened using S230 shot at 8A intensity and e. specimens peened using CW14 shot at 8A intensity subjected to a stress amplitude of 1089 MPa (cont'd)

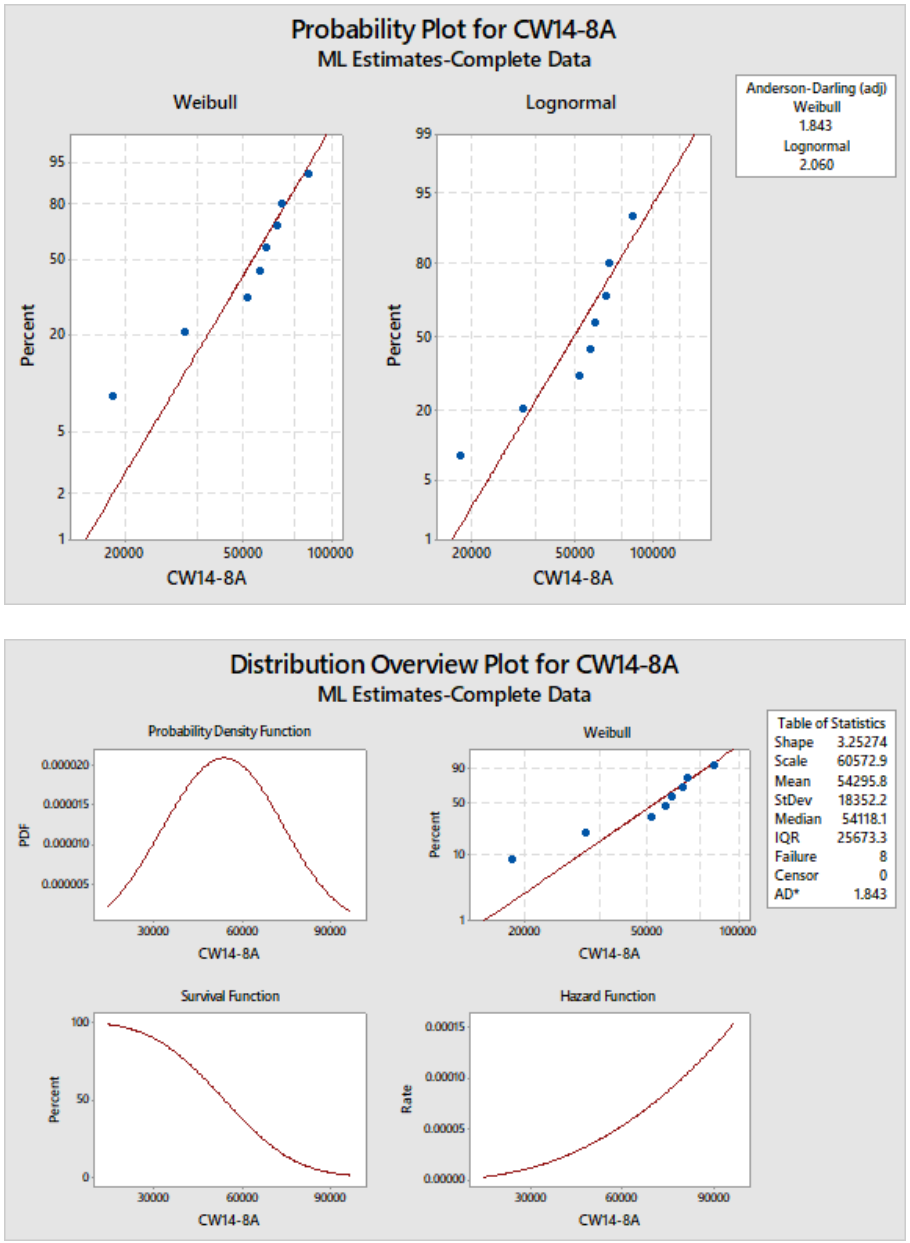

e.

Figure B.2 %Probability vs. fatigue life, probability density function (pdf) vs. fatigue life, survival % vs. fatigue life and hazard function vs. fatigue life plots for a. as-machined specimens, b. polished specimens, c. specimens peened using S230 shot at 4A intensity, d. specimens peened using S230 shot at 8A intensity and e. specimens peened using CW14 shot at 8A intensity subjected to a stress amplitude of 1089 MPa (cont'd)

APPENDIX C – SUMMARY OF FATIGUE AND FRACTOGRAPHY RESULTS

Fractography images and EDS analysis images for some of the fatigue specimens have been included in Appendix C.

C.1 Stress-controlled axial fatigue test results

Tables C.1 and C.2 list the crack initiation feature characteristics namely size, position, type and presence/absence of FGA for all fatigue specimens tested at a stress amplitude of 931 MPa and 1089 MPa respectively. Figs. C.1a-e and C.2a-e depict the crack initiation sites for the corresponding specimens given in Tables C.1 (931 MPa) and C.2 (1089 MPa). For specimens subjected to 1089 MPa stress amplitude, fractography images of only the specimens exhibiting the highest and lowest fatigue life have been shown.

Globular/ellipsoidal/irregular shaped inclusions consisting of Al, Mg, O, Ca elements (in varying proportions) and sometimes small amounts of Si and S. are referred to as Type A inclusions (Fig. C.1 b). Cubic inclusions composed of Ti, N, C sometimes with MgO inclusions embedded in them, are referred to as Type B (Fig. C.1 d). Fine granular area (FGA) (Fig. C.1 a, b, c, d) was observed for specimens with $N_f > 10^6$ cycles when the failure was triggered by subsurface inclusions.

For specimens subjected to 931 MPa stress amplitude, all specimens exhibited crack initiation at inclusions except a specimen peened with S230 shot at 8A intensity which showed surface crack initiation at a grinding mark. For this specimen, the main crack was found to change its plane of propagation at a depth of about 25µm which lies in the region of the maximum CRS. Moreover, the specimen exhibited a high fatigue life of 1.06 x 10^6 cycles which might indicate an effect of CRS on crack growth mechanism.

For specimens subjected to 1089 MPa stress amplitude, multiple crack initiation sites were observed for specimens with lowest fatigue lives while single crack initiation sites were observed for specimens with highest fatigue lives. Moreover, for most of the peened specimens except the specimen peened using CW14 shot at 8A intensity with the lowest fatigue life of 1.8 x 10^4 cycles, the main crack appeared at a depth of about 100µm which lies in the region of the peening induced

CRS. This may also indicate a role of the CRS in affecting the crack growth mechanism and should be further investigated.

Table C.1 List of crack initiation features for all fatigue specimens tested at a stress amplitude of 931MPa (R= -1), characterized by size, position, type and presence/absence of FGA (GM = Grinding mark)

Total fatigue life N_f (cycles)	Size of initiating feature (μm)	Distance of defect from the surface (μm)	Type	FGA (Yes/No)
		As-machined		
1.40×10^5	--	0	GM	--
5.09×10^5	--	0	GM	--
5.25×10^5	19.8	639.0	A	No
8.20×10^5	19.1	106.6	A	No
1.09×10^6	16.2	2652.9	B	Yes
		Polished		
4.83×10^4	19.9	9.94	A	No
3.45×10^5	33.9	572.7	A	No
6.46×10^5	19.9	1000.0	A	No
6.60×10^5	27.2	181.5	A	No
1.01×10^6	32.1	2339.4	A	Yes
		S230-4A		
1.11×10^5	41.7	849.6	A	No
2.37×10^5	27.0	556.6	A	No
2.72×10^5	30.0	736.6	A	No
2.78×10^5	34.0	2063.8	A	No
2.79×10^5	30.9	955.2	A	No

Table C.1 List of crack initiation features for all fatigue specimens tested at a stress amplitude of 931MPa (R= -1), characterized by size, position, type and presence/absence of FGA (GM = Grinding mark) (cont'd)

Total fatigue life N_f (cycles)	Size of initiating feature (μm)	Distance of defect from the surface (μm)	Type	FGA (Yes/No)
		S230-4A		
2.79 x 10^5	26.1	693.5	A	No
1.06 x 10^6	18.2	932.9	A	Yes
5.65 x 10^6	13.5	3074.8	A	Yes
		S230-8A		
1.64 x 10^5	51.1	1637.7	A	No
2.03 x 10^5	27.2	1200	A	No
3.17 x 10^5	26.6	591.1	A	No
3.02 x 10^5	21.2	1810.3	A	No
4.26 x 10^5	25.0	1508.6	A	No
5.23 x 10^5	23.2	1866.9	A	Yes
6.87 x 10^5	21.8	227.6	A	No
1.06 x 10^6	--	0	GM	--
3.42 x 10^6	12.7	239.0	B	Yes
		CW14-8A		
2.26 x 10^5	31.6	995.0	A	No
2.94 x 10^5	28.0	951.2	A	No
3.21 x 10^5	25.7	347.8	A	No
3.23 x 10^5	29.7	391.8	A	No
3.76 x 10^5	29.5	697.7	A	No

3.78×10^5	30.2	589.4	A	No
1.96×10^6	Runout (Failure at grip section)			

Table C.2 List of crack initiation features for all fatigue specimens tested at a stress amplitude of 1089 MPa (R= -1), characterized by size, position, type (GM/PD = Grinding mark/ Peening induced discontinuity)

Total fatigue life N_f (cycles)	Size of initiating feature (µm)	Distance of defect from the surface (µm)	Type
As-machined			
1.39×10^4	--	0	GM
2.08×10^4	--	0	GM
2.69×10^4	--	0	GM
2.79×10^4	--	0	GM
4.66×10^4	--	0	GM
8.43×10^4	22	2023	A
9.29×10^4	25.2	2571	A
1.20×10^5	--	0	GM
Polished			
1.88×10^4	15.3	8	A
2.11×10^4	28.1	14	A
2.17×10^4	12.0	6	A
2.44×10^4	13.8	7	A
2.59×10^4	8.0	4	A

Table C.2 List of crack initiation features for all fatigue specimens tested at a stress amplitude of 1089 MPa (R= -1), characterized by size, position, type (GM/PD = Grinding mark/ Peening induced discontinuity) (cont'd)

Total fatigue life N_f (cycles)	Size of initiating feature (μm)	Distance of defect from the surface (μm)	Type
	S230-4A		
4.50×10^4	42	598	A
5.61×10^4	37.7	1156	A
6.46×10^4	35.4	292	A
6.51×10^4	34.8	1753	A
	S230-4A		
7.25×10^4	--	0	GM/PD
7.77×10^4	26.6	344	A
1.39×10^5	21	371	A
1.50×10^5	--	0	GM/PD
	S230-8A		
4.30×10^4	--	0	GM/PD
4.85×10^4	--	0	GM/PD
5.18×10^4	--	0	GM/PD
5.25×10^4	--	0	GM/PD
5.28×10^4	31.0	2150	A
5.37×10^4	--	0	GM/PD
6.23×10^4	--	0	GM/PD
6.90×10^4	--	0	GM/PD

Table C.2 List of crack initiation features for all fatigue specimens tested at a stress amplitude of 1089 MPa (R= -1), characterized by size, position, type (GM/PD = Grinding mark/ Peening induced discontinuity) (cont'd)

Total fatigue life N_f (cycles)	Size of initiating feature (µm)	Distance of defect from the surface (µm)	Type
	CW14-8A		
1.80×10^4	--	0	GM/PD
3.15×10^4	30.3	2814	A
5.17×10^4	--	0	GM/PD
5.72×10^4	--	0	GM/PD
5.99×10^4	--	0	GM/PD
6.51×10^4	--	0	GM/PD
6.78×10^4	--	0	GM/PD
8.28×10^4	--	0	GM/PD

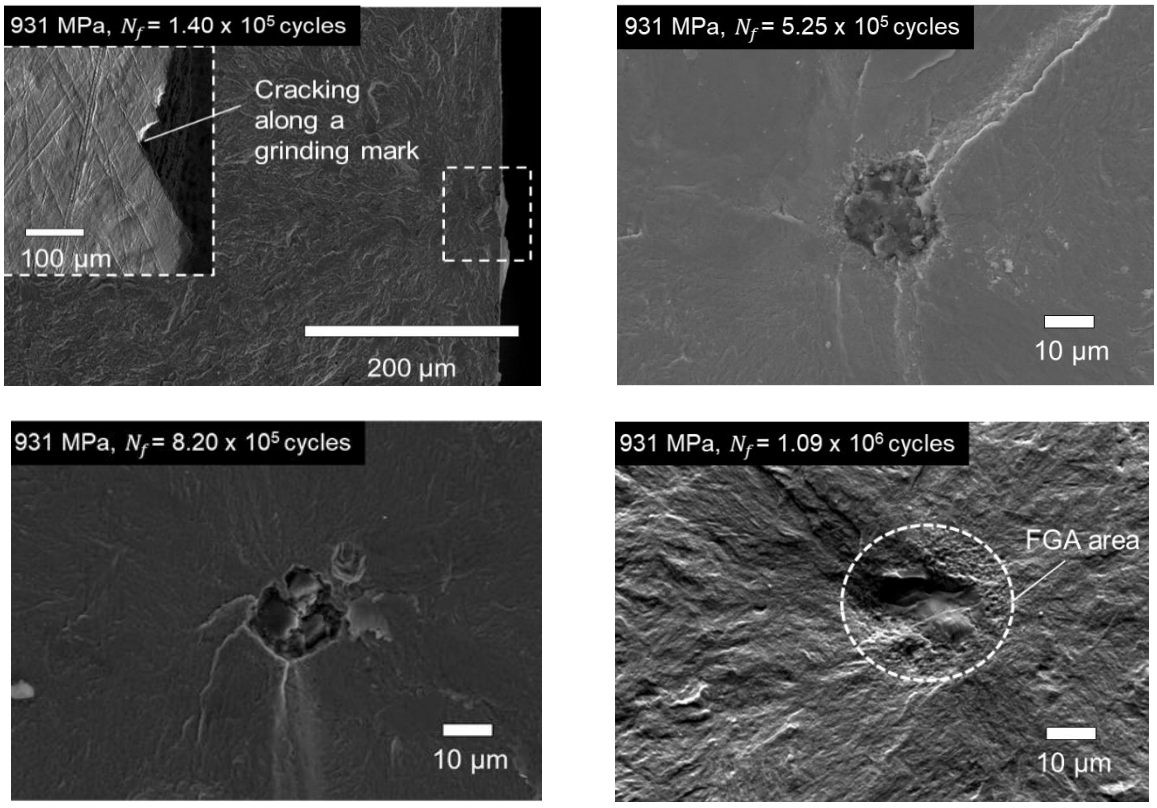

a.

Figure C.1 Crack initiation sites for a. as-machined specimens, b. polished specimens, c. specimens peened using S230 shot at 4A intensity, d. specimens peened using S230 shot at 8A intensity and e. specimens peened using CW14 shot at 8A intensity subjected to a stress amplitude of 931 MPa. For the specimens peened using S230 shot at 8A intensity where the surface crack initiation occurred at a grinding mark, the main crack appears to change its propagation plane at 25µm depth which corresponds to the region of maximum CRS

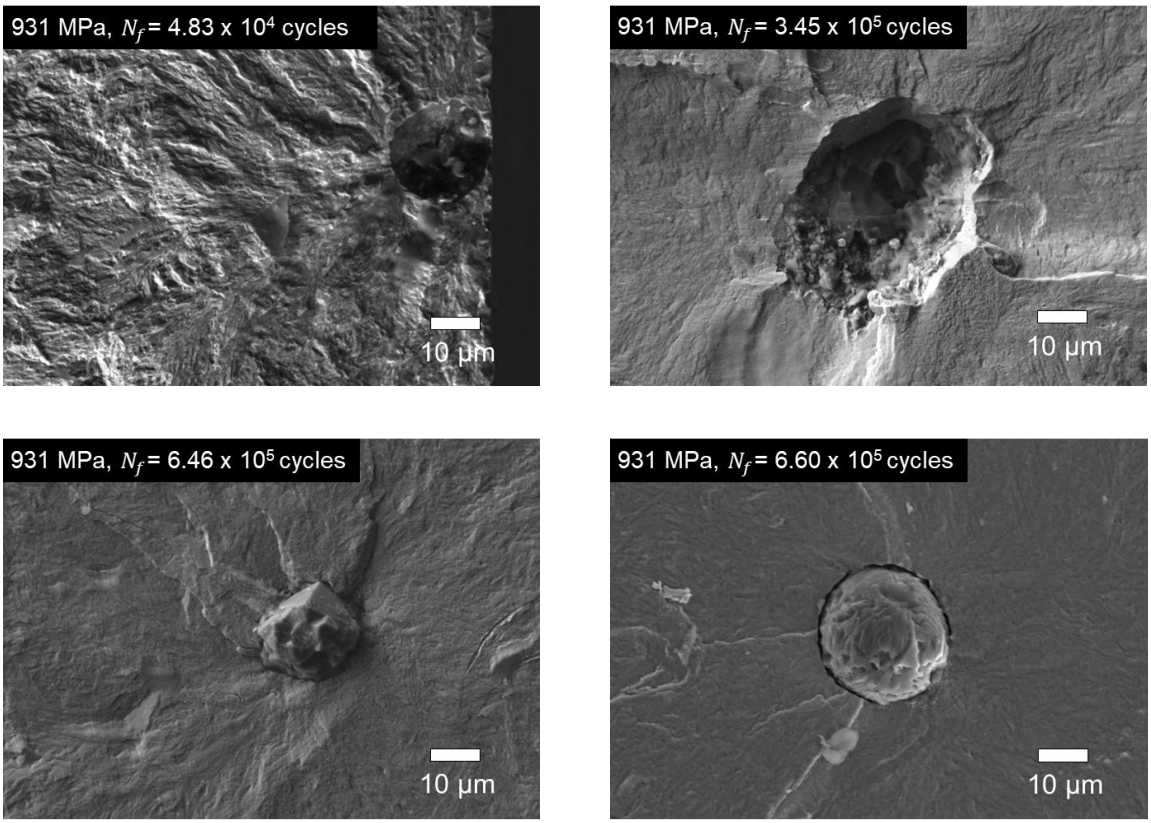

b.

Figure C.1 Crack initiation sites for a. as-machined specimens, b. polished specimens, c. specimens peened using S230 shot at 4A intensity, d. specimens peened using S230 shot at 8A intensity and e. specimens peened using CW14 shot at 8A intensity subjected to a stress amplitude of 931 MPa. For the specimens peened using S230 shot at 8A intensity where the surface crack initiation occurred at a grinding mark, the main crack appears to change its propagation plane at 25µm depth which corresponds to the region of maximum CRS (cont'd)

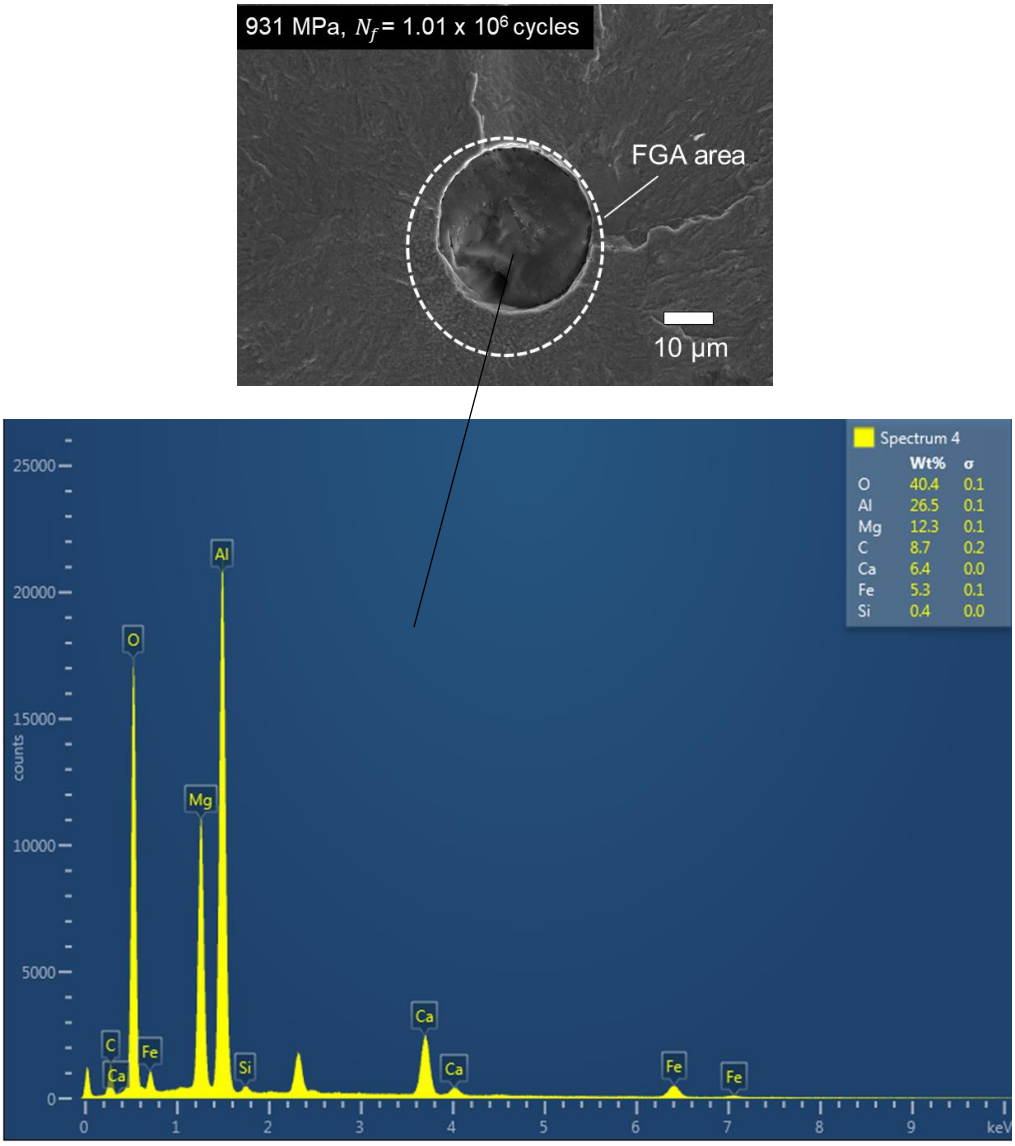

b.

Figure C.1 Crack initiation sites for a. as-machined specimens, b. polished specimens, c. specimens peened using S230 shot at 4A intensity, d. specimens peened using S230 shot at 8A intensity and e. specimens peened using CW14 shot at 8A intensity subjected to a stress amplitude of 931 MPa. For the specimens peened using S230 shot at 8A intensity where the surface crack initiation occurred at a grinding mark, the main crack appears to change its propagation plane at 25µm depth which corresponds to the region of maximum CRS (cont'd)

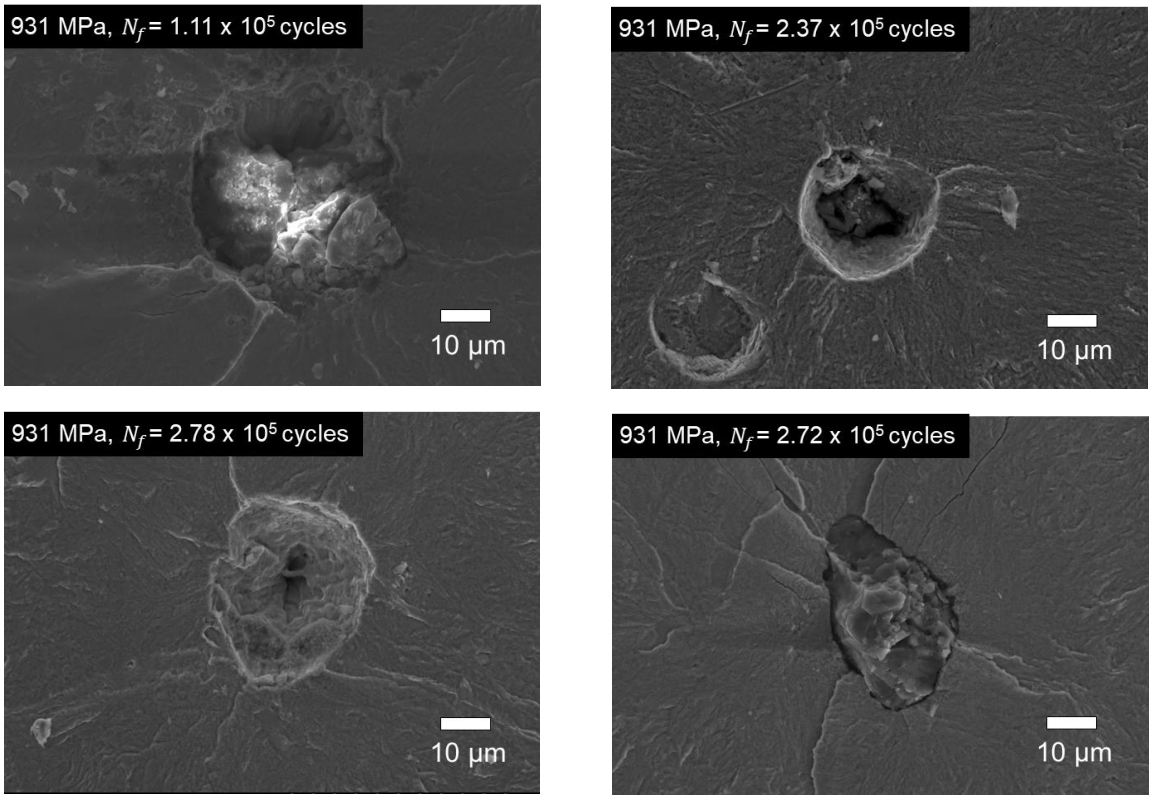

c.

Figure C.1 Crack initiation sites for a. as-machined specimens, b. polished specimens, c. specimens peened using S230 shot at 4A intensity, d. specimens peened using S230 shot at 8A intensity and e. specimens peened using CW14 shot at 8A intensity subjected to a stress amplitude of 931 MPa. For the specimens peened using S230 shot at 8A intensity where the surface crack initiation occurred at a grinding mark, the main crack appears to change its propagation plane at 25µm depth which corresponds to the region of maximum CRS (cont'd)

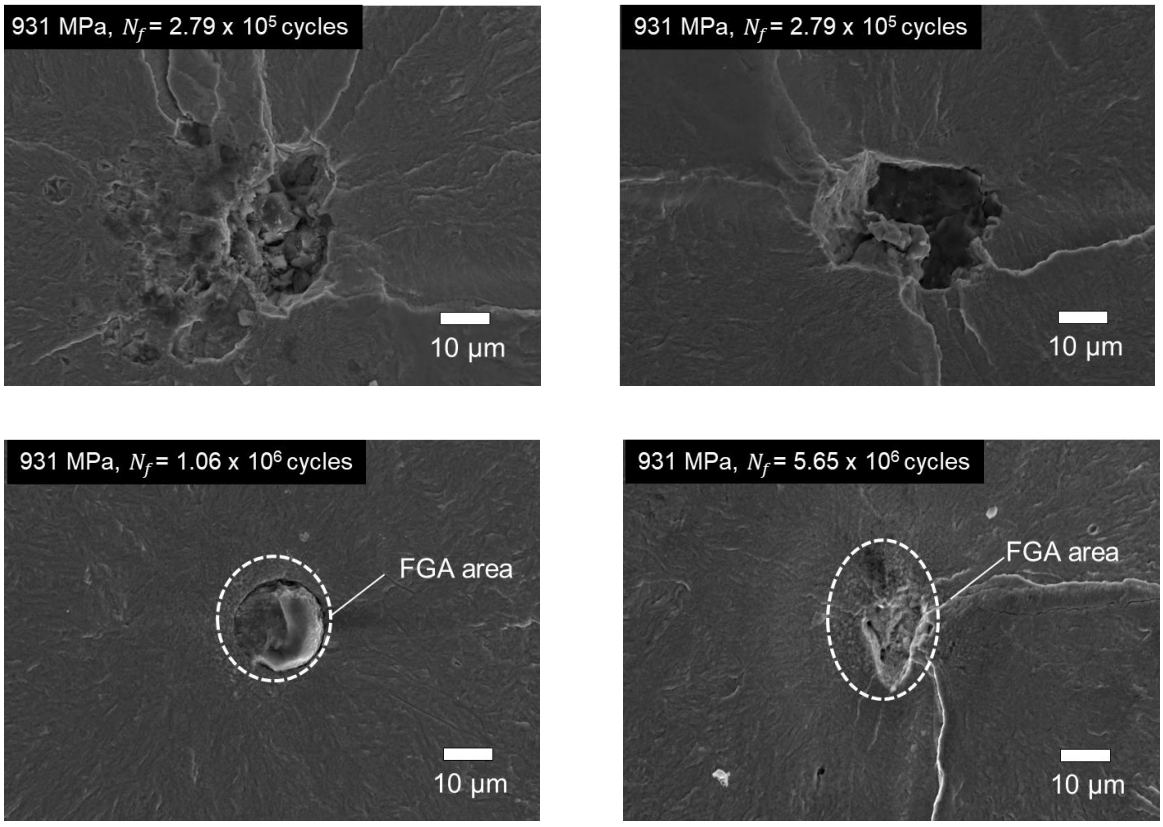

c.

Figure C.1 Crack initiation sites for a. as-machined specimens, b. polished specimens, c. specimens peened using S230 shot at 4A intensity, d. specimens peened using S230 shot at 8A intensity and e. specimens peened using CW14 shot at 8A intensity subjected to a stress amplitude of 931 MPa. For the specimens peened using S230 shot at 8A intensity where the surface crack initiation occurred at a grinding mark, the main crack appears to change its propagation plane at 25µm depth which corresponds to the region of maximum CRS (cont'd)

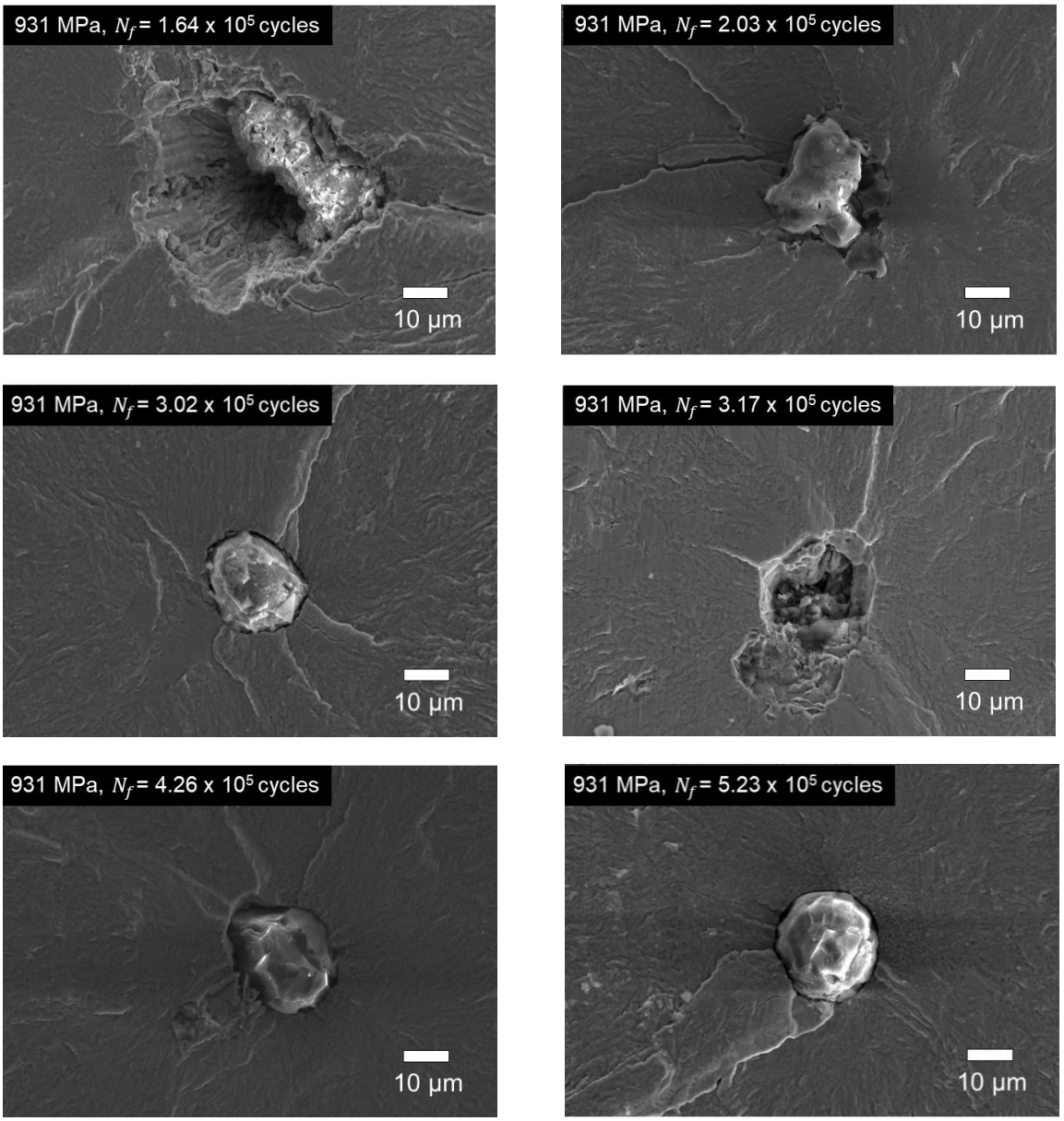

d.

Figure C.1 Crack initiation sites for a. as-machined specimens, b. polished specimens, c. specimens peened using S230 shot at 4A intensity, d. specimens peened using S230 shot at 8A intensity and e. specimens peened using CW14 shot at 8A intensity subjected to a stress amplitude of 931 MPa. For the specimens peened using S230 shot at 8A intensity where the surface crack initiation occurred at a grinding mark, the main crack appears to change its propagation plane at 25µm depth which corresponds to the region of maximum CRS (cont'd)

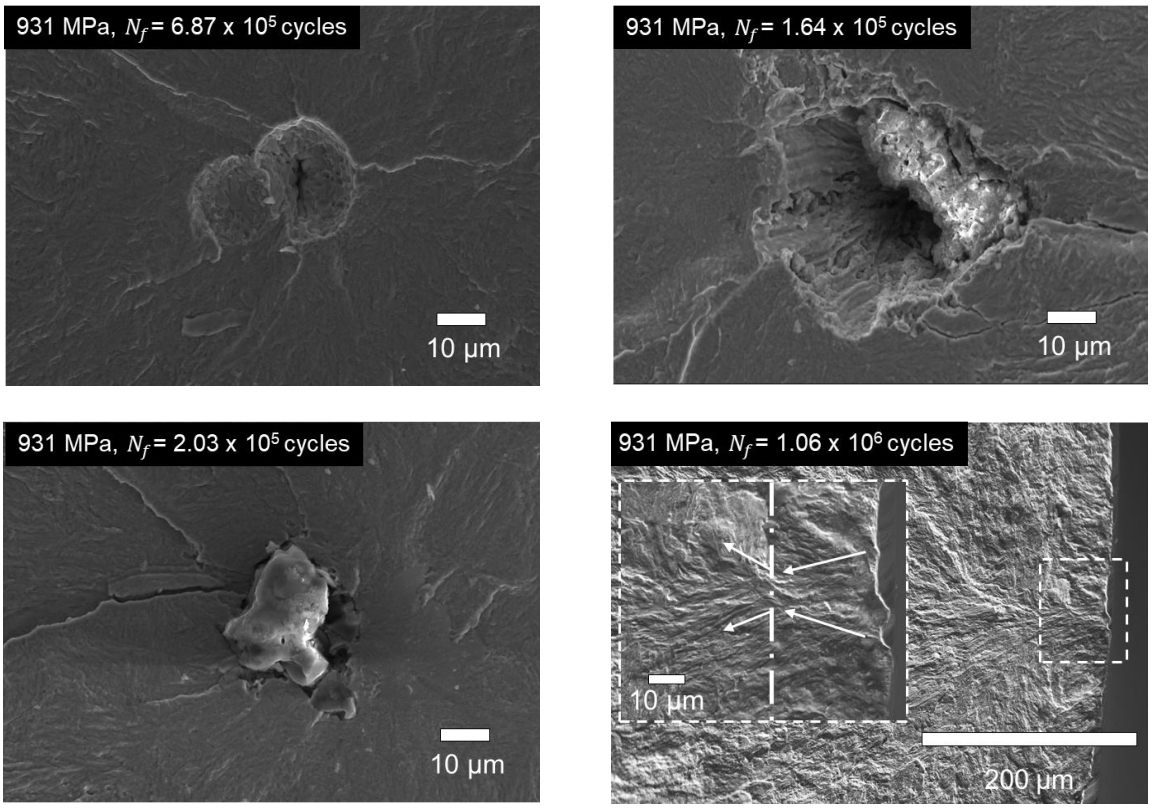

d.

Figure C.1 Crack initiation sites for a. as-machined specimens, b. polished specimens, c. specimens peened using S230 shot at 4A intensity, d. specimens peened using S230 shot at 8A intensity and e. specimens peened using CW14 shot at 8A intensity subjected to a stress amplitude of 931 MPa. For the specimens peened using S230 shot at 8A intensity where the surface crack initiation occurred at a grinding mark, the main crack appears to change its propagation plane at 25µm depth which corresponds to the region of maximum CRS (cont'd)

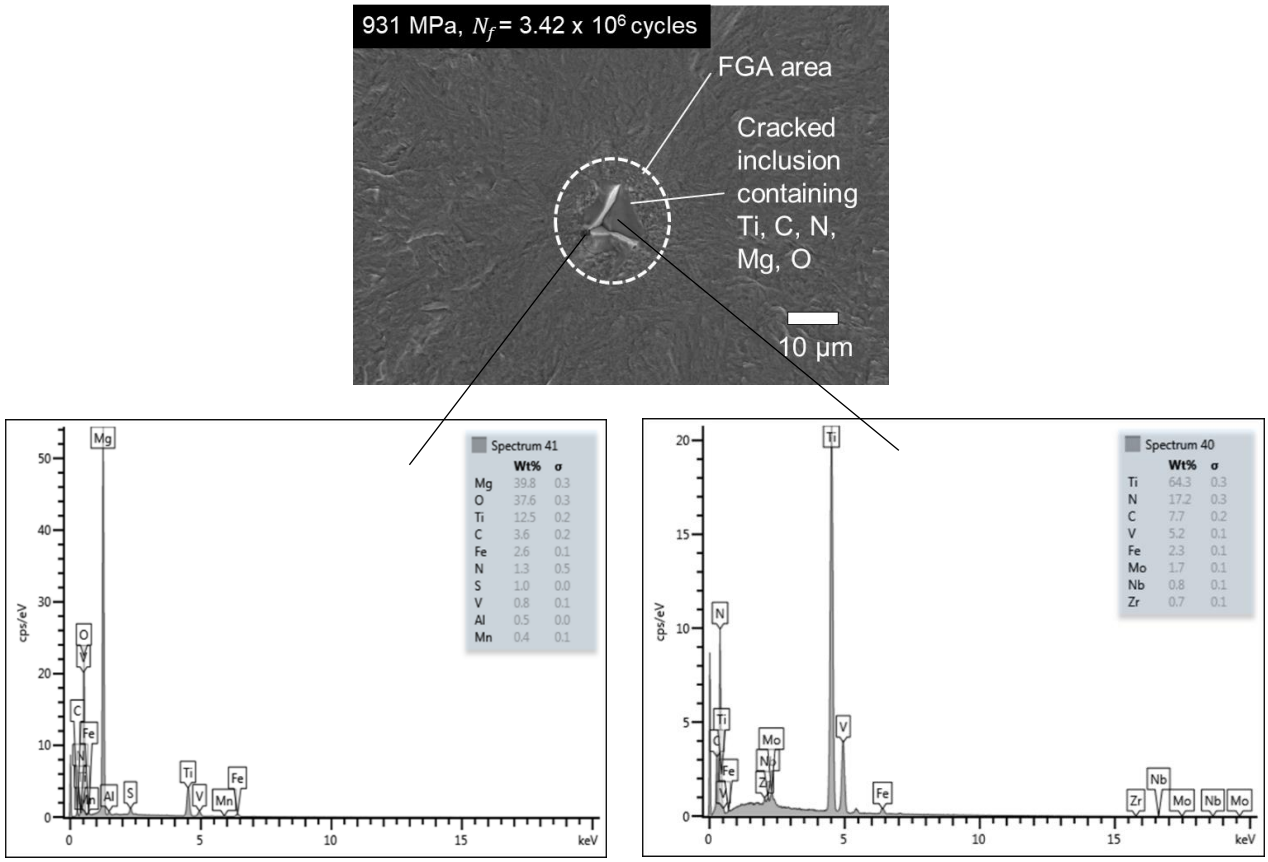

d.

Figure C.1 Crack initiation sites for a. as-machined specimens, b. polished specimens, c. specimens peened using S230 shot at 4A intensity, d. specimens peened using S230 shot at 8A intensity and e. specimens peened using CW14 shot at 8A intensity subjected to a stress amplitude of 931 MPa. For the specimens peened using S230 shot at 8A intensity where the surface crack initiation occurred at a grinding mark, the main crack appears to change its propagation plane at 25µm depth which corresponds to the region of maximum CRS (cont'd)

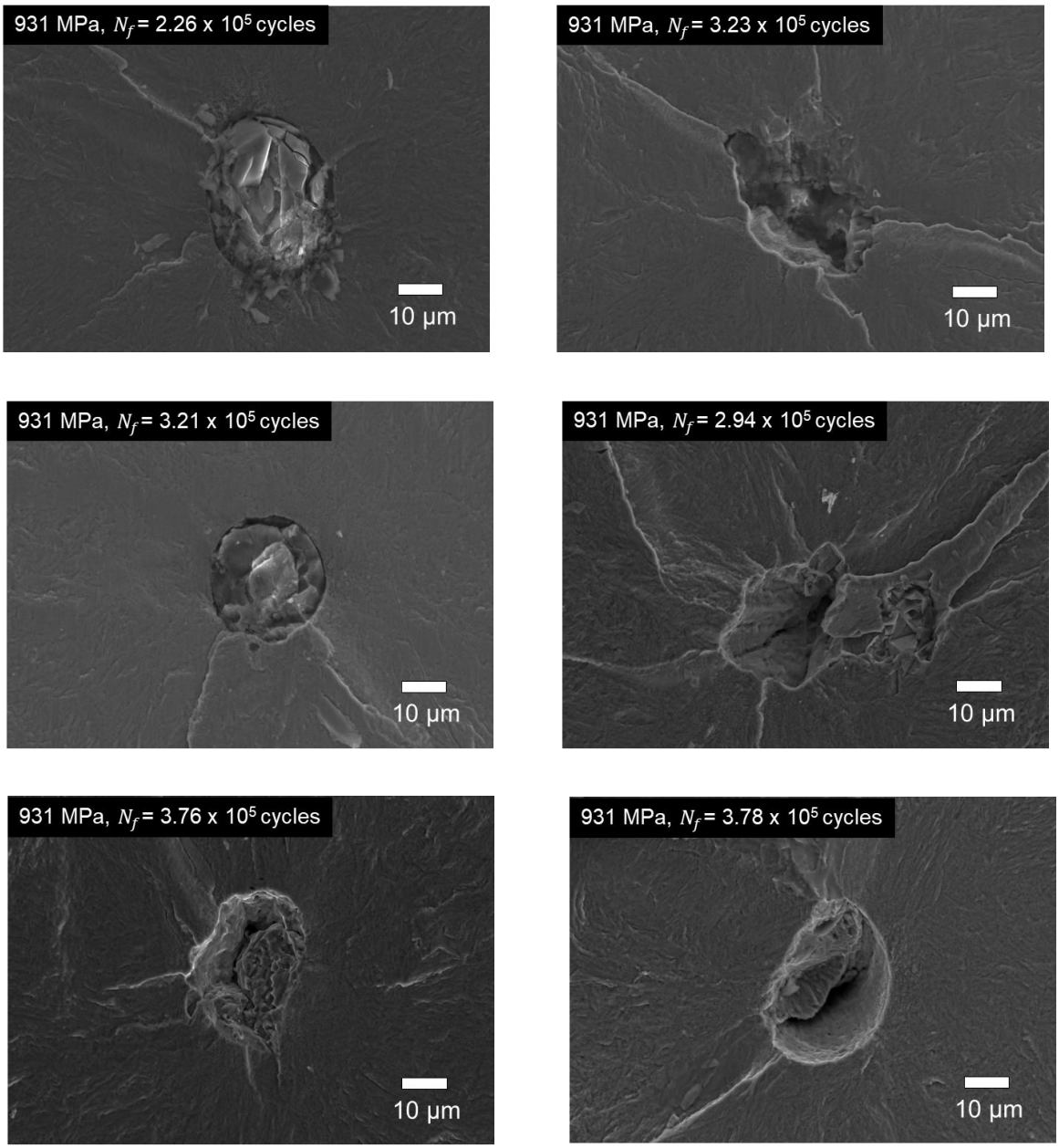

d.

Figure C.1 Crack initiation sites for a. as-machined specimens, b. polished specimens, c. specimens peened using S230 shot at 4A intensity, d. specimens peened using S230 shot at 8A intensity and e. specimens peened using CW14 shot at 8A intensity subjected to a stress amplitude of 931 MPa. For the specimens peened using S230 shot at 8A intensity where the surface crack initiation occurred at a grinding mark, the main crack appears to change its propagation plane at 25µm depth which corresponds to the region of maximum CRS (cont'd)

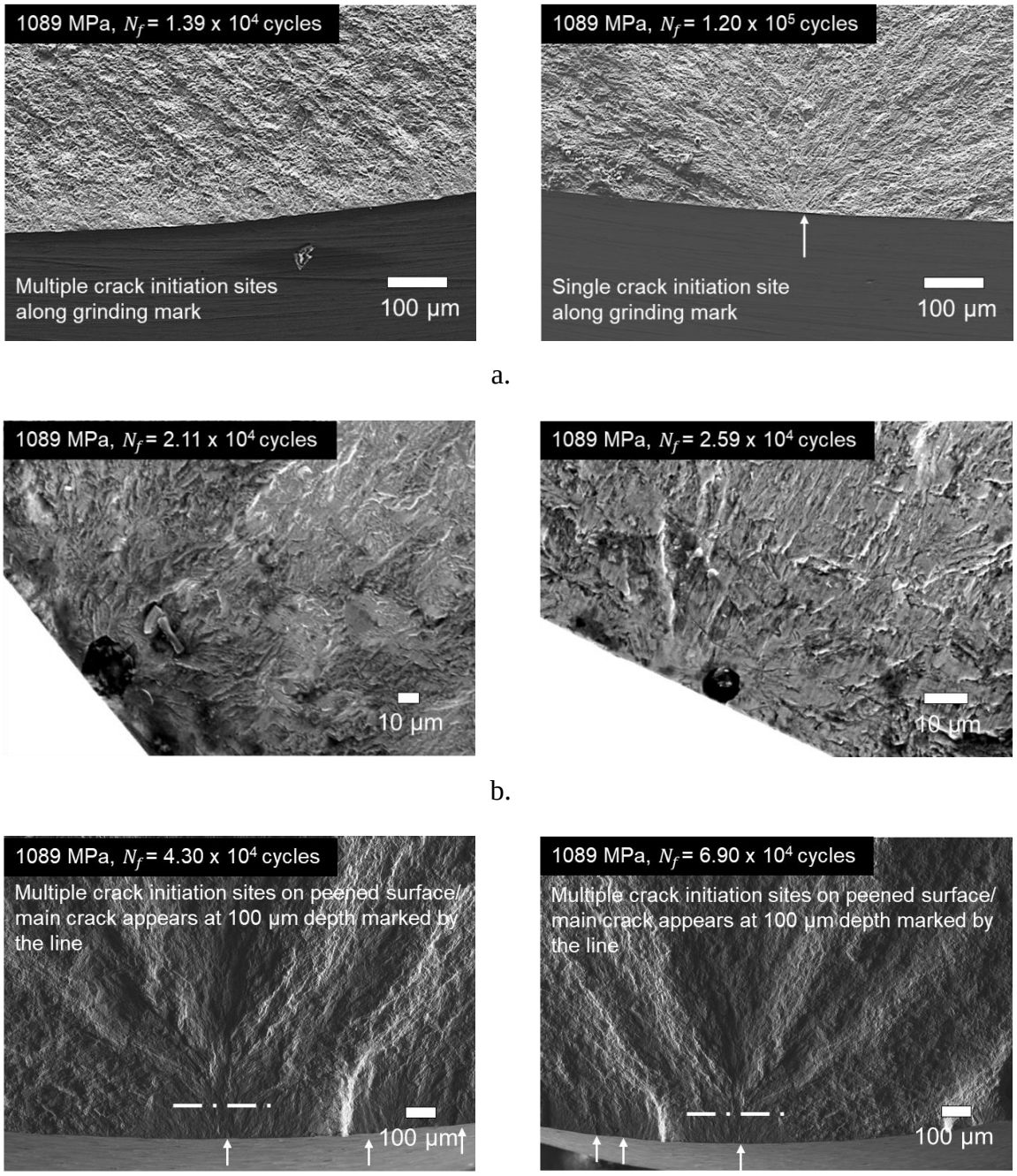

Figure C.2: Crack initiation sites for a. as-machined specimens, b. polished specimens, c. specimens peened using S230 shot at 4A intensity, d. specimens peened using S230 shot at 8A intensity and e. specimens peened using CW14 shot at 8A intensity subjected to a stress amplitude of 1089 MPa (Crack initiation sites for only the specimens with the highest and lowest fatigue lives for each condition have been depicted). Specimens with multiple surface crack initiation sites show lower fatigue lives than those with single crack initiation site. For most of the peened specimens, the main crack tends to appear at a depth of 100µm below the surface which is of the order of the depth of CRS

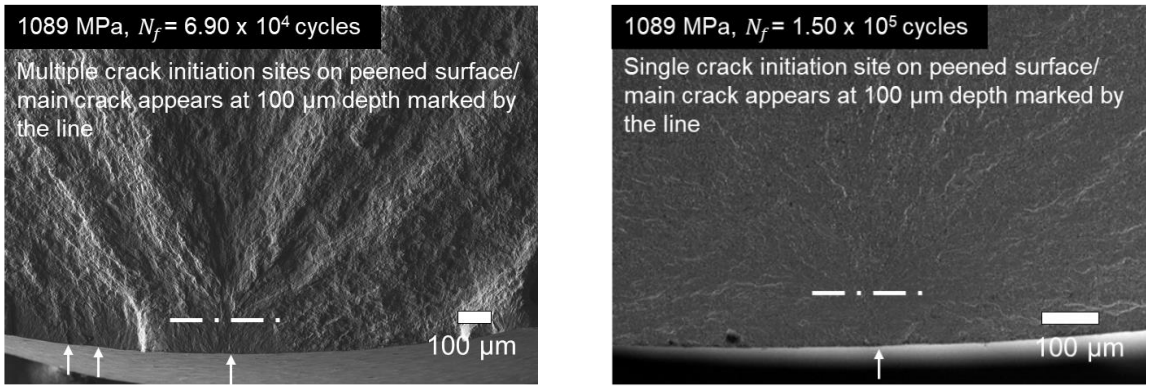

d.

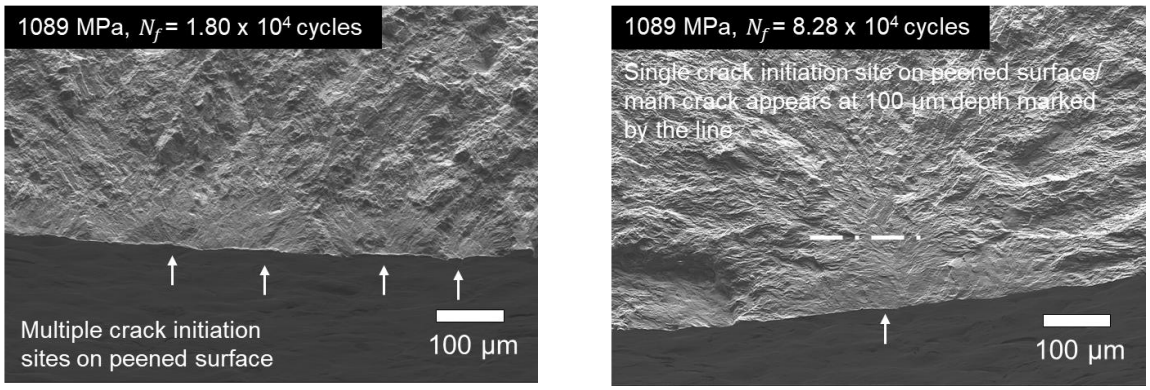

e.

Figure C.2 Crack initiation sites for a. as-machined specimens, b. polished specimens, c. specimens peened using S230 shot at 4A intensity, d. specimens peened using S230 shot at 8A intensity and e. specimens peened using CW14 shot at 8A intensity subjected to a stress amplitude of 1089 MPa (Crack initiation sites for only the specimens with the highest and lowest fatigue lives for each condition have been depicted). Specimens with multiple surface crack initiation sites show lower fatigue lives than those with single crack initiation site. For most of the peened specimens, the main crack tends to appear at a depth of 100µm below the surface which is of the order of the depth of CRS (cont'd)

APPENDIX D – MONOTONIC TENSILE & K_{IC} FRACTURE TOUGHNESS TEST RESULTS (BULK MATERIAL CHARACTERIZATION)

D.1 Monotonic tensile test results

Table D.1 presents the results of the 3 tensile tests along with the AMS 6257E standard requirements.

Table D.1 Monotonic tensile properties of the studied 300M steel

$\sigma_{y,0.2}$ (MPa)	σ_{UTS} (MPa)	E (GPa)	ν	% El (%)	G (GPa)
1690	2013	198	0.25	11.5	79.2
1700	2015	196	0.30	11.4	75.4
1690	2032	197	0.30	12.1	75.8
	AMS 6257E Minimum Tensile property requirements				
1585	1930	--	--	8	--

D.2 Plain-strain fracture toughness test results

Fig. D.1 depicts the plain-strain fracture toughness specimen fracture surface for the studied 300M steel. The K_{IC} values obtained for the 2 specimens were 67.37 and 68.8 MPa$\sqrt{m}$.

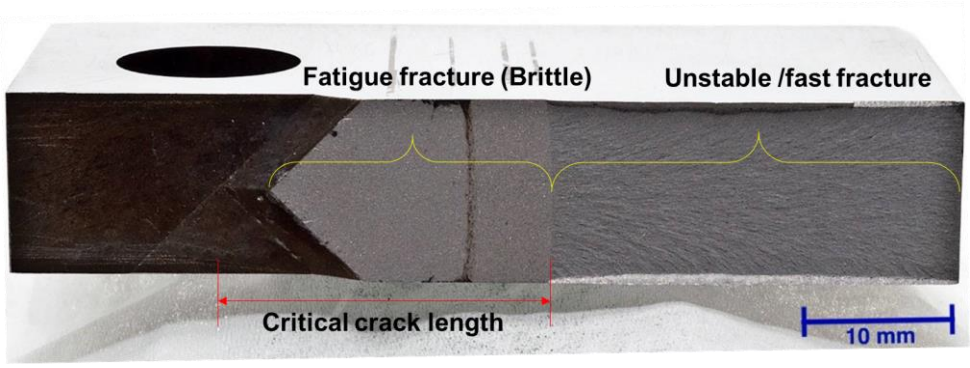

Figure D.1 Fracture surface of 300M steel plain-strain fracture toughness specimen